A Bayesian Approach to the Study of Dark Matter in Disk Galaxies

Peter R. Hague

Submitted in fulfilment of the requirements of the degree of
Doctor of Philosophy

June 25th, 2015

Theoretical Astrophysics Group
Department of Physics and Astronomy
University of Leicester

Abstract

A Bayesian Approach to the Study of Dark Matter in Disk Galaxies

by

Peter R. Hague

Studies of the rotation of disk galaxies have long been used to infer the presence and distribution of dark matter within them. Here I present a new Markov Chain Monte Carlo (MCMC) method to explore the extensive and complex parameter space created by the possible combinations of dark and luminous matter in these galaxies. I present exhaustive testing of this method to ensure it can retrieve dark matter halo parameters from artificial data, and apply it to real galaxies from The HI Nearby Galaxy Survey (THINGS) and other sources. The results of these studies can shed some light on how disk galaxies form and evolve.

Chapters 1 and 2 provide background for the physics and statistical methods respectively. Chapter 3 shows the testing of the MCMC method on artificial data, and applies it to DDO 154 to find a more robust constraint on the inner log slope than previous methods. Chapter 4 applies this method to a broad range of galaxies taken from the THINGS survey, constrains their physical properties, and presents a simple model of feedback to compare with. Chapter 5 applies the method to M33, mapping a degeneracy between the log slope of the dark matter halo and the mass-to-light ratio, that excludes the combination of a cored halo and a light stellar disk. Chapter 6 extends the MCMC method to an earlier stage of analysis by marginalising over the parameter space of possible disk models for simulated galaxies. Chapter 7 presents conclusions and discusses future work that can lead on from this thesis.

Acknowledgements

I would like to acknowledge the support of my supervisor, Mark Wilkinson, and the Theoretical Astrophysics Group at the University of Leicester. I acknowledge the STFC for financial support throughout my PhD. This research used the Complexity HPC cluster at Leicester which is part of the DiRAC2 national facility, jointly funded by STFC and the Large Facilities Capital Fund of BIS.

Chapter 2 Acknowledgements: This work made use of THINGS, "The HI Nearby Galaxy Survey" (Walter et al., 2008). This work is based [in part] on observations made with the Spitzer Space Telescope, which is operated by the Jet Propulsion Laboratory, California Institute of Technology under a contract with NASA. We would like to thank Walter Dehnen, Justin Read, Lia Athanassoula, Rodrigo Ibata for valuable discussions. We wish to thank the anonymous referee for their useful comments. The CosmoMC code was written by Anthony Lewis (Lewis and Bridle, 2002). We would also like to thank Erwin de Blok for providing model data (de Blok et al., 2008) in electronic format. MIW acknowledges the Royal Society for support through a University Research Fellowship. PRH acknowledges STFC for financial support. This research used the ALICE High Performance Computing Facility at the University of Leicester. Some resources on ALICE form part of the DiRAC Facility jointly funded by STFC and the Large Facilities Capital Fund of BIS. The project also made extensive use of the Complexity HPC cluster at Leicester which is part of the DiRAC2 national facility.

Chapter 3 Acknowledgements: This work made use of THINGS, "The HI Nearby Galaxy Survey" (Walter et al., 2008). This work is based [in part] on observations made with the Spitzer Space Telescope, which is operated by the Jet Propulsion Laboratory, California Institute of Technology under a contract with NASA. We would like to thank Walter Dehnen, Albert Bosma and Martin Bourne for valuable discussions. The CosmoMC code was written by Anthony Lewis (Lewis and Bridle, 2002). We would also like to thank Erwin de Blok for providing model data (de Blok et al., 2008) in electronic format. MIW acknowledges the Royal Society for support through a University Research Fellowship. PRH acknowledges STFC for financial support. This research used the Complexity HPC cluster at Leicester which is part of the DiRAC2 national facility, jointly funded by STFC and the Large Facilities Capital Fund of BIS.

Chapter 4 Acknowledgements: This work is based [in part] on observations made with the Spitzer Space Telescope, which is operated by the Jet Propulsion Laboratory, California Institute of Technology under a contract with NASA. The CosmoMC code was written by Anthony Lewis (Lewis and Bridle, 2002). We thank Edvige Corbelli for supplying the initial rotation curve decompositions. We acknowledge Wyn Evans for valuable discussions during a visit by MIW to the Aspen Center for Theoretical Physics, and Simon White for bringing work on M33 to our attention. We are grateful to the anonymous referee for detailed comments which improved the final version of the paper, and

to Carlos Frenk for useful comments. MIW acknowledges the Royal Society for support through a University Research Fellowship. PRH acknowledges STFC for financial support. This research used the Complexity HPC cluster at Leicester which is part of the DiRAC2 national facility, jointly funded by STFC and the Large Facilities Capital Fund of BIS.

Contents

Abstract i

Acknowledgements ii

1 Introduction 1
- 1.1 Background . . . 2
  - 1.1.1 Luminous matter . . . 7
    - 1.1.1.1 Mass . . . 7
    - 1.1.1.2 Non-circular Motions . . . 9
  - 1.1.2 Dark Matter Haloes in Galaxies . . . 9
- 1.2 Galaxy Formation . . . 11
- 1.3 Observational Data . . . 12
  - 1.3.1 Tilted Ring Modelling . . . 12
- 1.4 Hydrodynamical simulation . . . 16
- 1.5 Outline of thesis . . . 17

2 Markov Chain Monte Carlo 18
- 2.1 Monte Carlo Sampling . . . 19
- 2.2 Markov Chain Monte Carlo . . . 19
- 2.3 Specific issues . . . 20
  - 2.3.1 Parameter Correlations . . . 21
  - 2.3.2 Volume Effects . . . 21
  - 2.3.3 Boundary Effects . . . 23
- 2.4 Implementation . . . 25
  - 2.4.1 CosmoMC . . . 25
  - 2.4.2 RainfallMCMC . . . 25

3 Dark Matter In Disk Galaxies - I 27
- 3.1 Introduction . . . 28
- 3.2 Galaxy Models . . . 32

3.2.1 Baryonic components . . . 32
3.2.2 Halo models . . . 35
3.3 Markov Chain Monte Carlo . . . 37
3.3.1 Prior distributions and normalisation . . . 40
3.4 Tests on synthetic data . . . 42
3.4.1 Reduced observational errors . . . 44
3.4.2 Realistic Observational Errors . . . 44
3.4.3 High Surface Brightness galaxy . . . 48
3.4.4 Higher resolution data sets . . . 48
3.4.5 Data sets extending to larger radii . . . 50
3.4.6 Cored Profile Test . . . 53
3.4.7 Free stellar disk parameters . . . 54
3.4.8 High surface brightness test with free stellar parameters . . . 55
3.4.9 Over-estimated errors . . . 56
3.5 Comparison with previous methods . . . 58
3.5.1 Profile fitting . . . 58
3.5.2 MCMC approaches . . . 63
3.6 Application to DDO 154 . . . 64
3.7 Conclusion . . . 72

4 Dark Matter In Disk Galaxies - II **73**
4.1 Introduction . . . 74
4.2 Method . . . 75
4.2.1 Baryonic Mass Modelling . . . 76
4.2.2 Dark Halo Profiles . . . 77
4.2.3 Markov Chain Monte Carlo . . . 78
4.3 Analysis . . . 79
4.4 Results . . . 83
4.4.1 DDO 154 . . . 90
4.4.2 NGC 2403 . . . 90
4.4.3 NGC 2976 . . . 96
4.4.4 NGC 3198 . . . 96
4.4.5 NGC 3521 . . . 98
4.4.6 NGC 3621 . . . 99
4.4.7 NGC 7793 . . . 103

4.4.8 NGC 925 . . . 103
4.4.9 Rejected Galaxies . . . 109
4.5 Discussion . . . 111
4.5.1 Scale length correlation . . . 111
4.5.2 Feedback modelling . . . 115
4.6 Conclusions . . . 118

5 The degeneracy of M33 mass modelling and its physical implications 120
5.1 Introduction . . . 121
5.2 M33 Data . . . 124
5.3 Modelling of M33 . . . 124
5.3.1 Baryonic Mass Models . . . 124
5.3.2 Dark Matter Models . . . 125
5.3.3 MCMC analysis . . . 126
5.3.4 Convergence of MCMC Chains . . . 128
5.4 Results . . . 128
5.4.1 Individual Profiles . . . 129
5.4.2 Log Slope Degeneracy . . . 129
5.4.3 Impact of Rotation Curve Features . . . 133
5.4.4 Alternate mass-to-light priors . . . 135
5.5 Discussion . . . 138
5.5.1 Comparison with Previous Work . . . 138
5.5.2 $\Upsilon_{3.6} - \gamma_{\rm in}$ Degeneracy . . . 141
5.5.3 Alternate Gas Mass Models . . . 142
5.5.4 Comparison with cosmological simulations . . . 144
5.6 Conclusion . . . 144

6 Extending MCMC to disk modelling 146
6.1 Method . . . 147
6.1.1 Disks . . . 148
6.1.2 Likelihood estimates . . . 149
6.1.3 Asymmetric drift . . . 150
6.2 Models . . . 150
6.2.1 Simple models . . . 151
6.2.2 N-body rotation . . . 151
6.3 Results . . . 152

6.3.1 MCMC processing of rotation curves 152
6.4 Discussion 162

7 Conclusion **163**
7.1 Chapter 3 164
7.2 Chapter 4 164
7.3 Chapter 5 165
7.4 Chapter 6 165
7.5 Future work 165

A Removing degeneracy from the $\alpha - \beta - \gamma$ model **167**
A.1 Parameter Transform 168

References **170**

List of Figures

1.1 Constraint on possible rotation curves in v_c/r space 14

2.1 Example of correlated variables 22
2.2 Demonstration of MCMC Boundary Effect 24

3.1 γ_{in} prior distribution 41
3.2 Results for low surface brightness galaxy with small error bars 43
3.3 Results for low surface brightness galaxy with realistic error bars 45
3.4 Distributions of γ_{in} for low and high surface brightness models 45
3.5 Highest likelihood model from the high surface brightness test 46
3.6 Distribution of γ_{in} for a low surface brightness model with twice the sampling density 49
3.7 Results for a low surface brightness galaxy with an extended data range . 50
3.8 Results for a low surface brightness galaxy with a Burkert halo 51
3.9 Results for a low surface brightness galaxy with an additional free parameter for the stellar mass model 51
3.10 γ_{in} versus mass-to-light ratio in the case of a Hernquist profile and free stellar parameters 52
3.11 Results for a low surface brightness galaxy with an additional free parameter for the stellar mass model 53
3.12 Results for the high surface brightness test 56
3.13 Results for the Burkert halo test with artificially inflated error bars 57
3.14 Results for the Herquist halo test with artificially inflated error bars 57
3.15 γ_{in} distributions for Burkert and Hernquist profiles 59
3.16 γ_{in} distributions corresponding to input values of $\gamma = (0.1, 0.5, 0.9)$ 61
3.17 Overview of MCMC output for DDO 154 67
3.18 MCMC results for the DDO 154 test 68

4.1 Ratio of expelled dark matter ΔM_d to expelled baryons ΔM_b 82
4.2 Grid summarising the results of the MCMC process 87

4.3 Grid of rotation curve decompositions for THINGS galaxies 89
4.4 Distribution of $\gamma_{\rm in}$ values produced by the MCMC analysis of NGC 2403 91
4.5 Contour plot of f_Υ versus $\gamma_{\rm in}$ for NGC 2403 92
4.6 Comparison of $\gamma_{\rm in}$ distribution with different fixed IMF priors 93
4.7 Distribution of $\gamma_{\rm in}$ with a higher MCMC temperature 94
4.8 Distribution of $\gamma_{\rm in}$ values produced by the MCMC analysis of NGC 2976 97
4.9 Distribution of $\gamma_{\rm in}$ values produced by the MCMC analysis of NGC 3198 98
4.10 Plot of r_1 versus $\gamma_{\rm in}$ for NGC 3521 100
4.11 Mass-to-light versus r_1 for NGC 3521 101
4.12 Mass-to-light versus r_1 for NGC 3621 102
4.13 γ versus mass-to-light ratio for NGC 7793 104
4.14 Distributions of $\gamma_{\rm in}$ for NGC 7793 using different fixed IMF priors 105
4.15 Mass-to-light ratio versus r_1 for NGC 7793 106
4.16 Rotation curve decomposition of NGC 925 107
4.17 Impact of excluding inner data points on the γ distribution of NGC 925 . 109
4.18 Distribution of $\gamma_{\rm in}$ for NGC 5055 110
4.19 Dark matter core radius versus stellar disk radius 112
4.20 Comparison of MCMC output with simulation 113

5.1 Comparison of χ^2 values for proposed M33 haloes 123
5.2 Rotation curve of M33 130
5.3 Density plot of models produced by chain A1 131
5.4 Best single-model fits of the M33 rotation curve 132
5.5 Relation between $\Upsilon_{3.6}$ and $\gamma_{\rm in}$ in M33 134
5.6 Selection of rotation curves from M33 MCMC chain 135
5.7 Values of $\gamma_{\rm in}$ for the B1 model 136
5.8 Values of $\gamma_{\rm in}$ for B2 137
5.9 Density plot of all models produced by C1 139
5.10 Comparison of $\gamma_{\rm in}$ with two independent mass-to-light ratios 140
5.11 Degeneracy between inner log slope and mass-to-light ratio in M33 . . . 143

6.1 Demonstration of rotation finding with MCMC 154
6.2 Demonstration of finding disks not aligned with coordinate system 155
6.3 Rotation curve of simulated galaxy with cored halo 156
6.4 Relationship between r_1 and mass-to-light ratio for the cored halo case . . 157
6.5 Rotation curve decomposition for the cored halo model 158

6.6 Relation between $\gamma_{\rm in}$ and mass-to-light for the cusped model 159
6.7 Histograms of $\gamma_{\rm in}$ for the cusped case with a fixed mass-to-light ratio . . . 160
6.8 Halo axis ratios as a function of radius in the galaxy models 161

A.1 Comparison of the rotation curves obtained from a family of NFW profiles, illustrating the effect of varying $r_{\rm s}$ and $\rho_{\rm s}$ 168

List of Tables

3.1 Summary of the MCMC parameters 37
3.2 Input parameters for synthetic data sets 38
3.3 Single profile fitting of Burkert and Hernquist haloes 62
3.4 Single profile fitting of DDO 154 69

4.1 Properties of the THINGS galaxies studied 84
4.2 Results of MCMC runs on THINGS galaxies 114
4.3 Inferred gas fractions from feedback model 117

5.1 Properties of the M33 mass model 126
5.2 Properties of MCMC models of M33 128

6.1 Properties of galaxy simulations 150

For Arthur

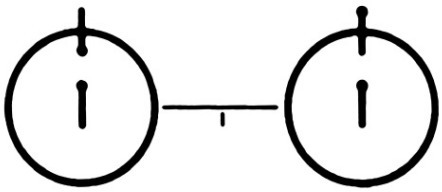

1

Introduction

The Milky Way is the largest structure visible in the night sky in terms of angular size, and its presence clearly indicates that, rather than being isotropically distributed, stars in the night sky are concentrated in a plane. Inferring a three dimensional structure from this anisotropy was first attempted by William Herschel, and later using more modern methods by Kapteyn (1922). Around the same time, thanks to the observations of Edwin Hubble, it became apparent that some of the patches of diffuse light known to astronomers as nebulae were in fact similar galaxies external to our own. We now have an understanding of the shape of our own galaxy, that of other galaxies, and the continuum of shapes they occupy. Galaxies consist of gas, populations of stars, and dark matter, and vary in size from $10^3\ M_\odot$ to over $10^{12}\ M_\odot$.

Galaxies are a product of the largest scale processes in the Universe, tracing their origin to density perturbations that can be observed in the cosmic microwave background (Spergel et al., 2003). The potential wells of their dark matter haloes increase the density of gas within them, and thus dictate the formation of stars and then planets at the smallest scales in astrophysics. This makes them of central importance to many astrophysical phenomena.

Dark matter is responsible for most of the total galactic potential, so must be studied in order to understand the dynamics of galaxies, which in turn is critical to the understanding all other aspects of galactic astrophysics which are ultimately driven by gravity and its interplay with gas physics.

Models of how dark matter is distributed in observed galaxies constrain predictive models of galaxy formation. The potential wells created by dark matter haloes provide the energy for baryon physics, but in turn baryonic phenomena can have a dynamical impact disproportionate to their length and mass scales through processes known as “feedback”. Active galactic nuclei (AGN), supernovae and bright stars are covered by the term, as they are all able to disturb large quantities of gas through their radiation output, which in turn alters the dynamics of the galaxy.

1.1 Background

Mass in the universe can be detected either by the radiation it emits or reflects, or by its gravitational effect. Beginning with the prediction of the planet Neptune, based on the inability to explain the orbit of Uranus using only the gravity of visible objects, the study of gravity has repeatedly implied more mass than can be accounted for by visible objects. Study of this discrepancy continues to be vital in astrophysics, and is complicated by the

fact that neither studying mass via the radiation of sources nor via their motion measures mass directly; modelling of sources is required to infer mass from radiation and modelling of the dynamics of the system is required to detect mass by its gravitational effects.

Oort (1932) measured the vertical velocities and accelerations of Milky Way disk stars, and from this calculated the vertical density profile of the galaxy. This indicated dark matter in excess of that which is present in stars - but it was not a surprising result. In the original sense, the phrase "dark matter" did not have any connotations of being different from ordinary baryonic matter, it simply contrasted with luminous matter (i.e. stars) that could be observed at the time.

What is now understood as dark matter was first proposed by Zwicky (1937) in the 1930s to explain the substantial discrepancy between the mass measurements of the Coma cluster derived through stellar population modelling and through dynamics. Zwicky used the scalar virial theorem

$$U = -2T \tag{1.1}$$

where U is the total potential energy of all particles in the system (at the time also referred to as the virial) and T is their total kinetic energy, with the particles in this case being the galaxies of the Coma cluster. By assuming a uniform distribution of mass, he was able to express this

$$\frac{3GM^2}{5R} = \sum m_{\rm n} v_{\rm n}^2 \tag{1.2}$$

where M is the total mass of the cluster, R is its radius, $m_{\rm n}$ is the mass of a particular galaxy and $v_{\rm n}$ its velocity averaged over time. This gives

$$M = \frac{5R < v^2 >}{3G} \tag{1.3}$$

Where $< v^2 >$ is the average squared velocity of each galaxy. Zwicky assumed an isotropic velocity distribution, and so $< v^2 >= 3 < v_{\rm los}^2 >$ and from this estimated the average mass of each galaxy at $M = 4.5 \times 10^{10}\, M_\odot$. This contrasted with the estimated average luminosity of the galaxies of $L = 8.5 \times 10^7\, L_\odot$, which he interpreted as a mass-to-light ratio for the members of the coma cluster of ~ 500. This was the first indication of substantial dark matter in astronomical systems, but did not immediately generate much impact.

Within external disk galaxies, dark matter is studied by the analysis of rotation curves. If we assume the baryonic disk of a galaxy can be approximated as a series of concentric

rings of particles on circular orbits of velocity v_c at radius r_i in an axisymmetric potential, Equation 1.1 can be written

$$\sum_i \phi(r_i) = -\sum_i v_c(r_i)^2 \tag{1.4}$$

where $\phi(r_n)$ is the gravitational potential at a particular radius, and the total mass of the system is cancelled from both sides. The gas component of a galaxy technically breaks the assumption of the matter being dissipationless, however in a mature galaxy the gas is arranged in the energetically minimal configuration of a thin disk, and as such we can assume it approximately conserves energy and is on non-crossing orbits. Given that the radii r_i are non-overlapping, so that relocating one of the circles would change only the corresponding potential and kinetic energy terms, this equation can be separated simply. In the plane of an axisymmetric potential, at a particular radius, the potential can be produced by a Keplerian potential which we can express in terms of an effective mass $M_{\rm eff}$

$$v_c(r_i)^2 = -\phi(r_i) = \frac{GM_{\rm eff}}{r_i} \tag{1.5}$$

which can also be obtained directly by equating the gravitational force of a mass $M_{\rm eff}$ with the force required to keep an object moving in a circle radius r_i at speed v_c. It is useful to consider it in terms of energy though, as the components of disk galaxies do not all have a spherical geometry.

If we wish to *decompose* the potential of a disk galaxy into various baryonic components and a dark matter halo, we are helped that the above discussion applies to any axisymmetric potential - disks, bulges and haloes alike. Because the total potential is just the sum of the potentials of each component

$$\phi(r_i) = \sum_{m=disk,bulge,halo} \phi_m(r_i) \tag{1.6}$$

or in terms of circular velocity

$$v_c^2(r_i) = \sum_m v_{c,m}^2(r_i) \tag{1.7}$$

where in both cases the index m denotes the different components. By proposing a velocity contribution due to a dark matter halo potential, we can add the velocity contribution due to the various baryonic components (stars, atomic gas, etc.) in quadrature and

produce a prediction for the overall rotation velocity of the galaxy as a function of radius, which can then be compared to observations. This is the general method of studying rotation curves, but is subject to various practical considerations which I will now discuss.

The study of dark matter by the decomposition of rotation curves began with Rubin and Ford (1970) who studied the rotation of M31 measured by the relative doppler shift of the HI line across the galaxy. This line is a hyperfine emission line produced by neutral atomic hydrogen, where the electron transitions from a parallel spin to an anti-parallel spin (Binney and Merrifield, 1998, §8.1). M31 was chosen for its very large angular diameter; its distance was estimated by Freedman and Madore (1990) through the use of the luminosity/period relation for Cepheid variables 770 ± 36 kpc (later work using alternate methods has produced values within 1σ of this, see McConnachie et al., 2005), meaning that an arcsecond corresponds to about 4 parsecs. Despite the excellent resolution, M31 does not have an ideal rotation curve for analysis for a number of reasons. Due to the fact that the M31 system has a line of sight velocity $v_{\rm LOS} = -301 \pm 1\,{\rm kms}^{-1}$ (van der Marel and Guhathakurta, 2008) and the flat part of its rotation curve is at $v_{\rm rot} \sim 250\,{\rm kms}^{-1}$ (Carignan et al., 2006) the receding side of the galaxy is subject to foreground contamination from atomic gas in the Milky Way (Cram et al., 1980). The central region of M31 ≤ 6 kpc is lacking in HI emission (Sofue and Kato, 1981), and as Figure 2 of Carignan et al. (2006) shows the rotation curve is essentially flat outside this point precluding any study of its shape. Other emission lines are not able to give the circular velocity as the stellar emission in the area of interest is dominated by the bulge (Widrow et al., 2003) and the molecular gas there shows complex non-circular motions (Stark and Binney, 1994).

In later work, Bosma (1981), was able to exploit higher resolution and better sensitivity to study galaxies with smaller angular diameters, and was able to measure the rotation curve to a radius 2-2.5 times the Holmberg radius (the radius of the 26.5 mag arcsec^{-2} isophote in the B band) which can be taken to define the outer edge of the visible stellar disk and thus the limit of the continuous contribution of stars to the rotation curve. This demonstrated the advantage of using the rotation of HI; the neutral gas disk of a galaxy extends to much greater distances than its stellar component, and has a smaller overall contribution to the enclosed mass at each point. Thus it allows the rotation to be studied at radii where baryons are a very marginal contribution to the gravitational potential, and the presence of dark matter is most apparent. Furthermore, HI emission is not absorbed by dust, and the atomic gas clouds are optically thin (Walter et al., 2008), allowing a straight conversion of flux to mass in each beam.

As the results from rotation curve analysis were beginning to suggest the presence of

dark matter within galaxies, an alternative explanation for the shape of rotation curves was proposed. Milgrom (1983) proposed that either gravity or inertia behaved differently below a certain acceleration a_0, such that $F = \mu m(a/a_0)a$, and that this would allow the fitting of rotation curves with only the visible mass. This was proposed purely to fit the observed data of galaxy rotation curves, and cannot explain galaxy clusters without the presence of some dark matter in the form of massive neutrinos (Sanders, 2003). Given this, and the cosmological evidence for dark matter given below, I will not be considering modified gravity further in this thesis.

Results from large scale cosmology also point to the existence of dark matter, and imply that it is non-baryonic in nature. The results from the WMAP (Wilkinson Microwave Anisotropy Probe) satellite presented in Spergel et al. (2003) provided compelling evidence that the baryon density Ω_b is roughly 17% of the matter density Ω_m, indicating that the overwhelming majority of the matter in the Universe is not baryonic. These two densities, and the other parameters of the ΛCDM model, are constrained by the acoustic peaks of the cosmic microwave background. A denser baryon fluid responds more slowly to the radiation pressure that acts against gravity as it falls into a potential well, and thus the maximum compression of oscillations in the early universe is larger if the baryon fraction is larger, whilst the maximum rarefaction remains them same. This manifests observationally as a difference between the magnitudes of odd numbered acoustic peaks in the CMB (representing the case where the oscillation was near maximum compression at the last scattering time) and the even numbered peaks (where the oscillation was near maximum rarefaction at this time). The baryonic density is also constrained by the cosmic deuterium abundance (about 10^{-5} relative to hydrogen from e.g. Burles et al., 2000), as the rate of nuclear reactions during the epoch of nucleosynthesis is determined by the baryon density (Gamow, 1946), and a high rate would see more deuterium converted to helium-4 thus reducing the deuterium abundance. This relation was shown numerically by Wagoner (1973). The deuterium abundance was fixed within minutes of the Big Bang, whereas the properties of the CMB are observed at ~400,000 years after the Big Bang, so the agreement of these results makes a strong case that the majority of matter in the universe is non-baryonic (Spergel et al., 2003). Constraints on the densities $\Omega_b h^2$ and $\Omega_m h^2$ have been more recently confirmed and refined by the results from the Planck satellite (Planck Collaboration 2013).

The distance and velocity of M31 relative to the Milky Way provide an additional test of dark matter in the Local Group. The expansion of the Universe will make all galaxies tend to recede, and so in order for M31 and the Milky Way to be moving towards

one another, their mutual attraction must reduce the distance between them more than the expansion of space increases it. This calculation was first done by Kahn and Waltjer (1959), who found a considerably larger mass than expected in the Local Group. To find a minimum mass they considered the two galaxies to be in a Keplerian orbit around their common centre of mass, with a period roughly equal to the Hubble time so that M31 is on its first infall, and applied Kepler's third law assuming no angular momentum

$$T^2 = \frac{4\pi^2}{GM} a^3 \tag{1.8}$$

where $T = 1.5 \times 10^{10}$ years, M is the total mass of the local group and G is the gravitational constant. This equation yields a, the semi-major axis of the assumed orbit. This represents the maximal separation of M31 and the Milky Way, at which they will have no relative radial motion. Thus a comparison of the conserved energy of the system at that point to the current state

$$\frac{GM}{2a} = \frac{GM}{D_0} - E_0 \tag{1.9}$$

where D_0 and E_0 are the present separation and kinetic energy per unit mass, uniquely constrains the total mass. Kahn and Waltjer (1959) found $M \geq 1.8 \times 10^{12} M_\odot$ using values for D_0 and E_0 that are of the same order as current estimates.

A recent 3D model of the local group (van der Marel et al., 2012), combining proper motions with the radial velocities already available for the main Local Group members (including M33), has constrained the mass of the Local Group to be $(3.17 \pm 0.57) \times 10^{12}\ M_\odot$, in agreement with values estimated by the timing argument.

1.1.1 Luminous matter

1.1.1.1 Mass

Determining the amount of dark matter present in a system requires determining the total mass present along with the total luminous mass present. In Zwicky's study of the coma cluster galaxies, the luminous matter was stars, but it is now possible to account for atomic hydrogen, molecular hydrogen (by observing more accessible transitions in CO molecules and applying a factor X_{CO} - see below) and dust. A contemporary example of this kind of mass decomposition can be found in Corbelli et al. (2014).

Much of the baryonic matter in galaxies is locked up in stars. The only data we have on stars at extragalactic distances is their emissions, so a means to convert the luminosity of

a stellar population into a mass is required in order to perform a rotation curve analysis. This conversion can be expressed as a mass-to-light ratio in a specific band, e.g. $\Upsilon_{3.6}$ would be the number of solar masses per solar luminosity in the Spitzer 3.6 μm band.

The stellar mass-to-light ratio is found to correlate with colour (Bell and de Jong, 2001), although it is subject to uncertainty due to the parameters of the stellar population and evolution models, and observational issues such as dust reddening. The relation between colour and stellar mass is a consequence of both the initial mass function (IMF) and evolutionary history of stellar populations. The IMF gives the number of stars formed of a given stellar mass in a single star formation event i.e. a single giant molecular cloud collapsing under gravity and fragmenting due to Jeans instability. The simulated evolution of a population selected from this function predicts the colour of stellar populations. A typical IMF is a power law such as $N(M) = N_0(M/M_\odot)^{-2.35}$ (Salpeter, 1955) where N_0 is a constant representing the scale of the star formation. Observational constraints on this law are more difficult at the low mass (and thus low luminosity) end, and so there are competing values for the slope of the power law below $1M_\odot$, such as the proposal by Kroupa (2001) which uses a piecewise power law IMF $(M/M_\odot)^{-\alpha}$, having exponents $\alpha = 0.3 \pm 0.7, 1.8 \pm 0.5, 2.7 \pm 0.3$ at stellar masses $(M/M_\odot) < 0.08, 0.50, 1.00$, and being compatible with the Salpeter IMF beyond that.

Atomic hydrogen is the simplest baryonic component of the galaxy to model due to the directness of HI observation, and the fact that it extends further than other components. This means that its velocity, rather than the velocity of the stellar component, is used in the construction of modern rotation curves.

Molecular hydrogen cannot be observed directly as the symmetrical molecule has no dipole, and generally occurs in clouds too cool to excite other modes, and so carbon monoxide is used a tracer of molecular gas (Leroy et al., 2009). A conversion factor $X_{\rm CO}$ is then applied. This relation between molecular hydrogen and CO has some uncertainty, as it is derived from Milky Way observations of molecular clouds with known mass (Dame et al., 2001), which is assumed to be universal. $X_{\rm CO}$ can be calibrated by studying the width of the CO line for spatially resolved molecular clouds (Solomon et al., 1987). The line width gives the velocity dispersion, and the size of the cloud is calculated from the distance and the size of the cloud on the sky.

$$S = D\tan(\sqrt{\sigma_{\rm l}\sigma_{\rm b}}) \tag{1.10}$$

Where S is the size parameter, D is the distance and $\sigma_{\rm l}$ and $\sigma_{\rm b}$ are the variances (i.e. the angular size of the emission) in Galactic longitude and latitude. This allows the total

mass of the cloud to be computed via the virial theorem, in a manner not dissimilar to the method described in §1.1.

$$M = 3 f_{\rm p} \frac{S \sigma_{\rm v}^2}{G} \tag{1.11}$$

Where $\sigma_{\rm v}$ is the line-of-sight velocity dispersion and $f_{\rm p} = 2.9$ is the projection factor, the ratio between $\sigma_{\rm v}$ and the total squared velocity dispersion. This formula allows dynamical masses of resolved molecular clouds to be computed, which can then be compared to the luminosity of CO emission to determine $X_{\rm CO}$.

The stellar mass-to-light ratio is the main uncertainty in the amount of luminous matter present in a galaxy, as the atomic gas is optically thin and the molecular gas is generally a lower mass component than both stars and atomic gas in nearby galaxies; Leroy et al. (2009) found that for the HERACLES galaxies (48 nearby galaxies, overlapping with the THINGS galaxies) the largest H_2-to-stellar mass ratio was 0.25, and only one galaxy had a H_2-to-HI ratio greater than 1, integrated over the optical disk.

1.1.1.2 Non-circular Motions

When constructing a one dimensional rotation curve, it is generally assumed that the non-circular motions of a galaxy will be outweighed by the overall circular motion. Non-circular motion formally has two components - radial and vertical - but the vertical component is typically small ($\leq$10 km/s in van der Kruit, P. C. and Shostak, 1982; Andersen et al., 2006) in HI disks due to the cooling of the gas, and so when studying HI rotation curves non-circular motion is generally taken to be radial. Random, symmetric deviations from circular motion are not especially problematic, as they will just be reflected in larger error bars. Systematic deviations may change the apparent circular velocity and thus the result of any analysis. Systematic deviations can be caused by asymmetric drift, azimuthal variation within the disk such as spiral arms, or by triaxiality of the dark matter halo (Schoenmakers et al., 1997).

The assumption of generally circular motion was found to hold for the THINGS galaxies by Trachternach et al. (2008), who performed a harmonic decomposition of the velocity fields in the survey, using a tilted ring model to subtract the circular motion component. The amplitudes of the remaining components, added in quadrature, were found to be 4.5 ± 2.9% of the maximum rotation velocity of the galaxies.

1.1.2 Dark Matter Haloes in Galaxies

While the ubiquity of dark matter haloes around galaxies is by now well established, observational determinations of the density *profiles* of galactic dark matter haloes have been, and remain, controversial. Flores and Primack (1994) used gravitational lensing and rotation curve analysis to argue against cusped haloes with $\rho(r) \sim r^{-1}$ and $\rho(r) \sim r^{-2}$, which were being predicted by N-body simulations of cosmological structure formation at that time (e.g. Dubinski and Carlberg, 1991, who found that the r^{-1} profile proposed by Hernquist (1990) best fit the haloes they obtained). During the 1990s, dark matter-only cosmological simulations continued to suggest that a universal, cusped dark matter density profile, independent of halo mass, should be the outcome of the hierarchical formation scenario for galaxy haloes (Navarro et al., 1996, hereafter NFW):

$$\frac{\rho(r)}{\rho_{\rm crit}} = \frac{\delta_{\rm c}}{(r/r_{\rm s})(1 + r/r_{\rm s})^2} \tag{1.12}$$

where $\rho_{\rm crit}$ is the critical density of the Universe, $r_{\rm s}$ is a scale radius equal to r_{200}/c with r_{200} being the virial radius and c being a concentration parameter that is only the free parameter in the model. $\delta_{\rm c}$ is a dimensionless parameter related to the concentration parameter by $\delta_{\rm c} = (200/3)(c^3/[ln(1 + c) - c/(1 + c)])$. Burkert (1995) proposed a cored profile - one with a uniform density interior to a finite core radius - based on the observations made at the time (e.g. Moore, 1994; Flores and Primack, 1994);

$$\rho(r) = \frac{\rho_0 r_0^3}{(r + r_0)(r^2 + r_0^2)} \tag{1.13}$$

where ρ_0 and r_0 are a density scale and a scale radius. As with the NFW profile, this tends towards a log slope dlogρ/dlogr $= -3$ at large radii. Given the resolution of the simulations which led to the NFW profile being proposed, and the fact they only included dark matter, it is reasonable to expect the profile to be most accurate at large radii where the potential is dominated by dark matter. The apparent disparity between the results of cosmological simulations and observations of real galaxies became known as the "cusp-core controversy".

Early work to resolve this controversy focused on low surface brightness (LSB) galaxies, on the basis that the stellar contribution could be ignored entirely in a first-order model. In van den Bosch and Swaters (2001) it was claimed that it was impossible to differentiate between flat cores and r^{-1} cusps using the data available at the time. They cited the insufficient radial range of the data, and the problem of beam smearing. Beam

smearing of HI rotation curve data is caused by the fact that each beam is larger than the scale over which the rotation speed changes. This, and several other observational issues that could lead to the false inference of cored haloes in galaxies which actually contained dark matter cusps, were investigated and discounted by de Blok et al. (2003). Deriving mass profiles from rotation curves without baryonic mass modelling, for a set of dark matter dominated galaxies, they also found that the outer regions of their sample galaxies were consistent with density profiles $\rho \sim r^{-2}$ while the inner regions required power laws which were typically shallower than $\rho \sim r^{-0.25}$.

Bosma (2003) claimed to rule out r^{-1} cusps at the 3-sigma confidence level for 17 galaxies (from a sample of 28) and, on this basis, stated that the slopes predicted by CDM models were not observed. He demonstrated that the position of the slit used at the time to observe rotation curves could not have been a factor in this result, by deliberately offsetting the slit and observing the effect on the measured rotation curve. Gentile et al. (2004) subsequently found that, when compared to the rotation curves of five nearby galaxies along with a baryonic mass model, the cored Burkert profile produced fewer discrepant data points ($> 2\sigma$) than the cusped Navarro-Frenk-White (NFW) in all cases. It should be noted that the exclusion of cusps in present-day galaxies is not synonymous with invalidating the ΛCDM paradigm, as baryonic effects could alter the haloes over time.

1.2 Galaxy Formation

Early galaxy formation is dominated by gravity and thus by dark matter. This is why hydrodynamics is not thought to be a major factor in large scale structure formation. Only when dark matter haloes form, and the in-falling baryons become dense, does hydrodynamics become critical. My work is concerned with disk galaxies, which are distinguished by their comparatively high angular momenta and gas content compared to elliptical galaxies.

Gas is able to form disks due to the fact it can radiate energy. For a given angular momentum, a disk is the configuration with the least energy, and therefore the state towards which radiating gas tends. This can also be understood in terms of momentum. Consider a spinning halo of gas in a co-rotating cylindrical coordinate system which is coaxial with the net angular momentum. Each particular particle with momentum in the z direction p_z, can be uniquely partnered with another particle (or combination of particles) with momentum $-p_z$. Such symmetry does not exist in L_z because there is net rotation in

the gas. Thus given a sufficient number of particle collisions (such that momentum can be transferred anywhere) there is no lower limit to the total magnitude of vertical motion $\Sigma|p_z|$ but angular momentum L_z must be retained, which describes a tendency towards an infinitely thin disk. This flattening increases the density of gas, leading to star formation, which accounts for why the majority of stars in such galaxies occur in the disk rather than the halo.

Feedback sources can alter the distribution of baryons in a galaxy, thereby altering the potential, and this can then impact the distribution of dark matter. This can be demonstrated through simulation, but in many cases it is useful to investigate galaxies using simpler approximate models. For example King (2003) was able to demonstrate how transitions from momentum-driven to energy-driven outflows from AGN are able to account for the $M - \sigma$ relation (the empirical relation between central black hole mass and velocity dispersion of a galactic bulge) through a simple spherically symmetric model. More complex numerical models (e.g. Zubovas and Nayakshin, 2014; Bourne et al., 2014) differ on small scales, but do not contradict the overall result. A mechanism by which matter can be removed from the centres of dark matter haloes to transform cusps into cores was discussed both through an analytical model and through simulations by Pontzen and Governato (2012), and another analytical model that transfers energy from oscillating baryons to those dark matter particles in resonance with the oscillation is proposed in Ogiya and Mori (2012).

Feedback from supernovae can, in galaxies with low mass, expel gas from a galaxy entirely and thus reduce the amount available for future star formation (Dekel and Silk, 1986). In higher mass disk galaxies, supernova feedback generates turbulence which leads to further star formation (Kim et al., 2011). In this model, the energy imparted into the interstellar medium by supernovae causes the gas disk to expand and become turbulent, and then as it cools more star formation occurs. A steady star formation rate is established when the rate at which energy is imparted matches the cooling rate. AGN feedback events are more powerful and can expel gas, entirely suppressing star formation as supernovae do in smaller galaxies (leading to the $M - \sigma$ relation described above), but they can also trigger star formation through compression of gas clouds too dense to be removed (Zubovas et al., 2013).

An approach to understanding these issues must bring together observational techniques and simulations, and attempt to find common agreement between them.

1.3 Observational Data

HI observations are now at the stage of being able to resolve galaxies at a resolution of $\sim 100\,\mathrm{pc}$ out to distances substantially greater than the extent of the stellar disk. In surveys such as THINGS (Walter et al., 2008), a grid of beams produces not only an image of the galaxy in HI, but a velocity profile in each beam based on the doppler shift of the emission line. These data are referred to as a velocity field. Hermite polynomials can be fitted to the HI spectrum of each beam, producing a series of 2D moment maps, which can then be used as input for a tilted ring model (detailed below).

1.3.1 Tilted Ring Modelling

The tilted ring model is a standard way of producing one-dimensional rotation curves of disk galaxies. It involves fitting concentric rings to a velocity field, and adjusting the parameters of these rings (an inclination and an azimuth) until the circular velocities they predict match the data well. The procedure is outlined in Begeman (1989).

This method assumes that the dominant velocity present in the galaxy is circular, and that any non circular motion is to be treated as noise to be removed by averaging over all azimuths. In other words, only that matter moving on or close to a circular orbit is considered useful as a tracer of the galactic potential. Each ring/bin of the model can be considered one of these circular orbits. This is the correct approach if a one dimensional rotation curve is required.

One current issue with rotation curves calculated through this method, as shown in papers such as Chemin et al. (2011), is that a number of quite different profiles all appear to provide fits with low χ^2_{red} values. This is a combination of two issues that are not well addressed in rotation curve studies at this time. First, the geometry of a disk galaxy limits greatly the possible rotation curves that can exist, and so an apparent good fit in the r versus v_{c} plane may be not be as significant as it appears. Figure 1.1 shows the rotation curves of two sample $\alpha - \beta - \gamma$ profiles:

$$\rho(x) \propto \frac{1}{x^{\gamma}(1 + x^{1/\alpha})^{\alpha(\beta-\gamma)}} \tag{1.14}$$

where $x = r/r_{\mathrm{s}}$ is a scaled radius and α, β, and γ are shape parameters. In one case $(\alpha, \beta, \gamma) = (1, 3, 0)$ and in the other $(\alpha, \beta, \gamma) = (1, 3, 1)$ - equivalent to an NFW halo. Both examples have a maximum velocity of 100km/s and a scale radius of $r_{\mathrm{s}} = 4\,\mathrm{kpc}$. Despite being analytically very different solutions, both of these extremes occupy a fraction of

the plane, and all haloes with inner log slopes between these two values would lie in this band.

Secondly, the rotation curves do not satisfy the assumptions behind χ^2 - specifically it is not clear that either the data points are independent, or that the reported errors are accurate and Gaussian.

These problems can be clearly illustrated by considering how a rotation velocity is calculated. Considering the outer region of the galaxy, where the majority of the potential is due to a spherically symmetric dark matter halo, we can state

$$v_{c,1}^2 \simeq \frac{GM}{r} \tag{1.15}$$

and

$$v_{c,2}^2 \simeq \frac{G(M + \Delta M)}{(r + \Delta r)} \tag{1.16}$$

Where $v_{c,1}$ and $v_{c,2}$ are any two data points in the outer region, M and r are the enclosed mass and radius at the first point, Δr is the difference in radius between the two points and ΔM is the mass of the shell of dark matter between the two bins. By substituting for the gravitational constant G in Equation 1.16 we can work out what fraction of mass enclosed at $r + \Delta r$ is in the shell between r and $r + \Delta r$, obtaining

$$\frac{\Delta M}{M} = \frac{v_{c,1}}{v_{c,2}} \left(\frac{r + \Delta r}{r} \right) - 1 \tag{1.17}$$

Assuming that this part of the rotation curve is not steeply rising, we can say the relative increase in enclosed mass $\Delta M/M$ is approximately equal to the relative increase in radius between the two data points $\Delta r/r$. It is thus obvious for most good rotation curves that the great majority of the mass enclosed at a particular radial bin is enclosed at bins interior to it. By this argument any curve that minimises the error in velocity at radial bin n will also be closer to minimising the error at bin $n+1$ than an independently selected velocity curve would be - the interior data point essentially acting as a prior. However the contribution to the χ^2 at this new point will still be counted as if it were an independent bin in most analyses, which is statistically incorrect.

A further complication is the method by which the errors are derived using the tilted ring method. Reported errors on rotation curves derived using this method are based on the distribution of azimuthal velocity (the difference between the median values on the approaching and receding sides of the galaxy in the case of de Blok et al., 2008). This contains the implicit assumption that all deviations from the circular velocity around a

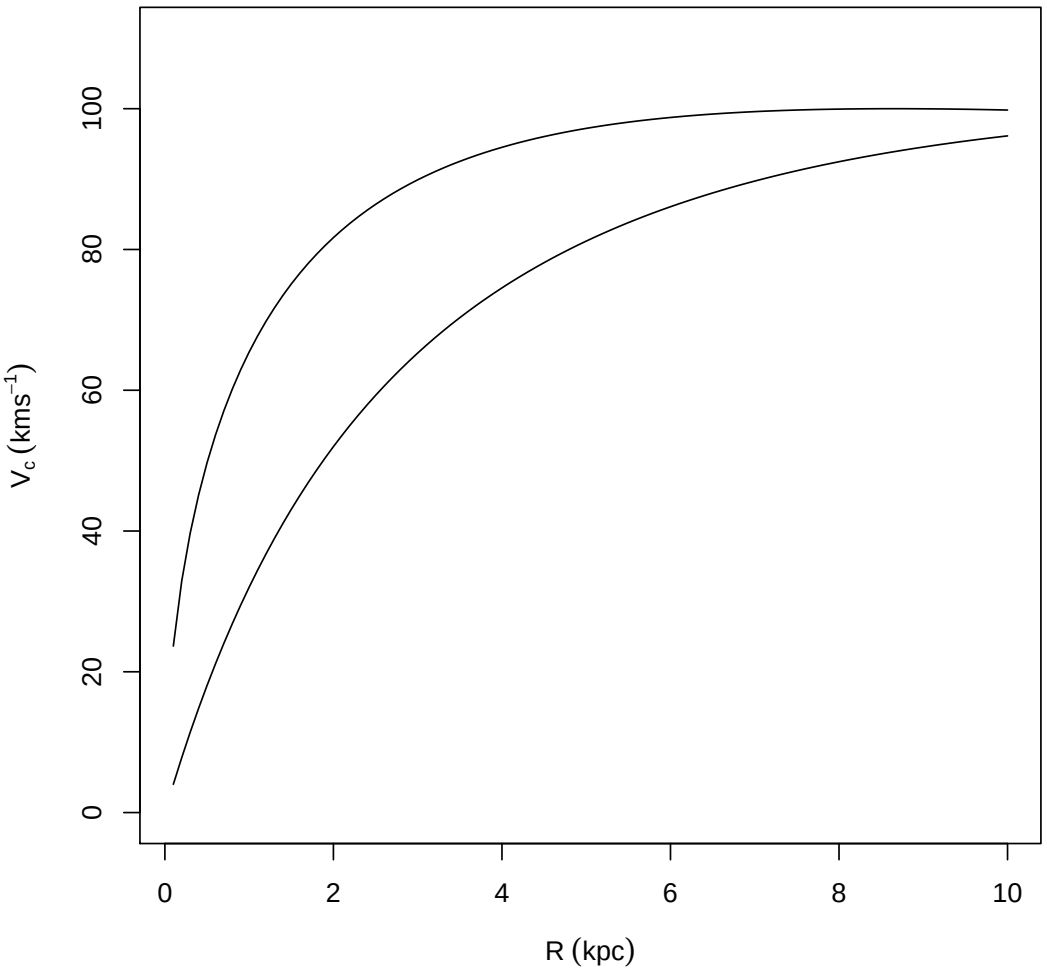

Figure 1.1: Modified NFW halo rotation curves with $\gamma = 0$ (lower curve) and $\gamma = 1$ upper curve. Both profiles have maximum velocity $v_{\max} = 100\,\mathrm{km/s}$ and scale radius $r_s = 4\,\mathrm{kpc}$.

particular ring are due to random motions that are separable from the overall circular motion through the epicycle approximation. In reality, non-circular motions may be systematic if there is significant asymmetric drift or the potential is asymmetric. The tilted ring model provides a good estimate of the rotation curve under the *assumption* of circular motion, but calculating a χ^2 value of the resultant rotation curve and its errors reifies this assumption, and produces a misleading estimate of the precision of the rotation curve determination.

To extend meaningfully beyond the tilted ring model, the assumption of pure circular motion must be abandoned. This immediately leads to the problem that, without a constraint on the inclination at the point a beam intersects the galaxy, circular velocity is degenerate with the tangental velocity, radial velocity, and total velocity. Furthermore, there is no longer a simple way to translate the speed of the matter in each beam to the potential of the galaxy.

Despite these limitations, the tilted ring model is a good enough approximation of the kinematics of a galaxy to use for the purposes of finding a radial density profile, and the errors are only problematic if they are interpreted incorrectly. By taking all points along a projected circle to be kinematically equivalent, the tilted ring model gives a (constrained) three dimensional velocity structure by viewing ostensibly identical points in the galaxy from different angles relative to their azimuth. Any attempt to extract more than line-of-sight velocity information from galaxy images must rest on assumptions (except in the case where a galaxy is close enough to provide proper motions) and the assumptions of the tilted ring model produce reasonable estimates of circular velocity.

1.4 Hydrodynamical simulation

As was mentioned earler, in order to bring simulation into closer agreement with observation, modelling of the hydrodynamics of galaxy formation is required. The profile of a galactic halo results from the interplay between a number of factors including the intrinsic physical properties of dark matter, the re-distribution of baryonic material by gas cooling, supernovae or AGN feedback, and its history of major or minor mergers with other galaxies (see e.g. Read and Gilmore, 2005; Maccio et al., 2011; Governato et al., 2012, for recent simulations of these processes at work on galaxy scales). Cored haloes may originally have had cusps - observations of the present day profiles constrain the end-state of galaxy formation, rather than the initial conditions. Because many baryonic phenomena occur at far smaller scales than the galaxies that they can radically impact, it

is not possible to directly simulate galaxies with enough resolution to produce analogues of real galaxies. In the case of black hole feedback, the radius of influence r_{I} of a central black hole is given (Binney and Tremaine, 2008, p. 352) by

$$r_{\mathrm{I}} = 11(M_{\mathrm{BH}}/10^8\,M_\odot)(\sigma_{\mathrm{LOS}}/200\,\mathrm{kms}^{-1})^{-2}\,\mathrm{pc} \tag{1.18}$$

where M_{BH} is the black hole mass and σ_{LOS} is the line-of-sight velocity dispersion of the galactic bulge. A sample of galaxies from Gültekin et al. (2009) shows a maximum $\sigma_{\mathrm{LOS}} \simeq 400\,\mathrm{kms}^{-1}$ which would give, for a $10^8\,M_\odot$ black hole, a radius of influence $r_{\mathrm{I}} = 16\,\mathrm{pc}$. This gives a characteristic timescale of $\sim 10^5$ years, far shorter than the timescales at which even individual galaxies must be simulated. Likewise, to simulate stellar feedback completely would require the simulation of all star formation and thus of individual stars (even of those stars with too little mass to contribute to feedback). A small cosmological starting point of a 10 Mpc side cube, at the critical density ρ_c, assuming a Hubble constant $H = 70\,\mathrm{kms}^{-1}\mathrm{Mpc}^{-1}$, would have a mass of $\sim 10^{14}\,M_\odot$. Thus to have enough particles to simulate individual stars would require the calculation of $\sim 10^{28}$ mutual forces, which is intractable even with simplifying algorithms. Some prescription of sub-resolution physics must therefore be introduced in order to overcome these problems.

This has been attempted in work such as Governato et al. (2007) and more recently in Illustris (Vogelsberger et al., 2014) and EAGLE (Evolution and Assembly of Galaxies and their Environments, Schaye et al., 2014). In both cases, the sub-grid model used is calibrated to produce a population of galaxies consistent with observed empirical relationships, such as those between stellar luminosity and dynamical mass (Trujillo-Gomez et al., 2011). Whilst successful, this process intentionally ignores the dynamics of the inner parts of the galaxy because they are far less clearly constrained and thus less able to provide a clear relationship across galaxies for comparison with simulations.

1.5 Outline of thesis

My work is a study of the kinematics of nearby galaxies, in order to determine the mass distribution of dark matter in these galaxies. From this it is possible to make inferences about the histories of these galaxies.

A starting point for my kinematic studies of dark matter in nearby galaxies was to produce a more generalised version of the previous one-dimensional work that has been done in this field. The current method (used for example in de Blok et al., 2008) applies

tilted rings to a velocity field, and then calculates the χ^2 values for various baryonic mass model/halo profile combinations. I have used Markov Chain Monte Carlo (MCMC), a Bayesian method that produces more informative results when applied to rotation curve modelling than maximum likelihood fitting. This thesis presents my work as follows:

Chapter 2 is a general discussion of Markov Chain Monte Carlo, and some specific issues that have arisen through this application of it.

Chapter 3 is a published paper (Hague and Wilkinson, 2013) that tested the MCMC method of constraining dark matter halo parameters against artificial rotation curves.

Chapter 4 is based on Hague and Wilkinson (2014) and applies the above method to a selection of galaxies from the THINGS survey, and also attempts to relate the result to feedback models.

Chapter 5 is based on Hague and Wilkinson (2015) and covers the particular case of M33, and some previous claims that have been made about this galaxy.

Chapter 6 is an as yet unpublished project which uses my new MCMC code `RainfallMCMC` and extends the scope of the MCMC method to the process of extracting circular motion from galaxies by constraining parameters of a disk model.

Chapter 7 presents general conclusions and suggestions for future work.

2

Markov Chain Monte Carlo

Here I provide a brief overview of Markov Chain Monte Carlo (MCMC) and its utility over earlier Monte Carlo methods. I also discuss the specific codes used in this thesis to implement MCMC.

2.1 Monte Carlo Sampling

Monte Carlo methods are united by the concept of random sampling of a parameter space, rather than doing so uniformly. Given a parameter vector $\mathbf{x}$, and wanting to find the posterior probability function $P(\mathbf{x})$, a discrete set of samples $\mathbf{x}_0, \mathbf{x}_1, ...$ is used to estimate the function. Monte Carlo methods are differentiated by their sampling techniques, and the means by which the sample is used to estimate $P(\mathbf{x})$.

Monte Carlo methods estimate a function randomly sampled N times in a volume of parameter space as

$$\int f dV \simeq V < f > \pm V \sqrt{\frac{< f^2 > - < f >^2}{N}} \tag{2.1}$$

where f is the function of interest, and N is the number of sampled points in that parameter space (Press et al., 2007, §7.7). For a large parameter space with many dimensions, this can require a prohibitively large number of samples.

2.2 Markov Chain Monte Carlo

Markov Chain Monte Carlo (MCMC) improves on this approach in that the samples are generated by a Markov chain, a sequence where each element x_{i} depends on the previous element $x_{\mathrm{i}-1}$.

The aim is to produce a list of points in parameter space $\mathbf{x_1}, \mathbf{x_2}, ...$ such that the number of points in any volume V is proportional to the likelihood of the function being evaluated f i.e.

$$N_{\mathbf{V}} \propto \int_{\mathrm{V}} f dV \tag{2.2}$$

A method of doing this is explained in Hastings (1970). If the points in the chain are distributed according to a non-normalised probability density function $\pi = Af$ where A is an unknown normalising constant, then there exists a transition function $p(a, b)$ (the probability of moving from point a to point b) such that

$$\sum_a p(a,b)\pi(a) = \pi(b) \tag{2.3}$$

and if the Markov chain obeys this transition function (which is straightforward enough to do by appropriately designing the function of $\mathbf{x}_{n-1}$ which selects $\mathbf{x}_n$) then a new point added to the end of the chain will also follow the probability density function π. This is the equilibrium state for the chain - if the models follow the distribution π then all subsequent models will also. If a Markov chain is allowed to explore a parameter space for long enough in such a way that all points can be reached, then after a long enough time it will find this state. In practice, "long enough" is a manageable number of models ($\sim 100,000$ is sufficient in the cases explored here) when an appropriate point selection function is used.

The particular version of MCMC described in Hastings (1970) (generalising the work of Metropolis and Rosenbluth (1953)) is known as the Metropolis-Hastings algorithm, where each parameter vector $\mathbf{x}_i$ is selected from a Gaussian distribution centred on $\mathbf{x}_{i-1}$. The purpose of this is to evaluate Bayes' theorem for any volume within parameter space

$$P(M_V|D) = \frac{P(D|M_V)P(M_V)}{P(D)} \tag{2.4}$$

Where D represents the data being evaluated and M_V the set of models within volume V. We want to know what the probability of a model being true is, given the data available (the *posterior probability* $P(M_V|D)$). Bayes' theorem allows us to derive this from the probability of the model producing the data (the *likelihood* $P(D|M_V)$) and the probability of the model independent of the data (the *prior probability* $P(M_V)$. $P(D)$ is generally assumed to equal 1 (i.e. the data is certainly the data). In this case, I apply the Metropolis-Hastings algorithm to the likelihood of a mass model fitting the rotation curve data, as a function of the parameters of the mass model.

2.3 Specific issues

The following are some issues I encountered using MCMC, and solved in the course of the work presented in Chapters 3-6.

2.3.1 Parameter Correlations

When the model parameters over which MCMC acts are chosen manually, there is the potential for correlation. Two parameters are correlated if the distribution of likelihoods for one parameter changes when the other parameter value is altered. If a region of high likelihood (for example, a region enclosing 68% of all models thus approximating a 1σ contour) has a clear diagonal axis in the plane described by the two parameters, this indicates they are correlated.

Correlation is troublesome because it weakens the constraint that can be found on either parameter. This can be understood by picturing a histogram of each parameter being a projection of the plane it describes with another parameter onto the axis. If the two parameters are correlated, the high likelihood region will be smeared out, compared to a purely independent case. For example, in Figure 2.1 correlated parameters x and y are selected from a Gaussian distribution of width 1, however the centre of the Gaussian in y is displaced by $x/2$. If this distribution were to be projected on to the y axis, the width of the distribution would be ~ 1.25.

One solution to this problem is Principal Component Analysis (PCA). The goal of this is to find the set of parameters that form orthogonal axes for the high likelihood region. In Chapters 3-6 we did this manually in our shift from the parameter ρ_s to v_{max}, in order to remove the correlation between the former and r_s. In general such manual realignment of the parameter axes is more time consuming and subject to human error than mathematically formal PCA, but in this case it allowed us to choose a new parameter that we found physically meaningful whilst resolving the correlation.

2.3.2 Volume Effects

The goal of MCMC is to produce a non-normalised likelihood distribution over a given parameter space. The output of the actual algorithm, however, is a list of models visited. The density of these models in any sub-volume of the parameter space should only depend on the likelihood function in that volume. However, this is not always the case.

If there is a region of the parameter space where one or more of the parameters no longer has an influence on the likelihood of the model, and models in this region have an adequate (but not optimal) likelihood, then the overall distribution of models may be biased towards this region and away from the actual optimal likelihood. This is analogous to the problem of generating a uniform distribution of points in circular coordinates (r, θ) - the fact that θ covers a smaller distance in space at smaller r means that if one naively

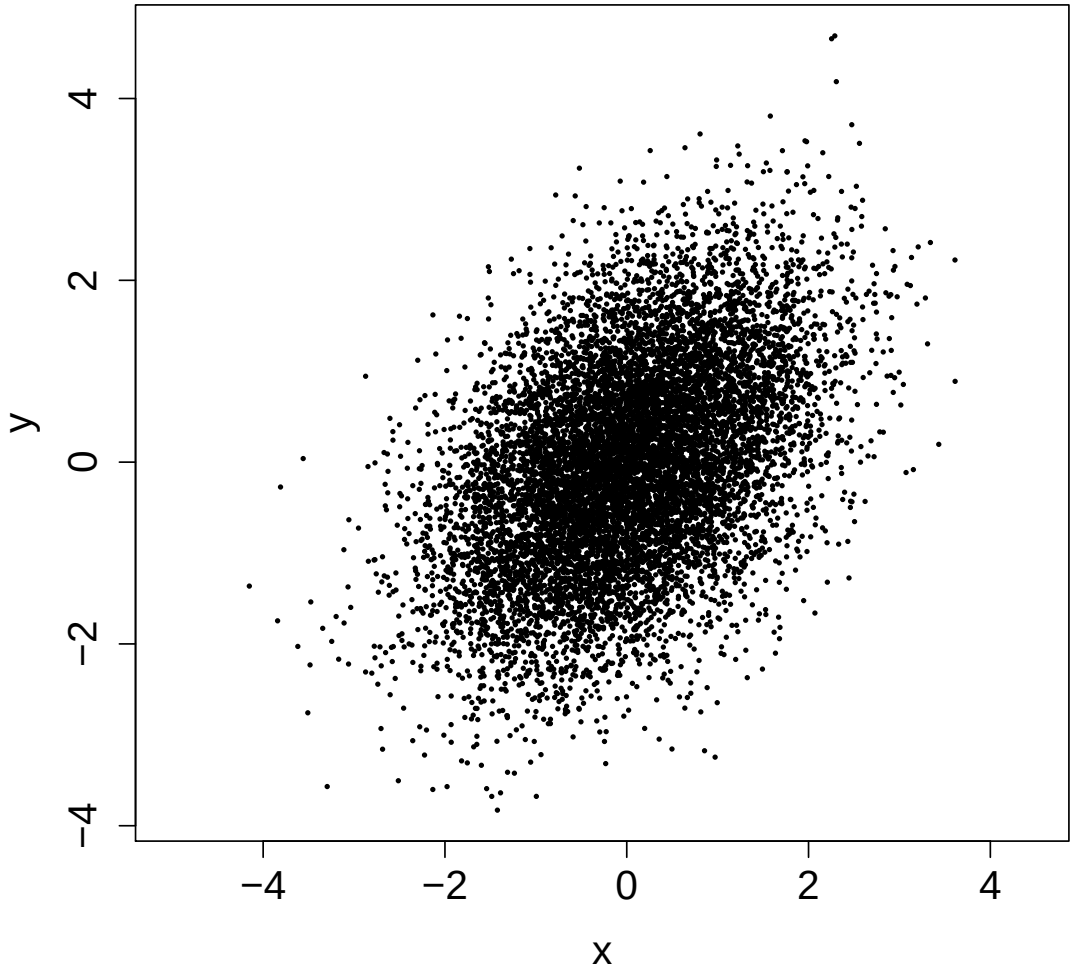

Figure 2.1: Example of correlated variables x and y

selects points from uniform distributions of r and θ, points cluster towards the origin.

An example of this can be found in fitting rotation curves; if a maximal disk is permitted by certain values of $\Upsilon_{3.6}$, then the shaping parameters for the necessarily reduced dark matter halo no longer influence the predicted rotation curve on the scale of the observational errors (and thus have no significant effect on the likelihood). If such models have adequate (not necessarily optimal) likelihood, then an MCMC chain can spend considerable time moving through this part of parameter space, varying irrelevant parameters, and creating a plateau in the parameter distribution which may not accurately represent the non-normalised probability distribution that is the desired goal. When such plateaus

begin to have comparable numbers of models in them to the actual peak, they can make analysis of the result more difficult.

2.3.3 Boundary Effects

It is important to consider how an MCMC process works at the boundaries of parameter space. One particular example of a boundary issue when applying MCMC to $\alpha - \beta - \gamma$ haloes is the behaviour of the γ parameter, which cannot be negative, and must be given uniform prior probability from $\gamma = 0$ upwards. This creates a hard boundary that can distort the posterior probability distribution.

For a volume near the edge of a parameter space, there are fewer nearby points from which it can be reached with high probability than there would be for a volume near the centre of the parameter space. This reduces the probability of the chain stepping into that volume, independently of the value of the probability density function in that volume, thus creating a bias.

This can be shown quantitatively. In Figure 2.2, the probability of moving from a position γ_n chosen from a uniform distribution (this effect would apply to non-uniform distributions as well, but it is easier to illustrate with a uniform prior) to γ^* is represented by a Gaussian selection function (in the case of the Metropolis-Hastings algorithm). The probability of arriving at γ^* from any point lower is

$$P(low) = \frac{1}{\sigma\sqrt{2\pi}} \int_{\gamma_{\min}}^{\gamma^*} e^{\frac{-(\gamma^*-\gamma)^2}{2\sigma^2}} d\gamma \tag{2.5}$$

and from any higher point

$$P(high) = \frac{1}{\sigma\sqrt{2\pi}} \int_{\gamma^*}^{\gamma_{\max}} e^{\frac{-(\gamma^*-\gamma)^2}{2\sigma^2}} d\gamma \tag{2.6}$$

Splitting equation 2.6 into two parts at the point $\gamma^* + \Delta\gamma$ (and dropping the normalising constant, which will not be needed) gives

$$P(high) \propto \int_{\gamma^*}^{\gamma^*+\Delta\gamma} e^{\frac{-(\gamma^*-\gamma)^2}{2\sigma^2}} d\gamma + \int_{\gamma^*+\Delta\gamma}^{\gamma_{\max}} e^{\frac{-(\gamma^*-\gamma)^2}{2\sigma^2}} d\gamma \tag{2.7}$$

and finally, the ratio between the low and high probabilities is

$$\frac{P(high)}{P(low)} = 1 + \int_{\gamma^*+\Delta\gamma}^{\gamma_{\max}} e^{\frac{-(\gamma^*-\gamma)^2}{2\sigma^2}} d\gamma \left[\int_{\gamma_{\min}}^{\gamma^*} e^{\frac{-(\gamma^*-\gamma)^2}{2\sigma^2}} d\gamma \right]^{-1} \tag{2.8}$$

due to the symmetry of the first term in equation 2.7 and equation 2.5. Because the

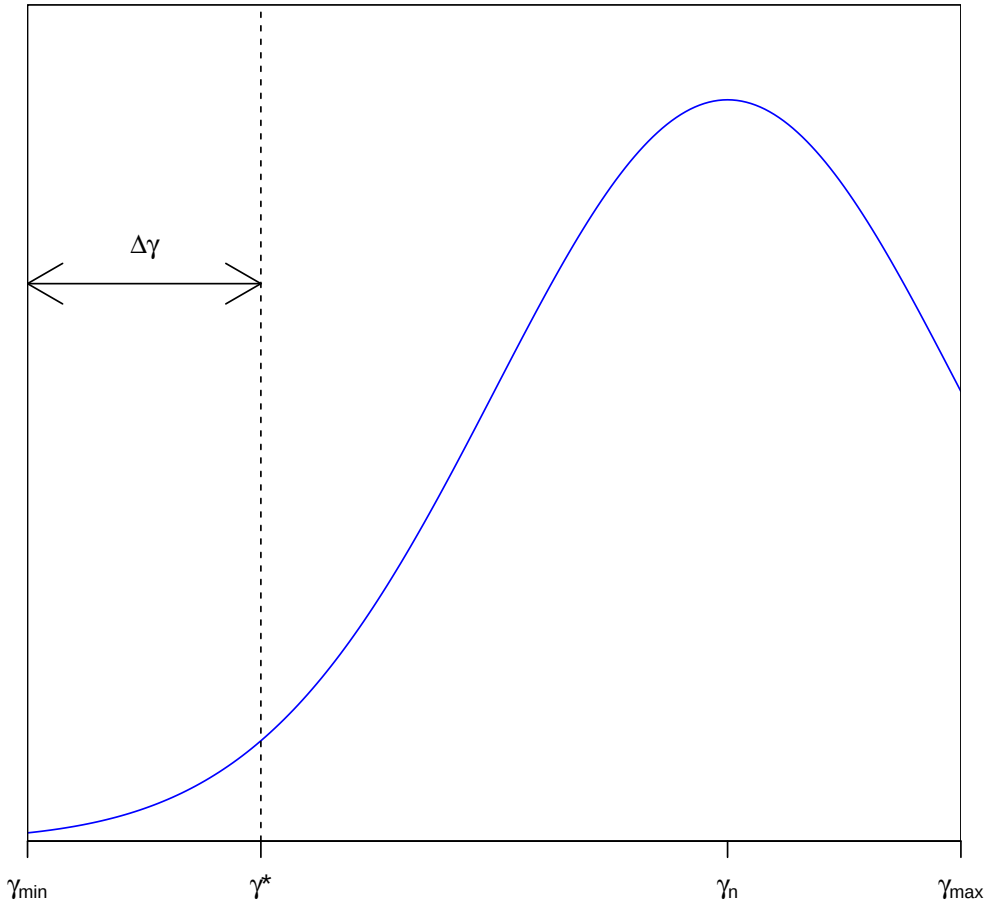

Figure 2.2: Plot of the γ axis of the parameter space, showing the probability of taking a step from a random position γ_n to a specific position γ^* as a gaussian. The probability distribution is not to scale.

Gaussian function is positive everywhere for real input values, this shows the probability of arriving at γ^* from a point nearer the centre of the parameter space must be larger than the probability of arriving from a point nearer the edge. If, when arriving at the nearby point in γ space, the algorithm stays there for some time before moving off again to another essentially random position, then this ratio of probabilities will be reflected in the final output of the chain.

To allow a full exploration of the area of parameter space around $\gamma = 0$, which is

necessary for modelling cored halos, the parameter space must be mirrored around this point, i.e. we select γ from $[-\gamma_{\max}, \gamma_{\max}]$ and use $|\gamma|$ for all likelihood calculations.

2.4 Implementation

The work here uses two implementations of the Metropolis-Hasting algorithm. The first, used in chapters 2-4, is `CosmoMC` in a generic mode provided publicly by Lewis and Bridle (2002), and the second is my own code `RainfallMCMC` used in chapter 5.

2.4.1 CosmoMC

A set of cosmological parameters produce a deterministic prediction for the result of cosmic microwave background surveys, and thus an application of MCMC to this parameter space permits the cosmological parameters to be constrained based on these data. This is what `CosmoMC` is written for, although it features a generic mode which permits the linking of an external likelihood function.

For my work I have added a likelihood function written in C, and a library of post-processing routines in R to make sense of the results when applied to rotation curve analysis.

2.4.2 RainfallMCMC

This is a program of my own design, which I have developed in the light of my experiences with the work in this thesis. I found that obtaining informative results from MCMC chains required a great deal of post-processing, which could be slow for large chains, and so I decided that much of it should be done as models are generated rather than as a batch at the end (which requires reloading the data). I also found that requirements for what data to produce and how to visualise it changed from task to task, and thus opted for the most modular design possible.

`RainfallMCMC`[1] is a generic MCMC driver by default, but it will include rotation curve analysis as an example in the publicly available code. In the course of my future work, I will develop this program in parallel with the application of MCMC to astrophysics problems. At the time of writing it only implements the Metropolis-Hastings algorithm, but will allow a broader range of MCMC techniques in the future. The design

[1] The name `RainfallMCMC` is intended to invoke the image of rain falling randomly on an uneven surface, and exploring the "parameter space" of terrain height to find the optimal (lowest) point

is entirely modular, so that facilities such as adaptive step size can be introduced at run time as dynamic libraries. The code is available publicly with the hope that, if others find it useful, a community can develop to build a library of add-ons.

3

Dark matter in disc galaxies - I. A Markov Chain Monte Carlo method and application to DDO 154

We present a new method to constrain the dark matter halo density profiles of disk galaxies. Our algorithm employs a Markov Chain Monte Carlo (MCMC) approach to explore the parameter space of a general family of dark matter profiles. We improve upon previous analyses by considering a wider range of halo profiles and by explicitly identifying cases in which the data are insufficient to break the degeneracies between the model parameters. We demonstrate the robustness of our algorithm using artificial data sets and show that reliable estimates of the halo density profile can be obtained from data of comparable quality to those currently available for low surface brightness (LSB) galaxies. We present our results in terms of physical quantities which are constrained by the data, and find that the logarithmic slope of the halo density profile at the radius of the innermost data point of a measured rotation curve can be strongly constrained in LSB ($[v_{\rm star}/v_{\rm obs}]_{\rm max} \simeq 0.16$) galaxies. High surface brightness galaxies ($[v_{\rm star}/v_{\rm obs}]_{\rm max} \simeq 0.79$) require additional information on the mass-to-light ratio of the stellar population - our approach naturally identifies those galaxies for which this is necessary.

We apply our method to observed data for the dwarf irregular galaxy DDO 154 and recover a logarithmic halo slope of -0.39 ± 0.11 at a radius of 0.14 kpc. Our analysis validates earlier estimates which were based on the fitting of a limited set of individual halo models, but constitutes a more robust constraint than was possible using other techniques since it marginalises over a wide range of halo profiles. Our method can thus reproduce existing results, has been verified on test data, and is shown to be capable of providing more information than is available from fitting individual halo profiles. The likely impact of future improvements in data quality on rotation curve decomposition using this technique is also discussed. We find that velocity errors are a limiting factor on the constraint that can be found, while spatial resolution is not.

3.1 Introduction

In order to understand the process of galaxy formation, it is important to have robust constraints on the gravitational potential wells in which observed galaxies reside. According to the current Λ Cold Dark Matter (ΛCDM) cosmological paradigm, dark matter haloes are generally thought to be an essential requirement for formation of a galaxy as they provide the means to collect and bind sufficient baryonic matter to create galaxies of sizes consistent with observations. Measurements of the velocities of gas moving in the disks of disk galaxies provide a valuable probe of the total gravitational potentials of such systems. Pioneering work by Bosma (1978) and Rubin et al. (1978) demonstrated

that the rotation curves of disk galaxies were generally flat to large radii, and the observed disparity between the measured rotation curves and those predicted based on their luminous components is now generally interpreted as evidence for the presence of dark matter haloes in these galaxies.

Observations of such a galaxy can give the rotation velocity at a specific radius r from the centre of the galaxy, the density of gas at this distance, and the amount of stellar light (and, hence the stellar mass, modulo certain assumptions about the mass-to-light ratio Υ) at each r. Calculating the rotation curves that would be expected from the two baryonic components generally gives a combined value that falls short of the observed rotation curve, and the difference can be used to infer the amount of dark matter enclosed at each r and thus a density profile for the halo.

While the ubiquity of dark matter haloes around galaxies is by now well established, observational determinations of the density *profiles* of galactic dark matter haloes have been, and remain, controversial. Flores and Primack (1994) used gravitational lensing and rotation curve analysis to argue against cusped[1] haloes with $\rho(r) \sim r^{-1}$ and $\rho(r) \sim r^{-2}$, which were being predicted by N-body simulations of cosmological structure formation at that time (e.g. Dubinski and Carlberg, 1991, who found that the profile proposed by Hernquist (1990) best fit the haloes they obtained). During the 1990s, dark matter-only cosmological simulations continued to suggest that a universal, cusped dark matter density profile, independent of halo mass, should be the outcome of the hierarchical formation scenario for galaxy haloes (Navarro et al., 1996; Navarro et al., 1997, hereafter NFW). On the other hand, a number of authors argued that observations of disk galaxy rotation curves pointed towards the existence of a universal rotation curve (Persic and Salucci, 1991; Burkert, 1995; Persic et al., 1996). The former claimed an inner halo profile of $\rho(r) \sim r^{-1}$ whilst the latter found uniform density central cores, and stated that the cusps implied by numerical simulations could be excluded. The apparent disparity between the results of cosmological simulations and observations of real galaxies became known as the "cusp-core controversy".

Early work to resolve this controversy focused on low surface brightness (LSB) galaxies, on the basis that the stellar contribution could be ignored entirely in a first-order model. In van den Bosch and Swaters (2001) it was claimed that it was impossible to differentiate between flat cores and r^{-1} cusps using the data available at the time. They cited

[1] In the literature, the terms cusp and core generally refer to negative log slopes at $r = 0$ of $\gamma_0 \geqslant 1$ and $\gamma_0 = 0$ respectively. In this chapter we discuss halos with intermediate inner slopes. We considered such slopes neither cusped nor cored, even though in the strict mathematical sense any halo $\gamma_0 > 0$ is cusped, in order to maintain coherence with previous discussions.

the insufficient radial range of the data, and the problem of beam smearing. Beam smearing of HI rotation curve data is caused by the fact that the each beam is larger than the scale over which the rotation speed changes. This, and several other observational issues that could lead to the false inference of cored haloes in galaxies which actually contained dark matter cusps, were investigated and discounted by de Blok et al. (2003). Using direct inversion of a large sample of rotation curves to determine mass profiles, they also found that the outer regions of their sample galaxies were consistent with density profiles $\rho \sim r^{-2}$ while the inner regions required power laws which were typically shallower than $\rho \sim r^{-0.25}$.

Bosma (2003) claimed to rule out r^{-1} cusps at the 3-sigma confidence level for 17 galaxies (from a sample of 28) and, on this basis, stated that the slopes predicted by CDM models were not observed. He demonstrated that the position of the slit used at the time to observe rotation curves could not have been a factor in this result, by deliberately offsetting the slit and observing the effect on the measured rotation curve. Gentile et al. (2004) subsequently found that the cored Burkert profile provided higher quality fits to the rotation curves of five nearby galaxies than either the cusped Navarro-Frenk-White (NFW) or a model based on Modified Newtonian Dynamics (MOND) that would not require dark matter. This growing weight of evidence has led to the widespread acceptance of the observational existence of cores. However, it is now recognised that exclusion of cusps in present-day galaxies is not synonymous with invalidating the ΛCDM paradigm. The profile of a galactic halo results from the interplay between a number of factors including the intrinsic physical properties of dark matter, the re-distribution of baryonic material by gas cooling, supernovae or AGN feedback, and its history of major or minor mergers with other galaxies (see e.g. Governato et al., 2012, for recent simulations of these processes at work on galaxy scales). Cored haloes may originally have had cusps - observations of the present day profiles constrain the end-state of galaxy formation, rather than the initial conditions.

In this context, it is important to note that “measured” halo properties should not be confused with the values of particular parameters in a profile with an assumed form. For example, a halo with an asymptotic inner slope of zero may exhibit a non-zero slope over the entire radial range probed by a particular observational data set and indeed may be well reproduced by an NFW profile over that radial range for an appropriate choice of parameters. Additional information may be used to argue that the NFW parameters are unrealistic (for example, based on their expected values using the scaling relations obtained from cosmological simulations). In our analysis, we therefore focus on physically

meaningful quantities such as the logarithmic slope at the radius of the innermost point in the rotation curve, rather than the values of particular parameters in our models.

The HI Nearby Galaxy Survey (THINGS) sample of galaxies provides high resolution 2D data which addresses many of the issues such as non-circular motions that have plagued rotation curve decompositions in the past (Walter et al., 2008). It is therefore timely to examine in detail the constraints which can be placed on the physical properties of the haloes of disk galaxies using these high resolution observations of their rotation curves. Somewhat surprisingly, research to date has generally focussed on specific halo models (e.g. de Blok et al., 2008), with particular interest in the NFW and Burkert profiles (see Sec. 3.2). Recently, Chemin et al. (2011) re-analysed the THINGS rotation curves using Einasto profiles and found that these provided improved fits to the observed data relative to earlier work. This is to be expected, as the Einasto profiles have an additional shape parameter which makes their form more flexible for the modelling of rotation curves.

Taking advantage of new data from THINGS, Oh et al. (2011) claim that a selection of dwarf galaxies (including DDO 154, the galaxy that we use as an example in this chapter) exhibit $r^{-0.29}$ inner profiles, which they classify as cores. This conclusion assumes a single dark matter halo for all dwarf galaxies, but not necessarily a truly universal profile. DDO 154 is a common target for studies of dark matter because it has a low surface brightness, and now thanks to THINGS there is more extensive rotation curve data for this galaxy than was available in older studies (Walter et al., 2008).

All the above analyses focus on a small number of possible profiles, and thus any comparison between them can only reveal which of the profiles considered best fits the data. They provide no context in which to discuss how well the "best" profile performs relative to all possible profiles. Furthermore, by restricting the set of profiles considered, these earlier studies have to some extent dictated the shape of the model rotation curve, so the slope of the best-fit model curve at any individual radius is based on the fit statistics of the entire curve. It is possible that the quality of the fit for one part of the curve might give a false impression of the quality of the fit for another part of the curve, when in actual fact there is not enough information at that point to constrain the slope.

In this chapter, we re-visit the problem of rotation curve decomposition and use a Markov Chain Monte Carlo (MCMC) algorithm to explore the parameter space of a very general family of dark matter haloes. Puglielli et al. (2010) have previously applied MCMC techniques to the problem of rotation curve decomposition, but considered a restricted set of halo profiles. Our three key innovations are: (1) the use of a more gen-

eral family of halo profiles than has previously been used, thereby permitting the models more freedom to match the observed data; (2) a focus on physical quantities which can be constrained by the data, for example, the log-slope of the halo profile at the innermost observed data point rather than the particular parameters of our models, for example the asymptotic values of the log-slope of the dark halo profile at radii smaller or larger than those probed by the data; (3) the potential for a detailed exploration of the degeneracies between the model parameters. This latter exploration enables us both to quantify the true uncertainties in the halo constraints we obtain as well as to determine what future observations would be most likely to improve these constraints.

The outline of the paper is as follows. Section 3.2 describes the galaxy models we use, both to analyse our artificially-generated data with known input values, and in our analysis of the THINGS data for DDO 154 obtained from de Blok et al. (2008). In Section 3.3 we present the algorithm we have developed for this purpose, employing CosmoMC (Lewis and Bridle, 2002) as an MCMC driver. Section 3.4 details the results of tests on artificial data while Section 3.5 compares the performance of our method with that of existing rotation curve fitting techniques (i.e. fits based on individual or small numbers of dark matter halo profiles). In Section 3.6 we present an application of our method to DDO 154 and finally Section 3.7 details our conclusions. An appendix is included which presents some additional technical details of our method.

3.2 Galaxy Models

Under the assumption that the gas in a disk galaxy moves along approximately circular orbits, the measured run of gas velocity with radius through the disk is a strong probe of the total underlying mass distribution. There are three main contributions to the mass distribution which we must account for in any mass model: the stellar disk, the gas disk, and the dark matter halo. The spatial distributions of these three components are significantly different and therefore their relative contributions are strong functions of radius. In the inner regions of many of the THINGS galaxies, the baryonic components contribute significantly to the gravitating mass, making it more difficult to determine the inner slope of the dark matter profile. In this chapter, we go beyond previous analyses by considering a more general family of halo density profiles and by explicitly exploring degeneracies between the parameters of our models, in particular between the dark matter and baryonic parameters.

3.2.1 Baryonic components

The Spitzer Infrared Nearby Galaxies Survey (SINGS: see Kennicutt et al., 2003) provides near-infrared photometric data for the galaxies in the THINGS catalogue, allowing the determination of accurate stellar surface density profiles. Conversion of the luminosity profile to a stellar mass profile requires information about the mass-to-light ratio of the stellar population. In this chapter, we make use of the stellar rotation curves calculated by de Blok et al. (2008). These curves are calculated by assuming that radial variations in the colour of the stellar populations indicate stellar population gradients which in turn lead to variations in $\Upsilon_{3.6}$, the mass-to-light ratio in the 3.6 μm band. As described below, our algorithm incorporates a scaling of the stellar rotation curve to account for uncertainties in the stellar population modelling. The same scaling is applied at all radii, and we thus implicitly assume the same radial gradients in Υ as de Blok et al. (2008).

In Section 3.4, we use DDO 154 as a template for LSB galaxies and NGC 7793 as an example of an HSB galaxy. We use the data for their stellar disks from de Blok et al. (2008). The surface brightness measured in the 3.6 μm band for NGC 7793 was taken from SINGS, while that for DDO 154 was obtained from the Spitzer archive. A Υ value was then calculated from the $J-K$ band of 2MASS, using a formula that assumes a "diet" Salpeter IMF (one with fewer low mass stars, necessary to keep some stellar disks sub-maximal). de Blok et al. (2008) also present results using a Kroupa IMF. However as we anticipate most difficulty analysing HSB galaxies, we choose the option that gives a more massive disk in order to find the limit of the effectiveness of our method.

de Blok et al. (2008) combined the surface brightness and Υ into a density profile, which they then converted to a velocity curve using the GIPSY[2] software. We approximate this velocity curve by fitting a thin exponential disk rotation curve (see e.g. Binney and Tremaine, 2008) to produce an estimate of the stellar contribution to the total rotation curve. The goodness of fit for this profile does not impact on the performance of our algorithm, as we marginalise over both the scale radius $R_{\rm d}$ and the amplitude (by varying the stellar Υ: see below). However, we note that it provides an excellent fit to the data for DDO 154, with a maximal deviation of $\lesssim 0.25\,{\rm km\,s^{-1}}$over the entire radial range, and significantly less than this interior to 1.5 kpc.

In our analysis, we apply a scaling factor f_Υ to explore the impact of observational uncertainty on the mass of the stellar disk. The inclusion of f_Υ as a free parameter in our analysis enables us to explore whether we can differentiate between those cases in which there is sufficient information to constrain the halo profile despite our lack of knowl-

[2]http://www.astro.rug.nl/~gipsy/

edge about the true Υ and those in which there is not. The latter cases will necessarily be beyond the scope of this technique until Υ can be determined with greater accuracy. However, by reducing the range of allowed f_Υ values explored by our algorithm, we would be able to determine what Υ precision is required to constrain the halo to a particular level of certainty. We allow f_Υ to vary between 0.1 and 2, which encompasses Υ values derived from the full Salpeter IMF (f_Υ = 1.43) and the Kroupa IMF (f_Υ = 0.71) that have been considered in the previous analyses of rotation curve by Chemin et al. (2011) and de Blok et al. (2008), without placing either one near the edge of the parameter space.

Radial variations in Υ, which occur due to age gradients in the disk and which are detected by means of color gradients, are already taken into account in the stellar rotation curves of de Blok et al. (2008) which we use in our modelling. This, and the fact that the 3.6 μm band is sensitive mainly to the older portion of the stellar population, means that our modelling technique is robust with respect to the stellar age.

The gas distribution for the THINGS galaxies is determined from their HI maps. The gas mass is estimated assuming that the gas is entirely composed of atomic hydrogen. While the presence of molecular gas would change the gas contribution to the overall potential well, we note that for the majority of galaxies in the THINGS survey, the ISM is dominated by atomic hydrogen (Leroy et al., 2008). However, for galaxies with a significant gas contribution to the gravitating mass, the composition of the ISM should be confirmed to test this assumption.

Similarly to the the stellar disk, we take our model gas profiles from the de Blok et al. (2008) data for DDO 154 and NGC 7793. Following de Blok et al. (2008), we have scaled the surface density given by THINGS HI data cubes by a factor of 1.4 in order to take into account the non-hydrogen contributions of the gas (galaxies with large amount of molecular gas having already been excluded from analysis at this point). They then used the GIPSY software to construct an infinitely thin disk rotation curve based on a titled ring modelling of the gas disk. We take this profile and apply the same smoothing to it as we did for the stellar curve to obtain the gas contribution to the rotation curve. No variation of the parameters of the gas disk are allowed in our modelling, as the mass and extent of the disk are assumed to be well-constrained by the observations.

In addition to the gas located in the disk, galaxies may also have a hot, ionised halo of gas. Miller and Bregman (2013) find that, in the Milky Way, the fraction of the total galaxy mass in this component is 0.07. This means that, assuming comparable fractions are present in nearby disk galaxies, the kinematic effect of this halo is smaller than errors due to non-circular motions.

It is well known that non-circular motions complicate the interpretation of galaxy rotation curves because the observed gas motions at a particular radius may not accurately reflect the underlying circular velocity at that location. Pizzella et al. (2008) show that rotation curves based on stellar velocities may be more reliable for determinations of the shape of the inner halo of a galaxy than those based on one-dimensional HI spectra. They note, however, that integral field gas velocity maps can be used to screen out galaxies with significant non-circular contributions to their velocity fields. The THINGS sample has been selected on the basis of strict criteria including favourable inclination angle relative to the line of sight (de Blok et al., 2008). Subsequently, Oh et al. (2011) examined the velocity field data for evidence of non-circular motions and determined an optimal rotation curve for each THINGS galaxy, which thus represents the best opportunity to determine the dark halo profiles of this sample. In the present paper, we therefore assume that the galaxy to be modelled has been checked for non-circular motion, and that the rotation curve has been corrected for such motions if required.

A further potential complication is asymmetric drift, which affects measurements of circular speeds obtained from gas or stars whose vertical velocity dispersion is not negligible compared to their ordered rotational velocities. In our modelling, we assume that asymmetric drift can be neglected, or has been corrected for in the rotation curve data, and as in de Blok et al. (2008) assume an infinitely thin gas disk.

3.2.2 Halo models

In common with most previous analyses, we assume that the dark matter halo of the galaxy is spherical. Whilst non-spherical haloes are in principle possible, and indeed are the likely outcome of either mergers and/or gas cooling (generically leading to triaxial haloes; see e.g. Vera-Ciro et al., 2011, for a discussion), the presence of triaxiality would typically lead to non-circular motion of the stars and gas in the disk. In their analysis of the rotation curve of DDO 47, Gentile et al. (2005) argued that the non-circular motions seen in that galaxy were at a level of $\lesssim 3\,\mathrm{km\,s^{-1}}$and concluded that any triaxiality in the halo of that galaxy was at a level which was irrelevant for rotation curve analyses. A study of the non-circular motions in the THINGS galaxies by Trachternach et al. (2008), based on harmonic decomposition of the velocity around each tilted ring, found that the amplitude of non-circular components was less than $1\,\mathrm{km\ s^{-1}}$ at all radii. Given that we are restricting our analysis to such galaxies which exhibit very low levels of non-circular motion, the assumption of a spherical halo is reasonable.

We assume that the dark matter halo can be parameterised by an (α, β, γ) profile (Zhao,

1996), which is a general, spherical halo density profile given by

$$\rho(r) = \frac{\rho_{\rm s}}{\left(\frac{r}{r_{\rm s}}\right)^{\gamma}\left(1+\left(\frac{r}{r_{\rm s}}\right)^{1/\alpha}\right)^{\alpha(\beta-\gamma)}} \tag{3.1}$$

where γ is the asymptotic log-slope of the profile at small r, β is the slope at large r, and α controls the transition between the two (lower values of α corresponding to sharper changes). The parameters $\rho_{\rm s}$ and $r_{\rm s}$ are the density and length scales, respectively. This family encompasses a number of the profiles which have previously been used to model disk galaxy haloes. The cusped NFW profile, proposed as a good approximation to the dark matter halo profiles obtained in dark mater-only cosmological simulations of structure formation, corresponds to $(\alpha,\beta,\gamma) = (1,3,1)$, while the cored isothermal halo, which is often used as an example of a cored halo profile has $(\alpha,\beta,\gamma) = (1/2,2,0)$. Another widely used cored halo is the Burkert (1995) profile,

$$\rho(r) = \frac{\rho_{\rm s} r_{\rm s}^3}{(r+r_{\rm s})(r^2+r_{\rm s}^2)} \tag{3.2}$$

which has been shown to provide a good fit to the rotation curves of a large sample of disk galaxy rotation curves (see e.g. Persic and Salucci, 1988, 1991; Salucci et al., 2007, and references therein). More recently, Chemin et al. (2011) showed that the Einasto profile (Einasto, 1969, 1965),

$$\rho(r) = \rho_s \exp\left[-\frac{2}{n}\left[\left(\frac{r}{r_{\rm s}}\right)^n - 1\right]\right] \tag{3.3}$$

where $r_{\rm s}$ is a scale radius, $\rho_{\rm s}$ is a density scale and n is a shape parameter, provides a better fit to the rotation curves of THINGS galaxies than the other three profiles. This profile, whose logarithmic slope varies continuously with radius, has been proposed as an improvement on the NFW profile in terms of fitting the results of the most recent cosmological simulations (Navarro et al., 2004). While the (α,β,γ) family does not explicitly include either the Burkert or Einasto profile, for suitable choices of the profile parameters it can closely reproduce them over a restricted radial range.

For any (α,β,γ) model, the enclosed mass at a particular radius is

$$M = \frac{4\pi\rho_{\rm s} r^3}{\gamma-3}\left(\frac{r}{r_{\rm s}}\right)^{-\gamma} {}_2F_1(a,b,c,z) \tag{3.4}$$

Parameter	Minimum	Maximum
α	0.1	2.5
β	3	5
γ	0	2
$r_{\rm s}$	$r_{\rm min}$	$r_{\rm min} + 2r_{\rm s,0}$
$v_{\rm max}$	0	$2v_{\rm max,0}$
f_{Υ}	0.1	2
$f_{R_{\rm d}}$	0.1	2

Table 3.1: Summary of the parameters explored by the algorithm. $r_{\rm s,0}$ and $v_{\rm max,0}$ are initial values determined by a single χ^2 best fit. $r_{\rm min}$ is the radius of the smallest radial bin of a particular data set. $f_{R_{\rm d}}$ is a scaling factor which is used to vary the stellar disk scale length.

where ${}_2F_1()$ is the hypergeometric function, with $a = \alpha[\beta - \gamma]$, $b = -\alpha[\gamma - 3]$, $c = 1 - \alpha[\gamma - 3]$, and $z = -[\frac{r}{r_{\rm s}}]^{1/\alpha}$.

In this chapter, we re-cast the (α, β, γ) profile in the form

$$\rho(r) = \frac{\Sigma_{\rm max}}{G} \frac{v_{\rm max}^2}{\left(\frac{r}{r_s}\right)^{\gamma} \left(1 + \left[\frac{r}{r_s}\right]^{1/\alpha}\right)^{\alpha(\beta-\gamma)}} \tag{3.5}$$

with $v_{\rm max}$ replacing the $\rho_{\rm s}$ paramater, and $\Sigma_{\rm max}$ being calculated from the remaining parameters via the formula

$$\Sigma_{\rm max} = \frac{\rho_{\rm s} r_{\rm max}}{M(\alpha, \beta, \gamma, r_{\rm s}, \rho_{\rm s})} \tag{3.6}$$

This transformation is explained in detail in Appendix A.1. Note that this is a different parameterisation of the same halo, rather than a distinct halo itself. The reason for introducing this parameter transform is to resolve the degeneracy between the halo parameters $\rho_{\rm s}$ and $r_{\rm s}$. The parameter $v_{\rm max}$ is a useful choice as it has a clear physical meaning, namely, the maximum circular velocity of the dark matter halo. This should not be confused with the maximum circular velocity of the observed rotation curve, although in the case of LSB galaxies they will be similar in value.

3.3 Markov Chain Monte Carlo

Model	α	β	γ	$\gamma_{\rm in}$	$r_{\rm s}$	$v_{\rm max}$	$R_{\rm d}$	$\frac{\Delta v}{v}$	Notes
A	1	4	1	1.07	6	50	2.15	0.02	Low surface brightness with small errors
B	1	4	1	1.07	6	50	2.15	0.1	Low surface brightness with realistic errors
C	1	4	1	1.05	6	80	2.50	0.1	High surface brightness with realistic errors[1]
D	1	4	1	1.07	6	50	2.15	0.02	Low surface brightness with high data resolution
E	1	4	1	1.07	6	50	2.15	0.1	Low surface brightness with realistic errors, extended radial range
F	–	–	–	0.08	6	50	2.15	0.1	Low surface brightness with realistic errors, Burkert profile[2]
G	1	4	1	1.07	6	50	2.15	0.1	Low surface brightness with realistic errors, free stellar disk parameters
H	1	4	1	1.05	6	80	2.50	0.1	High surface brightness with realistic errors, free stellar disk parameters[1]

Table 3.2: Input parameters for synthetic data sets. The columns show: (1) Model name; (2-4) (α,β,γ) parameters of the halo profile; (5) log slope of the halo profile at the innermost data point, $\gamma_{\rm in}$; (6) halo scale radius in kpc; (7) maximum velocity of the halo circular speed curve in $\mathrm{km\,s^{-1}}$; (8) disk scale length in kpc; (9) observational error. All except Model F use (α,β,γ) profile haloes, with parameter values corresponding to a Hernquist (1990) halo. All models except G and H assume a f_Υ of 1. For the LSB models, the innermost data point is located at a radius of 0.14kpc (based on DDO 154) and for the HSB models, the innermost data point is at a radius of 0.11kpc (based on NGC 7793). Notes: [1] the $\gamma_{\rm in}$ values for Model C and Model H are not directly comparable with the rest of the values as the radius at which they are measured is different; [2] the scale radius and scale density in the Burkert profile is not directly comparable to those from the (α,β,γ) profiles.

Our goal is to determine the distributions of parameters for the models described in the previous section which are consistent with a given observed HI rotation curve. We assume that the observed rotation curve can be modelled by summing, in quadrature, the contributions to the local circular speed of the gas disk, the stellar disk and the dark matter halo. For a given choice of model parameters, we calculate the expected rotation curve which we compare to the observed data by means of a χ^2 test.

Markov Chain Monte Carlo (MCMC; see e.g. Press et al., 2007) produces a non-normalised probability distribution for a parameter space by taking random steps through the space. The steps are randomly selected from a one-dimensional Gaussian in each parameter, with a variable step size, storing each model encountered on the way. A new model is accepted if its likelihood is greater than the previous model, while less likely models are accepted with a probability equal to the likelihood of the new model divided by the likelihood of the old one. If a new model is not accepted, the old model is repeated in the Markov chain. The choice of a Gaussian selection function is widespread, though not essential in MCMC; but it has the advantage that it favours small steps over large ones, and the probability of stepping between two points is identical in both directions. This second property ensures that the steps satisfy the Metropolis detailed balance condition (Hastings, 1970; Metropolis and Rosenbluth, 1953).

We use an MCMC method to explore models over a broad range of values for the halo parameters α, β, γ, r_s, and v_{max}, and stellar disk parameters f_Υ and f_{R_d}. A summary of the parameters and their ranges can be found in Table 3.1. We use the October 2012 release of the publicly available CosmoMC code (Lewis and Bridle, 2002) as an MCMC driver. CosmoMC was originally designed to determine cosmological parameters from the cosmic microwave background, but it has a generic MCMC mode that we utilise here. We choose stepping mode 4 "slow grid" - which is described in the CosmoMC documentation.

To facilitate the comparison between different parametric models, after the MCMC chains have been generated, we calculate the physical parameter γ_{in} - the logarithmic slope of the density profile at the location of the innermost radial bin of the measured rotation curve - as the basis for comparison. This allows us to explore the issue of whether our choice of a set of parametric profiles has a significant impact on the estimates of the log-slope of the halo profile.

For each data set we generate 16 MCMC chains, each of which contains $\sim 5 \times 10^5$ accepted models and has a different set of starting parameters. All results in this chapter have more than 7×10^6 models. The multiple starting points help to ensure that a local

maximum in the likelihood does not trap the algorithm - although due to the nature of MCMC this is unlikely to happen if the chains are run for sufficiently long. We are able to verify that MCMC chains have converged by comparing multiple chains (if converged they should all produce the same, smooth, distribution of values for each parameter), and all chains produced for this chapter have been checked for convergence in this way.

3.3.1 Prior distributions and normalisation

We assume uniform priors on all our parameters and as a result the shape of our parameter space is simply a uniform hypercuboid. However the non-linear transformation of this space into physical quantities such as $\gamma_{\rm in}$ or $\mathrm{d}\log\rho(r)/\mathrm{d}\log r$ means that the prior distributions of these quantities may no longer be uniform. This can be seen from Fig. 3.1 which shows the distribution of $\gamma_{\rm in}$ values generated by a "flat" run that returns $\chi^2_{\rm red} = 1$ for all models. There is a volume bias in (α, β, γ) space away from $\gamma_{\rm in} = 0$, due to the fact that the log slope only reaches zero at $r = 0$ and any finite scale radius will shift $\gamma_{\rm in}$ away from zero even when $\gamma = 0$. The derived parameter, $\gamma_{\rm in}$, therefore requires normalisation, because there is a one-to-many mapping between each value of $\gamma_{\rm in}$ and sets of parameter values, i.e. the parameter space for each value of $\gamma_{\rm in}$ is a different size. Without normalisation, this would bias a histogram of $\gamma_{\rm in}$ towards areas where the parameter space had a larger volume and away from $\gamma_{\rm in} = 0$. In what follows, all histograms of derived quantities such as $\gamma_{\rm in}$ are normalised by the corresponding histogram obtained from a flat run. We have verified that this normalisation process is robust in the sense that normalising the output of one flat run by that of another leads to a uniform distribution to within the bin noise.

Although in some of the figures in later sections we plot certain parameters using logarithmic scales, we have chosen, after extensive testing, not to use a logarithmic range for any of our parameters. Typically, logarithmic spaces are used for parameters whose values can range over several orders of magnitude. However, for a parameter whose values vary over a limited range, a uniform prior in a logarithmic space corresponds to a prior in linear space that favours smaller values of the parameter. Since CosmoMC dynamically varies the step sizes for all parameters, it is already able to survey a large range in parameter space while concentrating on small values of particular parameters if necessary. We therefore use uniform priors in linear space for all our parameters, as this greatly simplifies the interpretation of the output from the MCMC chains.

The $\gamma = 0$ boundary can lead to a bias of the MCMC chains away from models with very small values of γ. This effect came to light during early tests of our analysis and is

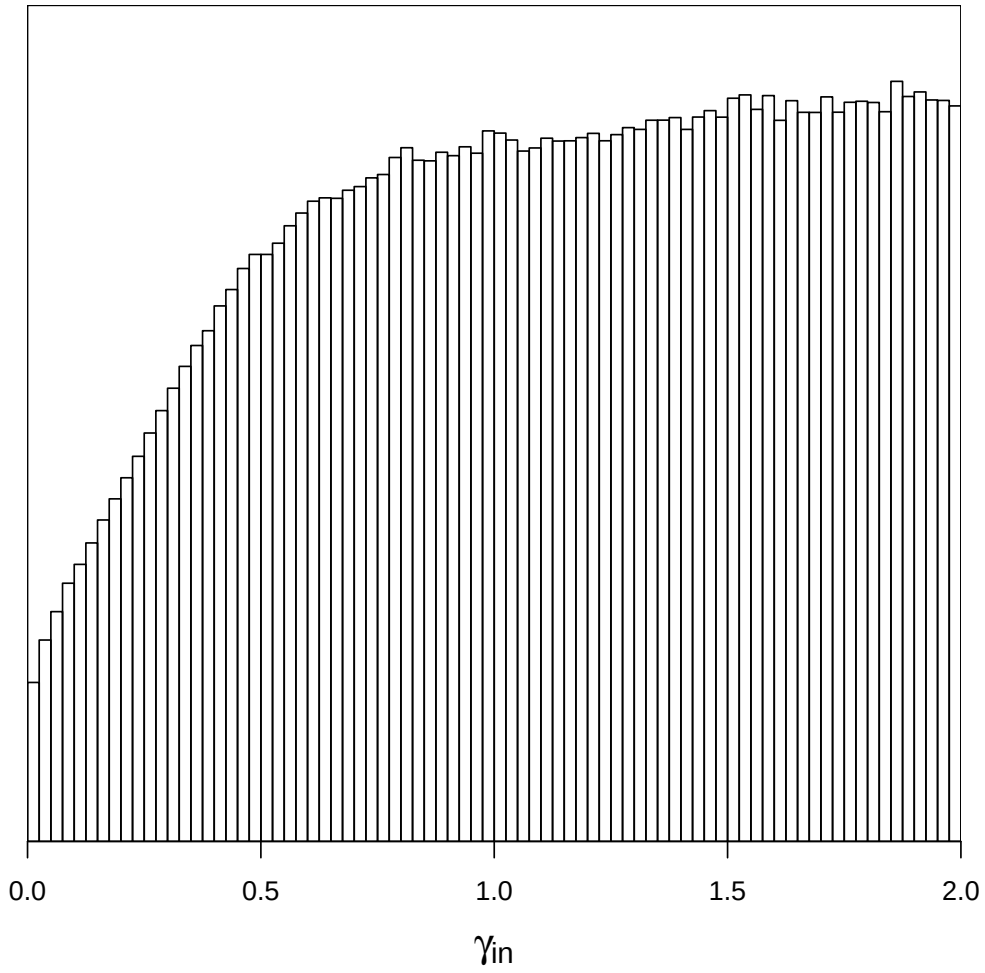

Figure 3.1: Histogram of $\gamma_{\rm in}$ for a "flat" run in which all parameter combinations are equally probable, illustrating the need to normalise histograms for derived quantities.

alleviated by extending the range of γ values to include $\gamma < 0$ (the actual range used is $[-2, 2]$) and using the modulus of γ in calculations of the halo rotation curve. This ensures that the models of most interest to us are not in an unusual portion of the parameter space. Tests on synthetic data presented in Section 3.4 confirm that the algorithm is indeed able to recover halo profiles with $\gamma \sim 0$.

3.4 Tests on synthetic data

Before applying the algorithm to observed data, it is essential to demonstrate that it can successfully recover the properties of galaxies with known characteristics. To this end, we generate a number of synthetic data sets for each of two galaxy types: (1) a low surface brightness (LSB) galaxy, based on the galaxy DDO 154, for which we expect the algorithm to perform well; and (2) a high surface brightness (HSB) galaxy, based on NGC 7793, which we use to demonstrate explicitly the strong degeneracies which occur in modelling this class of galaxy and the way in which the MCMC approach naturally identifies their presence.

To generate the artificial data, we fit a rotation curve for a thin exponential disk (Binney and Tremaine, 2008) to the stellar rotation curve provided by de Blok et al. (2008) (which uses a $\mathrm{sech}^2(z)$ vertical profile and is generated from surface brightness models using the ROTMOD task in GIPSY) , which includes estimates of the mass-to-light ratio. For DDO 154 and NGC 7793 we obtain disk scale lengths R_d of 2.15 kpc and 2.51 kpc, respectively.

We next assume a particular dark matter halo profile for each galaxy, and calculate the corresponding circular speed curve which we add in quadrature to the stellar rotation curve, assuming the same stellar $\Upsilon_{3.6}$ as de Blok et al. (2008). If we are allowing the stellar Υ to vary along the MCMC chains, the stellar circular speed at all radii is scaled by a factor $\sqrt{f_\Upsilon}$ before it is combined with the dark matter curve. Finally, the gas contribution is added (in quadrature) to obtain the total circular speed curve for our synthetic galaxy. The properties of the gas component are held fixed along the chains - we use the observed gas contributions in DDO 154 and NGC 7793 for the model LSB and HSB galaxies, respectively.

Before applying our algorithm to these synthetic data, we add Gaussian observational noise to each data point. The final data set passed to the algorithm is then the set of "observed" velocity data points and their error bars, and the contribution to the rotation curve of the stellar and gas disks, which are assumed to have been measured for the

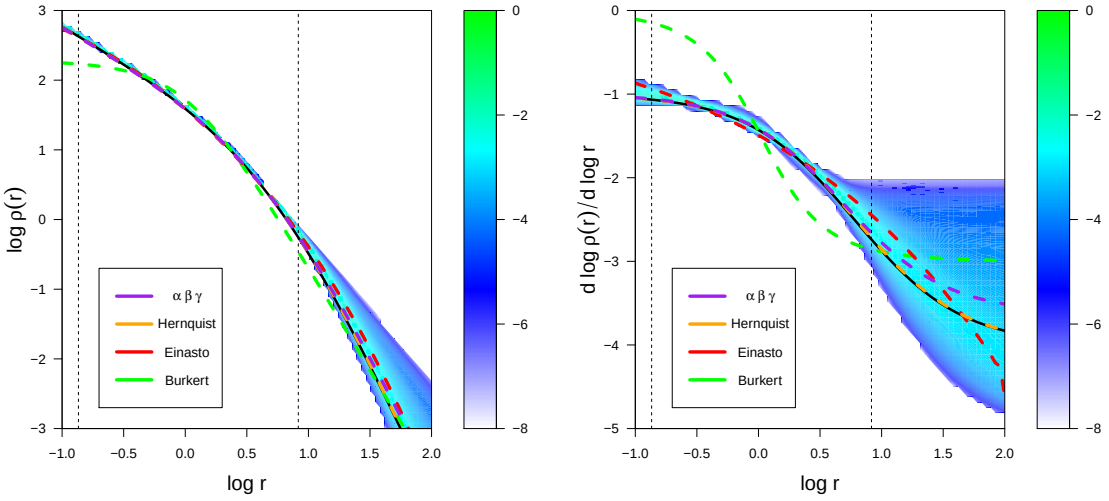

Figure 3.2: Results of the algorithm applied to model A, an LSB galaxy with small observational error bars. The colour scale is $\log[N(\mathbf{x})/N_{\rm total}]$, i.e. the log proportion of models going through a particular point. **Left:** the distribution of halo density profiles for all models accepted in the MCMC chains. The vertical dashed lines show the inner and outer limits of the input data, and the coloured dashed curves show the best fits of single profiles: purple for the (α,β,γ) profile, green for the burkert profile, red for the Einasto profile, orange for the Hernquist profile. The black curve is the input profile. **Right:** the distribution of halo density profiles in $(\mathrm{d}\log\rho(r)/\mathrm{d}\log r, \log r)$ space i.e. the log slope with respect to log radius. Overlaid profiles follow the same colour scheme as in the top panel.

observed galaxy, in the manner which has been done by de Blok et al. (2008) for the THINGS sample.

3.4.1 Reduced observational errors

In our first test, we explore the performance of the algorithm on almost "ideal" data by assuming fractional error bars of 0.02 on the velocities. These are about a factor of five smaller than the typical errors on the THINGS rotation curves. The dark matter halo is assumed to be a Hernquist profile, i.e. $(\alpha,\beta,\gamma) = (1,4,1)$, with parameters given in Table 3.2. For this test, we consider an LSB galaxy whose stellar mass profile is based on the exponential disk fit to DDO 154.

Fig. 3.2 presents the results of this test. As the left panel shows, given very precise input data, the algorithm is able to recover very accurately the density profile of the dark matter halo. The right panel shows the distribution of accepted models in the

$\mathrm{d}\log\rho(r)/\mathrm{d}\log r$ versus $\log r$ plane, indicating that the log slope is very well modelled at all radii within the data range (indicated by vertical dashed lines in the plot.) The performance of the algorithm is facilitated by the low surface brightness of the stellar disk. Although in this instance we did not allow f_Υ to vary, the full range in values of this parameter covers a range in amplitude of $\lesssim 1$ km s^{-1}in the total rotation curve. It is important to note, however, that the distribution of models in Fig 3.2 marginalises over all the model parameters and shows that the algorithm takes advantage of the freedom provided by the many parameters to recover the overall density profile of the galaxy. Although the individual model parameters are not necessarily recovered correctly, this does not affect our conclusion that the algorithm is unbiased, as our goal is to recover physical quantities such as the log slope as a function of radius rather than values for parameters of our particular form for the halo profiles.

The results of this test show that the algorithm performs well in the idealised case of high quality data for an LSB galaxy. We find no evidence of any modelling bias in either the shape or amplitude of the density profile and therefore conclude that the algorithm is working correctly. In the following sections, we consider its application to data sets of differing quality including realistic error bars that correspond to the quality of presently available rotation curves, as well as to data for HSB galaxies in which the uncertainty in the stellar mass to light ratio of the galaxy plays an important role.

3.4.2 Realistic Observational Errors

In this test, the underlying galaxy model is identical to that used in the previous section, but we now add observational errors of 10 percent to the total rotation curve which is more representative of the errors typical of current observed data sets, such as THINGS. Fig. 3.3 presents the results of this test. As expected, the most obvious difference with the previous test is that the distribution of halo models is much broader. Nevertheless, as the left panel of the Figure shows, the algorithm accurately recovers the input halo profile over the radial range probed by the rotation curve data. Outside this region, the range of consistent models expands significantly. We emphasise that outside the range of the observed data, the apparent constraints on the halo profile are the result of our assumption of a parametric model for the dark matter halo. In the absence of physical constraints at larger or smaller radii than those probed by the data, we are effectively using all five halo parameters to fit the rotation curve over the finite radial range covered by the data. The physical relevance of our models is thus limited to the volume probed by the data and, as stated earlier, the values of the parameters are less significant than the overall profile

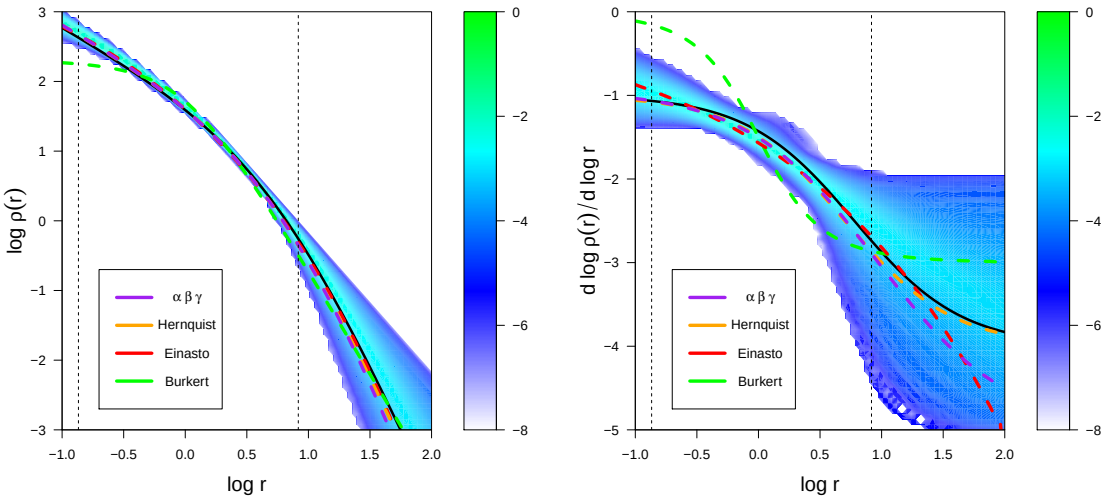

Figure 3.3: As in Fig. 3.2 but for model B, an LSB galaxy with realistic observational error bars. See text for a discussion.

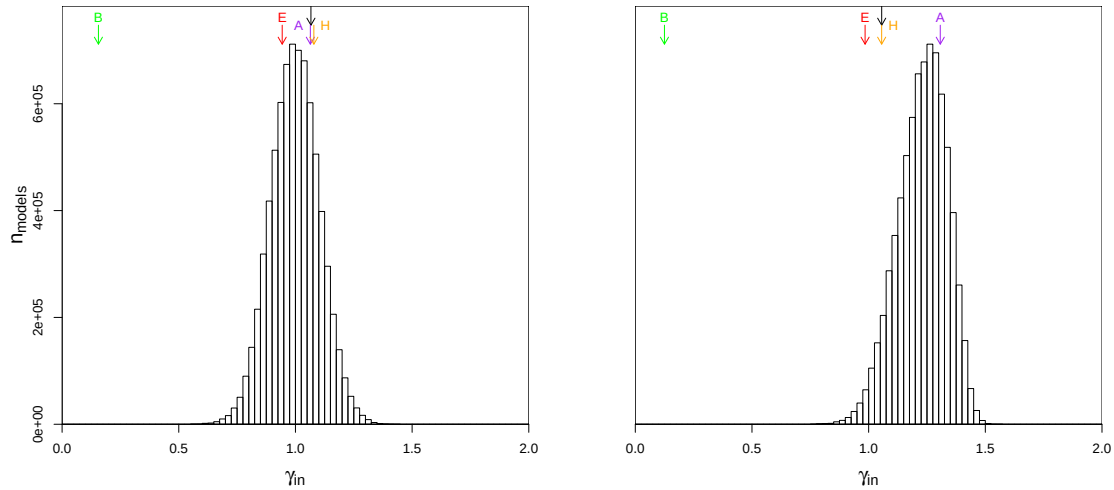

Figure 3.4: Histograms of $\gamma_{\rm in}$ for artificial data for the LSB galaxy model B (**left**) and the HSB galaxy model C (**right**). Arrows indicate the values of $\gamma_{\rm in}$ for the input model (black) as well as for the best-fit Burkert (green), Einasto (red), Hernquist (orange) and (α, β, γ) (purple) profiles. See text for a discussion.

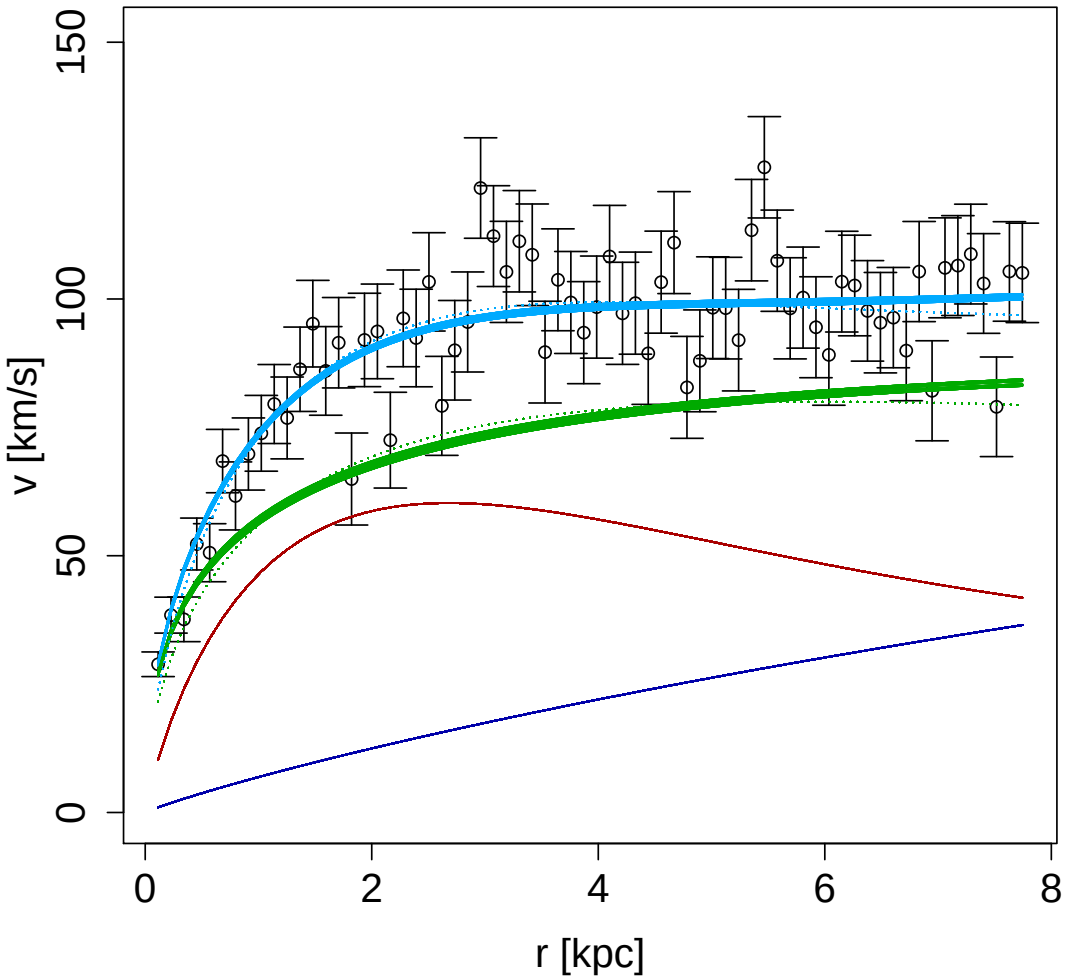

Figure 3.5: The highest likelihood model identified by the MCMC chains in the HSB galaxy model C. The dotted curves are the input model, while the solid curves are for the models in the MCMC bin (in the 7-dimensional parameter space) containing most models (the thickness of the curve is due to many similar models being over-plotted). The stellar disk is shown in red, the gas disk is dark blue, the dark matter halo is green, and the expected (total) rotation curve is light blue.

obtained in the range of the data.

Of particular relevance to the question of resolving the cusp-core issue, the lower panel shows that we are still able to exclude models with uniform density cores at a high level of confidence even in the presence of realistic velocity errors. This is made more quantitative by the histogram in the left panel of Fig. 3.4 which shows the distribution of the derived quantity $\gamma_{\rm in}$, the logarithmic slope of the halo density profile at the radius of the innermost data point. The various vertical arrows in the plot show the results of the direct fitting of a selection of individual halo models to the rotation curve data, rather than taking the MCMC approach. This is akin to the type of modelling that is more commonly applied to rotation curve data, and the models used span the range of models normal considered in such analyses. The peak of the MCMC histogram coincides with the values of $\gamma_{\rm in}$ for the directly fitted (α,β,γ), NFW and Einasto models. More importantly, the histogram shows that the input data (generated for a cusped halo model) are able to exclude Burkert halo profiles. This shows that our MCMC analysis is able to constrain the inner slope of the dark matter halo of an LSB galaxy.

The high surface brightness case shows a distribution that is more than 1σ from the input value, but as the best fit (α,β,γ) model still coincides with the peak of this distribution, this is not a problem with MCMC. Some realisations of the random errors may disfavour the input model compared to other ones, and the "correct" distribution that the MCMC should output is that which is pointed to by the data, which does not always correspond to the input values because of this.

We conclude that current data for LSB galaxies are sufficient to place constraints on the dark matter profiles of those galaxies. We are able to make this stronger claim than previous work due to the greater generality of our modelling.

3.4.3 High Surface Brightness galaxy

We now consider the case of an artificial data set for an HSB galaxy which we construct based on the higher surface brightness stellar contribution of NGC7793, but embedded in the same dark matter halo as in the previous sections so that the contribution to the simulated rotation curve from baryons is comparable to that of the dark matter. Because a maximal (or near maximal) disk could provide a reasonable fit to the data in this case (see Fig. 3.5), it is important to know whether or not it is still possible to constrain the dark matter halo parameters.

As the right panel of Fig. 3.4 shows, the algorithm is able to obtain a constraint on the dark matter halo profile which appears to be only marginally weaker than that returned in

the LSB test, as seen in the left panel and in Fig. 3.3. However, the results for the HSB galaxy exhibit a bias towards steeper slopes for the reasons stated above. The MCMC distributions for $\gamma_{\rm in}$ can be well approximated by a Gaussian for both these test cases, and thus can be used to estimate the uncertainty on this value. We find $\gamma_{\rm in} = 1.00 \pm 0.11$ and $\gamma_{\rm in} = 1.25 \pm 0.11$, for the low and high surface brightness cases, respectively. For comparison, a simple maximum likelihood fitting of the (α, β, γ) halo profile to these data yields $\gamma_{\rm in} = 1.06$ and $\gamma_{\rm in} = 1.31$, respectively, but without providing information about the distribution of allowed values.

It is important to remember that in this test we have assumed that the Υ and $R_{\rm d}$ of the stellar components are both known and are therefore fixed at their correct values along the MCMC chains. Given the significant contribution of the baryons to the overall gravitational potential in this case, the results will clearly be strongly sensitive to uncertainties in these two parameters. In Section 3.4.8 we return to this issue and consider the case in which the stellar parameters are only very weakly constrained.

3.4.4 Higher resolution data sets

We now investigate what would happen if, in the future, data sets of higher spatial resolution became available. Thus far, our artificial data sets have used the same radial bins as those in the THINGS rotation curves from de Blok et al. (2008) for the two galaxies on which they are based (i.e. DDO 154 for the LSB case and NGC 7793 for the HSB case). In this test, we generate a data set with twice the number of radial bins over the same radial range. We assume that the velocity error bars remain unchanged - while this may be pessimistic (higher resolution sampling of the rotation curve might be expected to coincide with improved velocity resolution also), it allows us to separate the impact of higher spatial resolution rotation curves from more precise velocity measurements. The current radial bin size for DDO 154 is 136 pc, which at a distance of 4.3 Mpc is an angular resolution of 6.5″ (de Blok et al., 2008), so this higher density data set would have an angular resolution of 3.25″.

Fig. 3.6 shows that a value of $\gamma_{\rm in} = 1.13 \pm 0.08$ is obtained from the high spatial resolution test, and whilst this gives a 27% reduction in reported error, the peak of the distribution remains offset from the input model value of 1.07 by a similar amount to the lower spatial resolution test. This indicates that there is relatively little to be gained at the present time from increased spatial resolution until the velocity errors are significantly reduced.

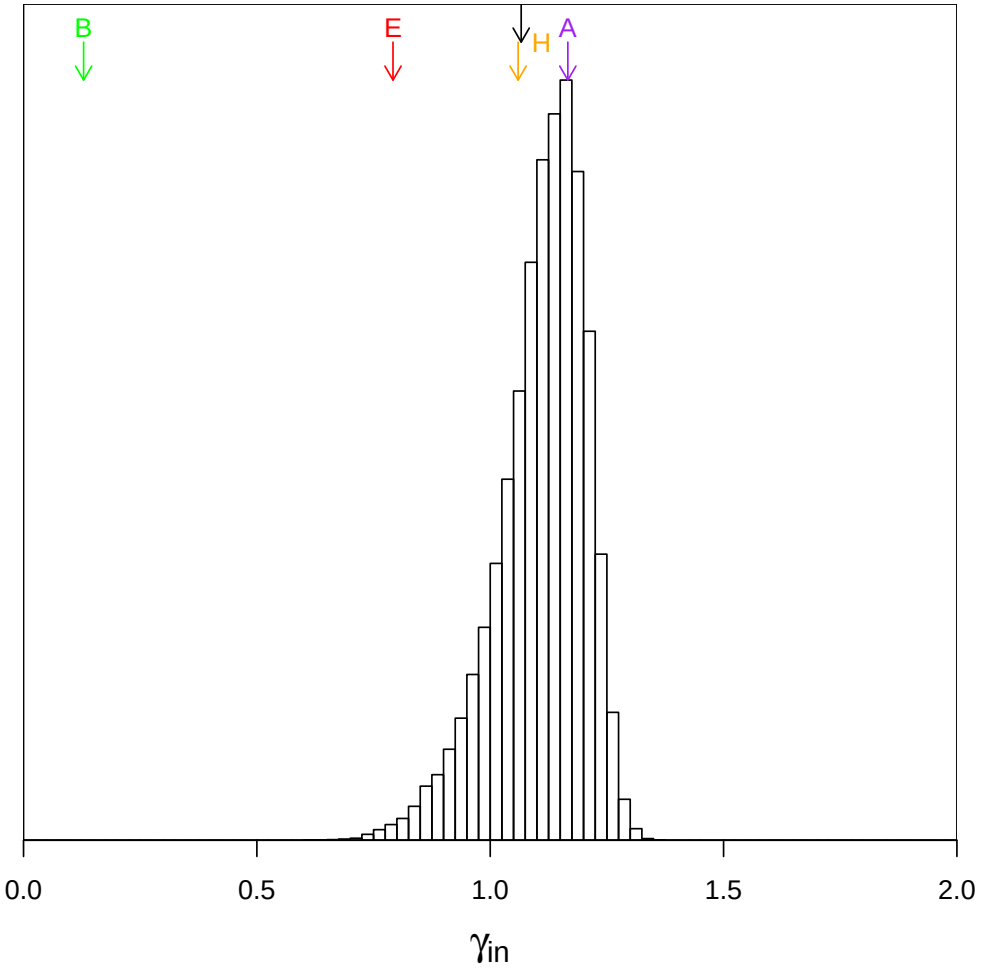

Figure 3.6: As in Fig. 3.4 but for artificial data for an LSB galaxy with realistic observational error bars (model D), and with the radial sampling density of the rotation curve increased by a factor of two. See text for a discussion.

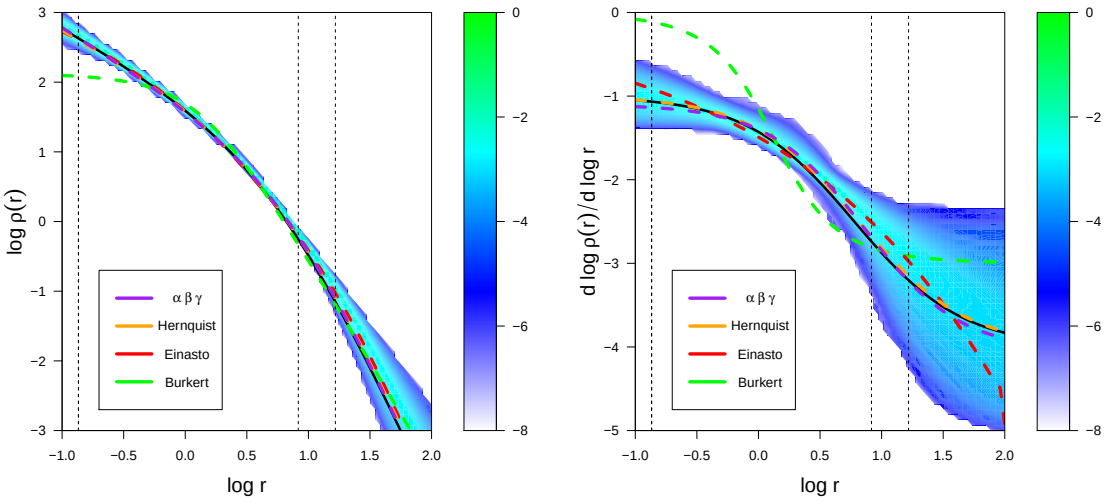

Figure 3.7: As in Fig. 3.2 but for artificial data for an LSB galaxy with realistic observational error bars and the data range extended by a factor of 2 (model E). The rightmost vertical dashed line represents the new maximum radius, centre vertical dashed line represents the original maximum radius in previous tests. See text for further discussion.

3.4.5 Data sets extending to larger radii

In this section, we apply our algorithm to data sets which extend to significantly larger radii than are probed by current rotation curve observations. We implicitly assume that the target galaxy has sufficient gas at these radii to make the observations possible, and that the baryonic disk remains relatively undisturbed so that our modelling assumptions remain valid. In principle, given a suitable target and sufficient observing time, it would be possible to obtain such a data set using existing instruments.

The left panel of Fig. 3.7 shows the constraints on the density profile which we obtain for a data set extending to $\sim$ 16 kpc with velocity errors typical of current observations. Comparing this with Fig. 3.3, one might be tempted to conclude that improved constraints are obtained at all radii, including the inner regions. It is important to note that this occurs only because the data at large radii place tighter constraints on parameters in our halo model such as β which leads to a reduced range of available parameter space at all radii. A non-parametric approach to the modelling would alleviate this situation, and we intend to pursue this in the future.

Comparison of Figs. 3.7 and 3.2 shows that the fit quality is not improved by as much as it is when the velocity errors are reduced. We conclude that future observational programs should concentrate on reducing the velocity errors rather than increasing the spatial

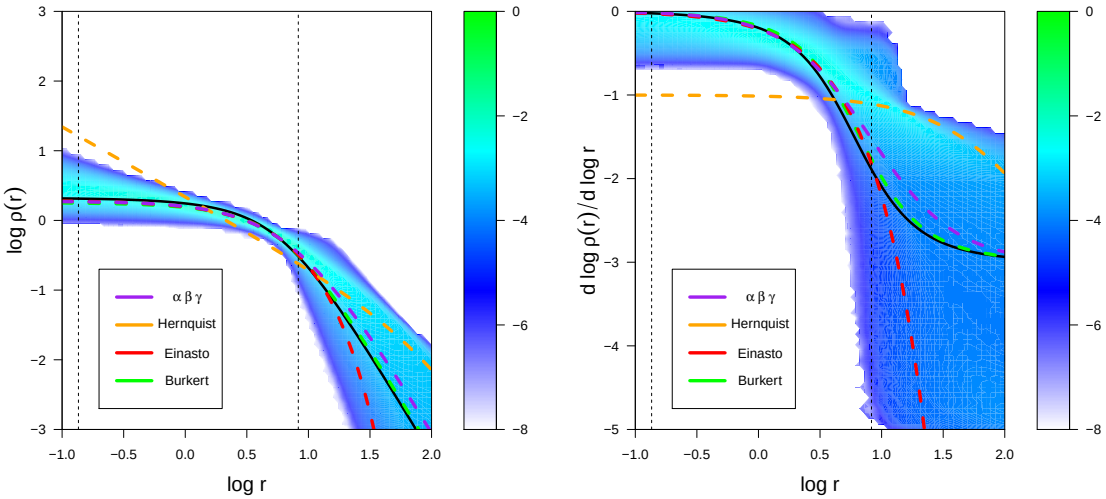

Figure 3.8: As in Fig. 3.2 but for artificial data for an LSB galaxy with a Burkert dark matter halo (model F).

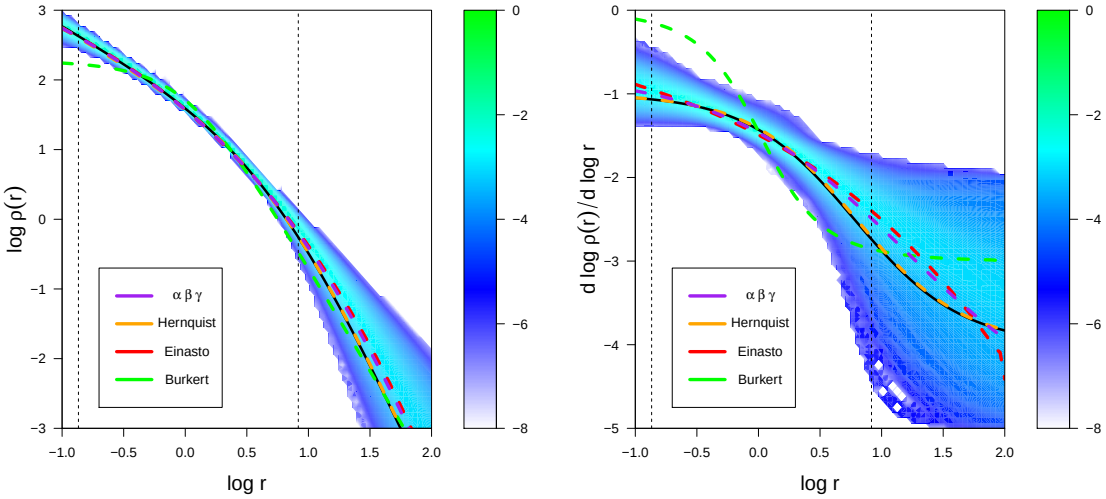

Figure 3.9: As in Fig. 3.2 but for artificial data for an LSB galaxy with realistic observational error bars, and free stellar disk parameters f_{Υ} and $f_{R_{\rm d}}$ (model G).

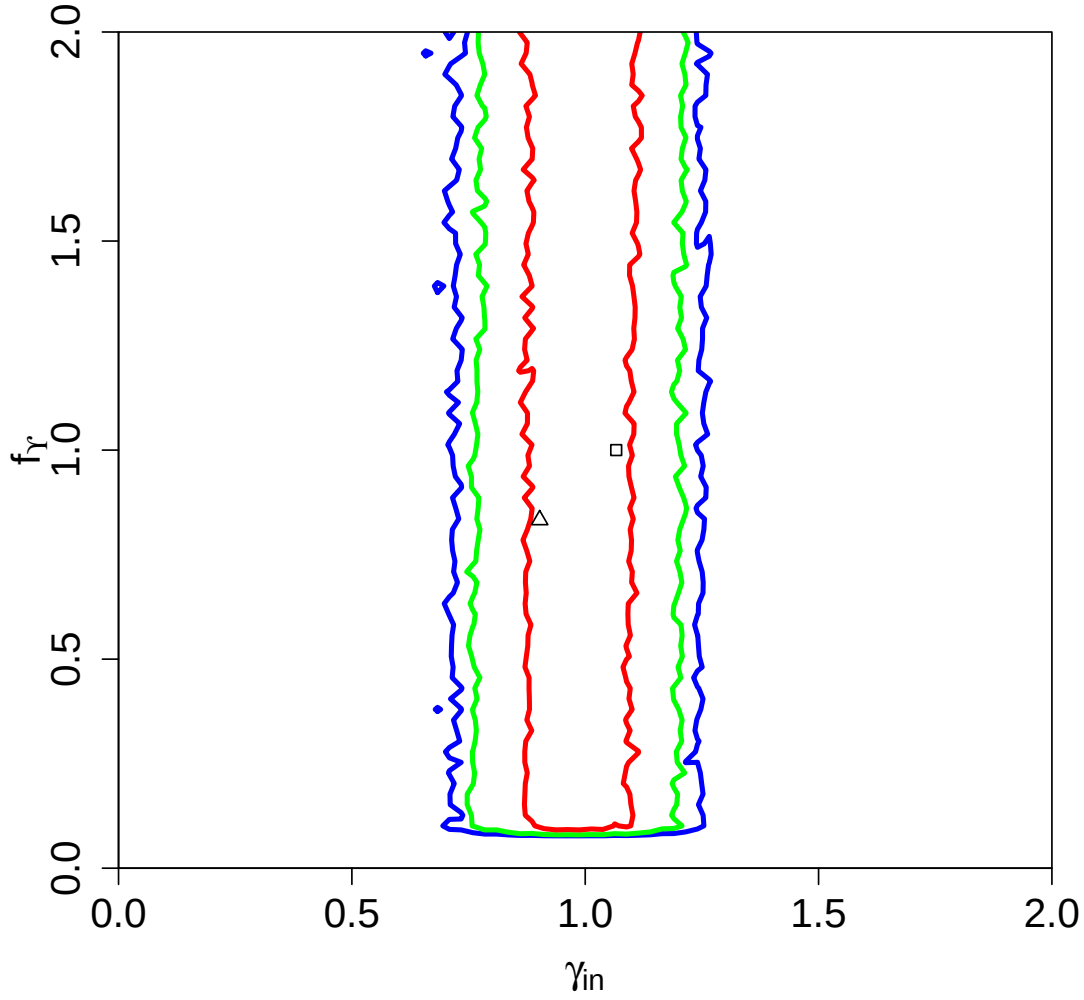

Figure 3.10: Contour plot of models for an artificial data set with a Hernquist input profile, free stellar parameters, and realistic errors (model G), in the f_Υ versus $\gamma_{\rm in}$ plane. The red contour encloses the region containing 0.683 of all models (equivalent to a 1σ contour), while the green and blue contours contain 0.95 (2σ) and 0.999 (3σ) of all models, respectively. The corresponding contours in the $f_{R_{\rm d}}$ versus $\gamma_{\rm in}$ plane show the same independence of $f_{R_{\rm d}}$ and $\gamma_{\rm in}$. The open triangle shows the model with the highest likelihood in the MCMC output, while the open square shows the input model.

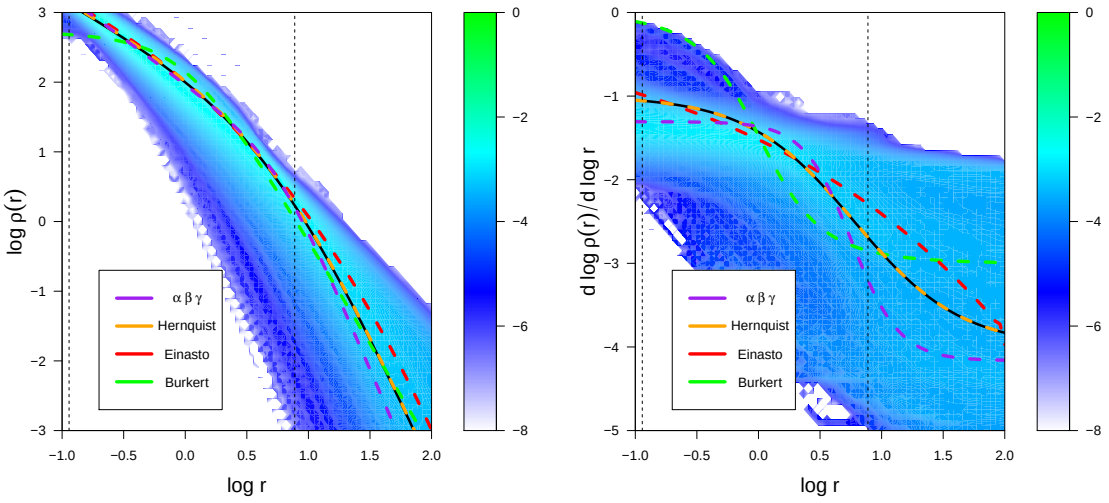

Figure 3.11: As in Fig. 3.2 but for artificial data for an HSB galaxy with realistic observational error bars, and free stellar disk parameters f_{Υ} and $f_{R_{\rm d}}$ (model H).

resolution or radial extent of the rotation curve data.

3.4.6 Cored Profile Test

Much of the original impetus for detailed rotation curve modelling came from interest in the question of whether galaxy haloes are cored or cusped. In the previous sections, our input data were generated from model galaxies with Hernquist dark matter haloes, which are cusped ($\gamma = 1$). We now consider the case of a galaxy whose halo has a Burkert profile, a widely-used cored halo profile, which also forms the basis of the Universal Rotation Curve analyses of galaxy rotation curves (e.g. Persic and Salucci, 1988, 1991; Persic et al., 1996). Another reason for selecting this particular cored profile is that it is not a member of the (α, β, γ) family (although over a restricted range of radii it can be closely represented by a profile from this set) and thus constitutes a test of the performance of the algorithm when the parameterisation of our models does not match the actual form of the dark matter halo. We assume radial sampling similar to that of DDO 154 and realistic velocity errors.

The results of this test are shown in Fig. 3.8. The distributions in both panels show that the MCMC chains are favouring models with shallow inner profiles. Comparison with the results in section 3.4.2 shows that the algorithm is able to distinguish between haloes with cored and cusped density profiles in the radial range probed by the rotation

curve. More quantitatively, the MCMC chains yield an estimate of $\gamma_{\rm in} = 0.15 \pm 0.13$, which excludes haloes with cusp slopes steeper than 0.67 with 4σ confidence.

We conclude that our algorithm is able to distinguish between cored and cusped halo profiles using extant observational data sets for LSB galaxies.

3.4.7 Free stellar disk parameters

We explore the impact of observational and modelling uncertainties in the Υ of the stellar population and the disk scale radius R_d by repeating our analysis from section 3.4.2 but now allowing both quantities to vary along the chains. This represents the fact that the stellar population of the target galaxies is not known precisely, which translates into an uncertainty in the disk Υ, and the simplification we make in the disk modelling by fitting a smooth function to the observed data, which may lead to uncertainty in the disk scale length $R_{\rm d}$.

We note that the distribution of f_Υ values from the MCMC chains is almost uniform, which indicates that the data are not able to constrain the f_Υ in this case. Nevertheless, Fig. 3.9 shows that the algorithm is able to constrain the halo density profile with a similar level of precision to that obtained when the stellar parameters were held fixed (Fig. 3.3). This behaviour can be understood by the fact noted earlier that the stellar disk contributes to the total rotation curve in quadrature, rather than linearly. As a result, the full range in disk f_Υ covers a range in amplitude of $\lesssim 1\,{\rm km\,s^{-1}}$in the total rotation curve.

Our test shows that a galaxy with a comparable ratio between surface brightness, observed rotation curve, and observation errors to the one we have synthesised here cannot constrain f_Υ, but can still constrain properties of the dark matter halo.

Fig. 5.5 presents contours in the f_Υ versus $\gamma_{\rm in}$ plane and shows explicitly that the estimate of $\gamma_{\rm in}$ is independent of f_Υ. The corresponding contours for $f_{R_{\rm d}}$ are very similar to those for f_Υ. This emphasises the power of the MCMC approach over simple model fitting. If the MCMC analysis of a real galaxy results in a flat distribution of the disk parameters whilst still being able to constrain dark matter parameters, and exhibiting no correlation between $\gamma_{\rm in}$ and the disk parameters, we are able to conclude with confidence that the halo parameters have genuinely been constrained independently of the disk.

3.4.8 High surface brightness test with free stellar parameters

Distinct from the question of whether a near maximal disk makes it impossible to constrain the properties of a dark matter halo, we wished to investigate the degeneracy be-

tween $v_{\rm max}$ and f_Υ, both of which affect the amplitude of the total rotation curve. We therefore applied the algorithm with free f_Υ and $f_{R_{\rm d}}$ to our HSB data set. The results are shown in Fig. 3.11. As one would naively expect, the degeneracy between $v_{\rm max}$ and f_Υ means that a much wider range of halo profiles may be consistent with the observed data set.

We therefore conclude that HSB galaxy rotation curves are of limited value for constraining dark matter halo profiles unless robust information about the stellar disk mass distribution is available either through stellar population-based estimates of Υ or estimates of the vertical velocity dispersion within the disk (see e.g. Bershady et al., 2010). This agrees with previous work: for example Gentile et al. (2004) who found that Burkert and NFW haloes yielded equally good fits to the data for NGC 7339 which they partly attributed to uncertainties in Υ and partly to the limited radial extent of the observed data.

Compared to the test in Section 3.4.3, Fig. 3.12 shows that we obtain a much weaker constraint on $v_{\rm max}$ here, which is an indication that the dark matter component is highly degenerate with the stellar component, and thus the result for the shape of the dark matter halo is unreliable. The right panel of Fig. 3.12, presents a contour plot showing the degeneracy between f_Υ and $\gamma_{\rm in}$ for this test. The input value $\gamma_{\rm in} = 1.05$ is much more strongly excluded for $f_\Upsilon = 1.5$ than for $f_\Upsilon = 1.0$. If such a degeneracy is seen when working with real data, it must be resolved before the likelihood distribution produced can be accepted.

In this case, we obtain an estimate of $\gamma_{\rm in} = 1.36 \pm 0.19$, giving the impression that the data are able to distinguish strongly cusped haloes from uniform cores. It is worth noting that the MCMC peak is consistent with the best fit (α, β, γ) curve - both exclude the input value of $\gamma_{\rm in}$ at $\approx 2\sigma$. The power of our MCMC approach to the problem is that we are alerted to the fact that these constraints may be spurious by the presence of strong degeneracies between parameters. We can thus explicitly and straightforwardly identify those cases in which the algorithm fails to constrain the halo parameters of the target galaxy. A simple fitting of a small set of halo profiles, on the other hand, could yield artificial constraints on the halo profile which were not actually arising from the properties of the data themselves.

3.4.9 Over-estimated errors

In our final test, we explore the performance of our algorithm on data sets in which the error bars do not reflect the scatter between successive data points along the rotation curve. This is seen in several of the THINGS galaxies, and is caused by the definition

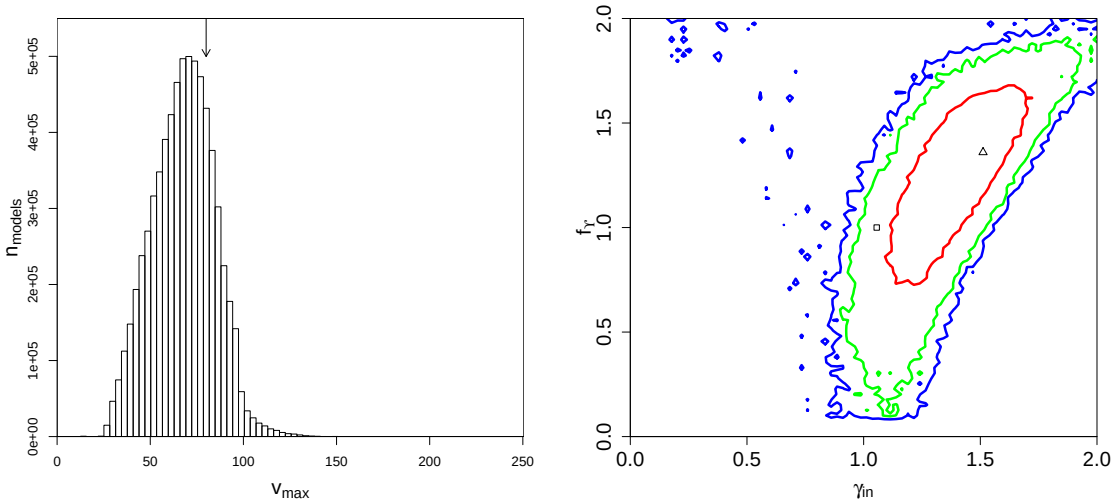

Figure 3.12: **Left:** The constraint of $v_{\rm max}$ in the HSB test (model H). **Right:** Contour plot showing the correlation between f_Υ and $\gamma_{\rm in}$ for the same model. Contours and symbols are as in Fig. 5.5.

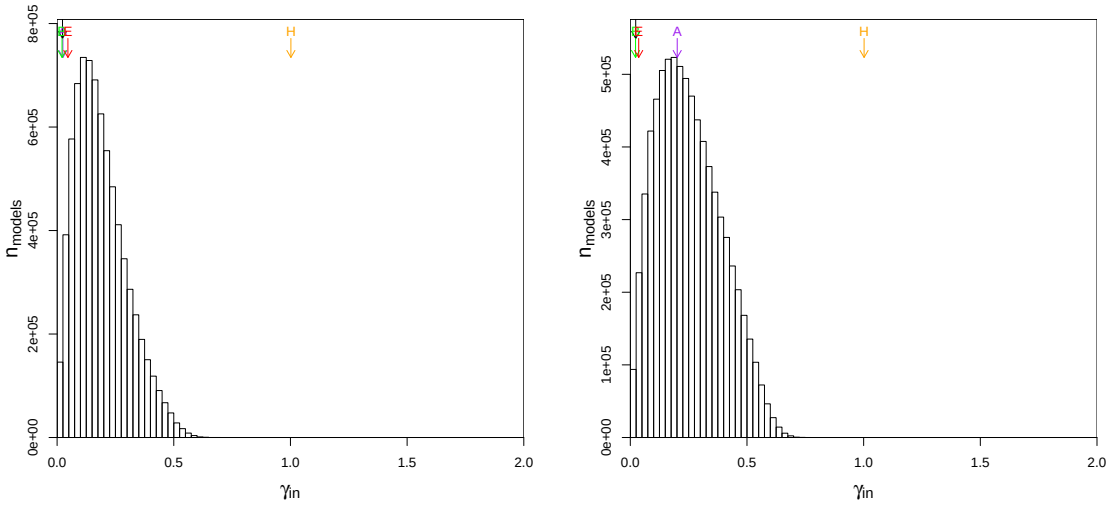

Figure 3.13: **Left:** Histogram of $\gamma_{\rm in}$ obtained for a data set generated for a galaxy with a Burkert model halo and realistic observational errors. **Right:** As in top panel, but with the error bars inflated by a factor of four relative to the actual Gaussian noise added to the data. Arrows are as in Fig. 3.4.

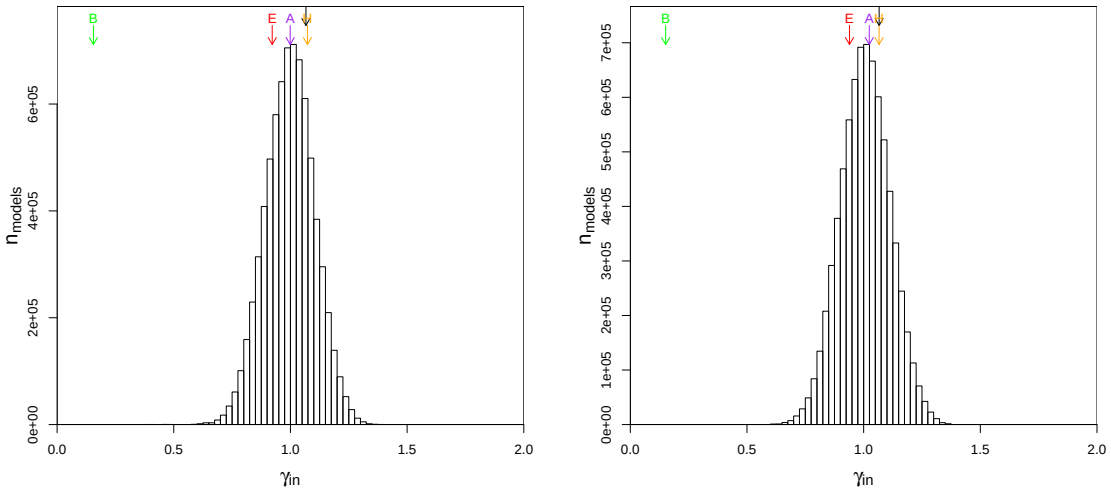

Figure 3.14: As in Fig. 3.13 but for data generated for a galaxy with a Hernquist dark matter halo.

of the error bars in terms of the variation between the rotation curve on either side of the rotation axis rather than purely the statistical noise around an annulus of the tilted ring model. Systematic differences between the rotation curve on either side of the axis can therefore lead to over-sized errors being quoted for the data, resulting in a series of data points whose error bars are much larger than the scatter between the points.

To test the effect of such error inflation, we generated Hernquist-based and Burkert-based models where the error bars on the data points were a factor of four larger than the noise which had been added to the observation - the noise added was the same as that added in Model B. All other model inputs remain the same. The noise added to the data is generated randomly for each realisation, rather than being the same errors scaled differently for each model.

Figure 3.13 shows, for the Burkert models, that the distribution of $\gamma_{\rm in}$ values returned by the MCMC chains is not greatly affected even by this significant level of over-estimation - the peak of the distribution moves by $\lesssim 0.1$ and the shape of the distribution is somewhat broadened. In the case of a galaxy with a Hernquist halo, Figure 3.14 shows that the effect on the distribution is even smaller. It is worth noting that in case of the Burkert halo, the best single fit of an (α, β, γ) halo (indicated by the purple arrow) moves considerably, whilst the peak of the distribution from the MCMC algorithm does not. This is a further demonstration of the robustness of our MCMC method.

For the Hernquist case, the correct error case gives a log slope $\gamma_{\rm in} = 1.00 \pm 0.11$ and

the over-estimated error case gives a log slope $\gamma_{\rm in} = 1.01 \pm 0.11$. In the Burkert case, the log slope changes from $\gamma_{\rm in} = 0.15 \pm 0.11$ to $\gamma_{\rm in} = 0.22 \pm 0.16$, which is clearly within the 1σ uncertainty.

3.5 Comparison with previous methods

3.5.1 Profile fitting

Before we apply our algorithm to the observed data for DDO 154, we carry out a quantitative comparison between performance of our algorithm and that of the standard model fitting approach most common in the literature. In these tests, we fit five individual halo profiles which are commonly used in previous work. For each profile we used the `optim` function in R[3] which employs a limited-memory BFGS method with box constraints (L-BFGS-B; Byrd et al., 1995). This method constrains the fitting to a specific parameter volume which we set to be the same parameter volume as that available to the MCMC algorithm in order to facilitate a fair comparison between the two approaches. We compare the best-fit model parameters returned by this method with (i) The model from the centre of the most favoured bin of the MCMC distribution (with 512 bins per parameter); (ii) the distribution of models returned by the MCMC analysis.

In these comparison tests, we use data generated using two input halo profiles: the Hernquist profile from the previous sections, as an example of a cusped halo, and the Burkert profile as a representative cored halo. For consistency with previous work which typically holds the Υ and R_d parameters constant, in this section we do not allow the stellar properties to vary along our MCMC chains.

The left panel of Fig. 3.15 compares the histogram of $\gamma_{\rm in}$ values returned by the MCMC analysis with the values obtained from the fitting of individual halo profiles. The consistency of the $\gamma_{\rm in}$ value for the best-fit (α, β, γ) model (purple arrow) with the peak of the MCMC-generated histogram, combined with an inspection of the MCMC chains for convergence, shows that the MCMC works with these data. The Hernquist, NFW and Einasto profiles yield also fits which are close to the MCMC peak.

More importantly, in this test the Burkert profile returns a $\gamma_{\rm in}$ value which is disfavoured by the MCMC distribution at the 3σ level. Reassuringly, its $\chi^2_{\rm red}$ values also disfavour these models relative to the NFW fit at the 3σ confidence level. This test suggests that the widely-used, simple curve-fitting approach can yield reliable results for

[3] http://www.r-project.org/

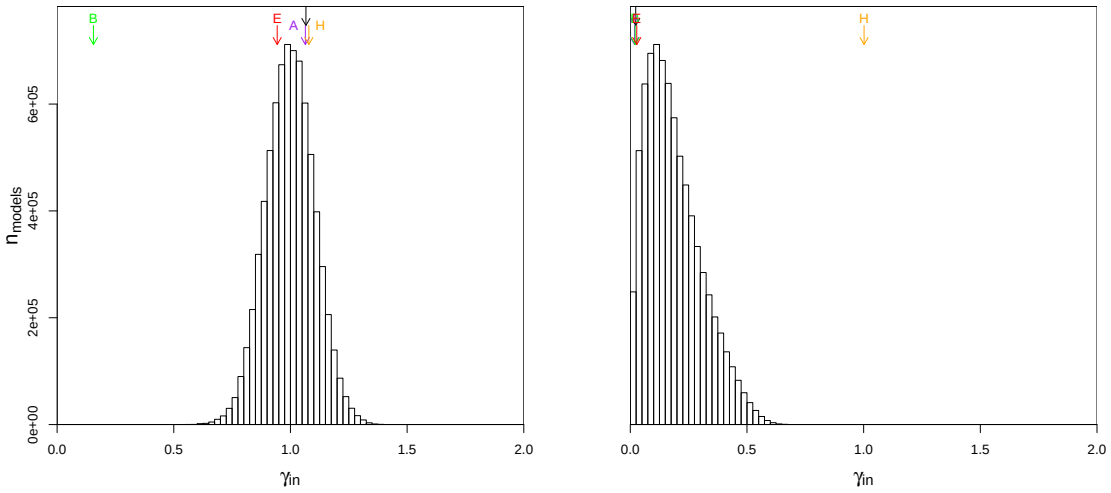

Figure 3.15: Histogram of $\gamma_{\rm in}$ values for a test with a Hernquist profile input (modelB, **left**) and a Burkert profile (model F, **right**). Arrows indicate the values of $\gamma_{\rm in}$ for the input model (black) as well as for the best-fit Burkert (green), Einasto (red), Hernquist (orange) and (α, β, γ) (purple) profiles. See text for a discussion.

cusped profiles, both in terms of recovering physical parameters and distinguishing between different halo models.

The $\chi^2_{\rm red}$ values for all single fits, and the parameters for these fits and for the optimal MCMC result, are shown in Table 3.3. In both cases the fits for the best MCMC result and the best-fitting (α, β, γ) model find very similar values for $\gamma_{\rm in}$, even though there is variation in the parameters.

In order to test the ability of our algorithm to distinguish between models with different values of $\gamma_{\rm in}$ we ran a series of models, based on Hernquist profiles $(\alpha, \beta, \gamma) = (1, 4, 1)$ but with γ values ranging from 0.1 to 0.9 in steps of 0.1 - uniform cored and $\gamma = 1$ cusped models having already been tested above. The distributions of $\gamma_{\rm in}$ for the three cases $0.1, 0.5$ and 0.9 are presented in Fig. 3.16. As the Figure shows, in each case, the MCMC chains are able to exclude both other values of $\gamma_{\rm in}$ at approximately 2σ confidence. We therefore conclude that provided the MCMC chains are properly converged, current observational data are sufficient to constrain $\gamma_{\rm in}$ to within $\lesssim \pm 0.25$. In addition to providing estimates of particular parameters, however, the MCMC approach returns the distributions of models which are consistent with the data, and is thus more informative than pure curve-fitting approaches.

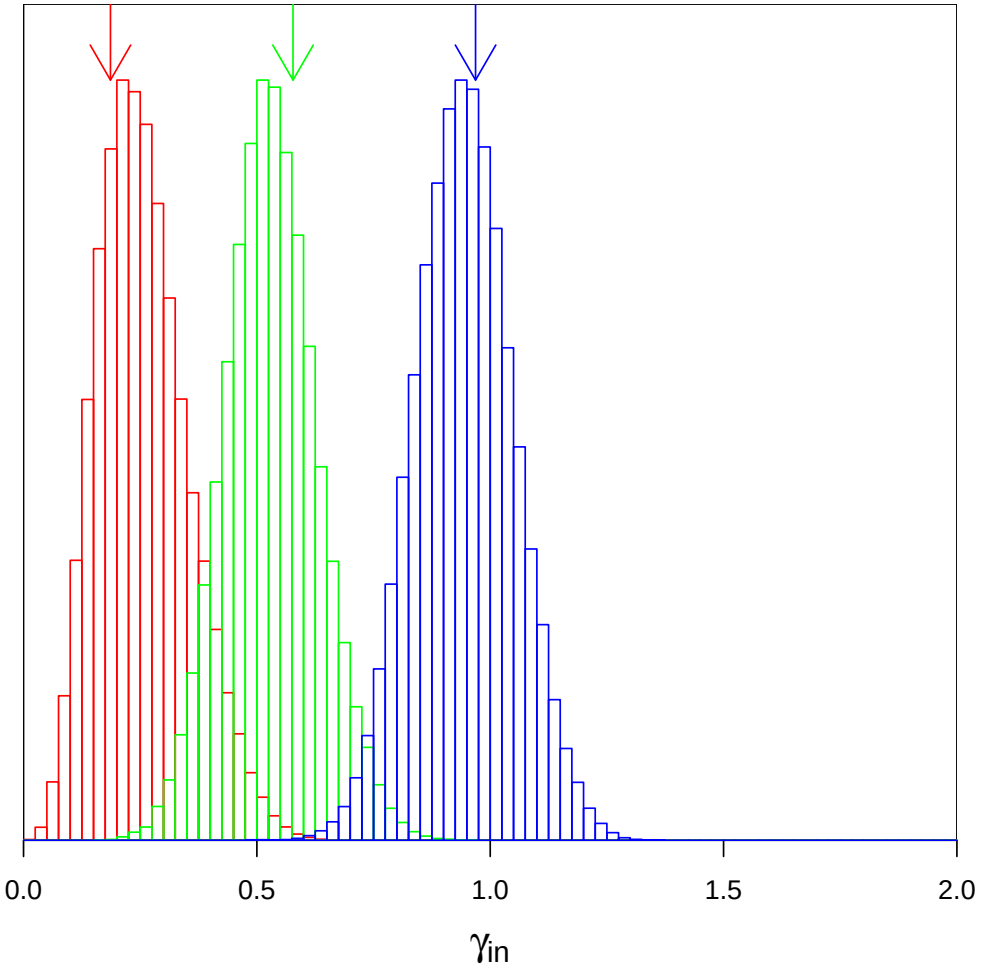

Figure 3.16: The constraint on $\gamma_{\rm in}$ for input values of $\gamma = (0.1, 0.5, 0.9)$ which are shown in red, green and blue respectively. The arrows show the values of $\gamma_{\rm in}$ for the input model - note that these are not the same as the input values of γ.

Input Profile	Fitted Profile	$\chi^2_{\rm red}$	r_s (kpc)	ρ_s ($10^{-3}\,{\rm M}_\odot\,{\rm pc}^{-3}$)	$v_{\rm max}$ (km/s)	n	α	β	γ	$\gamma_{\rm in}$
ModelB	(α,β,γ) (via MCMC)	–	3.84	102.485	48.085	–	1.86	3.409	0.73	1.105
ModelB	(α,β,γ) (via fitting)	1.325	9.09	10.425	48.141	–	1.216	5	0.94	1.064
ModelB	Burkert	2.091	1	206.215	48.969	–	–	–	–	0.156
ModelB	Einasto	1.276	2.597	7.308	47.945	3.927	–	–	–	0.943
ModelB	Hernquist	1.26	5.024	13.59	48.136	–	1	4	1	1.079
ModelF	(α,β,γ) (via MCMC)	–	10.841	2.583	41.962	–	1.157	2.894	0.004	0.067
ModelF	(α,β,γ) (via fitting)	0.967	8.061	1.876	33.947	–	0.799	3	0	0.018
ModelF	Burkert	0.918	6.667	1.807	30.558	–	–	–	–	0.021
ModelF	Einasto	0.932	9.063	0.271	29.339	0.982	–	–	–	0.028
ModelF	Hernquist	2.55	220.171	0.01	57.227	–	1	4	1	1.002

Table 3.3: Comparison of results obtained by fitting individual halo profiles to the data for Model B and Model F with the best-fit bin returned by the MCMC chains.

3.5.2 MCMC approaches

The application of MCMC techniques to the analysis of rotation curves was previously carried out by Puglielli et al. (2010). Their analysis was of a single galaxy, NGC 6503, using a more complex stellar model than is considered here (and, as a consequence, a higher dimensional parameter space). They used 18 parameters, and tested 4 distinct scenarios which effectively expanded the volume further, but without continuously parameterising the extra dimensions. The majority of the parameters related to the stellar distribution, while the dark matter halo was characterised by just three parameters: a density scale, a radial scale and an inner logarithmic slope. The other shape parameters of the halo were held fixed ($\alpha = 1$ and $\beta = 3$). They rejected the use of HI rotation curve data on the basis that the one dimensional data they were modelling could not differentiate between circular and non-circular motion. They instead use stellar rotation curves, which require additional calculation to take into account asymmetric drift.

Our motivation for allowing the parameters α and β to vary, in contrast to the approach of Puglielli et al. (2010), is that we wish to determine explicitly the extent to which the observed data can constrain the halo profiles. By using an MCMC approach, parameters which are unconstrained are easily identified as such. Further, MCMC permits easy identification of parameter degeneracies. This is a key advantage of the method as it makes it possible to determine which physical quantities are constrained by the data. It is important to note that although individual parameters in our models (e.g. the asymptotic log slope of the halo profile γ) may not be constrained, the data may nevertheless constrain physical quantities such as the log slope at the innermost data point (which is a non-linear function of all the model parameters). A simple example of this is that the gravitating mass within the outermost data point, which depends on all five model parameters, can be constrained simply by virtue of our assumption that the gas is moving on circular orbits at each radius. If we fix the shape of the halo at large radii, however, we limit the ability of the models to reproduce the data and may therefore bias the estimate of the mass. Including more parameters is justified provided that the MCMC results are interpreted with caution - no credence is given to individual parameters which are unconstrained, and all parameter correlations are carefully explored.

With the availability of two dimensional velocity fields, non-circular motion can now either be removed from HI data, or target galaxies can be selected on the basis of their exhibiting low levels of non-circular velocity. In either case, gas is a more reliable source for rotation curves as it does not require further modelling. This partly motivates our use of simpler models of the stellar components in this work than those used by Puglielli et al.

(2010). Additionally, however, we have found from our study that the inclusion of parameters which relate to physical quantities that are not constrained by the observed data creates the risk of biasing the analysis due to complications in the shape of the parameter space or the presence of degeneracies between these parameters and physical quantities which the data can constrain. In particular, if there is a region of the parameter space where one or more of the parameters no longer has an influence on the model likelihoods, and models in this region have an adequate (but not optimal) likelihood, then the overall distribution of models may be biased towards this region and away from higher likelihood models. For example, if a maximal disk is consistent with the data then a model which has a low value of $v_{\rm max}$ can have a wide range of $(\alpha, \beta, \gamma, r_{\rm s})$ without affecting its likelihood. The volume of parameter space associated with such high-Υ, low-$v_{\rm max}$ models is therefore increased, which may lead the MCMC chains to become biased in favour of maximal disk models.

We have therefore elected to take a bottom-up approach to the stellar modelling rather than an all-in approach and our models contain a minimal set of parameters. For the stellar distribution, two parameters is the least that are required to reflect the uncertainties in the data, and for the dark matter halo the $(\alpha, \beta, \gamma, v_{\rm max}, r_{\rm s})$ parameterisation is necessary to ensure that the full range of models which have previously been considered can be approximated within a single family.

3.6 Application to DDO 154

Having shown that our algorithm is able to produce reliable results, we now present an application to observational data for the LSB galaxy DDO 154. DDO 154 is a dwarf irregular galaxy whose mass has been estimated to be 3.0×10^9 $\mathrm{M}_\odot$ inside a radius of 8 kpc (Carignan and Purton, 1998). The galaxy also has an extensive gas disk, providing good data for the study of its rotation curve. In a recent study of the rotation curve of DDO 154, also based on THINGS data, Oh et al. (2011) found the log slope of its halo based on the inner data points to be $\alpha = 0.29 \pm 0.15$. This study excluded the innermost data point, where our $\gamma_{\rm in}$ is defined, but in what follows we take this as a general description of the inner slope for comparison with our results.

It is worth noting that the error bars on the rotation curve of DDO 154 presented in de Blok et al. (2008) appear, on inspection, larger than the noise in the data points, suggesting that they are not purely statistical errors and may be affected by the error inflation discussed earlier, in Section 3.4.9. While we have shown already that such outsized errors

do not strongly impact on the performance of our algorithm for an LSB galaxy, it is an undesirable feature of the tilted ring modelling approach to the determination of rotation curves which we plan to address in future work.

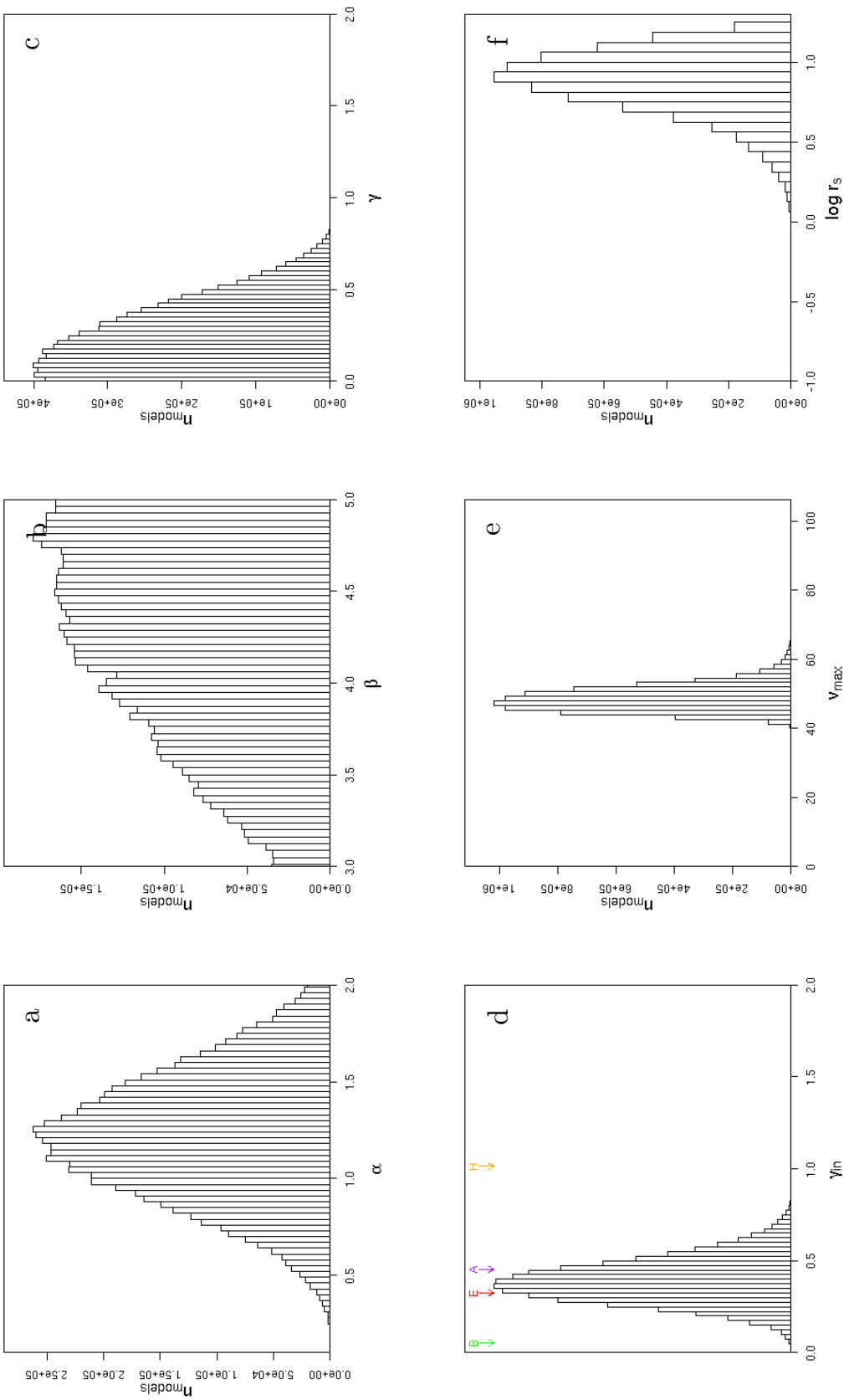
a
b
c
d
e
f
α
β
γ
γin
vmax
log rs
nmodels
A
B
C
D
E

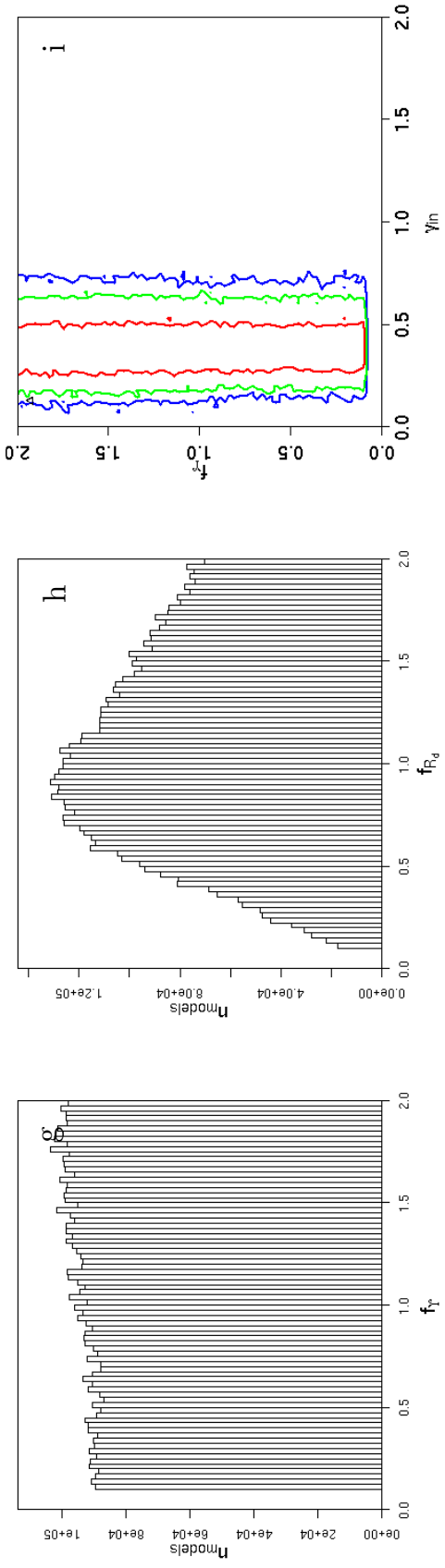

Figure 3.17: Detail of the output of the MCMC algorithm run on DDO 154 with free stellar disk parameters f_Υ and f_{R_d}. **a)** Histogram of α values. **b)** Histogram of β values. **c)** Histogram of γ values. **d)** Histogram of γ_{in} values. Arrows indicate the values of γ_{in} for the best-fit Burkert (green), Einasto (red), Hernquist (orange) and (α,β,γ) (purple) profiles. **e)** Histogram of v_{max} values. **f)** Histogram of $\log r_s$ values. **g)** Histogram of f_Υ values. **h)** Histogram of f_{R_d} values. **i)** As in Fig. 5.5 but for the case of DDO 154, showing that the constraint on γ_{in} is independent of f_Υ.

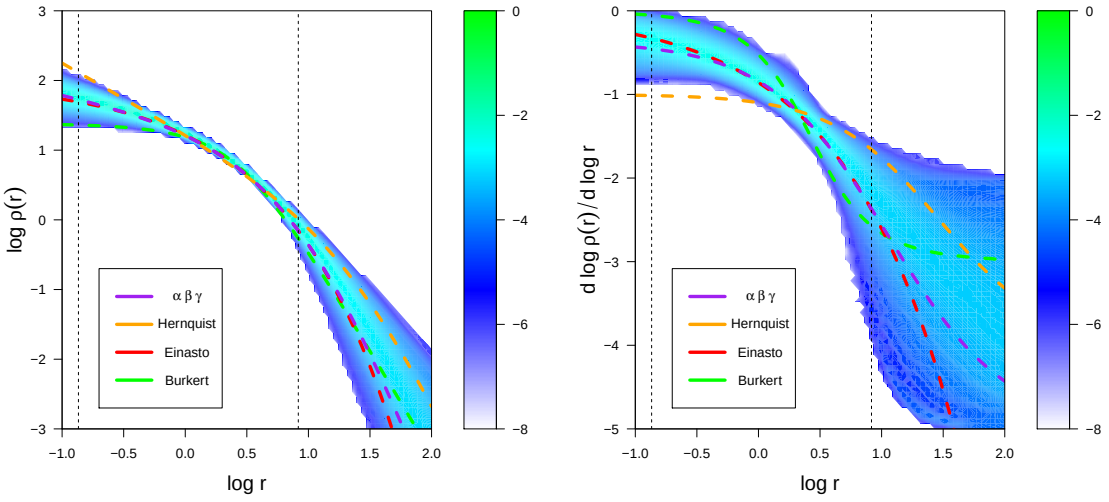

Figure 3.18: As in Fig. 3.2 but for DDO 154 data. Here we use free stellar disk parameters f_{Υ} and $f_{R_{\rm d}}$.

Fitted Profile	χ^2_{red}	r_s (kpc)	ρ_s (10^{-3} $M_\odot$ pc^{-3})	v_{max} (km/s)	n	α	β	γ	γ_{in}
(α,β,γ) (via MCMC)	–	10.422	37.665	48.399	–	1.443	4.558	0.129	0.337
(α,β,γ) (via fitting)	0.318	11.227	11.599	47.112	–	1.115	5	0.367	0.454
Burkert	0.55	2.648	24.171	44.395	–	–	–	–	0.054
Einasto	0.299	5.779	1.535	47.104	2.072	–	–	–	0.327
Hernquist	0.945	29.433	0.608	59.661	–	1	4	1	1.014

Table 3.4: Comparison of the most favoured MCMC bin of DDO 154 with the results of fits of individual halo profiles.

Fig. 3.17 presents the results of our MCMC analysis of DDO154 in the form of histograms of all the model parameters, as well as the physical parameter $\gamma_{\rm in}$. From the latter histogram, we find that the inner log slope of the DDO154 dark matter halo is $\gamma_{\rm in} = 0.39 \pm 0.11$. This result is consistent with the earlier result of Oh et al. (2011) ($\alpha = -0.29 \pm 0.15$, where α is an inner density slope derived from several data points). As the histogram shows, the data strongly exclude both $\gamma_{\rm in} = 1$ and $\gamma_{\rm in} = 0$. The $\gamma_{\rm in}$ histogram in Fig. 3.17 is similar to those shown in Fig. 3.16, which lends credibility to our MCMC constraints. We note that while the results shown in the Figure are based on runs in which the stellar parameters f_Υ and $f_{R_{\rm d}}$ are allowed to vary along the chains, the results obtained when we hold these parameters at their estimated values are very similar. This is consistent with our earlier findings that our analysis is able to return reliable constraints on the halo profiles of LSB galaxies independently of the quality of the constraints on the stellar parameters.

In order to compare our results for DDO 154 with those of previous studies of this galaxy in a quantitative manner, we have performed fits of individual halo profiles to the observed data in the same way as described in Section 3.5.1. A complete description of all the fits can be found in Table 3.4. These fits are also over-plotted on the MCMC data in Fig. 3.18, and their estimates of $\gamma_{\rm in}$ are indicated by the arrows in panel (d) of Fig. 3.17. The $\gamma_{\rm in}$ histogram shows that the Einasto and (α, β, γ) profile fits yield values of $\gamma_{\rm in}$ which are fully consistent with the distribution of values returned by the MCMC chains.

However, Table 3.4 shows that the $\chi^2_{\rm red}$ values for all the individually fitted profiles (including the (α, β, γ) and Einasto profiles) are less than unity. Comparisons between $\chi^2_{\rm red}$ values below unity are meaningless, as this represents consistently approaching data points within the 1σ error bars. The differences between these low values are essentially a measure of how effectively they model noise. Further, comparison of the $\chi^2_{\rm red}$ obtained from models with different forms and different numbers of fitting parameters is merely indicative of which models are preferred by the data, rather than being formally statistically robust. Our MCMC approach, on the other hand, allows us to compare the relative merit of the full space of (α, β, γ) halo profiles and hence to make meaningful statements about the generic properties of models which are consistent with the observed data. In a subsequent paper, we will exploit this power to obtain general results for the full set of THINGS galaxies (Hague & Wilkinson, in prep.).

Early work on the density profile of DDO 154 attempted to compare rotation curves for halo profiles whose parameters were determined by cosmological constraints. Moore (1994) excluded the Hernquist profile in favour of a cored profile, but only with a "cos-

mological simulation prior" on the Hernquist parameters. The same prior was later used by Burkert (1995) to argue for a "universal" dark halo profile. However, given the widely acknowledged limitations of cosmological simulations on kpc scales due to our incomplete understanding of the baryon physics on these scales we have opted not to restrict our parameter space by imposing priors in this manner.

In their analysis, Burkert (1995) drew on the work of Flores and Primack (1994) and concluded that the Burkert profile provides a better fit to the rotation curve of DDO 154 than a $\rho \propto r^{-1}$ cusp. The fact that this profile produced a good quality fit appears inconsistent with our result which excludes a purely cored halo at approximately the $\sim 2.5\sigma$ confidence level. However, the analysis in Burkert (1995) used $r_0 = 2.8\,\mathrm{kpc}$ for the Burkert halo and the innermost data point available at the time was at $r = 0.6\,\mathrm{kpc}$. The formula for the log slope of a Burkert profile is

$$\frac{\mathrm{d}\log\rho}{\mathrm{d}\log r} = -\left[\frac{r}{r+r_0} + \frac{2r^2}{r^2+r_0^2}\right] \tag{3.7}$$

so the shallowest slope within the data range then available was -0.26. It is also important to note that this data point has a very large error in v_c. At the same radius, the (α, β, γ) model at the peak in the $\gamma(r)$ histogram from our MCMC chains shows a log slope of -0.58. Burkert (1995) did not supply a fitting statistic nor errors for the Burkert fit parameters, so it is not possible from this information alone to determine if the result is truly incompatible. However, given the quality of the extant data at that time, it is possible that the uncertainties would be large enough to be consistent with our result. It is also worth noting that in addition to poorer quality velocity data, the stellar data that existed was not as detailed as that obtained from Spitzer and used in de Blok et al. (2008). In particular, from the figures provided by Flores and Primack (1994) it is clear that the dark matter rotation curve that was needed to reconcile their baryonic and total observed rotation curves was substantially and qualitatively different from that required for the current THINGS/Spitzer derived rotation curves. Nevertheless, we note that the shallowest log slopes from the Burkert (1995) and Oh et al. (2011) analyses are broadly consistent with that found by our study, with the caveat that they are measured at slightly different radii.

The principle conclusion of Burkert (1995) with regard to DDO 154 was that steeply cusped haloes were excluded by the data. Notwithstanding the differences in the observed data used in our study, their conclusion is fully consistent with the $\sim 4\sigma$ exclusion of such haloes by our method.

3.7 Conclusion

We have presented a new approach to the modelling of disk galaxy rotation curves which uses a Markov Chain Monte Carlo algorithm to explore the parameter space of a very general family of dark matter halo profiles. Through extensive testing on artificial data sets, we have demonstrated that our method can both recover dark matter halo profiles reliably and can provide robust constraints on the distribution of acceptable models in parameter space. More critically, when the observed data are unable to constrain particular parameters, or indeed the entire profile, the output of our algorithm shows this explicitly. This is a useful property, as it means that it does not require pre-judgement or pre-processing to determine whether or not a particular galaxy is amenable to this form of analysis; if a galaxy has too high a surface brightness to allow the dark matter halo parameters to be meaningfully constrained, the algorithm will explicitly show the degeneracy between dark matter and stellar contributions.

In particular, we have shown that the logarithmic slope of the dark matter halo profile at the location of the innermost data point in an observed rotation curve can be robustly constrained in the case of an LSB galaxy. This conclusion is insensitive to moderate over-estimation of the observational errors in the data sets. We have further shown that a reduction in the velocity errors of the data would improve constraints more than an increase in spatial resolution.

We have applied the method to the recently obtained THINGS data set for the LSB galaxy DDO 154, obtaining an estimate of -0.39 ± 0.11 for the logarithmic slope of the dark matter halo at a radius of 0.14 kpc, the radius of the innermost data point in the measured rotation curve. We have compared our MCMC results with those obtained by fitting individual dark matter halo profiles to the data. While the numerical value of our result is consistent with the results of previous studies of this galaxy, the marginalised probability distributions for the parameters that can be produced through MCMC give significantly more information than it is possible to obtain through the fitting of small set of halo profiles. Based on our analysis, it is possible to exclude logarithmic slopes of both 0 and 1 with high significance.

Clearly, our method has the potential to yield interesting results when applied to large samples of galaxy rotation curves. In future work, we intend to apply it to the full set of THINGS galaxies in order to obtain a general picture of the range of halo mass profiles which are consistent with current observed data.

4

Dark Matter In Disk Galaxies II: Density Profiles as Constraints on Feedback Scenarios

The disparity between the density profiles of galactic dark matter haloes predicted by dark matter only cosmological simulations and those inferred from rotation curve decomposition, the so-called cusp-core problem, suggests that baryonic physics has an impact on dark matter density in the central regions of galaxies. Using a Markov Chain Monte Carlo (MCMC) analysis of galactic rotation curves we constrain density profiles and an estimated minimum radius for baryon influence, r_1, which we couple with a feedback model to give an estimate of the fraction of matter within that radius that must be expelled to produce the observed halo profile. We examine the rotation curves of 8 galaxies taken from the THINGS data set and determine constraints on the radial density profiles of their dark matter haloes. For some of the galaxies, both cored haloes and cosmological $\rho \propto r^{-1}$ cusps are excluded which requires finely tuned baryonic feedback. For galaxies which exhibit extended cores in their haloes (e.g. NGC 925), the use of a split power-law halo profile yields models without the unphysical, sharp features seen in models based on the Einasto profile. We have found there is no universal halo profile which can describe all the galaxies studied here.

4.1 Introduction

Disk galaxies are presumed by ΛCDM cosmology to be dominated by dark matter e.g. (e.g. Bosma, 1978). An understanding of the arrangement of dark matter is therefore necessary for understanding the kinematics and dynamics of these galaxies. Analysis of galactic rotation curves, as well as of N-body cosmological simulations, has produced numerous models describing how dark matter density varies with distance from the centre of a galaxy.

Dark matter only cosmological simulations were found by Dubinski and Carlberg (1991) and Navarro et al. (1996) to produce haloes with an approximately universal density profile, with density proportional to r^{-1} towards $r = 0$ and r^{-3} towards $r = \infty$. These haloes follow a set of scaling relations with virial mass such that they behave as a single parameter family of models (Bullock et al., 2001).

The halo density profiles inferred from observing the rotation of disk galaxies appear to contradict this picture. For example, Gentile et al. (2004) inferred the density profiles of 5 spiral galaxies and found them to be consistent with flat cores. Rotation curves of 17 galaxies analysed by Bosma (2003) were also found to contradict simulations and exclude r^{-1} cusps. This has become known as the cusp-core problem. The possibility of the difference being due to erroneous inference of cores from observations has been discussed, and

refuted, in de Blok et al. (2003). This, coupled with an increase in resolution of kinematic data, has at this point resolved such concerns.

High quality data from The HI Nearby Galaxy Survey, THINGS (Walter et al., 2008) has allowed the generation of more detailed rotation curves, that extend to smaller radii than those used in previous treatments of the cusp/core problem (de Blok et al., 2008). An analysis of these rotation curves by Chemin et al. (2011) showed that an Einasto profile $\rho \propto \exp(-r^n)$, provides a better formal fit than cored profiles such as the Burkert profile (Burkert, 1995) or the NFW profile. Also using THINGS data, Oh et al. (2011) claimed that a selection of dwarf galaxies (including DDO 154, which we studied using an MCMC method in Chapter 3) exhibit $r^{-0.29}$ central slopes. They found all the dwarf galaxies in their study to be inconsistent with r^{-1} inner haloes. Velocity fields were also obtained via integral field spectroscopy and used to compare NFW haloes to pseudo-isothermal haloes for 17 galaxies by de Naray et al. (2008), claiming that a maximal disk and an NFW halo were mutually exclusive.

Simulations have been used to try and resolve the cusp-core problem. Read and Gilmore (2005) demonstrated that the baryon physics left out of pure N-body simulations can account for this disparity, in the case of dwarf galaxies, through time asymmetric mass loss (e.g. baryon infall and outflow), and Governato et al. (2010) used supernovae feedback to explain both the flattening of the inner dark matter density profile and the absence of bulges in dwarf galaxies. Another approach by Katz et al. (2014) attempted to account for the current density profile of a subset of THINGS galaxy dark matter haloes using only adiabatic contraction. They fit NFW profiles to the rotation curve data from de Blok et al. (2008) and compare the concentration parameter with that of a primordial halo.

In this chapter we attempt to provide an improved modelling of dark matter density profiles in a selection of THINGS galaxies using a more general parameterised density profile, the $\alpha - \beta - \gamma$ profile (Zhao, 1996), and a Markov Chain Monte Carlo (MCMC) method to explore the parameterisation. We also explore the implications of our improved density profiles for out understanding of feedback processes. The structure of this chapter is as follows; Section 4.2 summarises the rotation curve decomposition and MCMC techniques used to derive dark matter density profiles. Section 4.3 describes a simple analytic model that can be used to constrain formation scenarios for an individual galaxy given its halo density profile and rotation curve. Section 4.4 discusses the results for individual galaxies, and Section 4.5 draws conclusions from the analysis when applied to our full sample of galaxies.

4.2 Method

The rotation curve analysis method used in this chapter is described fully in Chapter 3. Here we will briefly summarise our data processing chain: first the method used by de Blok et al. (2008) to derive rotation curves from the THINGS velocity fields, secondly the halo density profile we fit to this data and the parameter space defined by it, and then finally the Markov Chain Monte Carlo (MCMC) method that we use to constrain the density profiles of the dark matter haloes. The output of this method is a distribution of halo models, and thus provides not only a best fit model but also robust errors.

4.2.1 Baryonic Mass Modelling

The rotation curve decompositions we used were provided by de Blok, and we describe their generation here for completeness. A more thorough description can be found in de Blok et al. (2008). Data from the Spitzer Infrared Nearby Galaxy Survey (SINGS: see Kennicutt et al., 2003) provides surface brightness data that, when mapped onto tilted rings and combined with an estimate of the mass-to-light ratio Υ for the stellar population, can give a radial mass distribution for the stellar component of the galaxy. When modelling 1D rotation curves, we assume it is sufficient to model this as an axisymmetric disk with exponentially decreasing density as a function of radius.

In de Blok et al. (2008) there are two values for Υ used; one derived from a Kroupa IMF and one derived from a version of the Salpeter IMF with the mass reduced by 30% that is referred to as a diet Salpeter IMF. Bell and de Jong (2001) found that reducing the number of low mass stars relative to the original Salpeter IMF was required in order to make the stellar disk "consistent with the maximum disk constraints". We use this value for Υ only as a centre point for the parameter range, half a dex either side of the values given in Table 3 in de Blok et al. (2008), which in all cases besides DDO 154 (due to its very low surface brightness) already encompasses baryonic mass scalings up to, and including, a maximal disk.

Gas can be modelled in the same way, from the THINGS data, but there are fewer issues determining the mass of gas present. HI emission is proportional to the neutral hydrogen present, and a scaling factor of 1.4 is applied that takes into account the amount of helium and metals that will also be present. Again, an exponential disk model is used in order to generate an axisymmetric potential and thus a 1D rotation curve contribution.

Our models do not include molecular gas, but following the method of de Blok et al. (2008) we assume that the density distribution of this gas follows that of the stars and is

a small fraction of the stellar surface density. There would be no benefit to introducing a parameter describing the ratio of stars to molecular gas, as it would be entirely degenerate with Υ.

There is some uncertainty in the inclinations of the galaxies studied here, which would manifest itself in a rotation curve as a systematic shift in the circular velocity. It would be possible to include the inclination as a parameter in our study, however it would also be degenerate with Υ; stellar and gas mass modelling are insensitive to inclination unless significant extinction occurs. This can only happen when the galaxy is near to edge on, and the galaxies in our set have already been selected to have intermediate inclination (see de Blok et al., 2008).

4.2.2 Dark Halo Profiles

We make three assumptions about the dark matter haloes of the galaxies analysed in this chapter

1. They are spherically symmetric
2. The density monotonically decreases with radius
3. The log slope is continuous and differentiable with respect to radius

Satisfying these constraints, a general, spherically symmetric, halo density profile has been selected, which either analytically encloses, or closely emulates, all commonly used density profiles. We start with the $\alpha - \beta - \gamma$ profile (Zhao, 1996)

$$\rho(x) = \frac{\rho_s}{x^\gamma(1 + x^{1/\alpha})^{\alpha(\beta-\gamma)}} \tag{4.1}$$

where ρ_s is the scale density, r_s is the scale radius and α, β, and γ are shape parameters. γ determines the log slope at $r = 0$, β determines the log slope as $r \to \infty$ and α the rate at which the profile transitions between the two power laws, with lower values being a sharper transition. We transform the parameter space of this profile thus:

$$\rho(x) = \frac{\widetilde{\Sigma}_{\rm max}}{G} \frac{v_{\rm max}^2}{x^\gamma(1 + x^{1/\alpha})^{\alpha(\beta-\gamma)}} \tag{4.2}$$

where $x = r/r_s$, with r_s the scale radius, $v_{\rm max}$ is the peak velocity of the dark matter rotation curve and $\widetilde{\Sigma}_{\rm max}$ is given by

$$\widetilde{\Sigma}_{\rm max} = \frac{\rho_s r_{\rm max}}{M(r_{\rm max})} \tag{4.3}$$

where $r_{\rm max}$ is the radius at which the profile's rotation curve reaches its maximum

velocity, $M(r_{\max})$ is the mass enclosed at that radius. A derivation and more complete description of this can be found in Chapter 3. The degeneracy removed by our transformation can be seen in Figure 1 of Katz et al. (2014) the case of an NFW profile (a subset of the $\alpha - \beta - \gamma$ halo) which applies a similar Monte Carlo method to ours to a simpler parameter space.

Because double power laws with respect to radius can be approximately modelled (provided the transition between the two powers is smooth) by a single power law over a finite range, we assert that our two power model can represent any profile containing more power laws, over a finite radial range, as long as a similar condition of smoothness is met.

4.2.3 Markov Chain Monte Carlo

A Markov Chain Monte Carlo (MCMC) method (Hastings, 1970) is used to integrate over the parameter space defined by the profile given in equation 4.2 along with two disk scaling parameters; a mass-to-light ratio multiplier f_Υ which scales the magnitude of the stellar contribution (relative to the mass-to-light ratio Υ for the diet Salpeter IMF case in de Blok et al., 2008). We consider f_Υ in the range [0.316, 3.16] which encloses the Kroupa IMF and the factor of 2 variation in infrared IMF suggested by Bell and de Jong (2001). We use `CosmoMC` (Lewis and Bridle, 2002), in a generic mode, together with a likelihood function of our own as our MCMC engine. MCMC is a Bayesian method that generates a probability distribution in the parameter space of a set of models. Bayes' Theorem states that

$$P(M[\mathbf{x}]|D) = \frac{P(D|M[\mathbf{x}])P(M[\mathbf{x}])}{P(D)} \tag{4.4}$$

where M is a proposed model defined by parameter vector $\mathbf{x}$, and D is the data. Assuming that $P(D) = 1$, we can then generate a series of values for $P(D|M)$ via a Markov chain process. Starting at a random point, the algorithm generates a new candidate point based on a random step drawn from a probability distribution, which in this case we take to be Gaussian. The new point $\mathbf{x}'$ is added to the Markov chain with a probability

$$P_{\text{accept}} = \min\left[\frac{P(D|M[\mathbf{x}'])}{P(D|M[\mathbf{x}])}, 1\right] \tag{4.5}$$

if the new point is not accepted, the current point is added again to the Markov chain. This process is repeated and, provided the chain is able to converge, produces a distribu-

tion of $P(D|M[\mathbf{x}])$, which can be combined with the prior distribution $P(M[\mathbf{x}])$ to calculate the probability distribution we seek.

A condition required for an MCMC run to converge well is that the step size (measured in our Gaussian case by a standard deviation σ in each parameter) is appropriate to the distribution. This can either be done by trial and error, or by a step size that adapts during the course of the run. We opt for the second approach, updating the probability distribution of candidate points relative to the current point based on a covariance matrix generated from the most recent half of the models generated. `CosmoMC` then samples $P^{1/T}(D|M[\mathbf{x}])$ where T is a temperature value which we set equal to 1 (reducing to Equation 4.5) unless there are specific problems finding a constraint, where we use $T = 2$.

A further condition for convergence is that the parameter space be able to cover the entire range of models that are likely to fit the data. In our case, this condition is of most concern for those haloes where $\gamma \to 0$, which are required to model the flat-cored Burkert (1995) halo. Boundary effects at the edge of the parameter space not only cause problems integrating there due to cutting off part of the Gaussian selection function, but also necessarily mean that the distribution is not normalised. Strictly, MCMC produces a non-normalised distribution, but the distribution can be normalised correctly if the probability tends towards zero at the boundaries of the parameter space, and the distribution can be assumed to have no models with nonzero probability outside this space.

To resolve this boundary issue, we mirror the parameter space around $\gamma = 0$. The MCMC explores a parameter range γ' in the range [-2, 2], and generates parameter values using $\gamma = |\gamma'|$, so the actual parameter γ is only explored in the range [0,2]. We do not consider negative values of γ physically consistent with our model of the dark matter halo.

We use 8 independent MCMC chains, each using approximately 5×10^6 models (the code terminates once the first chain completes, but as the run time for the chains is quite consistent this does not usually cause the chains to be unduly shortened.) The first 1×10^5 models in each chain are treated as burn in, the process by which the MCMC algorithm initially finds and moves into the main body of the distribution, and discarded.

Previous work on rotation curves such as Chemin et al. (2011) and Oh et al. (2011) has tested a small number of proposed density profiles against the data; these profiles represent single points (or in the case of the Einasto profile, curves) within the parameter space we explore. By fully characterising the parameter space, we are able to put these previous fits in a wider context.

4.3 Analysis

Once we have generated distributions of density profiles for each galaxy, we investigate their systematic properties, with reference to previous claims regarding the nature of dark matter haloes. Our primary focus is to find properties of the dark matter haloes that could constrain formation scenarios.

In previous work (see e.g. van den Bosch and Swaters, 2001), haloes whose density profiles became flat as $r \rightarrow 0$ are referred to as 'cored' whereas haloes that show density profiles approaching $\rho \propto r^{-n}$ where $n \geq 1$ are referred to as cusped. Terminology for intermediate haloes (i.e. those with $0 < n < 1$) is unclear. For the purposes of our discussion, we consider such haloes neither fully cusped nor fully cored.

The parameter γ, the asymptotic log slope of the profile as $r \rightarrow 0$, is a property of the profile that describes the shape of the halo outside the data range. Therefore we generate, from the halo profiles, an alternative parameter $\gamma_{\rm in}$. This is the log slope of the dark matter halo density profile at the innermost data point of the measured rotation curve. As the data sets all start at a different radius, direct comparisons between galaxies using $\gamma_{\rm in}$ are not possible. It is, however, a useful quantity because if it is substantially above zero, it excludes the existence of a core within the data range.

Another value we extract from our density profiles is r_1. This is the radius at which the log slope (which must monotonically decrease for all profiles) reaches -1. As we will show, this a well constrained and useful scale radius[1]. In order to demonstrate its utility, we construct a simple model for the formation of the galaxies we study here.

If we assume that the starting point for a dark matter halo is an NFW profile (or some other cosmological profile that tends towards a log slope of -1 at $r = 0$), then the density profile must have a logarithmic slope of $d\log\rho/d\log r = -1$ or steeper at all radii, so any part of the density profile that has a shallower slope can clearly be stated to be inconsistent with a cosmological profile derived from pure dark matter N-body simulations. Thus r_1 gives us a radius to which the effects of any process which modifies the shape of the halo must reach in order to account for the current density profile, and we now show that this is a conservative estimate.

The choice of the parameter r_1 is based on the minimisation of assumptions. To construct an exact model of an observed galaxy at the time of its formation would require

[1] In some work (e.g. Chemin et al., 2011), the radius r_2 is also used (sometimes written as r_{-2}, but we exclude the sign in order to maintain consistency with the positive sign of the parameters in the $\alpha - \beta - \gamma$ profile.) For individual profiles (such as Burkert profiles) the relationship between these is a straightforward, constant ratio.

knowledge of the density of the Universe and assert the exact correctness of a particular halo model such as NFW or Einasto (whereas we only assume that the halo had a cusp of some kind). Using r_1 allows a degree of physical modelling without having to resolve these unknowns.

In order to investigate the origins of non-cosmological (i.e. $\gamma < 1$) haloes, we construct a simple model of feedback, where outflows of gas on timescales shorter than the dynamical time of the halo can impart energy to the halo and alter its density profile. The source of this feedback can either be an accreting central black hole, supernovae, or other stellar feedback.

Our model features an inhomogenous spheroid of gas in a spheroid of dark matter, and a disk. Gas is removed entirely from the galaxy instantaneously and permanently during an outflow (realistic, given velocities of various possible outflows in e.g. Governato et al., 2010; King, 2003). Spheroidal symmetry allows us to make a number of simplifying assumptions in the discussion which follows in both the spherical case, and the oblate spheroidal case (Binney and Tremaine, 2008). Hereafter we only discuss radius, however the arguments still apply using the equivalent coordinate in an oblate spheroidal system.

Given the assumed geometry, dark matter particles can only respond to changes in the mass interior to their current position. If a certain portion of this mass is removed, a particle will respond by moving outwards. Assuming a much longer timescale for the removed mass to fall back in (if it does at all) the upper limit to the instantaneous change in the total energy of dark matter particles at any particular radius, taking the potential to be relative to r_1 is the change in potential interior to that radius. As baryons and dark matter move in the same potential, we assume a mass of baryons outflowing past r_1 can bring the same mass of dark matter with it. The change in dark matter mass of the halo interior to r_1 is obtained from

$$M_{\mathrm{I,dark}}(r_1) = M_{\mathrm{F,dark}}(r_1)(1 - f_{\mathrm{b}})^{-1} \tag{4.6}$$

where $M_{\mathrm{I,dark}}(r)$ is the initial mass interior to r and f_{b} is the fraction of mass that is in baryons and thus available for an outflow. We assume that the available gas is arranged in a diffuse spheroid the follows the density profile of the dark matter. In this case we are modelling a single outflow, or multiple outflows where any gas falling back in negates the effects of its initial outward movement exactly. In reality, infall happens over a much larger timescale than outflow (see e.g. Governato et al., 2010), but modelling this is beyond the scope of the simple model we are constructing here, and will be addressed in later work.

We assume here that the amount of dark matter removed from inside a radius r is approximately equal to the amount of gas removed. To verify this, we ran a series of 2×10^6 particle N-body simulations using `falcON` (Dehnen, 2000, 2002), using spherical initial haloes with inner log slopes $\gamma = 0, 0.25, 0.5, 7/9, 1$, and removing a fraction of mass equal to $f_b = 0.02, 0.04, 0.08, 0.16, 0.24, 0.48, 0.64, 0.90$. Mass is removed equally from all of the particles in the simulation. Under conditions of spherical symmetry this does not produce a different result from removing all the mass interior to r_1, and does not require an extra step of calculating the position of r_1.

We compared mass before and after, within the scale radius, and found that for a cosmological baryon fraction, the fraction of dark matter carried away with gas outflow is of order unity, as shown in Figure 4.1. The ratio decreases as the fraction of matter expelled (considered to be f_b here) as there is less dark matter in total to expel.

The starting conditions for these simulations were constructed in equilibrium using `mkhalo` from the same software suite - in reality the response of the dark matter to gas outflow is dependent on the velocity structure of the halo. This velocity structure depends on the precise history of the halo, as shown in Read and Gilmore (2005) where halo cores are formed by moving particles from tangential to radial orbits. Thus the exact order of the curves in Figure 4.1 should not be taken as strictly realistic, but it does demonstrate that the ratio between the dark matter removed and the gas removed at a certain radius should be of order unity.

From equation 4.6, assuming an initial and a final mass profile, we can compute the spheroidal baryon content at the time the outflow(s) occurred. In reality this could be raised by contraction of the gas content of the galaxy, or lowered due to baryons leaving the spheroidal gas component through either clumping, or becoming part of the disk, and either way being too dense to participate in an outflow event. However, we are able to produce a consistent model to predict f_g - the fraction of matter available as gas of sufficiently low density to be part of the feedback process.

Assuming the dark matter halo mass interior to the outermost data point we have observed is unchanged through feedback, there exists an NFW profile (using the scaling relation established in cosmological simulations) that gives a value for $M_\mathrm{I}(r_1)$ and the model above then gives f_g. In Section 4.5 we determine this value for this set of galaxies, and discuss whether they are realistic.

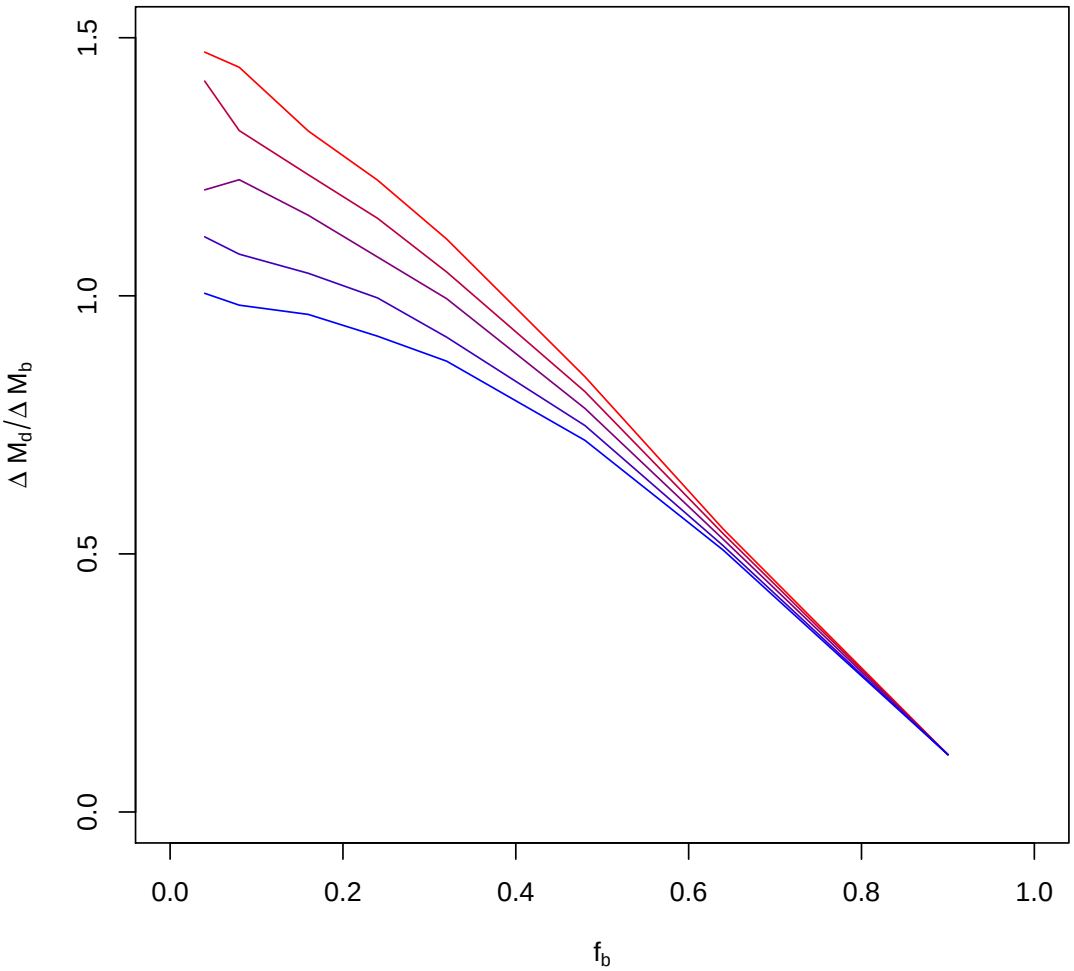

Figure 4.1: Ratio of the mass of dark matter removed from the simulated halo after outflow $\Delta M_{\rm d}$ to the mass of baryons removed during outflow $\Delta M_{\rm b}$, from N-body simulation, for a range of initial conditions. Red to blue denotes increasing log slope (0, 0.25, 0.5, 7/9, 1). Simulations were run with expelled fractions of the initial matter $f_b = 0.02, 0.04, 0.08, 0.16, 0.24, 0.48, 0.64, 0.90$. The ratio decreases as the fraction of matter expelled as there is less dark matter in total to expel. Deviations of the curves at low f_b are due to $\Delta M_{\rm b}$ being a smaller multiple of $M_{\rm particle}$.

4.4 Results

Table 4.1 shows relevant physical information for the galaxies in our sample and some detail of the MCMC output. We have sampled 4×10^7 models in each case, using 8 independent MCMC chains which have converged to similar distributions. The quantitative convergence statistic we use here, provided by the `getdist` program which accompanies `CosmoMC`, computes the variance of the means of the chains $\sigma(\hat{x})$, divided by the mean of the variances of the chains $\hat{\sigma}(x)$, and must be smaller than unity for a set of chains to be converged. This statistic is calculated for each parameter, and the largest value is taken to be an overall measure of convergence.

Galaxy	$V_{c,max}$(kms^{-1}) (1)	$A_{r,1kpc}$(kms^{-1}) (2)	Absolute B Magnitude (3)	H_2/HI ratio (4)	Models (5)	T (6)	$\sigma(\hat{x})/\hat{\sigma}(x)$ (7)
DDO 154	53.28 ± 3.79	$1.43\pm^{0.14}_{0.53}$	−14.23		38880635	1	0.0085
NGC 2976	86.23 ± 3.46	$2.18\pm^{0.77}_{0.55}$	−17.78	0.36	39310884	1	0.0098
NGC 7793	117.6 ± 5.0	$3.41\pm^{0.64}_{0.48}$	−18.79		39539819	1	0.0529
NGC 2403	143.9 ± 4.5	$2.60\pm^{0.59}_{0.48}$	−19.43		34880553	2	0.1315
NGC 925	114.5 ± 7.4	$9.45\pm^{0.64}_{2.98}$	−20.04	0.04	38180473	1	0.0959
NGC 3621	157.0 ± 5.7	$5.52\pm^{0.94}_{3.21}$	−20.05		38025138	1	0.3916
NGC 3198	158.7 ± 3.2	1.50	−20.75	0.04	36688012	1	0.3113
NGC 3521	218.8 ± 28.0	$3.12\pm^{12.67}_{1.77}$	−20.94	0.38	36845437	2	0.7693

Table 4.1: Galaxies studied in this chapter, ordered by absolute B magnitude. (1) Maximum circular velocities taken from rotation curves. (2) Amplitudes of non-circular motions, in the inner 1 kpc of each galaxy, from Trachternach et al. (2008). NGC 3198 only has one data point inside this radius so no bounds are available. (3) Absolute B magnitude from Walter et al. (2008). (4) Molecular gas to atomic gas ratio, calculated from HERACLES data (Leroy et al., 2009), where available. (5) The number of models sampled, excluding a burn in of 10,000 models in each of 8 chains. (6) The temperature parameter used with `CosmoMC`, which samples $P^{1/T}$ of each model. (7) Largest (i.e. worst) value of the statistic used to check that chains are converged on to the same likelihood distribution. See text for details.

The galaxies we study are modelled by de Blok et al. (2008), utilising HI velocity maps from THINGS to derive the rotation speed, the same HI data to derive a radial gas density profile, and 3.6 μm maps from SINGS (along with assumed Υ ratios) to derive the stellar components. Some of the galaxies in this sample are modelled with a single stellar disk, whilst some are modelled with a stellar disk and a separate bulge component.

Figure 4.2 shows the distribution of halo log slope profiles for all accepted models in the MCMC chains. We categorise as having cored haloes NGC 925, NGC 3198, NGC 3521, and (with a weaker constraint) NGC 2976. We find cusps in NGC 2403 and NGC 3621, and intermediate inner log slopes in DDO 154, NGC 3198 and NGC 7793. Figure 4.3 shows the rotation curve decomposition of the most populated bin of parameter space in the MCMC chains.

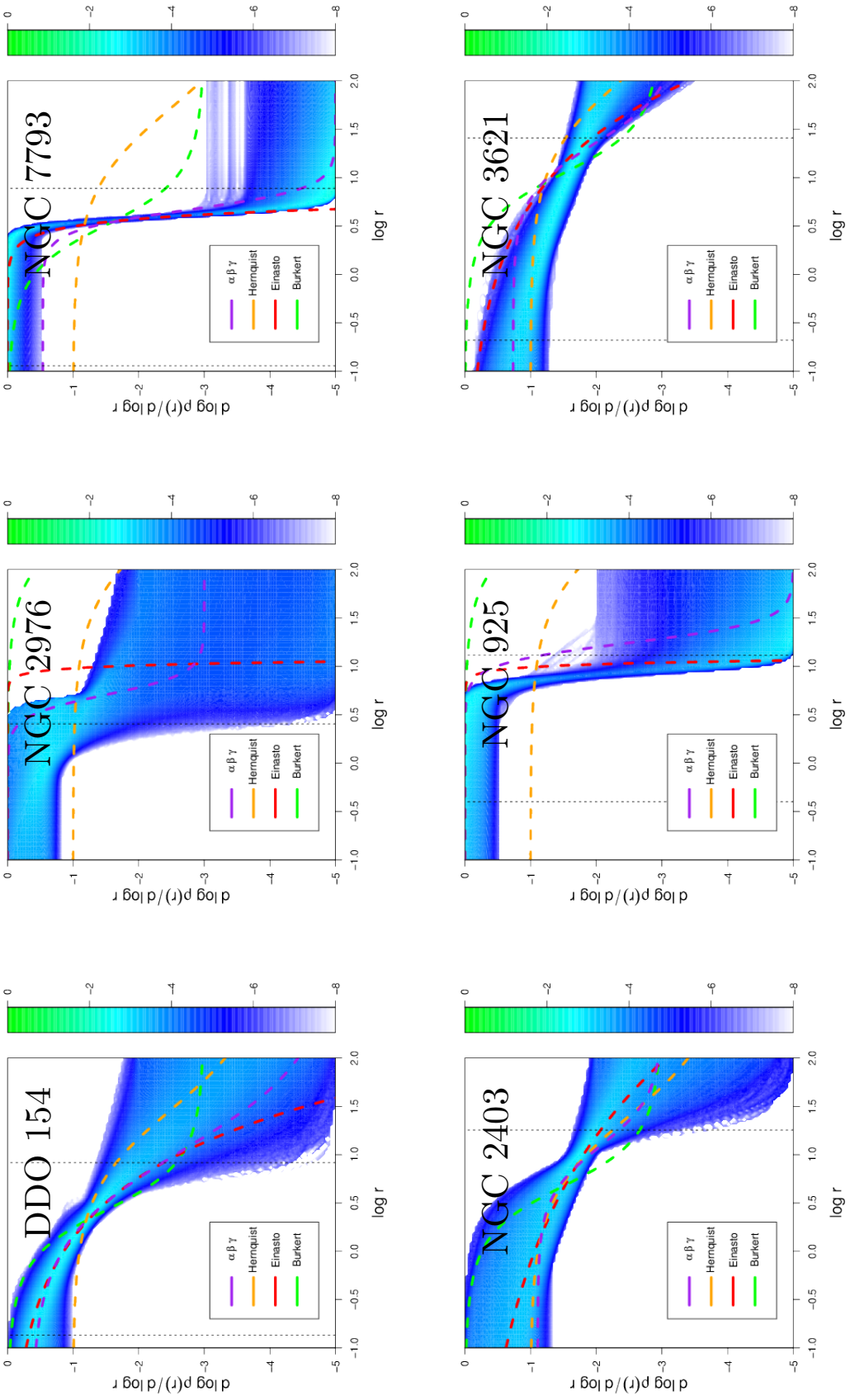
NGC 7793
NGC 3621
NGC 2976
NGC 925
DDO 154
NGC 2403
α β γ
Hernquist
Einasto
Burkert
log r
d log ρ(r)/d log r

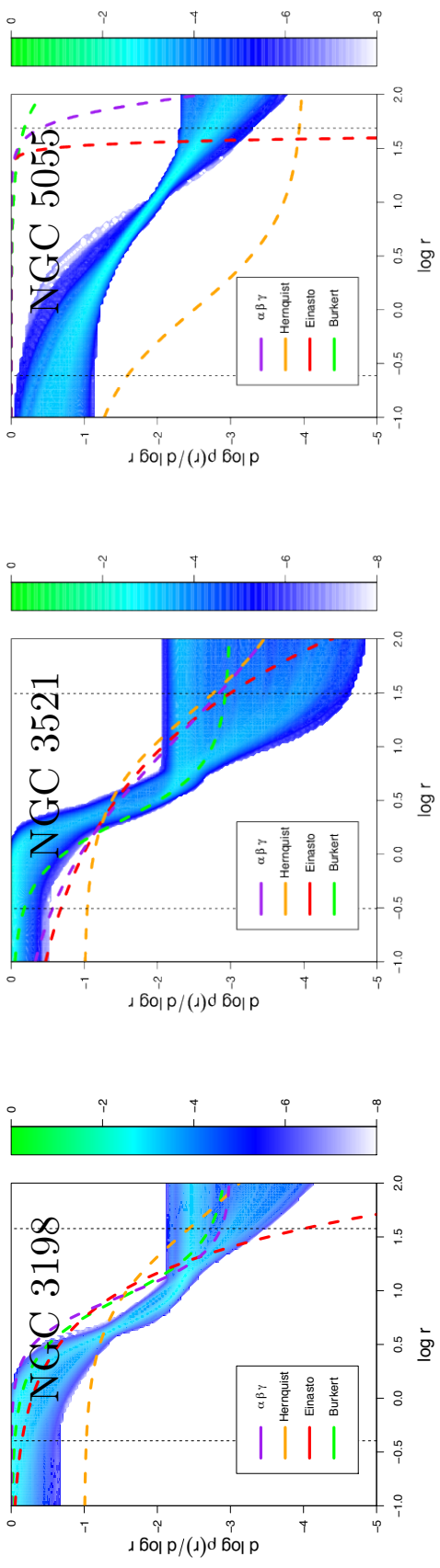

Figure 4.2: Overlay of all models produced by the MCMC algorithm for each galaxy, in log$r$ – dlogρ/dlog$r$ space. The log density scale on the right of each plot is relative to total number of models. Vertical dotted lines indicate the radial range of the observed rotation curve data, with the inner limits for NGC 2976 and NGC 2403 being below $logr = -1.0$. Dashed curves are least squares minimisation fits of common density profiles (Green: Burkert profile. Orange: Hernquist profile. Purple: $\alpha - \beta - \gamma$ profile. Red: Einasto profile.) NGC 5055 is included for comparison although it is one of the galaxies rejected from our analysis. See text for a detailed discussion.

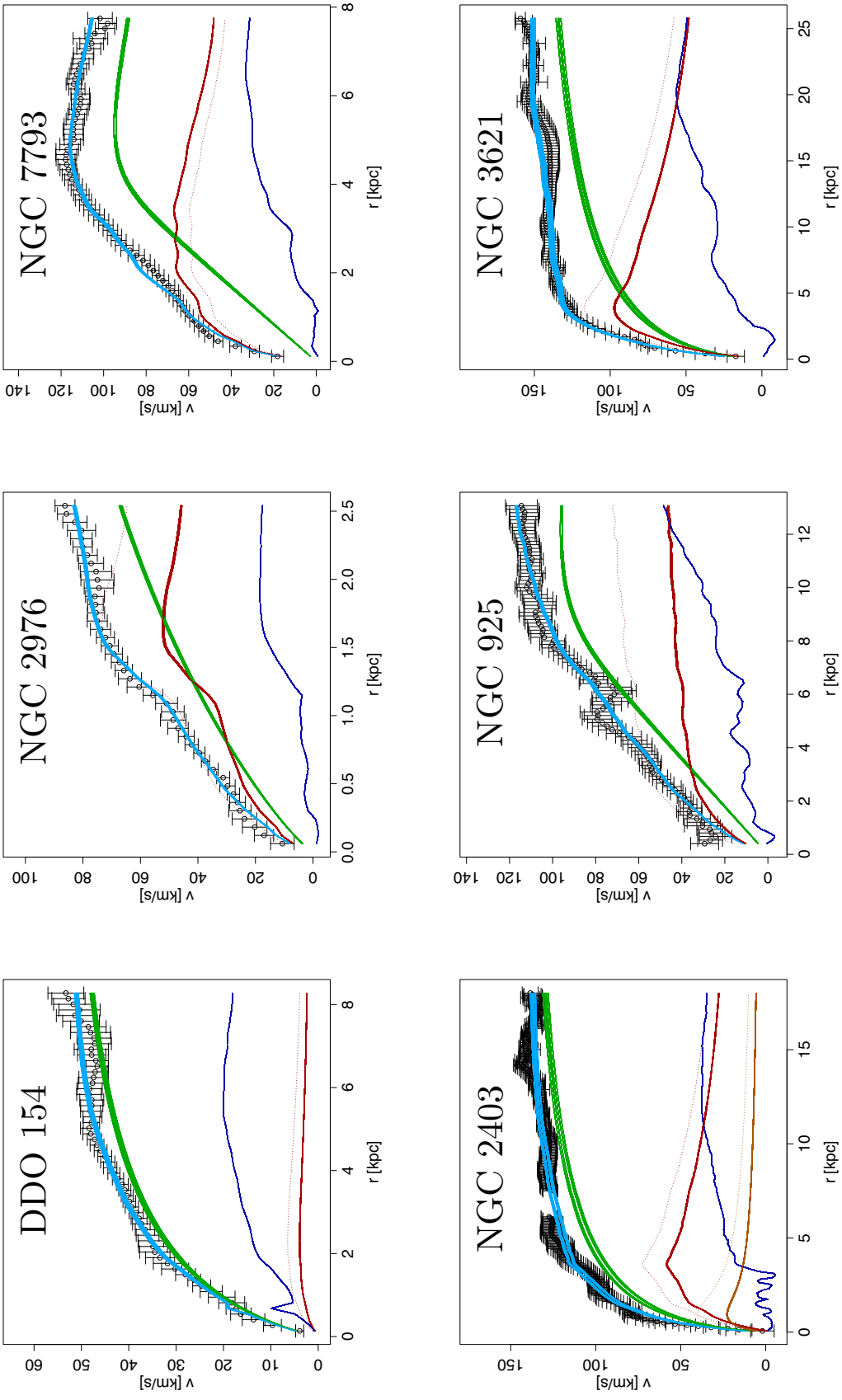
NGC 7793
NGC 3621
NGC 2976
NGC 925
DDO 154
NGC 2403
v [km/s]
r [kpc]

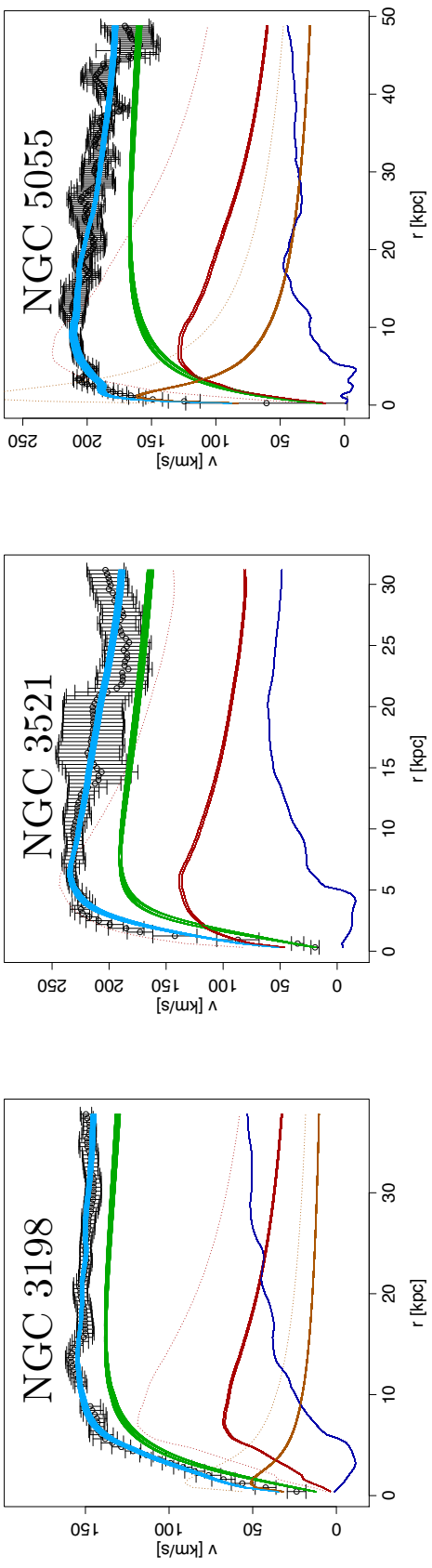

Figure 4.3: Rotation curve decompositions showing the dark matter haloes corresponding to the most populated bin in the parameter space distribution. Black points represent the observed HI circular velocities, the dark blue curves are the inferred contribution of neutral atomic gas, the solid red curve is the stellar contribution in the best fitting bin, the dotted red curve is the input value for the stellar contribution (which assumes a diet Salpeter IMF), the green curve is the dark matter contribution and the light blue curve is the resulting combined curve. The green and light blue curves have a thickness as they are the superposition of multiple models in the most populated bin. Two stellar curves are present in NGC 2403, NGC 3198 and NGC 5055 as these galaxies were modelled with two stellar components in de Blok et al. (2008).

4.4.1 DDO 154

This is the least massive galaxy in the set we are examining, having a mass of $3 \times 10^9\, M_\odot$ according to Carignan and Purton (1998), and thus has lower rotation speeds overall than the other galaxies. Given that its low surface brightness makes the dark matter halo parameters easier to constrain, we used it as a test case for the method that we discussed in Chapter 3. The chapter contains some analysis of the result.

The HI velocity field of this galaxy is asymmetric in the outer parts (illustrated in Figure 81 in de Blok et al., 2008), but as we are concerned mainly with the potential at small r, this is not an obstacle to the constraint of $\gamma_{\rm in}$. The rotation curve is well constrained and, based on the errors which are calculated from the difference between the two sides of the rotation curve, quite symmetrical in the region of interest. We find a well constrained $\gamma_{\rm in}$ value, with an intermediate log slope at the innermost datapoint ($r = 135.7\,$pc.) Unsurprisingly this value is unaffected by the chosen value of f_Υ due to the low contribution of the stellar disk to the rotation curve.

In Chapter 3, the gas curve for this galaxy was represented by the rotation curve of a smooth exponential disk. We have opted to no longer do this, first because the gas contribution does not significantly alter the result anyway, and secondly because any smoothing that is necessary should be handled by the MCMC process. We now directly use the gas distribution data from de Blok et al. (2008). This reasoning is supported by the fact that we indeed get the same value for $\gamma_{\rm in}$, within error, as that reported in Chapter 3.

4.4.2 NGC 2403

The data for this galaxy have large error bars relative to their scatter (Figure 70, de Blok et al., 2008). However we demonstrated in Chapter 3, using test data, that our method is robust to this issue.

The constraint on the inner log slope is shown in Figures 4.4 and 4.5. With a freely varying mass-to-light ratio, the distribution of $\gamma_{\rm in}$ is clearly not Gaussian, showing a plateau towards more cored values. This part of the parameter space is noisy, and the level of the noise is not consistent across parameter space. Whilst formally converged ($\sigma(\hat{x})/\hat{\sigma}(x) = 0.73$), the presence of the plateau reveals something interesting about the parameter space, as well as pointing to the need for judicious use of convergence statistics. The peak at the high end of the $\gamma_{\rm in}$ distribution appears in all chains. Figure 4.6 shows that the inner log slope has a single smooth peak when f_Υ is fixed by assuming either a diet Salpeter or Kroupa IMF, in both cases consistent between chains, indicating that the

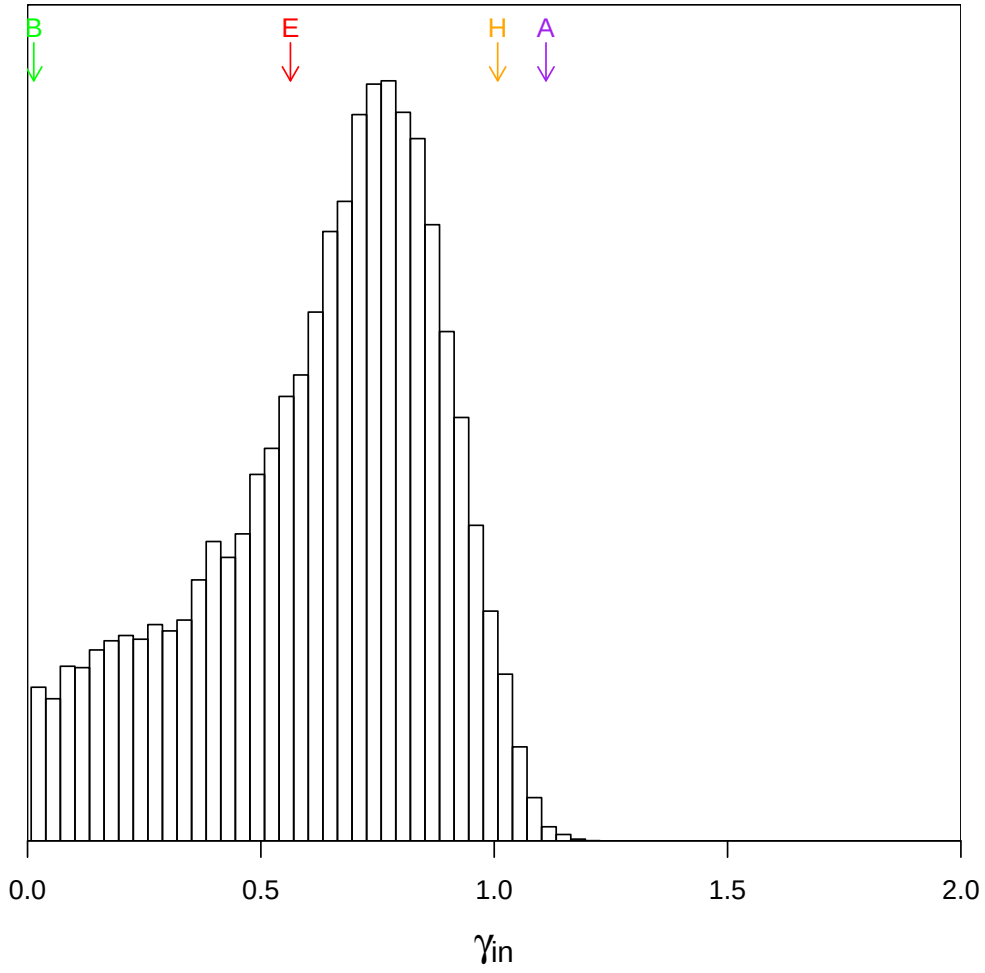

Figure 4.4: Histogram of $\gamma_{\rm in}$ values produced by the MCMC analysis of NGC 2403 with a freely varying mass-to-light ratio multiplier (f_Υ). Arrows indicate the logarithmic slope at this radius of single profile fits (Green: Burkert profile. Orange: Hernquist profile. Purple: $\alpha-\beta-\gamma$ profile. Red: Einasto profile.)

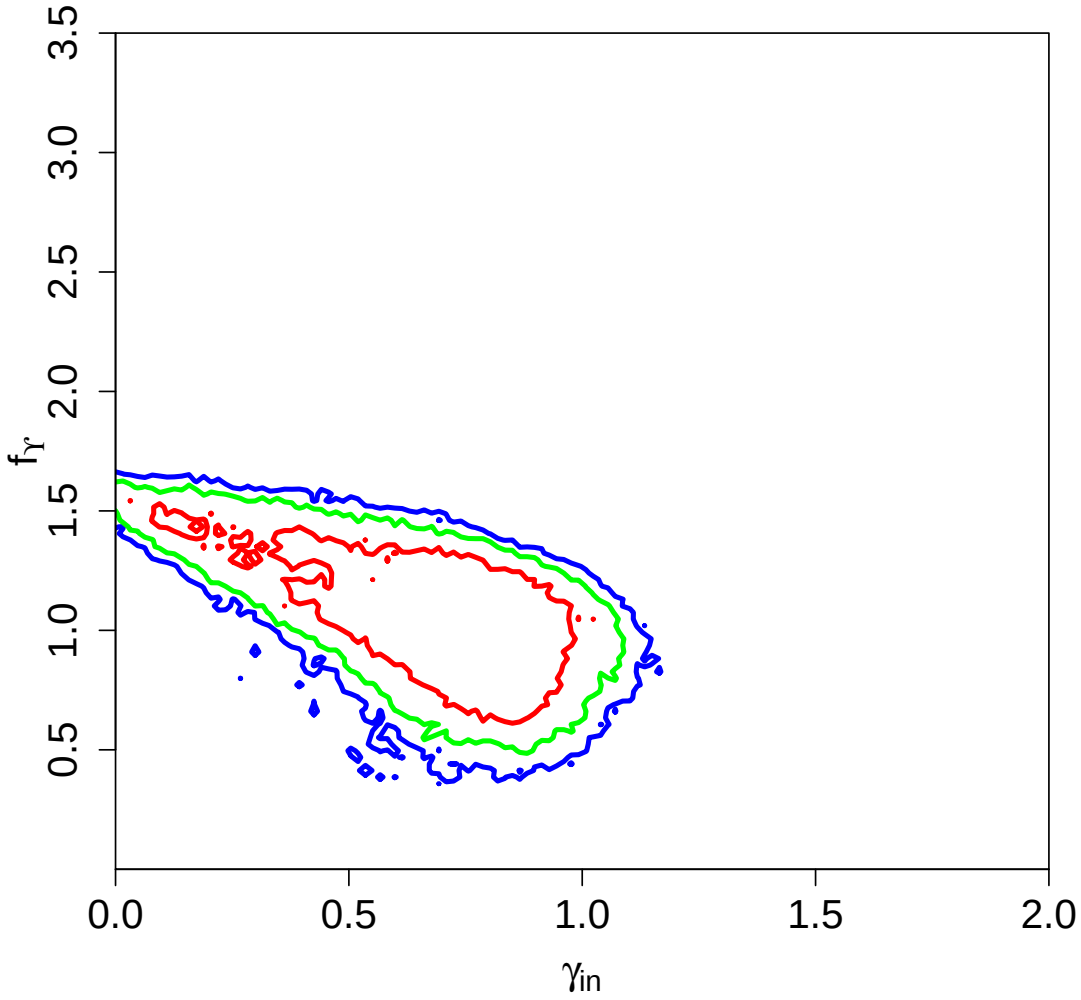

Figure 4.5: Contour plot of f_Υ versus γ_{in} demonstrating the nature of the degeneracy between the two parameters. The red contour encloses 0.68 of all models in the MCMC chains, the green contour encloses 0.95 and the blue contour encloses 0.99.

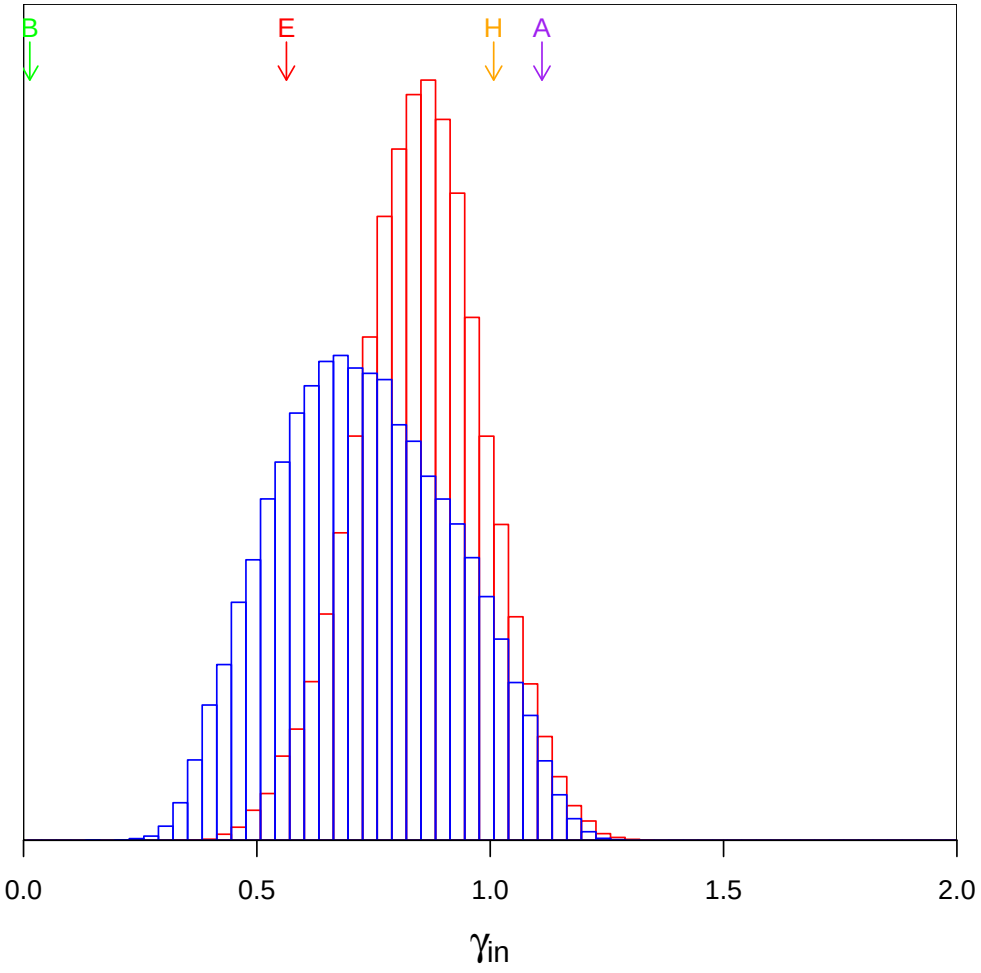

Figure 4.6: Histograms of $\gamma_{\rm in}$ values produced by MCMC analyses of NGC 2403 with fixed stellar IMF. **Blue** with a fixed f_Υ derived from a diet salpeter IMF. **Red** with f_Υ derived from a Kroupa IMF (Kroupa, 2001). Arrows are as in Figure 4.4.

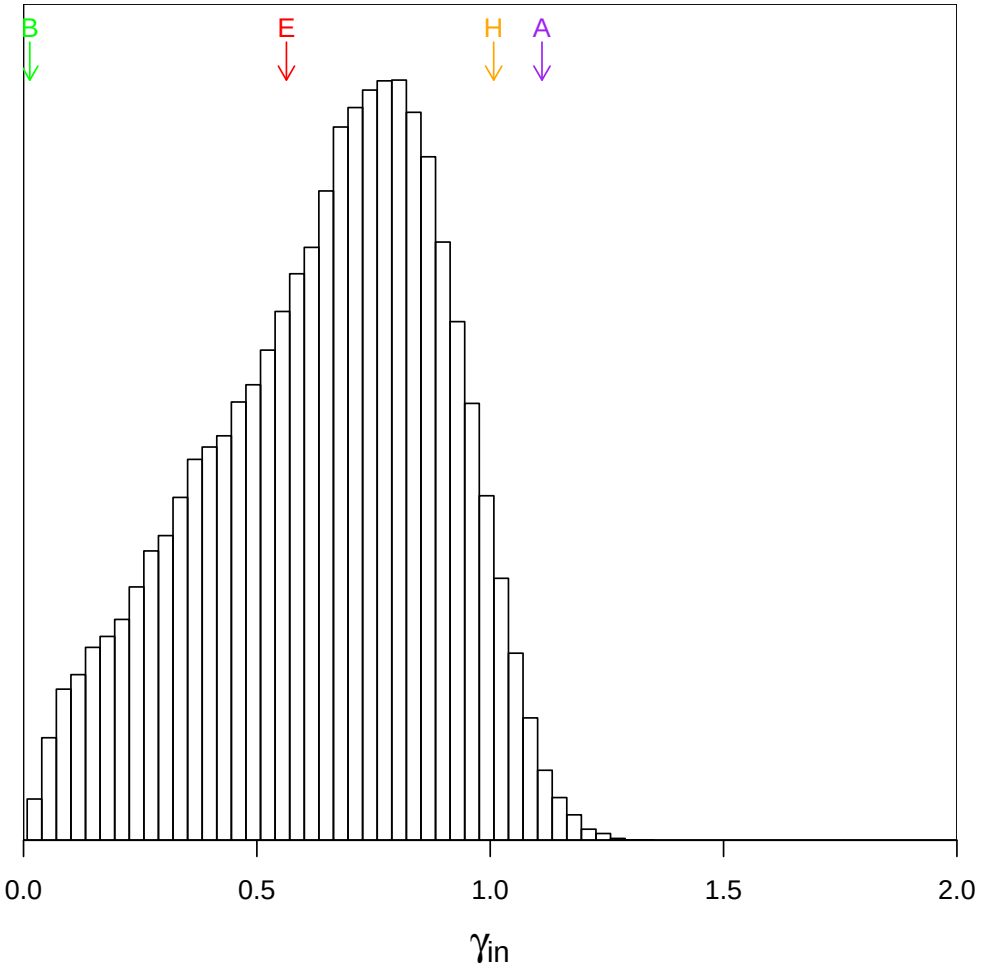

Figure 4.7: Histogram of $\gamma_{\rm in}$ values produced by the MCMC analysis of NGC 2403 with a freely varying mass-to-light ratio multiplier (f_Υ), and a temperature $T = 2$. Arrows are as in Figure 4.4. See text for detailed discussion.

additional tail in the free f_Υ case is due to a degeneracy (shown in Figure 4.4) between the dark matter halo parameters and the mass-to-light ratio. This is to be expected for a higher surface brightness galaxy - at higher values of f_Υ, the stellar contribution is able to model the rotation curve alone, and the MCMC then finds fits with low dark matter density where the exact shape of the halo is less important.

The small, cored plateau represents models which attempt to fit maximal disk models to the data, and such models require very high values of f_Υ. Furthermore, the fact that these models cannot form a second peak in the distribution indicates they do not reproduce the data as well as those in the peak. We now explore this in more detail. The maximal disk part of parameter space occupies a large volume, due to the fact that the shape parameters of the dark matter halo are no longer significant, and can be freely varied without compromising the quality of the fit. This can bias the MCMC chains towards that volume, so if models there were of a higher fitness than those in the peak, the plateau region would be strongly favoured in all chains. If we disregard these models on this basis, we can conclude that NGC 2403 has a moderate cusp. As shown in Figure 4.6 a cusp is also indicated when using a fixed f_Υ derived from either Kroupa or diet Salpeter IMF.

We took a subsample of 1423 models from the MCMC chain, that were randomly selected after burn-in with a probability of 10^{-4} for each model, and then divided this into 2 subsamples either side of $\gamma_{\rm in} = 0.5$. We found no difference in reduced χ^2 for either side, to 2 significant figures. Both produced a 90% confidence interval of $\chi^2_{\rm red} = 0.30, 0.31$. Given the very definite preference of the MCMC chain, and the fact that values of $\chi^2_{\rm red} < 1$ are of little use for comparison, we conclude that the algorithm is still able to produce a meaningful result. We also note that the number of degrees of freedom is treated as a constant when using $\chi^2_{\rm red}$, but the nature of the problem means that in some parts of the parameter space not all of the parameters contribute significantly to the fit - for example, if $v_{\rm max}$ is low and f_Υ is high then the shaping parameters of the dark matter halo can be freely varied whilst maintaining a nearly constant proposed rotation curve. This inherent weakness in $\chi^2_{\rm red}$ does not apply to our MCMC method, as we use the ratio between a proposed model and the current one to determine the next step in the chain, and thus $\chi^2_{\rm red}$ is equivalent to χ^2 (which we use) as the degrees of freedom cancel.

In order to try and produce a better convergence for the tail, we reran the MCMC algorithm using a temperature $T = 2$ (and thus sampling $P^{1/2}$ rather than P.) The result was more consistent across independent chains, and produced a smoother distribution overall when the chains are summed, as shown in Figure 4.7. This produces the same constraint on $\gamma_{\rm in}$ within 1σ errors. The numeric values discussed in later sections are

derived from this version.

4.4.3 NGC 2976

This galaxy has a high surface brightness, so is not expected to produce as strong a constraint on the dark matter halo as some of the other galaxies have done. This is borne out by the $\gamma_{\rm in}$ distribution in Figure 4.8.

As shown in Figure 4.3, the rotation curve data for NGC 2976 show a sharp increase just outside 2 kpc, and it is possible to get a mathematically credible fit to the data without treating this as a feature at all. However, the shape of the stellar contribution to the rotation curve suggests that this is the region where dark matter should begin to dominate. Interior to this, the rotation curve follows the features of the stellar contribution well. Therefore, an adequate fit (from the perspective of χ^2 only) can be obtained using $f_\Upsilon \geq 1$ and ignoring the last few data points.

We find, however, that MCMC selects lower values of f_Υ that are able to fit the entire range of data using both dark and visible components, as shown in Figure 4.3. The free f_Υ run gives $r_1 = 1.94\pm^{1.76}_{0.4}$ kpc (90% confidence), which has an upper bound outside the data range. The lower bound roughly corresponds to the point where the contribution to the circular velocity from the dark matter halo first exceeds that of the stellar disk.

4.4.4 NGC 3198

This galaxy has a well-studied rotation curve (e.g. Begeman, 1989). Error bars show the disk is roughly axisymmetric, and there is good kinematic data from the HI map at all radii (Figure 75 in de Blok et al., 2008).

One notable feature of the rotation curve for NGC3198 is that the circular velocity contribution of atomic gas is less than zero in the inner part. This represents a void where the net gravitational effect of the gas disk is outwards, and has to be subtracted in quadrature rather than added. This occurs in the same region as the peak of the inner stellar component in the rotation curve, so if the lack of atomic gas could indicate a large amount of molecular gas in the disk (observations of which are not part of any of the original data sources used here) then the contribution of such gas can be modelled by the freedom in f_Υ. Under this assumption, f_Υ no longer functions purely as a factor of stellar mass-to-light ratio.

NGC 3198 is another high surface brightness galaxy, but this itself does not preclude a constraint. The initial run produced differing constraints for each chain, as did a run using

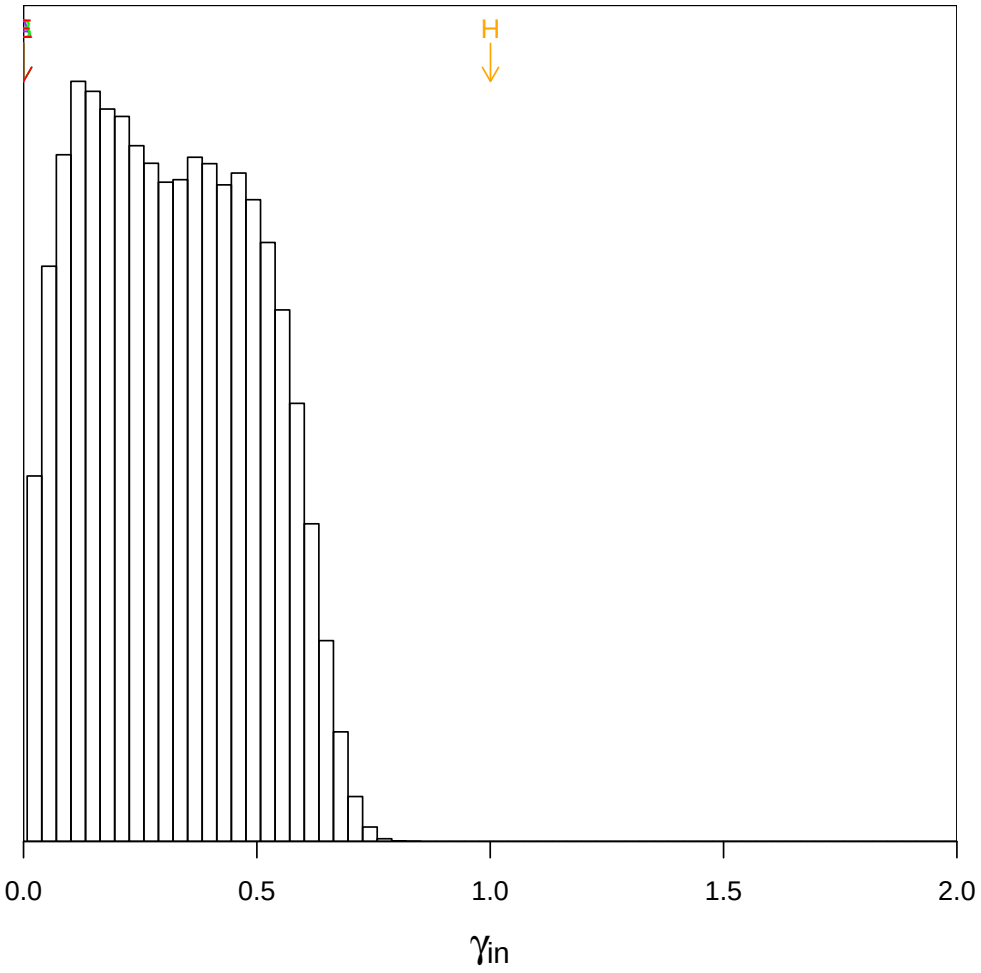

Figure 4.8: Histogram of the $\gamma_{\rm in}$ value of all the models produced by the NGC 2976 MCMC run. Arrows are as in Figure 4.4.

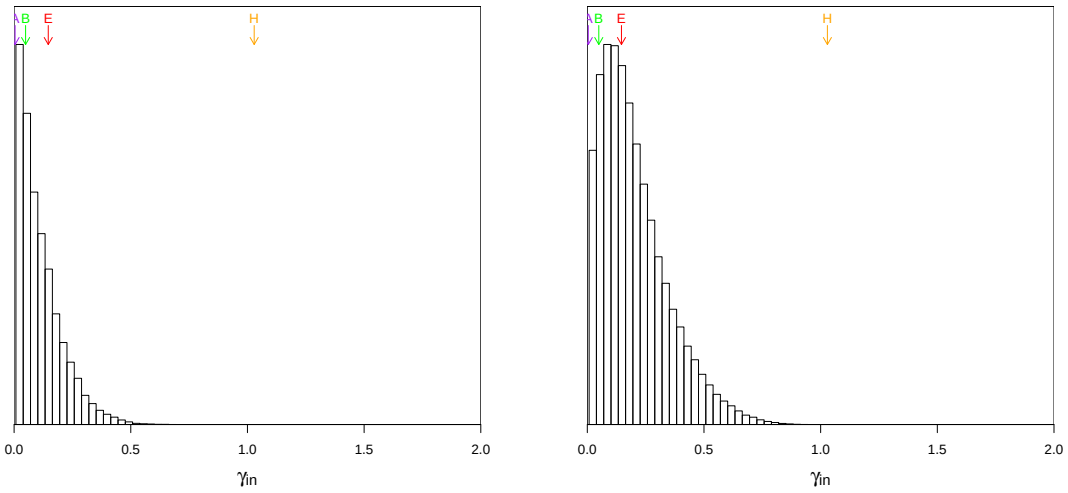

Figure 4.9: Histogram of the $\gamma_{\rm in}$ value of all the models produced by the NGC 3198 MCMC run using fixed f_Υ. **Left** Results derived from a Kroupa IMF and **right** results derived from a diet Salpeter IMF. Arrows are as in Figure 4.4.

the higher temperature setting $T = 2$, but we were able to produce a consistent constraint by also excluding those data points where the neutral gas contribution is negative - which also includes the supermaximal inner stellar component. This constraint had a γ peak greater than 1, and thus no meaningful value for r_1.

Constraints at $T = 1$, using the entire data range, were possible using a fixed f_Υ, with the results shown in Figure 4.9. As these both produce constraints on $\gamma_{\rm in}$ that agree to within 1σ, we classify this galaxy as having a core, but this assumes that the stellar mass-to-light modelling is robust. The models produced by the free mass-to-light multiplier run are almost entirely ($> 88\%$) below $f_\Upsilon = 0.341$, indicating that the MCMC prioritises keeping the stellar contribution low in order to keep the inner part of it lower than the observed circular velocity of the galaxy. Better stellar mass modelling is required for a more definitive constraint.

4.4.5 NGC 3521

We used a temperature setting of $T = 2$ for this galaxy as the lower temperature run produced a constraint value of $\sigma(\hat{x})/\hat{\sigma}(x) = 2.91$ for β. Due to the nature of the data, and the area of our interest being the central region of the galaxy, having a poorly constrained outer log slope is not in itself grounds for a rejecting a result, but in this case both α and

r_s also had $\sigma(\hat{x})/\hat{\sigma}(x) > 1.0$ when $T = 1$, so we only present the higher temperature run here.

A preference for a core is obtained, as shown in Figure 4.10, being flat to within reasonable error at the innermost data point. This remains unchanged regardless which of our initial assumptions about stellar mass-to-light is used, although in the cases of fixed IMF the dark matter contribution is negligible at the smallest radial bin ($r = 312\,\mathrm{pc}$.) A strong constraint is however produced on r_1 as shown in Figure 4.11. There is no dependency of r_1 on f_Υ, which is also strongly constrained, in the free mass-to-light case. However, the exact value that r_1 is constrained to changes if we use a fixed f_Υ based on a Kroupa or diet Salpeter IMF. This is discussed further in Section 4.5.

The rotation curve decomposition for NGC 3521, shown in Figure 4.3, indicates a gap in the neutral atomic gas disk and also a stellar contribution that is larger than the total rotation curve for the input value of f_Υ, corresponding to a diet Salpeter IMF. Only using the data in the range where the neutral gas contribution to the rotation curve is positive would not permit modelling of the density profile shape as all the contributions and the observed rotation curve in the remaining region is almost flat. The rising part of the dark matter halo contribution to the rotation curve is required in order to differentiate between a central core and a cusp. An MCMC run excluding the data points where the velocity of the gas contribution is negative produced a peak $\gamma_{\mathrm{in}} \geq 2$, but as stated above this cannot be considered a meaningful value.

4.4.6 NGC 3621

This galaxy has a stellar disk and a rotation curve of similar maximum velocity and shape as that of NGC 3198, and like that galaxy has a high surface brightness. However, the galaxy exhibits significantly more of a cusp when analysed.

In Figure 4.12 we see there is a slight degeneracy between γ_{in} and f_Υ. Although γ_{in} is well constrained when the mass-to-light ratio parameter varies freely (the red contour on the map showing the 1σ level, with an overall range $\gamma_{\mathrm{in}} = 0.91\pm^{0.13}_{0.33}$), or when the ratio is fixed to a particular value, the position of the distribution varies from moderately cored ($\gamma_{\mathrm{in}} = 0.33\pm^{0.31}_{0.16}$ when using a diet Salpeter IMF) to almost entirely cusped ($\gamma_{\mathrm{in}} = 0.89\pm^{0.16}_{0.2}$ when using a Kroupa IMF.)

The cusped interpretation is favoured when the MCMC can control f_Υ, however this distribution is a product of our prior assumptions. The correct value of f_Υ also needs to account for any molecular gas not included in the model, so it is difficult to give a precise value for it. We cannot at this point state which of the γ_{in} values is correct from just this

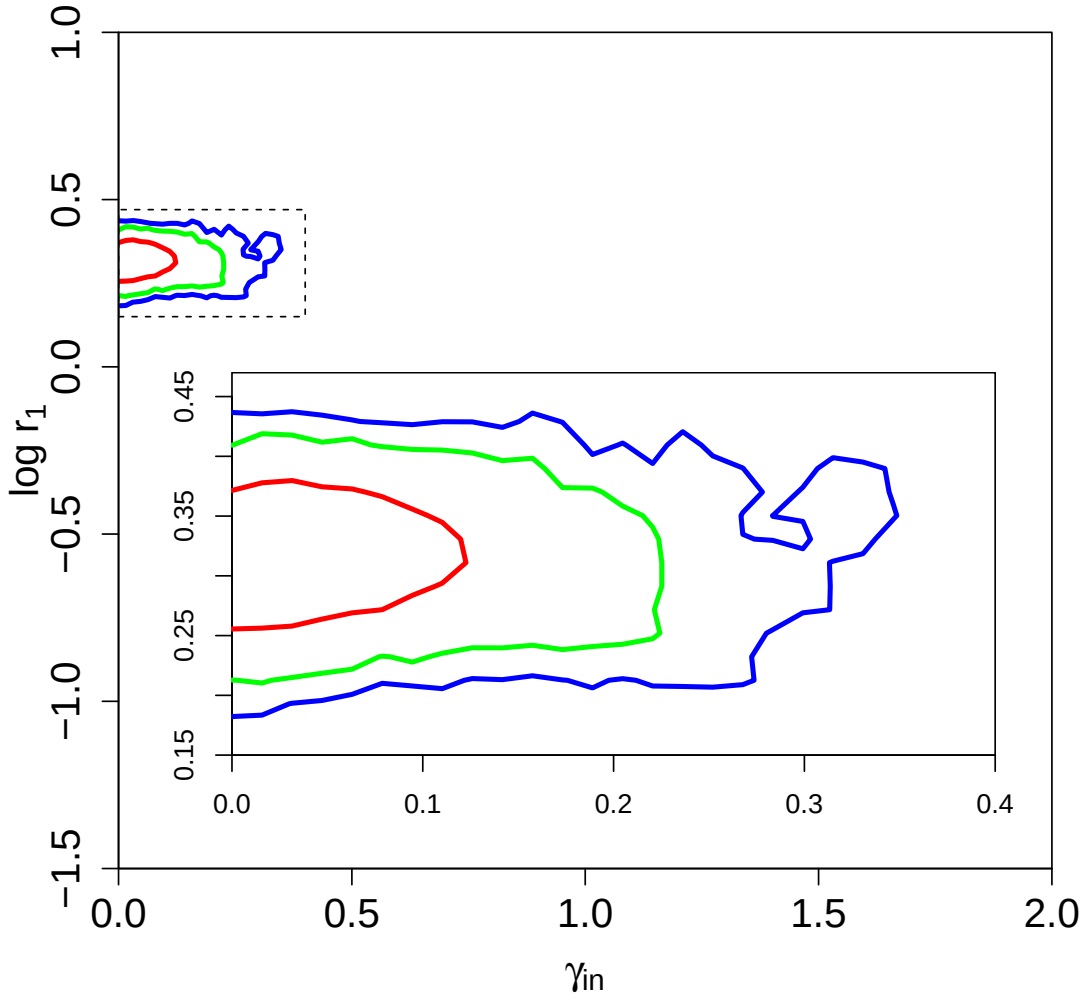

Figure 4.10: Contour plot of log r_1 versus $\gamma_{\rm in}$ for NGC 3521. Inset shows a zoom in on the contoured region.

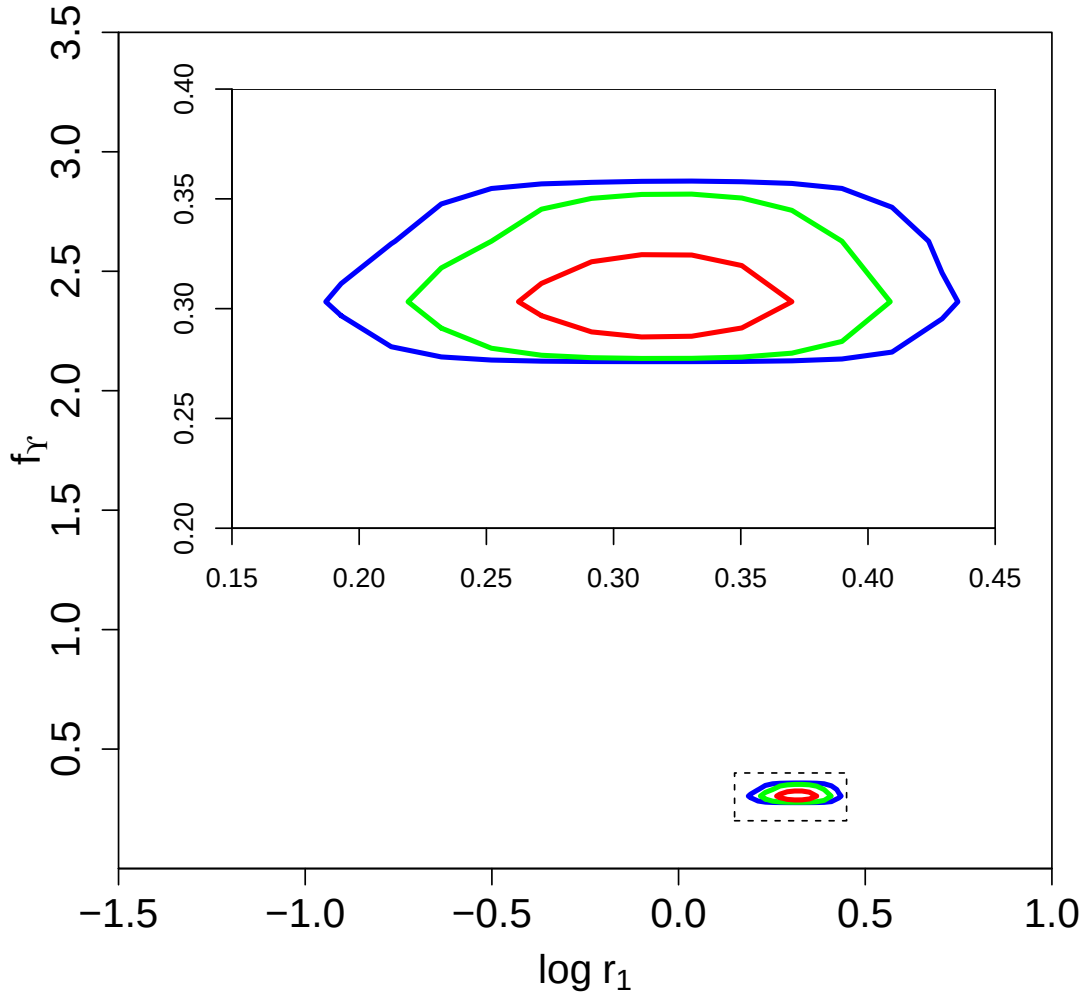

Figure 4.11: Contour plot of the mass-to-light multiplier f_Υ versus r_1 of all the models produced by the NGC 3521 MCMC run.

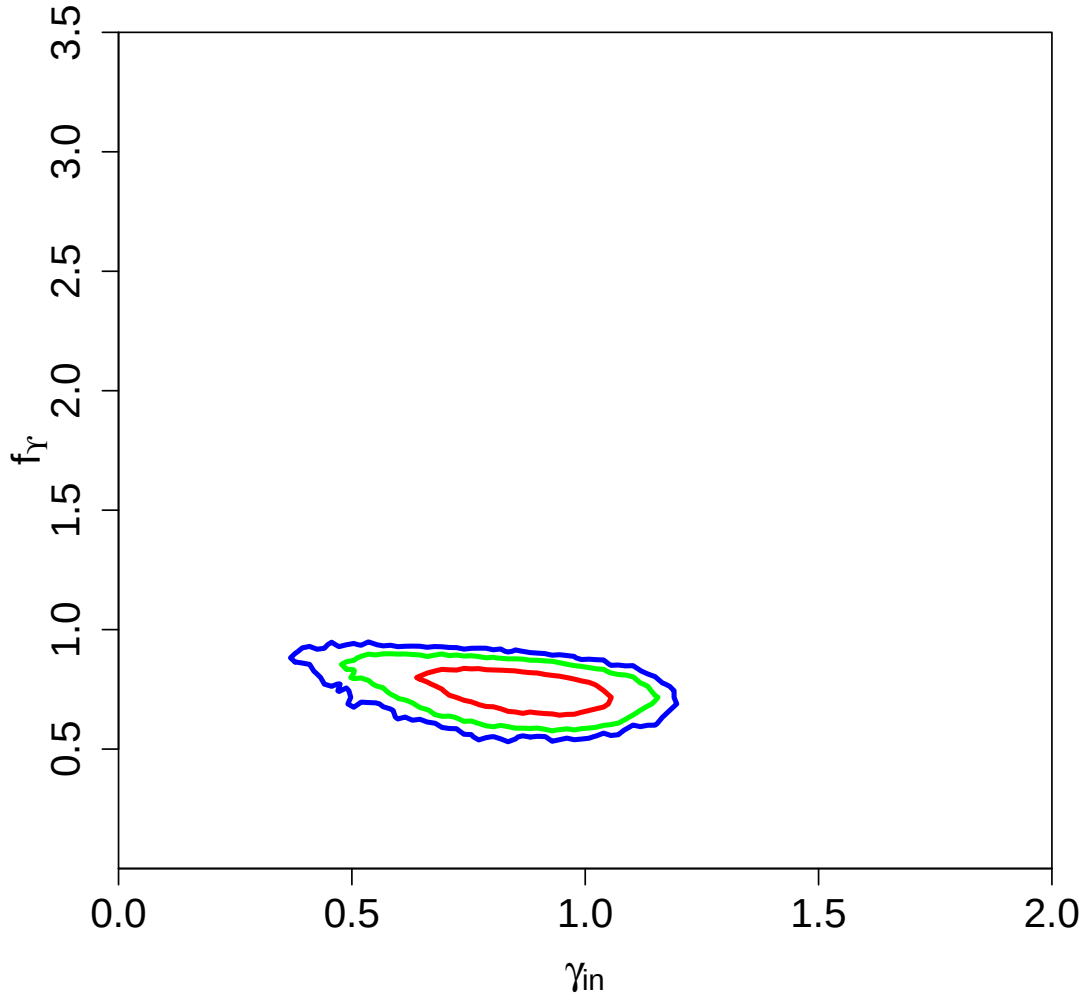

Figure 4.12: Contour plot of the mass-to-light multiplier f_Υ versus $\gamma_{\rm in}$ of all the models produced by the NGC 3621 MCMC run.

analysis.

4.4.7 NGC 7793

NGC 7793 is another high surface brightness galaxy, but at first sight we appear to be able to constrain it reasonably well. We generated a test case for high surface brightness galaxies based on NGC 7793 in Chapter 3.

According to Figure 4.13, both the inner log slope and the mass-to-light multiplier f_Υ are well constrained and show a clearly cored profile. However, the constraint indicates a mass-to-light ratio which is substantially higher than that implied by a diet Salpeter IMF, possibly due to the involvement of molecular gas. Different values, with equally tight constraints, are found when a fixed mass-to-light ratio is chosen, as shown in Figure 4.14

This demonstrates a reason why the likelihood distributions in Figure 4.14 must be used with caution. Each distribution, taken in isolation, returns a very strong constraint - but it is only apparent through a broader analysis of the parameter space of the result that this constraint is entirely dependent on the initial assumption about the stellar mass-to-light ratio. This emphasises the value of the MCMC approach.

4.4.8 NGC 925

This galaxy is described in de Blok et al. (2008) as having a weak bar, which is found in Elmegreen et al. (1998) to have a length of 5.4 kpc. The impact of this bar on the kinematics, and thus the rotation curve, of the galaxy must be taken into account in our analysis. We do this through two separate runs of this galaxy, one with the entire data range from de Blok et al. (2008), and one excluding the data points inside $r = 5.6$ kpc in order to minimise the impact of bar kinematics on our result.

In a previous analysis (Chemin et al., 2011), the calculated rotation curve of this galaxy was found to be well fit by an Einasto profile dark matter halo that featured a sharp change in the rotation curve, caused by the single Einasto shaping parameter (n in Chemin et al. 2011 but also referred to as α in Navarro et al. 2004) being very low. Such a halo was avoided in our analysis through the availability of more shaping parameters.

The fits to this halo strongly point to the existence of a core, with a radius that encompasses most of the data range. Forcing a fixed mass-to-light multiplier does not change the result, it merely reduces the size of the tail of the distributions. Assuming a diet Salpeter IMF results in a supermaximal disk i.e. the calculated stellar contribution being higher than the observed rotation velocity, for a number of points towards the inner part of the

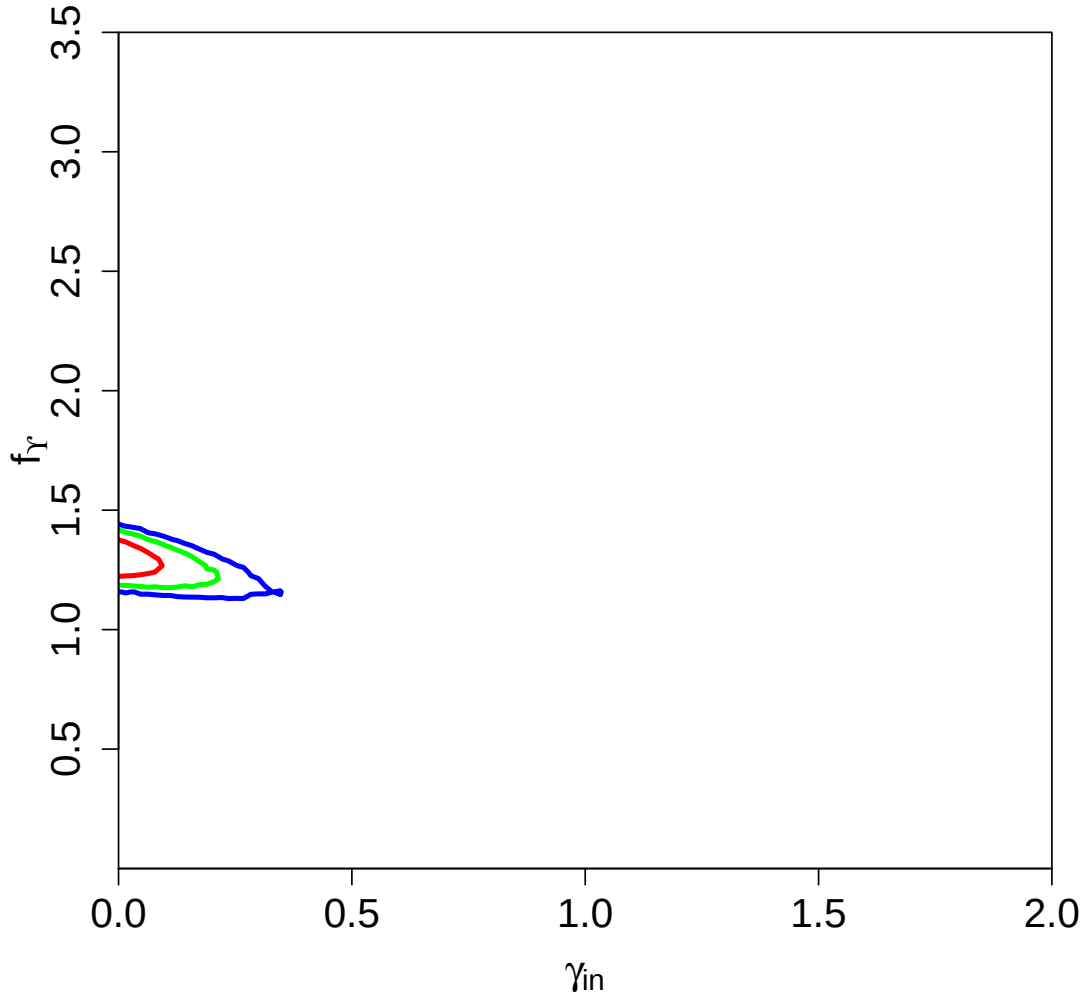

Figure 4.13: Contour plot of the γ value versus mass-to-light multiplier f_Υ of all the models produced by the NGC 7793 MCMC run.

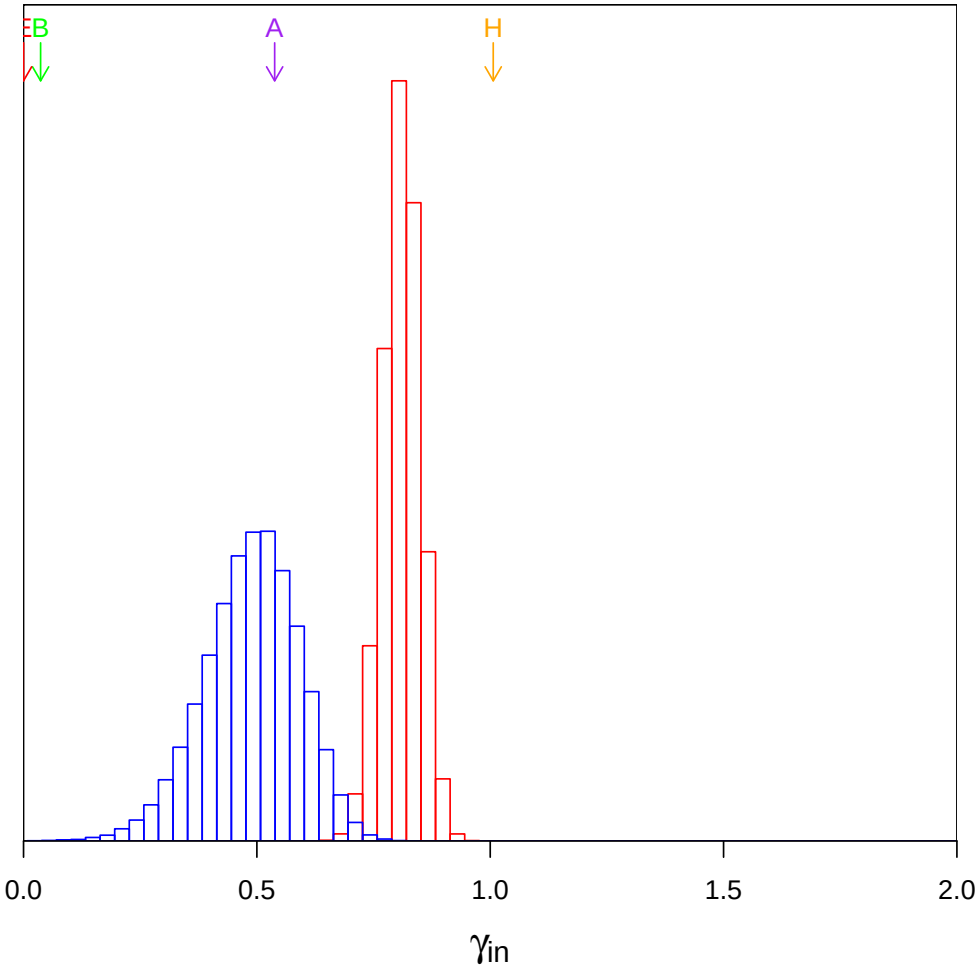

Figure 4.14: Histograms of $\gamma_{\rm in}$ values for NGC 7793 runs **blue** using a diet Salpeter IMF derived mass-to-light ratio, and **red** using a Kroupa IMF (Kroupa, 2001) derived mass-to-light ratio. Histograms are scaled to have equal integrated area. For a Kroupa IMF, $f_\Upsilon = 0.72$ and for a diet Salpeter IMF $f_\Upsilon = 1$.

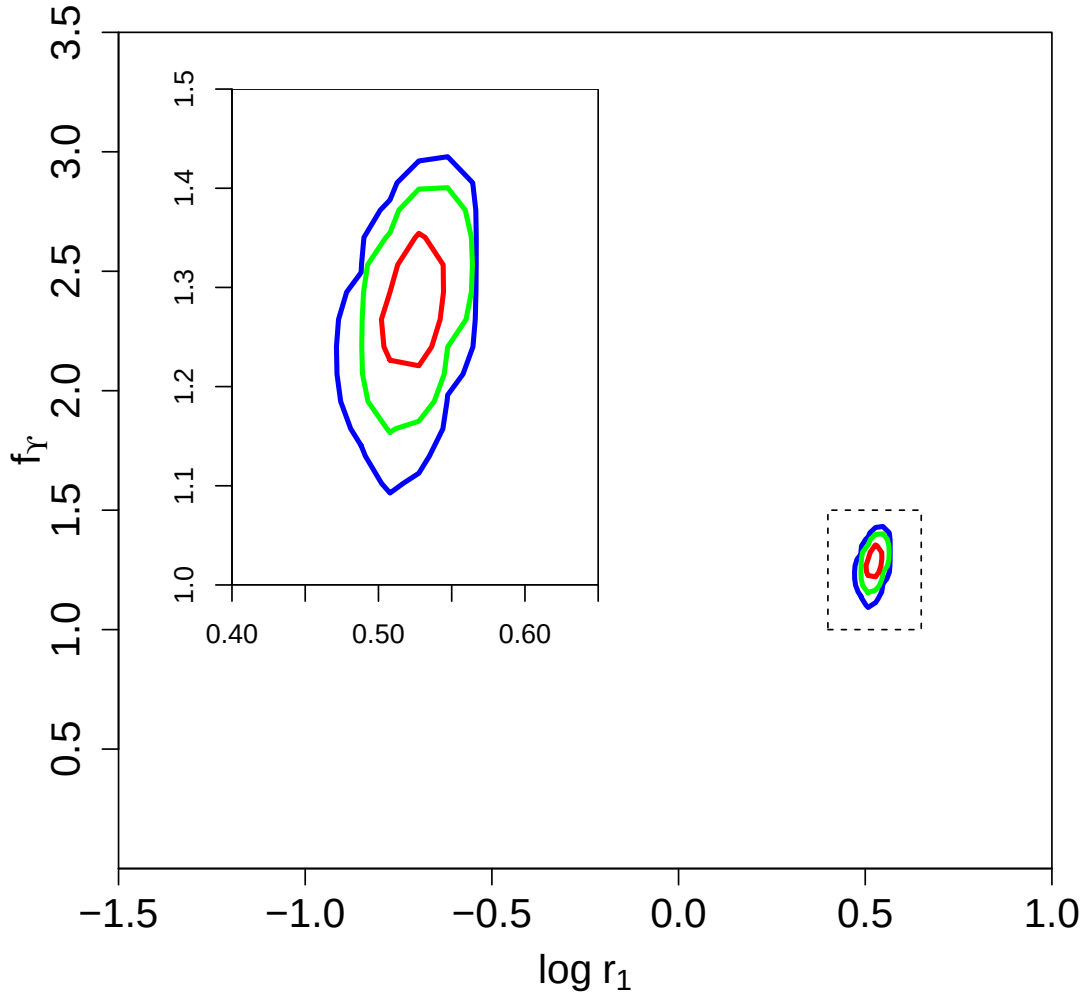

Figure 4.15: Contour plot of f_Υ versus r_1 for NGC 7793. Inset shows a zoom in on the contoured region.

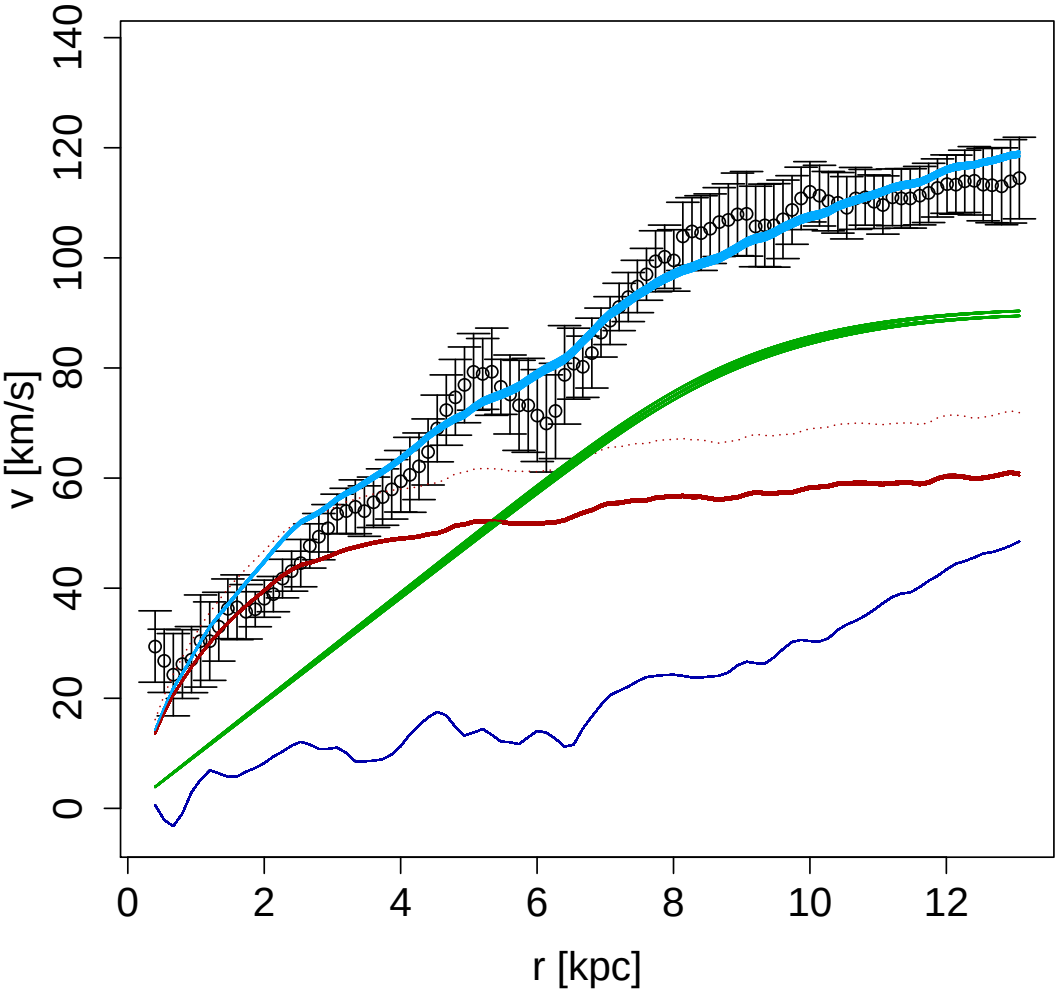

Figure 4.16: Rotation curve produced by the MCMC analysis of the data for NGC 925 assuming a fixed Kroupa IMF. The black data points are HI rotation curve data, the red solid line is the modelled stellar contribution derived from a Kroupa IMF to the rotation curve, the dark blue line is the modelled gas contribution, the green line is the dark matter halo model at the peak of the distribution, and the light blue line is the expected rotation curve produced by all these components. For comparison the dotted line shows the stellar component assuming a diet Salpeter IMF, which is not used in this calculation.

rotation curve, so we conclude that the Kroupa IMF derived stellar component represents a more realistic fixed Υ.

As shown in Figure 4.16, the contribution of the stellar component is high at small r, but the surface brightness becomes much lower further out in the disk. This could mean that the cored profile (which has the steepest rotation curve) is simply the one which allows the dark matter contribution to most quickly transition from almost irrelevant, to being the dominant contribution, as radius increases. There is also a feature at around $r = 5\,\mathrm{kpc}$ that is not modelled well by either the baryons or the proposed dark matter halo, and may be related to the bar.

The above does not prevent our result being robust. The cored portion of the proposed dark matter halo extends from where the stellar contribution stops matching the shape of the observed rotation curve, through to where the dark matter contribution is dominant. So, whilst the innermost data points may not able to constrain a core, if there were not a flat density profile at these points, the overall profile would be surprising as it would have uniform density at intermediate radii, and a rising density again interior to this.

Due to the influence of the bar, and the fact that the rotation curve indicates a larger stellar contribution than that of dark matter at small r, we do not consider the log slope here itself to be evidence of a cored density profile. However, we note that analysis of this galaxy gives a value of $r_1 = 6.84\pm^{0.41}_{0.53}\,\mathrm{kpc}$ (90% confidence interval) which places the scale radius beyond the radial extent of most of the bar.

Our second run, excluding the inner part of the rotation curve, showed $r_1 = 6.77\pm^{0.65}_{0.75}\,\mathrm{kpc}$. In this case γ is less well constrained, as illustrated in Figure 4.17. This shows that for this galaxy the r_1 result is not compromised by any relation between γ and r_1. We conclude that r_1 is well constrained for this galaxy, but γ_{in} is much less well constrained. However, it should be noted that higher values of γ_{in}, associated with a cusped profile, are much more difficult to reconcile with the value we have for r_1 as it would imply a very slow change in log slope and thus provide a poor fit at larger r.

Our modelling can also explain the anomalous result obtained for this galaxy by Chemin et al. (2011). The rotation curve requires a flat log slope over a large radial range in order to produce a good fit, and the only way to do this with an Einasto halo is to lower the shape parameter n radically, which also leads to an unphysical, sharp drop in density near $r = 10\,\mathrm{kpc}$. A profile with more parameters (in this case, γ controlling the inner log slope and α controlling the rate of transition from the inner to the outer asymptotic log slopes) avoids this problem.

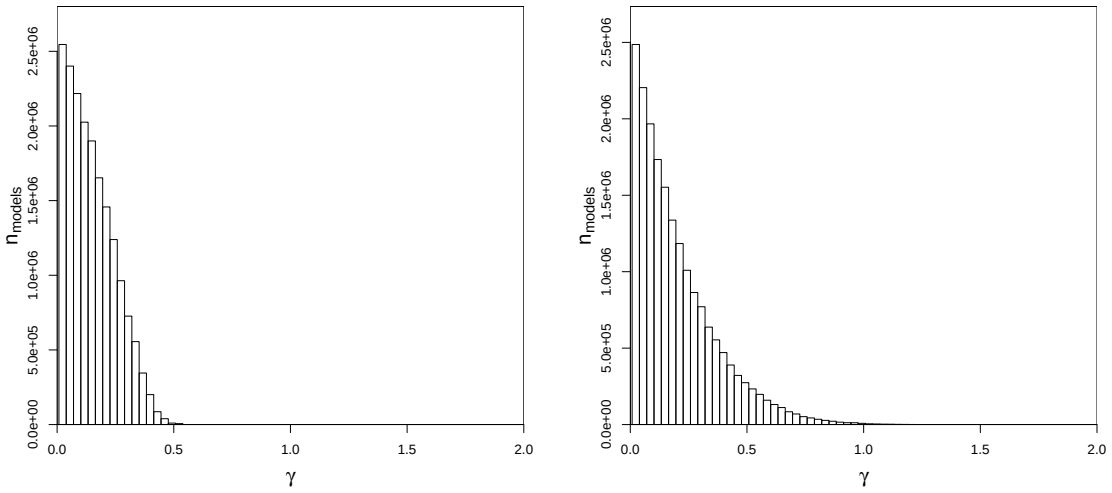

Figure 4.17: Distributions of γ for NGC 925 using all data points (**left**) and using only those data points outside $r_1 = 6.77\,\mathrm{kpc}$ (**right**). Note that we do not use γ_{in} for this comparison as the two cases have different inner radial bins. See text for a discussion.

4.4.9 Rejected Galaxies

We attempted to apply this technique to NGC 2841, NGC 2903, NGC 3031, NGC 4736, NGC 5055 and NGC 7331, but we found that there was either inadequate kinematic data for the MCMC algorithm to find a genuine fit to the data, or there was sufficient underlying asymmetry in the disk to prevent the MCMC method finding a useful constraint.

In the case of NGC 5055, the morphology of the galaxy and the shape of the rotation curve both appear promising as a target for this technique. However, when we applied an MCMC analysis, we were unable to constrain any parameters. In Figure 4.3 we showed the peak of the distribution. The halo corresponding to the most populated bin in the parameter space fits the data well, and relying purely on the value of $\chi^2_{\mathrm{red}} < 0.5$ without the context of the parameter space, the conclusion would be that the halo has been correctly modelled.

The extra information provided by the MCMC process allows us to show that this is not the case. In Figure 4.18 we see the distribution of γ_{in} values is not smooth over a length scale comparable to the initial step size of the MCMC chain, suggesting the 8 parallel chains have not converged to the same distribution, despite them visiting over $\sim 4 \times 10^7$ models between them. At temperature settings T=1, 2, and 3 we were unable to produce a set of chains with a convergence statistic $\sigma(\hat{x})/\hat{\sigma}(x) < 1$ for all parameters. Without a repeatable probability distribution, we cannot draw any conclusions.

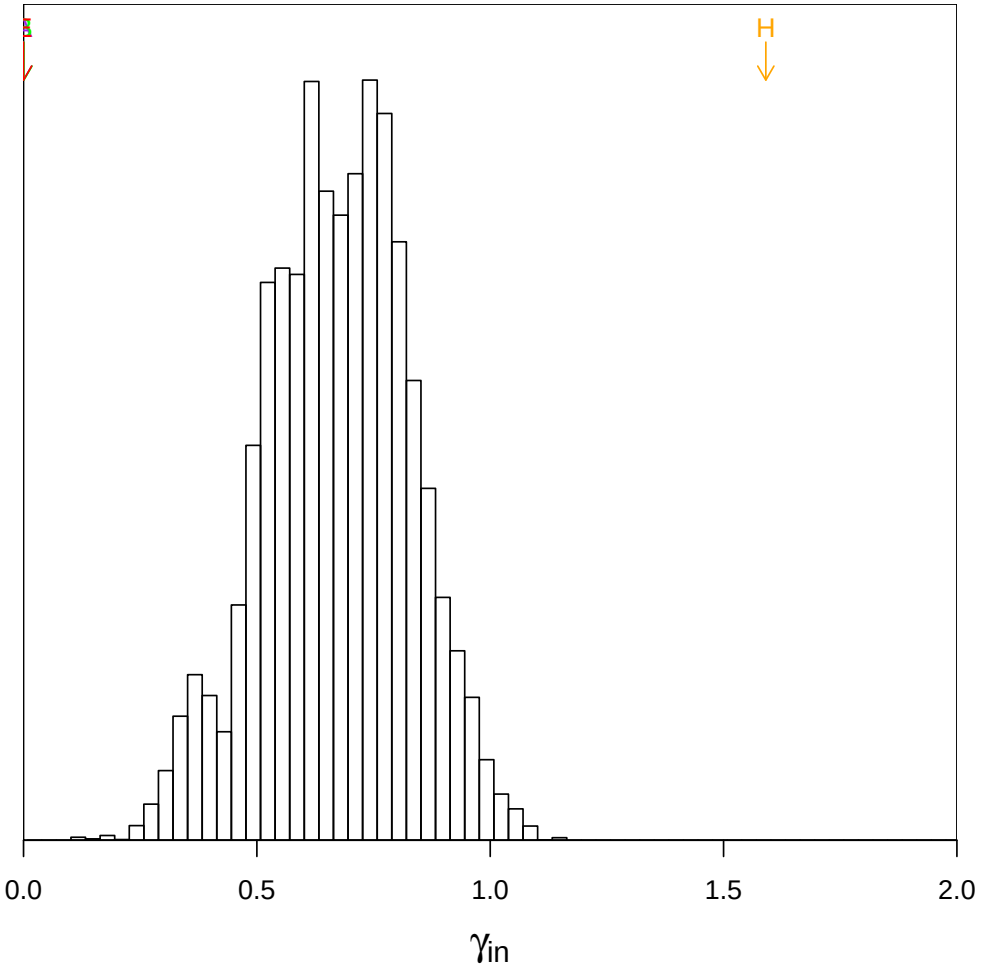

Figure 4.18: Histogram of $\gamma_{\rm in}$ values from an MCMC run on NGC5055 with a temperature setting $T = 1$. There are $\sim 4 \times 10^7$ models included from 8 independent chains. Arrows are as in Figure 4.4.

4.5 Discussion

Our MCMC method has produced good constraints on r_1 in those galaxies where such a constraint is possible. We now place these estimates in the context of other work, and then use the model we outlined in Section 4.3 in order to explore what we can deduce about their formation history.

4.5.1 Scale length correlation

In Donato et al. (2004) it is suggested that, for a set of 25 galaxies, the scale length of the dark matter halo is proportional to the scale length of the stellar disk. The cored density profile used to argue for proportionality with the disk scale is a pseudo-isothermal halo, given by

$$\rho(r) = \rho_0 \frac{r_c^2}{r^2 + r_c^2} \tag{4.7}$$

and the stellar component is modelled by an exponential disk with a scale length R_D. The profile (4.7) does not show the same degeneracy between ρ_0 and r_c as the $\alpha - \beta - \gamma$ profile, because it becomes independent of r_c at small radii. However it is effectively a single parameter profile. In our analysis we have found that v_{max} is strongly constrained, and this constraint translates into a constraint on $\rho_0 r_c^2$ at large radii. Therefore, for any given value of ρ_0 (which controls the core behaviour on its own) there is little freedom in r_c. This in itself does not imply that r_c is necessarily meaningless, so we have investigated whether or not there is an equivalent correlation to that found in Donato et al. (2004) in the galaxies we are examining.

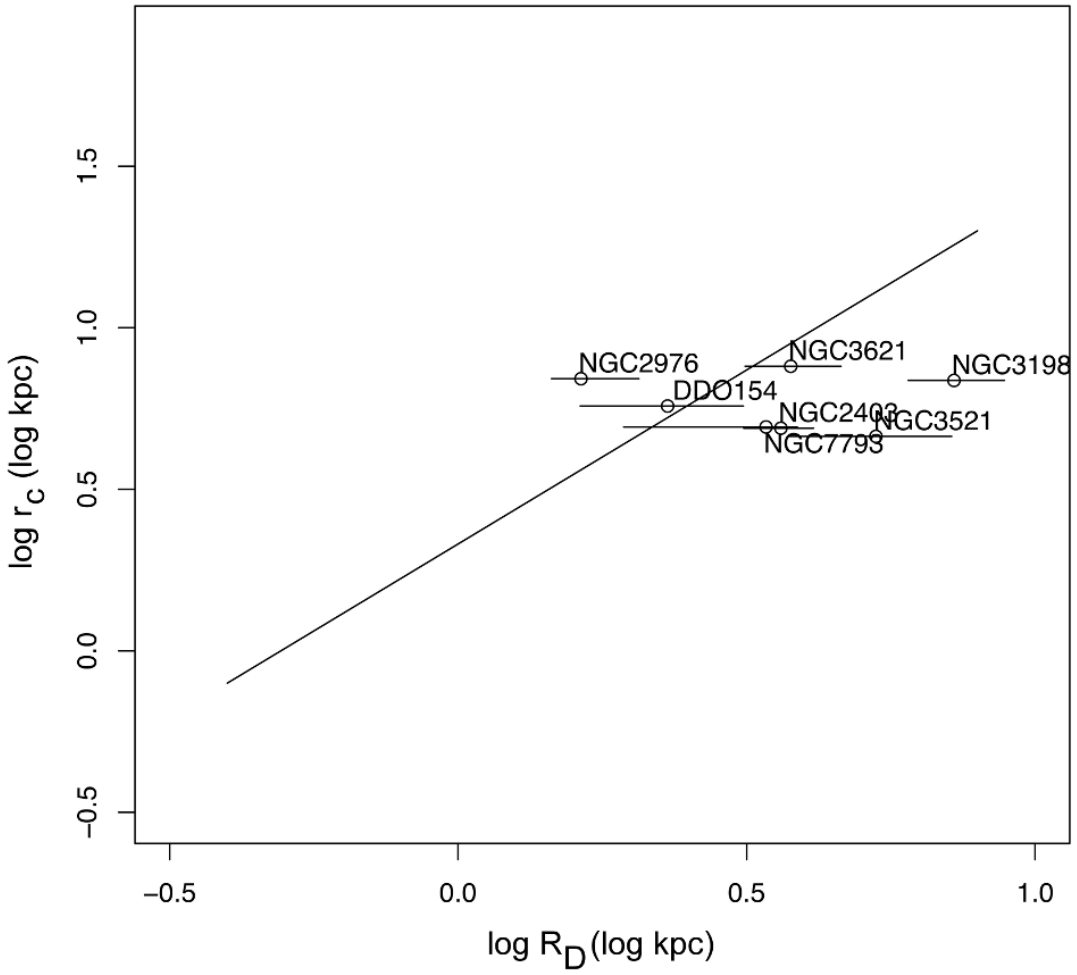

Figure 4.19: The relation between the dark matter core radii, as defined in equation 4.7 and stellar disk radii for our set of galaxies assuming a cored psuedo-isothermal halo profile. NGC 925 is off the right hand edge of this plot. The overlaid solid line is the relation identified by Donato et al. (2004).

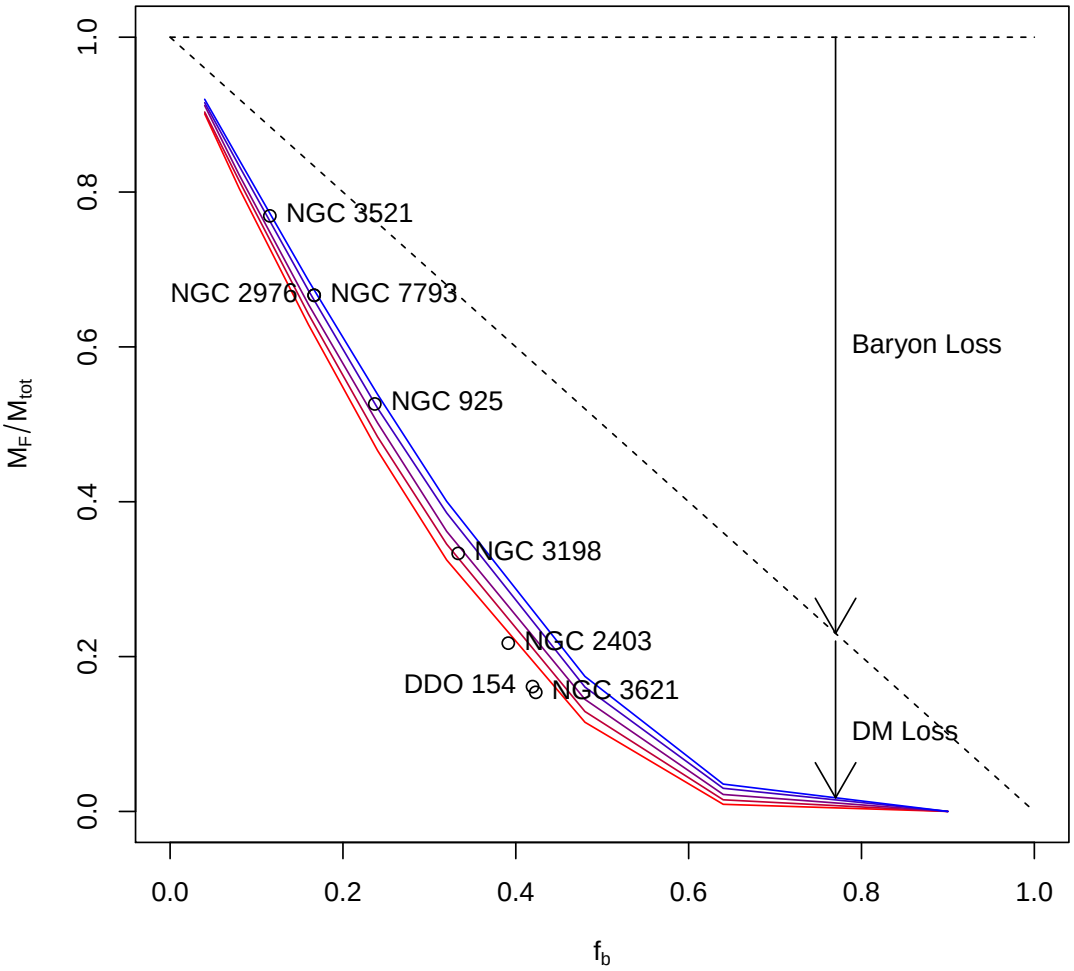

Figure 4.20: Comparison of data from Table 4.3 with simulated predictions. $M_{\rm tot} = M_{\rm I} + M_{\rm b}$ is the total mass, baryons and dark matter, interior to r_1. The dotted line shows the remaining mass after baryon removal, and the solid lines show the overall mass loss after 1Gyr for various halo profiles. As in Figure 4.1, red to blue denotes increasing log slope (0, 0.25, 0.5, 7/9, 1). Simulations were run for baryon fractions $f_b = 0.02, 0.04, 0.08, 0.16, 0.24, 0.48, 0.64, 0.90$. The positions of the galaxies are determined by the analytical model, which always assumes equal baryon and dark matter loss and thus they must all lie on in a single line. The simulation results are not by construction forced to agree with the analytical results. Vertical arrows illustrate the decrease in mass due to the baryon loss (simulated by reduction of particle masses) and the resultant decrease in dark mass.

	Free f_Υ			Kroupa IMF			diet salpeter IMF		
Galaxy	r_1 (kpc)	$\gamma_{\rm in}$	$\chi^2_{\rm red}$	r_1 (kpc)	$\gamma_{\rm in}$	$\chi^2_{\rm red}$	r_1 (kpc)	$\gamma_{\rm in}$	$\chi^2_{\rm red}$
DDO154	$1.28\pm^{0.41}_{0.28}$	$0.42\pm^{0.24}_{0.15}$	0.2	$1.18\pm^{0.31}_{0.24}$	$0.43\pm^{0.23}_{0.14}$	0.2	$1.17\pm^{0.46}_{0.33}$	$0.5\pm^{0.25}_{0.21}$	0.13
NGC2976	$1.94\pm^{1.76}_{0.4}$	$0.47\pm^{0.16}_{0.38}$	0.26	$3.24\pm^{1.14}_{0.89}$	$0.09\pm^{0.26}_{0.07}$	0.32	< 4.18	< 0.97	0.58
NGC7793	$3.3\pm^{0.14}_{0.14}$	< 0.13	0.52	$2.93\pm^{0.13}_{0.17}$	$0.81\pm^{0.06}_{0.07}$	0.67	$3.15\pm^{0.15}_{0.28}$	$0.51\pm^{0.14}_{0.18}$	0.36
NGC2403	< 2.81	$0.72\pm^{0.29}_{0.49}$	0.15	$0.35\pm^{0.15}_{0.25}$	$0.8\pm^{0.2}_{0.17}$	0.29	$0.75\pm^{0.44}_{0.5}$	$0.7\pm^{0.34}_{0.26}$	0.15
NGC925	$6.76\pm^{0.46}_{0.51}$	< 0.29	0.25	$7.43\pm^{0.45}_{0.4}$	$0\pm^{0.06}_{0}$	0.42	$8.4\pm^{7.99}_{0.75}$	< 0.09	0.55
NGC3621	< 1.44	$0.87\pm^{0.18}_{0.26}$	0.28	< 0.88	$0.9\pm^{0.17}_{0.2}$	0.27	$4.61\pm^{1.04}_{1.6}$	$0.39\pm^{0.36}_{0.21}$	0.18
NGC3198	$3.33\pm^{0.14}_{0.97}$	$0.09\pm^{0.28}_{0.07}$	0.38	$4.19\pm^{0.4}_{0.7}$	$0.05\pm^{0.3}_{0.03}$	0.67	$6.36\pm^{1.6}_{1.71}$	$0.14\pm^{0.41}_{0.09}$	0.6
NGC3521	$2.02\pm^{0.36}_{0.26}$	$0.03\pm^{0.17}_{0.02}$	0.68	$3.88\pm^{1.36}_{1.2}$	$0.08\pm^{0.38}_{0.04}$	1.25	$30.58\pm^{20.74}_{12.27}$	< 0.03	2.09

Table 4.2: Table of all calculated $\gamma_{\rm in}$ and r_1 values, with 90% confidence intervals. Reduced χ^2 values shown are estimates of the peak likelihood, taking the 90th percentile of a randomly selected sub-sample of $\sim 10^3$ models from the MCMC chains. The r_1 value for NGC 3521, assuming a diet Salpeter IMF, is outside of the data range, as are the confidence intervals for all r_1 values for NGC 2976. Values for NGC 2403 and NGC 3521 use a temperature $T = 2$, sampling $P^{1/2}$ rather than P. See text for detailed discussion.

In order to exclude the possibility of the reported correlation being an artefact, we generated sets of 100 rotation curves with random, uncorrelated scale radii for the stellar disk and dark halo of $R_d = 3 \pm 1$ kpc and $r_s = 5 \pm 2$ kpc respectively. We added Gaussian noise to the data and included 1σ error bars of the corresponding size. The dark halo models were either Burkert, pseudo-isothermal, or NFW. We then found the best fitting pseudo-isothermal haloes, given a free mass-to-light ratio. In none of the cases did we find a correlation. Give that Donato et al. (2004) found that maximal disks were favoured in their models, we then forced a maximal disk to be used before fitting the pseudo-isothermal halo. Again, we did not find a correlation.

We investigated whether there is a comparable correlation from our own data set (shown in Figure 4.19), by assuming a maximal disk and fitting a single pseudo-isothermal profile to each galaxy. We do not see a relation as presented in Donato et al. (2004), although we note that our sample is smaller and has a narrower range of properties. It should also be noted that in order to produce maximal disk fits, higher f_Υ values than we allowed in our MCMC modelling had to be assumed in many cases.

4.5.2 Feedback modelling

The question of whether or not there is a relation between any parameters of the baryonic component of a galaxy and parameters of its dark matter halo is relevant to understanding galaxy formation. It is presumed, based on cosmological models by Navarro et al. (1996) and others, that the centres of dark matter haloes begin strongly cusped, and then become cored by some interaction with baryonic matter (e.g. Governato et al., 2010).

The r_1 parameter we calculate can be used to gain some insight into this. Any process which reshaped the halo must be able to disrupt the potential of the galaxy to at least this radius, under the assumptions of an NFW starting point and a spherically symmetric halo. In Table 4.2 we show that for galaxies DDO 154, NGC 2403, and NGC 2976 the values of r_1 are for each galaxy within the 90% confidence intervals of each other for all prior assumptions about mass-to-light ratio used here. In the case of NGC 7793, the intervals do not entirely overlap but, as Figure 4.15 shows, the constraint on r_1 is very strong and not dependent on f_Υ so this is not an issue of baryonic modelling.

We now focus on DDO 154, the smallest galaxy in our set, because work such as Governato et al. (2010) focuses on feedback in dwarf galaxies. Considering supernova feedback, if each $100\,M_\odot$ of star formation leads to a single supernova which feeds back 10^{44} J of energy ($5.6 \times 10^{-6}\,M_{\rm intial}$ equivalent solar masses), and assuming the current stellar mass is $\approx 88\%$ of the initial mass (using a Kroupa IMF gives an initial composition

where 12% of the total stellar mass is O stars (Kroupa, 2001), and have all undergone supernova), the feedback energy is $210\,M_{\odot}c^2$. This is larger than the energy change required in the dark matter halo to modify its density profile; the difference in total kinetic energy between DDO 154 and the closest NFW halo (based on least squares fitting) is $1.2\,\pm^{1.6}_{0.9}\,M_{\odot}c^2$. Energy production is in this galaxy therefore does not constrain this process, so we must focus on how this energy can be transferred to the dark matter halo.

Feedback from a central star forming region in DDO 154 was modelled in Gelato and Sommer-Larsen (1999) as an attempt to explain the discrepancy between observations of the galaxy and the NFW halo model. They were only able to reproduce the observed rotation curve by assuming a disk more massive than that which is observed in HI emissions, and furthermore Read and Gilmore (2005) shows that their method of contracting the dark matter halo cusp could bias its final state after outflow towards being more flat, due to the assumed isotropic velocity structure of the halo. Applying the method described in Section 4.3 to DDO 154, we find a gas fraction available for feedback $f_{\rm g} = 0.42$, compared to the estimate of the currently observed baryon fraction of 0.1 by Carignan and Purton (1998), which supports the conclusion that this galaxy requires additional baryonic mass to account for its dark matter halo profile (although it still leaves open the question of where this mass is now). The complete set of values for $f_{\rm g}$, for all the galaxies studied here, are are shown in Table 4.3.

Our calculated values for $f_{\rm g}$ are minima, as the contraction of the baryonic component prior to outflow can only increase the dark matter content interior to r_1, and thus require a greater amount of gas outflow to remove. If we assume that the process of contracting dark matter through baryon motion has efficiency of order unity for infall as well as for outflow (that is, each unit mass of baryons moved past r_1 in either radial direction brings with it a unit mass of dark matter) then significant infall and contraction would move the value of $f_{\rm g}$ towards 0.5.

In Figure 4.20 we show the values from Table 4.3 in the context of the output from the simulations in Section 4.3. The construction of the analytical model forces all the galaxies on to one straight line of the plot, so this should not be taken as a physical confirmation of the simulations. The simulations are shown to be consistent one of the main assumptions of the analytical model; that the amount of dark matter removed during an outflow is comparable to the amount of gas removed.

The disk of DDO 154 is dominated by neutral hydrogen gas, whose presence must be accounted for when suggesting an energetic outflow (Carignan and Purton, 1998). Zubovas et al. (2011) present a simulated model of the Fermi bubbles above and below

Galaxy	$M_{\rm F,dark}/(M_{\rm I,dark} + M_{\rm I,gas})$	f_g	$\gamma_{\rm in}$
DDO 154	0.16	0.42	$0.42\pm^{0.24}_{0.15}$
NGC 2976	0.67	0.17	$0.47\pm^{0.16}_{0.38}$
NGC 7793	0.67	0.17	< 0.13
NGC 2403	0.22	0.39	$0.72\pm^{0.29}_{0.49}$
NGC 925	0.53	0.24	< 0.29
NGC 3621	0.15	0.43	$0.87\pm^{0.18}_{0.26}$
NGC 3198	0.33	0.34	$0.09\pm^{0.28}_{0.07}$
NGC 3521	0.77	0.12	$0.03\pm^{0.17}_{0.02}$

Table 4.3: Inferred available gas fractions at the time of outflow, based on a simple spherical model, along with $\gamma_{\rm in}$ values taken from the free f_Υ case. Note that $M_{\rm I,gas}$ here refers to the baryon mass interior to r_1, so $f_{\rm g}$ is a factor 2 smaller than the total mass deficit.

the disk of the Milky Way, detected in γ rays (Su et al., 2010). These bubbles are part of a black hole outflow that is pinched in the centre due to the density of the gas in the Galactic disk. A black hole outflow scenario is compatible with the gas-richness of DDO 154's disk if the density of that gas is high enough that an outflow able to reach r_1 would not significantly disturb it. If we assume that the density of the dark matter halo can be approximated as $\rho \propto r^{-1/2}$ inside r_1 (as an average log slope, assuming the halo becomes flat at $r = 0$), and that the disk density can also be approximated near the centre of the galaxy by a $\rho \propto r^{-1/2}$ profile, the energy required to lift all matter inside r_1 to r_1 is

$$U = \frac{3}{5}\frac{GM(r_1)^2}{r_1} \tag{4.8}$$

Imparting the same amount of energy to both components, and cancelling the enclosed mass of both components, gives

$$\frac{M_{\rm halo}(r_1)}{r_1} = \frac{M_{\rm disk}(R_{\rm outflow})}{R_{\rm outflow}} \tag{4.9}$$

where $R_{\rm outflow}$ is the distance gas can be swept up in the disk with the same energy required to sweep up all halo gas to r_1. For the $\rho = \rho_0(\frac{r}{r_0})^{-1/2}$ density profile we use,

$$M = 4\pi \int_0^r \rho(r')r^2 dr = \frac{8}{5}\pi\rho_0 r^{5/2} r_0^{2/3} \tag{4.10}$$

assuming equal scale radii and substituting into (4.9) we can calculate how an outflow that sweeps up all gas to a specific radius would travel in the two different media

$$R_{\rm outflow} = \left(\frac{\rho_{0,\rm halo}}{\rho_{0,\rm disk}}\right)^{\frac{2}{3}} r_1 \tag{4.11}$$

Taking the model of Banerjee et al. (2011) for the inner regions of the gas disk of DDO 154, with a pseudo-isothermal scale density of dark matter $\rho_{\rm dm} = 0.028\,{\rm M}_\odot{\rm pc}^{-3}$, $\Sigma_{\rm HI} = 5.7\,{\rm M}_\odot{\rm pc}^{-3}$, and gas scale height $h = 100\,{\rm pc}$, we derive $\rho_{0,\rm halo} = 4.8 \times 10^{-3}\,{\rm M}_\odot{\rm pc}^{-3}$ and $\rho_{0,\rm disk} = 0.057\,{\rm M}_\odot{\rm pc}^{-3}$. We use the halo model of Banerjee in this calculation because their disk model is calculated assuming a pseudo-isothermal halo - however, our rotation curve data is the same. Given the value $r_1 = 1.21$ kpc for DDO 154, we therefore estimate $R_{\rm outflow} = 192\,{\rm pc}$. The first radial bin in this galaxy is situated at $R = 135\,{\rm pc}$, which means a Fermi bubble-like outflow cannot be excluded based on the presence of gas in the disk.

4.6 Conclusions

We have applied the MCMC method described in Chapter 3 to a number of nearby galaxies and been able to constrain the density profiles of their haloes with less ambiguity than would be possible with simpler statistical methods. From these constraints, we have determined that the sample of galaxies studied here cannot be described by a single, universal, halo profile. We have also calculated from the modelled haloes the values of physical quantities (r_1 and $f_{\rm g}$) which can be used to constrain formation scenarios for these galaxies.

Contrary to work such as de Naray et al. (2008) and Chemin et al. (2011), we find that a lower reduced χ^2 value does not necessarily indicate a better description of the data. Their assertion requires the errors be correct, and that the degrees of freedom be constant across the parameter space, neither of which is necessarily correct for these data and these models. Our MCMC method only relies on the χ^2 values being locally meaningful for consecutive members of the Markov chain, and the use of a more general profile removes the strong prior link between the inner and outer haloes imposed by other profiles such as NFW.

The sample investigated here is subject to a selection bias. The THINGS galaxies were subsampled for generation of rotation curves by de Blok et al. (2008), based on inclination and other factors, and then subsampled again here on the basis of whether or not they can produce meaningful outputs from our MCMC technique. Our conclusions must be interpreted in this context.

The selection biases we experience also apply to any attempt at rotation curve decomposition. The cases where MCMC cannot find a constraint should be taken as an indication that the fitting of an individual profile, that is part of our parameter space or closely approximated by a profile that is, cannot produce a result that is credible without

further discussion of the issues that prevent a constraint with MCMC. Our technique has the potential to overcome these bias using different data, or different modelling of the data (that incorporates more well constrained stellar populations for instance.) The behaviour of our MCMC technique with potential future data sets is described in Chapter 3 and is found to be promising.

We have identified several degeneracies in the parameter space. Some we are unable to break, such as the degeneracy between Υ and the inner log slope $\gamma_{\rm in}$ for NGC 3621. One of the most important degeneracies we discovered is between $\rho_{\rm s}$ and $r_{\rm s}$, which has been resolved in all cases presented here. This degeneracy precludes these two parameters being independently considered as physical. Our transformation of the parameter $\rho_{\rm s}$ into $v_{\rm max}$ removes this degeneracy, but unfortunately $r_{\rm s}$ still cannot be interpreted as a physically meaningful radius, because its position is degenerate with the shaping parameters α, β and γ.

Scale radii fixed by the points at which the curve reaches a particular log slope (i.e. r_n where n is the negative log slope) are more useful for a discussion of the actual morphology of dark matter haloes. We chose r_1 due to the fact that parts of the halo interior to this distance cannot be modelled by a cosmological halo such as NFW. Thus r_1 corresponds to a radius over which baryonic physics must act in order to produce the measured halo.

We have shown that r_1 is useful and well constrained, and that it can be used to constrain a simple feedback-based formation model. The relevance of r_1 is first as a constrainable physical parameter within the data range of the galaxies studied here, secondly as a required scale of mass loss (under reasonable assumptions) and thirdly as a common scaling parameter with which to compare observationally derived haloes to simulated ones in a physically meaningful way. The second reason applies only for r_1 and not for other radii. However we recognise that other radii may have similar uses, and such radii may also be constrained well with an MCMC method, as we have used here.

The model we use to derive $f_{\rm g}$ is simple, but links a physically viable outflow scenario to a quantity derived by MCMC analysis of observations, and could be refined iteratively by using it as an initial condition in formation simulations. This value cannot be reliably derived from simpler fitting methods due to the complexity of the parameter space, and the low quality of measures such as $\chi^2_{\rm red}$ as absolute goodness of fit statistics for these data. MCMC provides a firm enough constraint, and a confidence that the parameter space has been properly explored, to allow results such as $f_{\rm g}$ to guide simulations.

5

The degeneracy of M33 mass modelling and its physical implications

The Local Group galaxy M33 exhibits a regular spiral structure and is close enough to permit high resolution analysis of its kinematics, making it an ideal candidate for rotation curve studies of its inner regions. Previous studies have claimed the galaxy has a dark matter halo with an NFW profile, based on statistical comparisons with a small number of other profiles. We apply a Bayesian method from our previous paper to place the dark matter density profile in the context of a continuous, and more general, parameter space. For a wide range of initial assumptions we find that models with inner log slope $\gamma_{\rm in} < 0.9$ are strongly excluded by the kinematics of the galaxy unless the mass-to-light ratio of the stellar components in the $3.6\,\mu$m band satisfies $\Upsilon_{3.6} \geq 2$. Such a high $\Upsilon_{3.6}$ is inconsistent with current modelling of the stellar population of M33. This suggests that M33 is a galaxy whose dark matter halo has not been significantly modified by feedback. We discuss possible explanations of this result, including ram pressure stripping during earlier interactions with M31.

5.1 Introduction

Cosmological models of the formation of dark matter haloes predict cusped density profiles (Dubinski and Carlberg, 1991; Navarro et al., 1996), which do not appear to match the dark matter density profiles inferred from observations of rotation curves of disk galaxies (Gentile et al., 2004).

Decompositions suggesting uniform central density haloes (Flores and Primack, 1994; Moore, 1994) led Burkert (1995) to propose a universal, cored profile. Rotation curves were originally measured with a slit along the principal axis of the galaxy, but most current measurements use a tilted ring method to extract rotation curves from velocity fields (Begeman, 1989). Using this method Gentile et al. (2004) found that cored haloes were preferred to both ΛCDM haloes and MOND (MOdified Newtonian Dynamics) for a sample of five galaxies. Observations of galaxies from THINGS (The HI Nearby Galaxy Survey; Walter et al., 2008) have provided improved observational constraints on the rotation curves (and thus density profiles) of nearby galaxies, as explored in de Blok et al. (2008) and Hague and Wilkinson (2013) (the paper that formed the basis of Chapter 3). These improved velocity data permit more precise constraints on halo density profiles than were possible in previous papers that addressed the cusp-core problem.

Hydrodynamics simulations have been used to attempt to reconcile dark matter-only ΛCDM simulations with observations. Governato et al. (2010) found that feedback from supernovae is able to flatten the inner density profile of isolated dwarf galaxies and pro-

duce a rotation curve comparable to that observed in the dwarf galaxy DDO 39. In contrast, Parry et al. (2011) found that satellites of a Milky Way-like simulated galaxy, generated using a hydrodynamical simulation that was able to reproduce the observed population and kinematics of the Milky Way system, did not have their dark matter haloes significantly altered by baryonic activity, although they note that they are unable to resolve the innermost parts of the profile due to the force resolution of their simulations. Di Cintio et al. (2013) found a relation between maximum rotation velocity $v_{\rm rot}$ and the inner log slope of the dark matter profile in 31 simulated galaxies, with cores being seen in smaller ($v_{\rm rot} \sim 50\,{\rm kms}^{-1}$) galaxies and profiles approaching NFW in larger ($v_{\rm rot} \sim 150\,{\rm kms}^{-1}$) galaxies.

In this chapter we apply the Bayesian method presented in Chapter 3 to the galaxy M33, which previous work has shown can be fitted over the entire radial range of HI data by a single power law $\rho \propto r^{-1.3}$, compatible with the NFW profile (Corbelli and Salucci, 2000). Later work in Corbelli (2003) added molecular gas to the mass model, resulting in an inner density profile $\rho \propto r^{-1.5}$ being excluded. We also examine the more recent claim of Seigar (2011) that the NFW profile itself best represents the dark matter halo of M33. This result is at odds with some observational claims (e.g. de Blok et al., 2008) that smaller galaxies are best described with cored halo profiles. In Hague and Wilkinson (2014) (the paper that formed the basis of Chapter 4) we found, using our Bayesian method, a broad range of inner log slopes in a subset of the THINGS galaxies.

Previous work on rotation curves (e.g. Chemin et al., 2011; Gentile et al., 2004; Seigar, 2011) has taken the reduced χ^2 values of mass models to be an accurate representation of the quality of the fit, and further have inferred support for the particular properties of their dark halo models from these values. This is problematic for three main reasons; first the degrees of freedom cannot be trivially inferred from examination of the profile, as it is not clear that all the parameters impact the fit independently at all points in parameter space (see Section 5.5). Secondly, even using non-reduced χ^2, the errors that occur in rotation curves derived using the tilted ring model are not Gaussian, and thus the χ^2 statistic is not strictly valid in this case. Thirdly, there are many halo density profiles that vary considerably in their essential qualities that produce comparably good fits measured by χ^2, as shown in Figure 5.1 where modifying the inner log slope of an NFW profile and then finding the best fit with a free mass-to-light ratio gives good χ^2 for profiles that span the range between cusps and cores. In this context, we present an alternative approach based on MCMC that attempts to overcome these issues, and uses χ^2 as a local estimate of the relative likelihood of nearby models rather than a rigorous global goodness of fit.

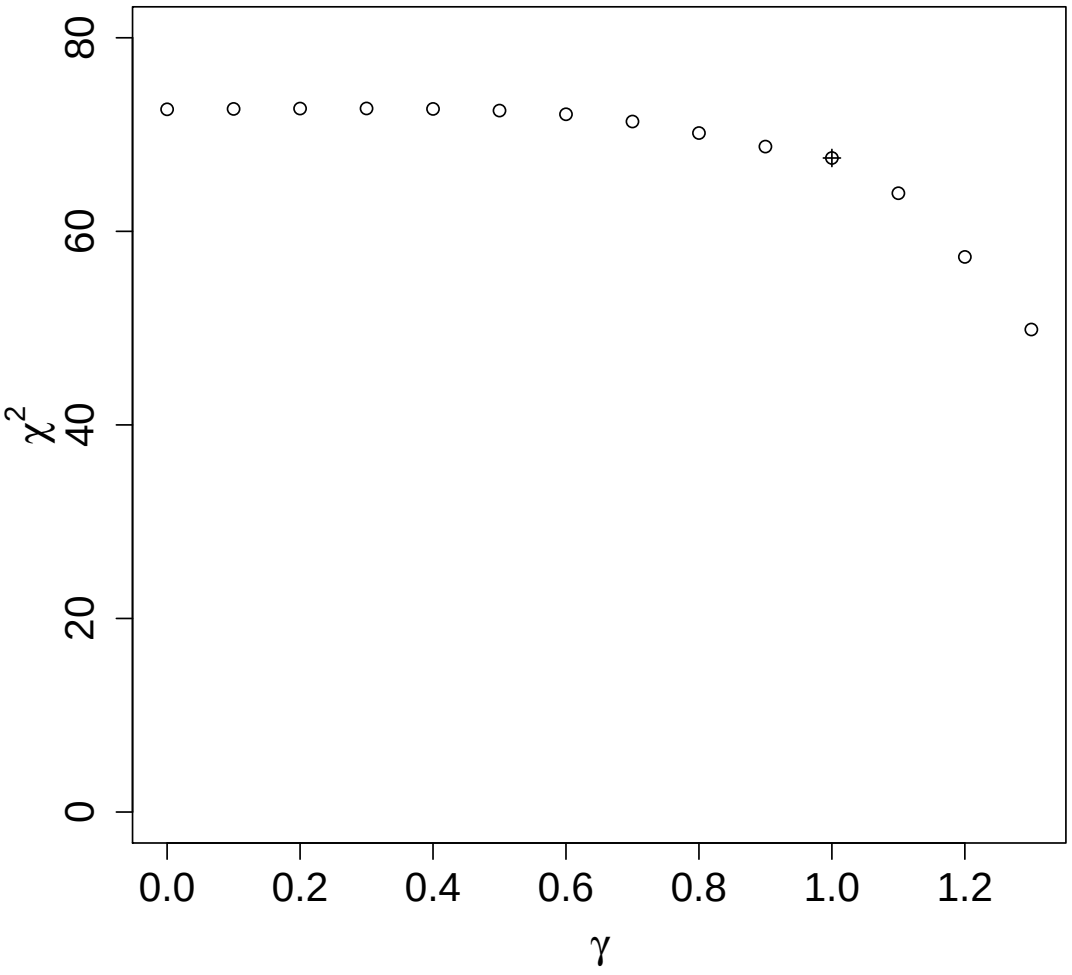

Figure 5.1: Variability of best fit χ^2, using the rotation curve data presented in Section 5.2, with inner log slope for a range of modified NFW profiles $\rho \propto (r/r_s)^{\gamma}(1 + r/r_s)^{3-\gamma}$, where γ is the inner log slope. Free mass-to-light ratios are allowed for both stellar components. The unmodified NFW halo is the marked point.

In Section 5.2 we present the data we use in this analysis. In Section 5.3 we describe how we reproduce the baryonic mass modelling and rotation curve of M33, and the MCMC technique we use with this model. In Section 5.4 we analyse the output of the MCMC chains and in Section 5.5 we discuss our result in the context of previous papers and the current paradigm of galaxy formation.

5.2 M33 Data

We use the rotation curve and gas surface density from Corbelli (2003). This gas model includes both neutral atomic and molecular gas. The rotation curve is derived from HI velocity cubes of the galaxy using a tilted ring model with 11 free rings. Our stellar luminosity data are taken from Seigar (2011), which divides the stellar component into a centrally concentrated component (referred to as a bulge in that paper) and a more extended component.

A more extended rotation curve is shown in Corbelli et al. (2014), but these data do not provide higher spatial resolution and primarily introduce new circular speed bins in the outer (>16 kpc) part of the galaxy. As we are focusing on the profile of the inner halo, and the impact baryons have on it, these data are not relevant here. Also, as we explain in § 5.3.2, we specifically use a dark matter density profile that allows for independent fitting at large and small radii, which therefore does not impose a prior relation between the slope of the inner profile and the outer profile.

5.3 Modelling of M33

We decompose the rotation curve of M33 into four components: two stellar disks, a gas disk and a dark matter halo. The circular velocity contribution of each component is added in quadrature to produce a proposed rotation curve, to be compared with observations.

5.3.1 Baryonic Mass Models

The Seigar (2011) model consists of a gas component taken from Corbelli (2003), along with two stellar components. These latter components are distinguished photometrically, rather than by velocity structure. The more extended component is assumed to be exponential, whilst the more centrally concentrated component is taken to be a Sérsic profile (although in this case the best fit was found to be $n = 1$, making it equivalent to an

exponential profile). Table 5.1 shows the values used to generate the two components. Values for the inner component appear to differ from those quoted in Seigar (2011) as we have converted them from those of a Sérsic profile to the equivalents for an exponential disk. We explore models with a freely varying baryonic mass-to-light ratio, $\Upsilon_{3.6}$, the solar masses per solar luminosity in the Spitzer 3.6μm band, and with a number of fixed mass-to-light ratios taken from previous work or derived from stellar mass modelling. We do not include a mass-to-light gradient in the disk as the estimated gradient in Seigar (2011) ($-0.014\,\mathrm{kpc}^{-1}$) gives rise to a change in the total predicted velocity which is less than 0.75 of the observational error bars at all radii. However we investigate the potential impact of varying mass-to-light ratio with radius in models D1 and D2.

Our first model for the stellar mass allows the mass-to-light ratio of the stellar disks to vary freely over a large range. We consider a second, fixed stellar model using the stellar population mass modelling of Oh et al. (2008), along with the $J - K$ values for M33 taken from the 2MASS Large Galaxy Atlas (Jarrett et al., 2003). These values are based on integrated magnitudes measured within a 20 mag arcsec^{-2} isophote, which in M33 corresponds to a radius $r \approx 6\,\mathrm{kpc}$. For M33, $[J - K] = 0.891$ which gives a mass-to-light ratio $\Upsilon_{3.6} = 0.67$. This is more consistent with current estimates of mass-to-light ratios of similar nearby galaxies (e.g. Meidt et al., 2014) than the value from Seigar (2011) of $\Upsilon_{3.6} = 1.25$.

We have been provided with the radial surface density of neutral atomic gas and molecular gas used in Corbelli (2003) by the authors. We processed this using the `ROTMOD` task in `GIPSY`[1], which employs the method described in Casertano (1983) to generate a rotation curve contribution. We use a sech^2 vertical density law, and the value for $z_{\mathrm{gas}} = 0.5\,\mathrm{kpc}$ given in Corbelli and Salucci (2000), who note that an infinitesimally thin disk yields an identical result. Other density laws do not produce a sufficiently large difference to impact the analysis, and the gas rotation curve is consistent with that shown in Figure 5 of Corbelli (2003). The gas contribution used in Seigar (2011) is that of Corbelli and Salucci (2000), which does not include molecular gas. However, as shown in Corbelli (2003), the molecular gas mass is 10% of the atomic gas and so the result from Seigar (2011) is suitable for a first order comparison.

[1] http://www.astro.rug.nl/~gipsy/

Parameter	Definition	Value
h_1 (kpc)	Inner stellar disk scale length	0.235
M_1 ($M_\odot$)	Inner stellar disk mass	6.07×10^8
h_2 (kpc)	Outer stellar disk scale length	1.7
M_2 ($M_\odot$)	Outer stellar disk mass	3.81×10^9
$z_{\rm gas}$ (kpc)	Gas disk scale height	0.5
$M_{\rm gas}$ ($M_\odot$)	Gas disk mass	3×10^9

Table 5.1: The two stellar components are modelled as exponential disks using parameters from Seigar (2011). For definiteness, we use their mass-to-light ratio $\Upsilon_{3.6} = 1.25$ here (although can be a free parameter or takes different values in our models, see Table 5.2), and the gas component is modelled using radially binned surface density data provided by Corbelli (2003).

5.3.2 Dark Matter Models

To model the dark matter halo we used an $\alpha-\beta-\gamma$ profile, but as in Chapter 3 transformed to remove the degeneracy between $\rho_{\rm s}$ and $r_{\rm s}$

$$\rho(r) = \frac{\widetilde{\Sigma}_{\rm max}}{G} \frac{v_{\rm max}^2}{(\frac{r}{r_{\rm s}})^\gamma (1 + (\frac{r}{r_{\rm s}})^{1/\alpha})^{\alpha(\beta-\gamma)}} \tag{5.1}$$

where $r_{\rm s}$ is the scale radius, $v_{\rm max}$ is the peak velocity of the dark matter rotation curve, α, β and γ are shaping parameters, and $\widetilde{\Sigma}_{\rm max}$ is the normalised surface density at $r_{\rm max} \equiv r(v_{\rm max})$, given by

$$\widetilde{\Sigma}_{\rm max} = \frac{\rho_{\rm s} r_{\rm max}}{M(r_{\rm max})} \tag{5.2}$$

which means that the parameterisation replaces $\rho_{\rm s}$ with $v_{\rm max}$ but retains the same number of parameters, since $\widetilde{\Sigma}_{\rm max}$ is fixed at each point in parameter space.

Contrary to the statements in Adams et al. (2014), it does not matter that the parameters of this halo profile are still degenerate to some extent as we focus on physical properties of each halo model, within the data range, rather than parameters such as γ. Our approach has the advantage that we do not impose as strong a prior link as all previous authors between the log slope of the halo at small and large radii (due to the larger parameter space) and we do not extrapolate beyond the data range. We have confirmed the utility of this approach through extensive testing in Chapter 3.

5.3.3 MCMC analysis

We use a Bayesian Markov Chain Monte Carlo (MCMC) method to explore the parameter space of our models. This method produces a non-normalised probability distribution, which can be argued to be normalised if there are no physically credible models outside the parameterisation. The method is described, along with the extensive testing we have done on simulated data, in Chapter 3. Starting at a random position in the parameter space defined by $[\alpha, \beta, \gamma, v_{\rm max}, r_{\rm s}, \Upsilon_{3.6}]$, each MCMC chain moves through the space using a Metropolis-Hastings algorithm (Hastings, 1970) which chooses a new model based on a Gaussian step from the existing one, and then moves there if the new model shows a higher likelihood, or with a probability equal to the ratio of the new likelihood divided by the current one if the new likelihood is lower. This results in the chain seeking, and spending most time in, likelihood peaks, but also enables it to move out of peaks to explore other parts of the parameter space. The posterior probability distributions of the parameters are then calculated from the density of models in the parameter space by multiplication with the prior probability. For explicit parameters (e.g. α, β, γ etc.) we assume a flat prior to allow the data the greatest freedom to constrain the models. For derived parameters (e.g. $\gamma_{\rm in}$) this leads to an implicit prior which we calculate numerically (see §3.1 of Chapter 3).

We use χ^2 to calculated a likelihood value at each chosen point in parameter space, but the validity of our approach only depends on the relative values of χ^2 for nearby models being a reasonable proxy for relative likelihood. There are many halo profiles that produce good χ^2 values for this rotation curve, and the strength of the MCMC method is that it allows us to differentiate between these models and determine what, if any, actual constraint exists.

Following the method in Chapter 3 we use the publicly available `CosmoMC` code (Lewis and Bridle, 2002) to implement our MCMC chains. We ran 8 chains in parallel, with a total of $\sim 4 \times 10^7$ models. We have shown in Chapter 4 that this method can be applied to galaxies spanning a wide range of mass and surface brightness.

We present the results for eight runs, shown in Table 5.2. For the A runs we allowed a free mass-to-light ratio, $\Upsilon_{3.6}$, with a range [0.1, 5] to generously cover possible stellar contributions from no disk contribution through to a super-maximal disk. For the B runs we model the baryonic components as in Seigar (2011); for the C runs we use the mass-to-light ratio calculated above (Section 5.3.1), and the D runs use two independent values for $\Upsilon_{3.6}$ for the inner and outer stellar components, using the same ranges as the A runs.

The parameter space is mirrored around $\gamma = 0$, using a range [-2,2] for model selection but taking the absolute value in the range [0,2] for likelihood testing, so that potentially

Run	$\Upsilon_{3.6}$	Radial Bins	Number of Models
A1	[0.1, 5]	27	34969550
B1	1.25	27	39147303
C1	0.67	27	39285713
D1	[0.1, 5]	27	33891283
A2	[0.1, 5]	25	34169361
B2	1.25	25	39634524
C2	0.67	25	39455690
D2	[0.1, 5]	25	31798101

Table 5.2: The number of radial bins in models in the second set of models is reduced by ignoring the feature at the outermost part of the rotation curve in Corbelli and Salucci (2000). The priors for $\Upsilon_{3.6}$ are (1) a freely varying $\Upsilon_{3.6}$ in the range [0.1, 5] (models A, D); (2) the value from Seigar et al. (2008), who used a central mass-to-light ratio in the Spitzer 3.6μm band of $\Upsilon_{3.6} = 1.25 \pm 0.10$ (model B); (3) a value for $\Upsilon_{3.6}$ derived in this chapter with assumptions from Oh et al. (2008), as described in the text (model C).

viable cored profiles are not located at the boundary of the parameter space (see Chapter 3 for details).

We have discarded 10,000 models from the beginning of each chain to allow for burn-in, which we find is sufficient for all the chains to move to areas of high likelihood ($\chi^2_{\rm red} < 2.5$). However, after this point some chains explore secondary peaks before finding the main peak. These secondary peaks are a genuine part of the distribution, as can be verified by the fact that chains sometimes leave the main peak to explore them for an extended period. Our use of MCMC in our analysis thus gives us a more complete picture of the multi-modal probability distribution. However, we note that the high $\Upsilon_{3.6}$ tail of the distribution is very weak, and only partially resolved by our chains. Thus, a comparison of likelihood values between these peaks is not meaningful.

5.3.4 Convergence of MCMC Chains

To check that all 8 chains are converged on the same distribution, we calculated the ratio of the variance of the means of the chains $\sigma(\hat{x})$, to the mean of the variances of the chains $\hat{\sigma}(x)$, for each parameter x. This number is not meaningful for γ, as the distribution is bimodal, but the highest value for other parameters was 0.17 for β indicating good convergence. Inspection of the distribution for each chain showed that in some cases the chain had found only the main peak shown in Figure 5.5 whereas in other cases the chain only found the left hand side of the tail. As some chains managed to integrate the entire distribution as shown in Figure 5.5, it is reasonable to assume that given enough time

any chain will converge on the same result. Combining the distributions may produce an incorrect relative model density between the density of the main peak and the tail, but our analysis does not make use of these values. The aim here is to include the broadest possible range of alternate hypothesis in order to demonstrate that the areas avoided by the MCMC are truly excluded. Calculating the precise likelihood of each peak explored is not required for this purpose.

5.4 Results

Our main finding is that models of M33 exhibit a well defined degeneracy between stellar mass and halo inner slope. Furthermore, we are able exclude models with both slopes shallower than $\gamma_{\rm in} < 0.9$ and stellar mass to light ratios in the 3.6μm band $\Upsilon_{3.6} < 2$, for a generous range of priors. Runs A1, A2, D1 and D2 all show the degeneracy, and runs B1, B2, C2 and C3 find values for fixed values of $\Upsilon_{3.6}$ that are consistent with the distribution found with less restrictive mass-to-light priors. We use A1 as our primary example here, and the other runs to demonstrate the insensitivity of the degeneracy to different priors.

5.4.1 Individual Profiles

A rotation curve from the most populated bin of the A1 distribution is shown in Figure 5.2, with parameters $(\alpha, \beta, \gamma, r_{\rm s}, v_{\rm max}, \Upsilon_{3.6}) = (0.36, 3.85, 1.22, 32.6\,{\rm kpc}, 135.4\,{\rm kms}^{-1}, 1.53)$. A density plot of all the profiles produced in this run is shown in Figure 5.3, showing the best fits of other commonly used density profiles. The highest density of models occurs in a band centred on a single power-law profile with log-slope ~ -1.25, in agreement with the findings of Corbelli and Salucci (2000). We note that the sharp lower boundary of the distribution between $\log r = -1$ and $\log r \approx 0.5$ corresponds to the limit of a maximal halo.

Figure 5.4 shows the halo of the most favoured part of the parameter space compared to other commonly used halo profiles, which have been fitted by minimising $\chi^2_{\rm red}$, using a free $\Upsilon_{3.6}$ parameter. All the halos are able to capture the data in the inner part of the galaxy reasonably well whilst not fitting the outer data points well. This does not preclude a low value of $\chi^2_{\rm red}$, as the poor fit at large radii can be compensated for by a tight fit at low radii, which is the case in these curves. This further underscores the danger of applying a statistic such as $\chi^2_{\rm red}$ to these data.

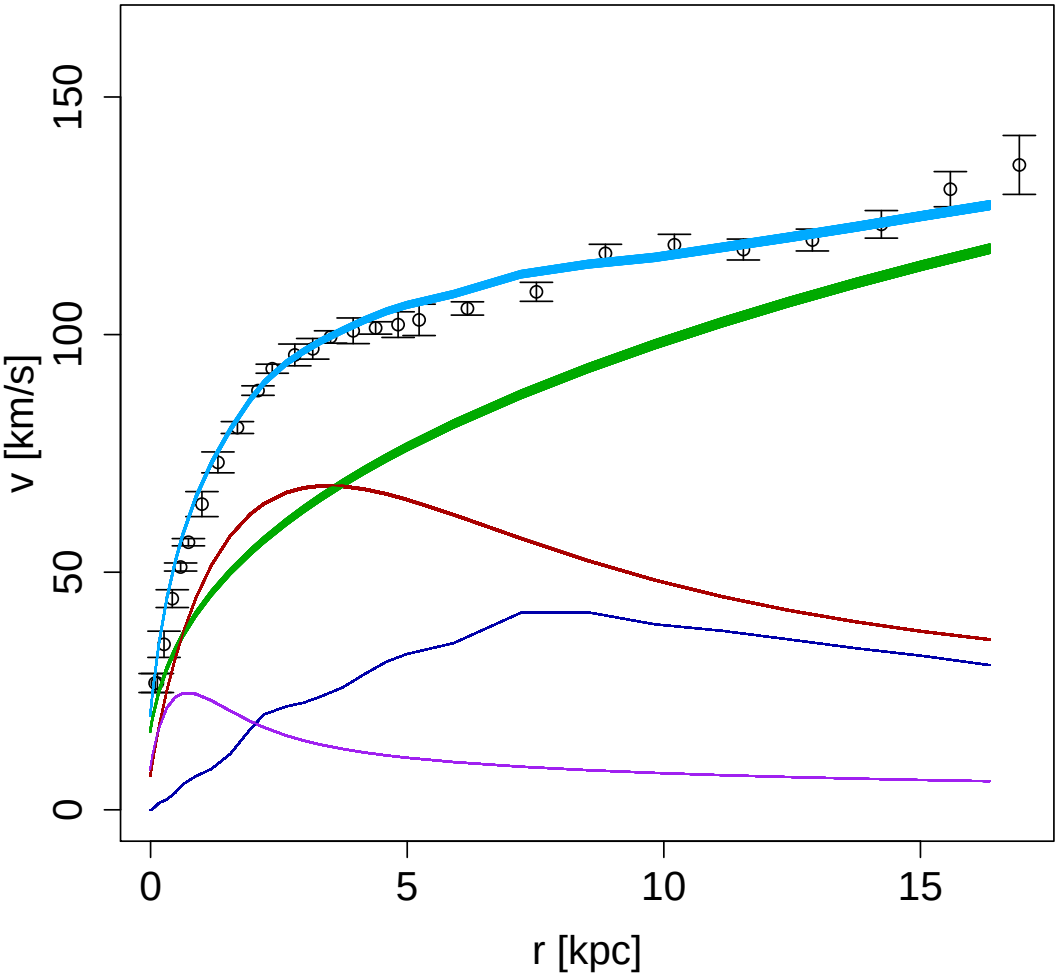

Figure 5.2: Rotation curve of M33. The dark blue curve is the gas (atomic and molecular) contribution, the purple curve is the inner stellar component, the red curve is the outer stellar component, the green line is a proposed dark matter halo (taken from the most occupied bin from the parameter space of the A1 run) and the light blue line is the expected rotation curve. Observed data from Corbelli (2003) are in black. The mass-to-light ratio of the stellar components has been found by fitting the rotation curve rather than by modelling the stellar population in this case.

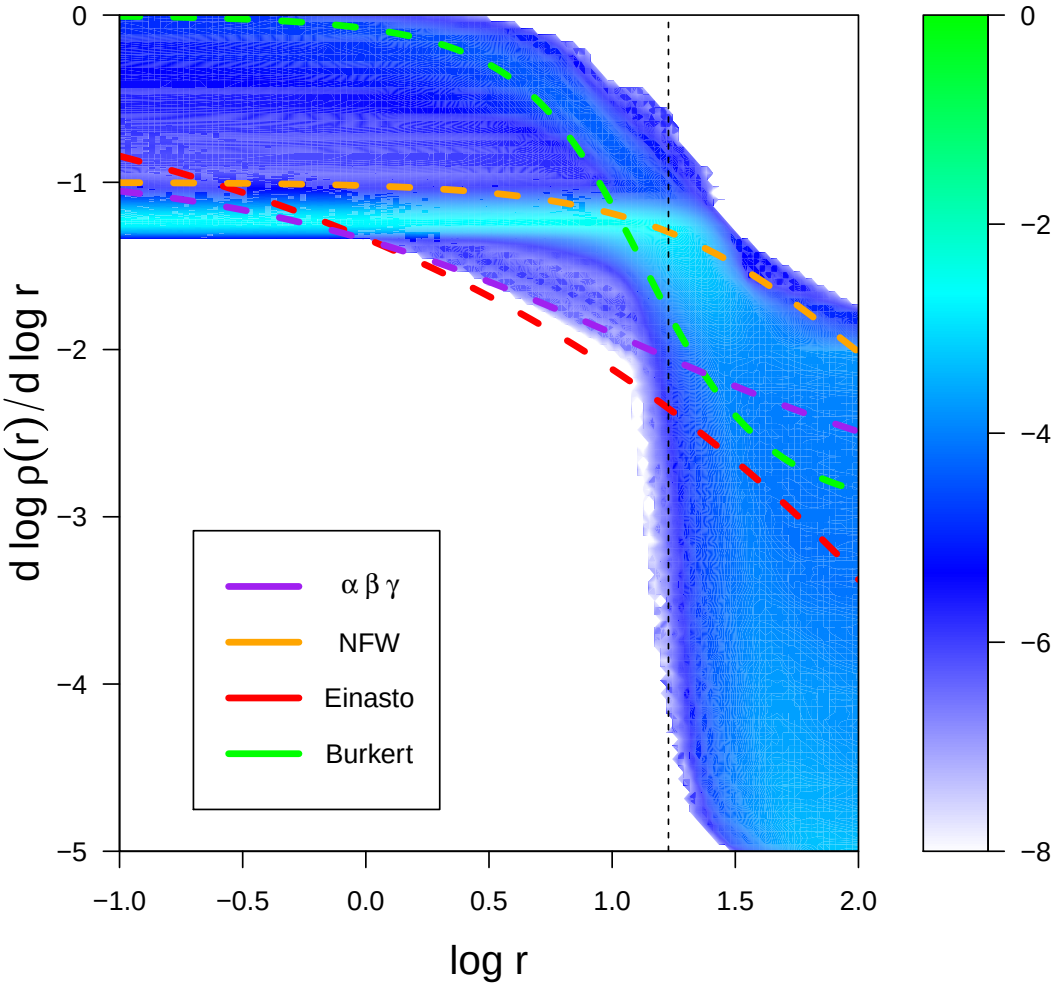

Figure 5.3: Density plot of all the models produced by A1, in $dlog\rho/dlogr$ space. Overlaid are fits of commonly used profiles to the M33 data. The vertical dashed line marks the outer edge of the observed rotation curve data.

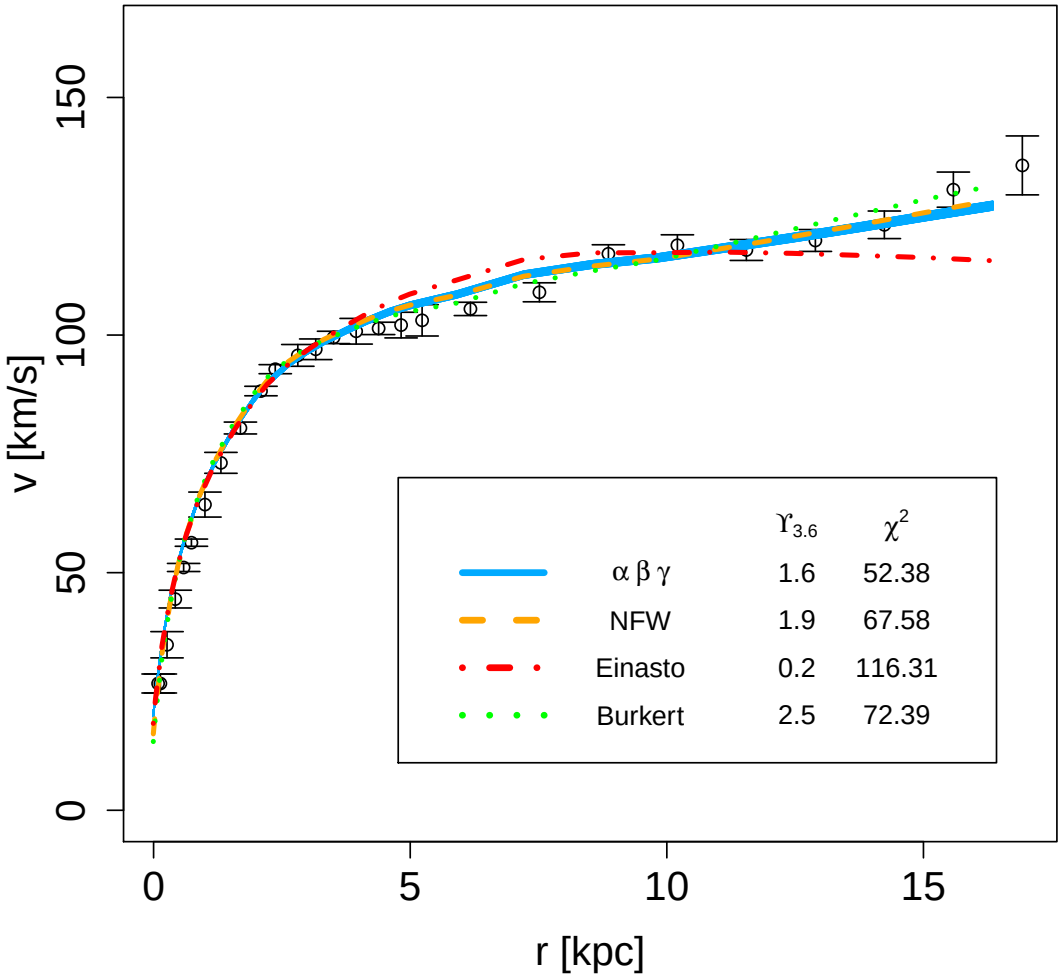

Figure 5.4: Best models of the M33 rotation curve where the blue band is the best fitting MCMC bin, the green dotted line is the best Burkert halo χ^2 fit, the red dot-dashed line the best Einasto halo fit, and the orange dashed line the best NFW profile fit. In each case the rotation curve was fitted using a free mass-to-light ratio $\Upsilon_{3.6}$. The quoted χ^2 value for the NFW profile is not the same as that found by Seigar (2011) as we use slightly different rotation curve data (see Section 5.2). The similarity of the χ^2 value for the NFW halo and the Burkert halo (separation of < 1 in terms of reduced χ^2) illustrates that this fitting statistic cannot be used to clearly differentiate between cusps and cores in this application and that a more sophisticated technique such as MCMC is needed.

5.4.2 Log Slope Degeneracy

We measure the inner log slope of each model at the innermost data point, $\gamma_{\rm in}$, rather than relying on the parameter γ, so that our measurement of the slope is not an extrapolation outside the data range.

For A1, we found $\gamma_{\rm in}$ to be degenerate with the mass-to-light ratio as shown in Figure 5.5. The distribution is binned on a 128×128 grid and then contours placed that enclose 68%, 95%, and 99% of all models. Our analysis favours models with steep inner cusps and high mass-to-light ratios, with a tail in the distribution moving towards flat haloes with even higher values of $\Upsilon_{3.6}$. The two areas are connected by a bridge of models which is not shown here as the density is below the 3σ level. The exact combination of stellar disk mass and dark matter halo favoured in Seigar (2011) ($\Upsilon_{3.6} = 1.25$ and $\gamma_{\rm in} \simeq 1$) is disfavoured at over 3σ when using the free prior here. However, this does not mean that it cannot fit the rotation curve, or that it is not the most favoured result given a more constraining prior on $\Upsilon_{3.6}$. The question we address here is not whether the NFW halo can fit the data (it can, as has been established in the work of Seigar (2011) and Corbelli et al. (2014) and confirmed here). Rather, we are asking whether other models provide better fits, and thus what can actually be inferred from the fact that a particular profile does fit the data.

At the low $\gamma_{\rm in}$ end of the plot is the maximal disk case, where the baryonic component of the galaxy contributes almost all of the rotation curve. Note that despite being flat, this region is not flush with the upper boundary of the $\Upsilon_{3.6}$ range - higher values are excluded by the rotation curve data themselves.

We further illustrate the degeneracy by binning the MCMC models along the $\gamma_{\rm in}$ axis and showing a sample of rotation curves from each bin. This is presented in Figure 5.6, which clearly shows the degeneracy between the disk and halo contributions. The right-hand panel shows the case of models near the peak of the probability distribution, and the left and middle panels show models from the tail towards shallower profiles. These are substantially disfavoured relative to the peak.

5.4.3 Impact of Rotation Curve Features

The rotation curve presented in Corbelli and Salucci (2000) and Corbelli (2003) shows an apparent feature in the outermost part of the rotation curve where the rotation velocity begins to increase, after having levelled off (see Figure 5.2). We now explore the extent to which these two data points influence our result on the distribution of $\gamma_{\rm in}$ by re-running

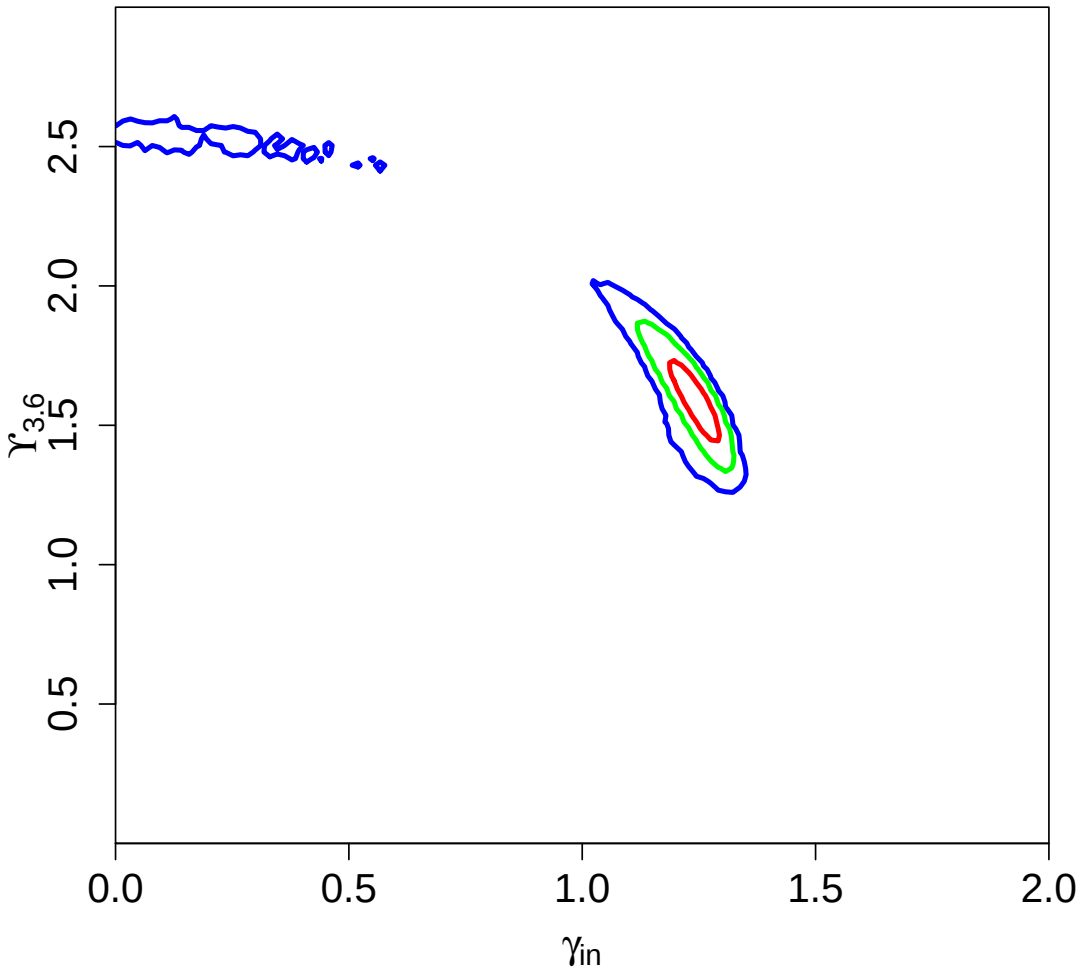

Figure 5.5: Contour plot of the mass-to-light $\Upsilon_{3.6}$ versus inner log slope $\gamma_{\rm in}$. The red contour contains 68% of all the models in the MCMC chains, the green contour contains 95% and the blue contour contains 99%.

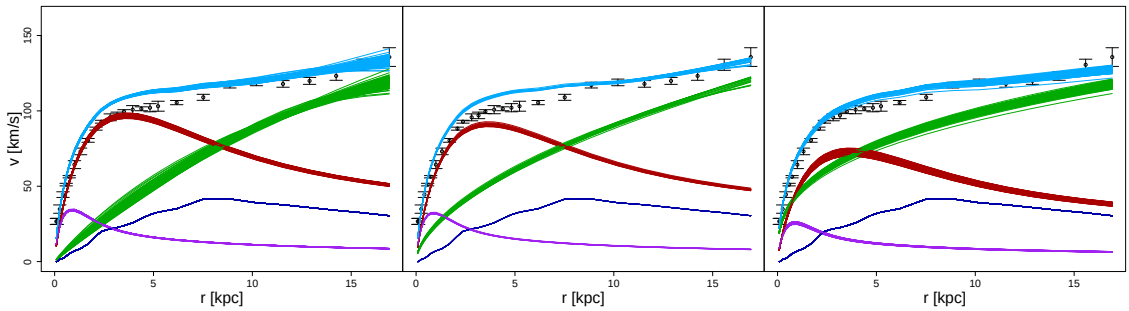

Figure 5.6: Overlay of representative samples of rotation curves from Figure 5.5 illustrating the degeneracy between halo slope and stellar mass-to-light ratio. From left to right the panels show models with $0.1 < \gamma_{\rm in} < 0.2$, $0.8 < \gamma_{\rm in} < 0.9$ and $1.3 < \gamma_{\rm in} < 1.4$, respectively. Key is as in Figure 5.2.

our MCMC chains without the two outmost data points. This is required as we wish to show that our result is independent of the inclusion or not of these two data points.

The feature may be modelled by a flat dark matter density profile extending throughout the radial range, coupled with the maximal baryonic component to model the shape of the rotation curve at small r. We confirm this by calculating r_1, the radius at which the log slope of the dark matter halo reaches -1. We find that this value is high (on the order of the radial extent of the data) for high values of $\Upsilon_{3.6}$ (which from Fig. 5.5 correspond to $\gamma_{\rm in} \approx 0$).

If these outermost data points represented a genuine feature of the density profile and the disk were not maximal, it would require an anomalous increase in the dark matter density at this point as the baryonic component is marginal here. As there is no obvious mechanism to form such a shell of dark matter, we cannot take this model to be correct at large r.

We consider an artefact of the tilted ring method used to generate this rotation curve to be more a likely explanation of this rotation curve feature. In Corbelli and Salucci (2000), an initial set of radial bins in this rotation curve are generated by fitting a parameterised ring to the HI velocity field of the galaxy, under the assumption of entirely circular motion, and then additional radial bins are calculated from interpolating between the neighbouring rings. If the assumptions of the model do not hold e.g. in the presence of significant radial motion, then the parameters of a particular ring may be invalid. An underestimate of inclination would lead to an overestimation in rotation velocity, and due to the interpolation, a single incorrect inclination can account for the apparent feature seen in the last two radial bins. Considered without the final two radial bins, it is not clear the feature exists at all.

In Corbelli et al. (2014) there are data that cover a greater radial extent than earlier papers. However, as can be seen in Figure 5 of that paper, data further out than the outmost limit of the rotation curve used here (from $\sim$ 15 kpc) have large errors and can be clearly approximated by a flat rotation curve. This confirms the above assessment, and means that there would be little to be gained for our specific goal of constraining $\gamma_{\rm in}$ by using the more extended rotation curve.

5.4.4 Alternate mass-to-light priors

Figure 5.7 shows that for run B1 (where $\Upsilon_{3.6}$ is taken from Seigar (2011)), the distribution of $\gamma_{\rm in}$ favours a cusped density profile, steeper than the best fitting NFW profile. This does not imply that an NFW halo does not fit the rotation curve, merely that other regions of parameter space are favoured. The distribution is bimodal, but removing the last two data points removes the second peak (Figure 5.8). This peak is then purely dependent on a feature which may be an artefact.

In runs C1 and C2, we found a log slope compatible with the NFW profile. However, this was in a region that is disfavoured by the run with a free value of $\Upsilon_{3.6}$. In Figure 5.9 we show the equivalent result to Figure 5.3, which demonstrates that in this case a single power law is not favoured. The smaller stellar contribution to the kinematics requires the shape of the rotation curve to be primarily modelled by the dark matter halo, and the NFW profile is unable to do this for the entire radial range. The inner part ($\log r < 0.5$) would require a different concentration parameter $c_{\rm vir}$ than the outer part ($\log r > 0.5$) and in the fitting statistic χ^2 is weighted towards the inner part of the galaxy as there are more data points there.

Runs D1 and D2, with an additional free parameter for the $\Upsilon_{3.6}$ value of the inner stellar component, produced a similar degeneracy to the A runs. Figure 5.10 shows the relation between $\gamma_{\rm in}$ and both values of $\Upsilon_{3.6}$. There is a weak, secondary peak of models featuring a maximal inner component and a flat ($\gamma_{\rm in} < 0.5$) inner slope, but the main peak in $\Upsilon_{3.6,\rm outer}$ versus $\gamma_{\rm in}$ is unaffected. We repeated this test, imposing a prior that the value of $\Upsilon_{3.6}$ for the inner component always be greater than that for the outer component, and found that the result shown in Figure 5.10 remained unchanged. It should be noted that the smooth variation of these two components effectively parameterises a mass-to-light gradient across the stellar disk (which we elected not to model, see Sectionmassmodels) and demonstrates that its inclusion would not impact the result. In general, we find that cusped halo models exhibit smaller gradients than cored models. The distribution of $\Upsilon_{3.6,\rm inner}$ is unsurprisingly wide, due to its dependence on a small number of the innermost

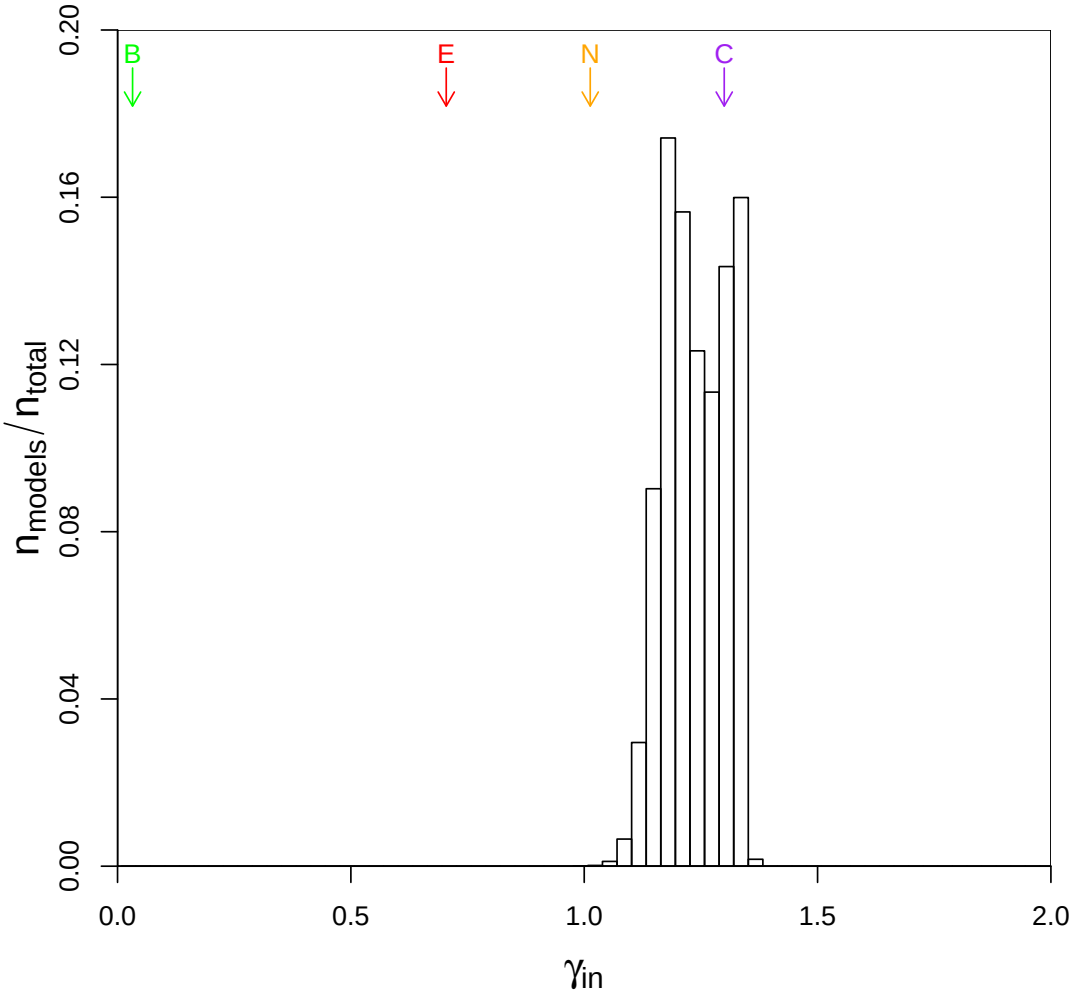

Figure 5.7: Histogram of values of γ_{in} in case B1 where $\Upsilon_{3.6}$ is fixed at 1.25 (i.e. using the mass-to-light value from Seigar, 2011). Vertical axis shows number of models, normalised to give the histogram a total area of 1. Arrows show log slopes for maximum likelihood fits of four individual profiles: green is the Burkert profile, red is the Einasto profile, orange is the NFW profile, and purple is the single power-law found in Corbelli and Salucci (2000). Note that the value calculated in Corbelli et al. (2014) corresponds closely to the value for the NFW profile shown here.

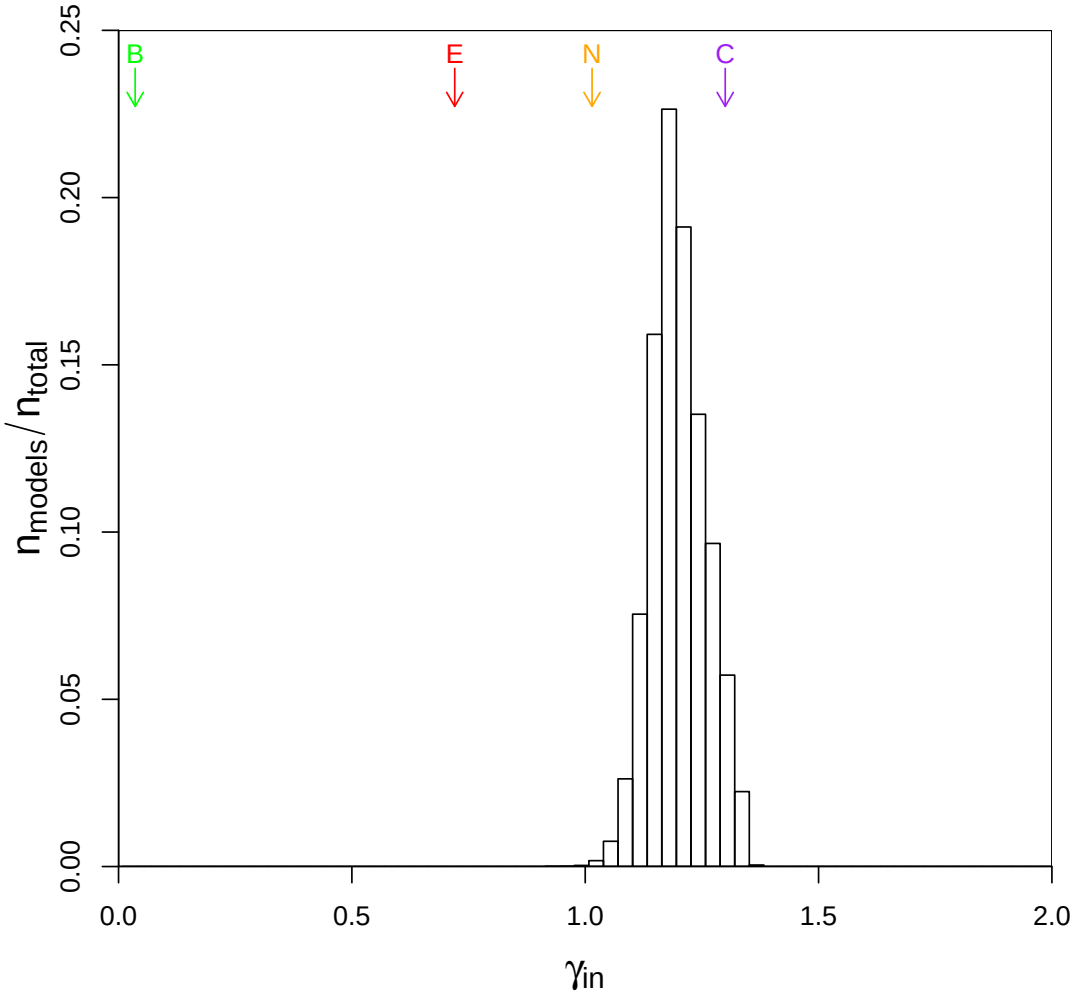

Figure 5.8: Histogram of values of γ_{in} in case B2, where the last two data points are excluded. Key as in Figure 5.7.

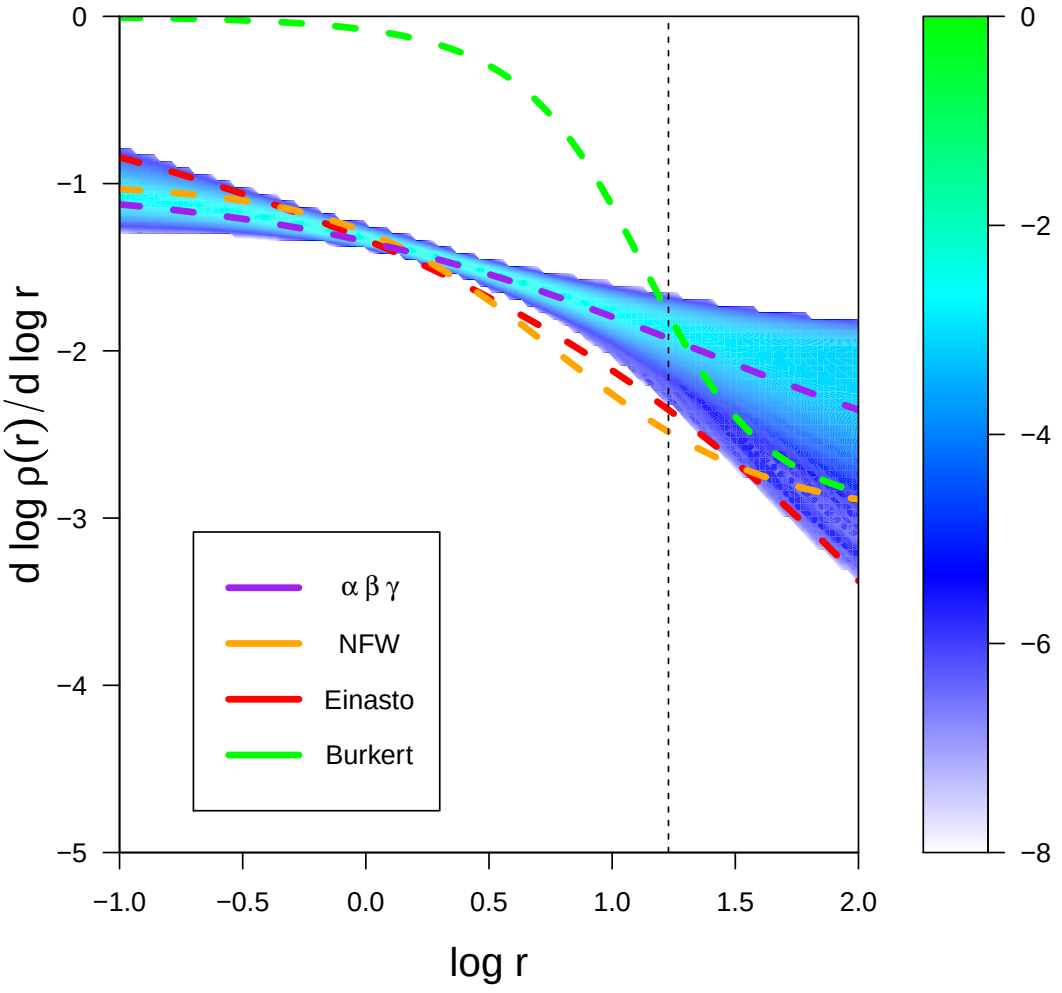

Figure 5.9: Density plot of all the models produced by C1, in $d\log\rho/d\log r$ space. Key as in Figure 5.3.

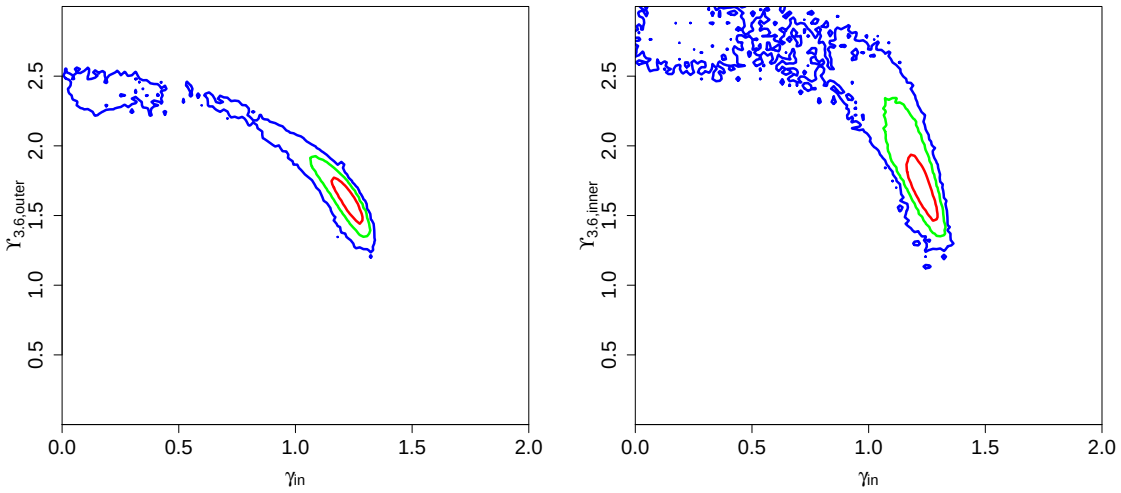

Figure 5.10: For run D1. Correlation between γ_{in} and **(left)** mass-to-light ratio $\Upsilon_{3.6}$ for the outer stellar component and **(right)** $\Upsilon_{3.6}$ for the inner stellar component. There is a prior constraint that the inner mass-to-light ratio be higher.

data points.

5.5 Discussion

5.5.1 Comparison with Previous Work

We have found a result more in agreement with the value of $\gamma_{in} = 1.3$ implied by Corbelli and Salucci (2000) than the assertion by Seigar (2011) that M33 is best described by an NFW halo. Whilst the NFW halo does fit the rotation curve decomposition with $\chi^2_{red} = 1.18$, there are many other haloes (mostly steeper) that also fit the same data equally well.

We noted in Chapter 3 that with multi-parameter models, χ^2_{red} is not reliable across the entire parameter space because it is calculated assuming that the degrees of freedom are constant across the parameter space. This cannot be assumed to be the case. For instance, if a model includes a high stellar mass, and a reduced contribution of the dark matter halo to the rotation curve at small r, then any shape parameters of the halo are going to become less relevant to the quality of the fit. This was described, in an extreme case, in Chapter 3 for the case of constructed high surface brightness rotation curves where the dark matter contribution to the rotation speed was smaller than the error bars. Even in less extreme cases, the parameter β is often not fully utilised, if the scale radius of the halo is

large enough that β does not become the dominant shape parameter within the data range. Model comparison on the basis of $\chi^2_{\rm red}$ alone is thus not necessarily meaningful.

The probability of adding a model, a point in parameter space, to one of our MCMC chains is not based on the absolute value of its χ^2 but on the gradient of the goodness of fit, i.e. the relative goodness of fit compared to some other point the chain may arrive from. The final result is essentially an integral of this value over all possible starting points - but with a substantial weighting towards nearby points due to the Gaussian shape of the model selection function in the Metropolis-Hasting algorithm. This means that the MCMC result does not rely on the goodness of fit being a globally correct representation of likelihood. Given that in a tilted ring model, errors are computed from azimuthal variations in the inferred circular velocity, it is not immediately clear they satisfy the requirements of being independent, Gaussian errors as assumed when χ^2 is used to calculate a statistically robust likelihood. An analysis (such as ours - see Chapter 3) that does not rely on the assumption of Gaussian errors is preferable.

In Chapter 3 we showed that the MCMC method was able to recover the correct halo model from synthetic data with artificially inflated error bars more tightly than would be naively expected. We attribute this not only to the method being less dependent on the actual values of the goodness of fit, but also to the physically reasonable prior assumption of a smooth dark matter density profile. Smoothness is inherent in the $\alpha-\beta-\gamma$ profile for reasonable values of α, but for an even freer prior, smoothness would have to be imposed separately. A non-parametric halo, with a log slope for each data point in the rotation curve, would have to impose a constraint on these values such that together they form a physically realistic density profile.

In Seigar (2011) it is claimed that fitting of the NFW profile to rotation curve bins outside $r = 7\,$kpc is evidence that the this profile "best represents these data". Only the prior assumption of an NFW profile makes the fit to the outer rotation curve relevant to the determination of the inner density profile. Without assuming a strong link between inner and outer data points as a prior, we find that a steeper inner density profile is favoured when using the $\Upsilon_{3.6}$ value used in that paper.

The fact that the NFW profile is able to fit the rotation velocities in previous work does not itself convey the properties of the NFW profile (i.e. a log slope of -1 at $r = 0$) upon the galaxy, given that we have shown there are many profiles with differing properties that also provide good fits. Thus, it cannot be concluded that a low reduced χ^2 value for an NFW fit gives a high posterior probability for specific analytic properties of the NFW profile, e.g. the central $\rho \propto r^{-1}$ cusp. Allowing more freedom in the profile, and fully

exploring the parameter space with MCMC, resolves these issues and provides a more robust description of the dark matter density profile across the entire radial range of the rotation curve data.

The second claim of Seigar (2011) is that the NFW concentration parameter $c_{\rm vir}$ is related to the spiral arm pitch angle P. Taking $c_{\rm vir}$ purely as a density profile parameter without any implications for inner profile slope, correlations between it and other physical parameters are not necessarily in conflict with our conclusions.

5.5.2 $\Upsilon_{3.6} - \gamma_{\rm in}$ Degeneracy

It is clear from our result that there is a substantial degeneracy between the baryonic mass-to-light ratio $\Upsilon_{3.6}$ and the inner log slope $\gamma_{\rm in}$. The scale length of the stellar disk is approximately equal to the radius at which the total rotation curve transitions from rising to flat, so the most obvious cause of the degeneracy is the degree to which the rising part of the stellar contribution to the circular velocity is used to model the rising part of the overall rotation curve. To investigate this, we assume that the degeneracy of the fit near the peak of the disk rotation curve approximates that of the entire rotation curve, and that the inner dark matter halo can be taken to be a single power law (which in our results it can; over 98% of models in A1 have a scale radius outside the data range). We can then represent the degeneracy using

$$v_{\rm max,star}^2 + v_{\rm DM}(R_{\rm max})^2 = \text{constant} \tag{5.3}$$

where $v_{\rm max,star}$ is the maximum velocity contribution of the stellar component and $v_{\rm DM}(R_{\rm max})$ is the velocity contribution of the dark matter halo at that radius. Given that $v_{\rm max,star}^2 \propto \Upsilon_{3.6}$ and $v_{\rm DM}(R_{\rm max})^2 \propto (R_{\rm max}/r_{\rm s})^{2-\gamma_{\rm in}}$ (as $\gamma_{\rm in}$ is assumed to be representative of the log slope at this radius, due to our assumption of a single power law) we can write

$$\Upsilon_{3.6} = a - bc^{2-\gamma_{\rm in}} \tag{5.4}$$

where a, b, and c are constants. This is not meant to imply that the galaxy is well fitted by a single power law; this is merely meant to approximate the dark matter halo density profile well in the region which is most sharply affected by the degeneracy. The curve in $\gamma_{\rm in} - \Upsilon_{3.6}$ space described here is not a physical description, nor a prediction, but is useful as a parameterised, quantitative summary of the degeneracy determined by the MCMC method.

We binned $\gamma_{\rm in}$ values of a subset of models from A1 (34846 models chosen from all

chains with a probability 10^{-5}, ignoring the first 10,000 models for burn-in) to produce a set of 2000 bins with a uniform number of points. We fit the relationship (5.4) to these data and find $a = 2.6$, $b = 6.3$, and $c = 0.089$ as shown in Figure 5.11. The baryonic mass-to-light ratio in the maximal disk case is $\Upsilon_{3.6,\mathrm{max}} = a - bc^2$ and the halo slope in the no disk case is $\gamma_{\mathrm{in,no}} = 2 - (\log a - \log b)/\log c$.

In runs D1 and D2, we tested whether this degeneracy would be changed by having independent $\Upsilon_{3.6}$ values for both stellar components. The scale radius of the inner component is too short to meaningfully contribute to the circular velocity at the radius at which we model the degeneracy between γ_{in} and $\Upsilon_{3.6,\mathrm{outer}}$ above.

5.5.3 Alternate Gas Mass Models

We now consider whether it is possible that the apparently large stellar mass in our cored models could be accounted for by molecular gas. The gas density profile we obtained from Corbelli (2003) included the molecular gas fraction, calculated from CO emission, along with the atomic gas contribution to the rotation curve. The factor used to calculate total molecular gas mass from CO emission, X_{CO}, is estimated based on observations of the Milky Way (Wilson, 1995) and may not be correct for M33. In the mass modelling we use, the stellar disk has a mass $3.8 \times 10^9\, M_\odot$ and the molecular gas disk component has a mass $3 \times 10^8\, M_\odot$, so this would represent an increase in $\Upsilon_{3.6}$ of ~ 0.1. (Note that, following de Blok et al. (2008), we have assumed that the scale length of the molecular gas is that same as that of the stars). To account for the difference between the modelled $\Upsilon_{3.6} = 0.67$ and the $\Upsilon_{3.6} = 2.5$ required for a flat halo would require X_{CO} to be 37 times larger. In Dame et al. (2001) the 1σ relative error for this ratio was found to be less than 0.17 for nearby clouds in the Milky Way and thus a factor 37 increase seems unlikely.

5.5.4 Comparison with cosmological simulations

Given that we have confirmed earlier claims that the halo profile of M33 is steeper than in other galaxies of similar luminosity, it is worth asking whether there is a natural explanation for this difference. In their models of the Local Group Bekki (2008) found that M33 encountered M31 with a periapsis of ~ 100 kpc at 4-8 Gyr before present. Ram pressure stripping of M33 by an outflow from M31 could also have had an impact on the progression of feedback in M33 (e.g. Nayakshin and Wilkinson, 2013). The prompt removal of low density gas by stripping would cause the dark matter halo to relax into a shallow, less concentrated state (as modelled in Gnedin and Zhao, 2002; Read and Gilmore, 2005;

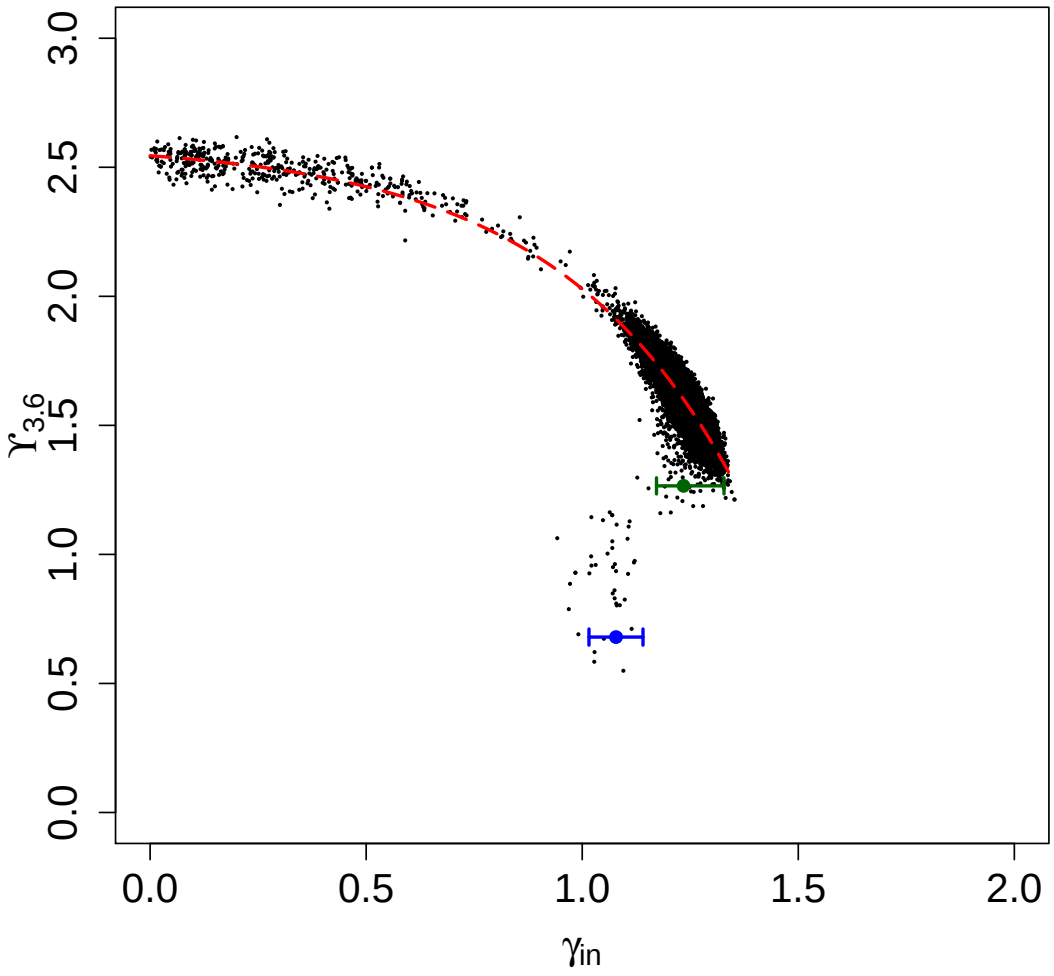

Figure 5.11: Fit to the degeneracy between log slope at the inner most bin ($\gamma_{\rm in}$) and mass-to-light ratio in the Spitzer 3.6μm band ($\Upsilon_{3.6}$). Points are 34846 models chosen from the chain, after burn-in, with a probability 10^{-5}. The line shows the relationship $\Upsilon_{3.6} = 2.6 - 6.3 \times 0.089^{2-\gamma_{\rm in}}$, fitted to 2000 bins, and should not be taken as valid outside the range of the models shown. Green and blue points are constraints on $\gamma_{\rm in}$ found by models B1 and C1 respectively. See text for discussion.

Governato et al., 2010, and Chapter 4), so it might be reasonably assumed that such an event would lead to a cored dark matter halo, but this is not necessarily the case, as we now discuss.

It is reasonable to assume the the process of contraction would mean that after initial baryon infall, but before feedback begins, the dark matter halo would have an inner log slope steeper than $\gamma_{\rm in} = 1$. Feedback models such as Read and Gilmore (2005), Governato et al. (2010), Parry et al. (2011) and Ogiya and Mori (2012) require multiple outflow and inflow events to account for the transition from such steep initial haloes to their flatter inner haloes at later times. If this process were interrupted early on, it could prevent a sufficiently large amount of feedback that, even though the event itself would flatten the halo slightly, it would still retain an inner halo that is steep relative to those of similar galaxies.

5.6 Conclusion

We have modelled the rotation curve of M33 using the MCMC-based approach we presented in Chapter 3. We have quantified and understood the degeneracy between baryonic mass-to-light ratio $\Upsilon_{3.6}$ and the log slope of the dark matter halo at the inner bin $\gamma_{\rm in}$. We cannot resolve the conflict between observations of similar galaxies (Kuzio de Naray et al. (2006) and de Naray et al. (2008)) and the MCMC analysis of the M33 rotation curve without assuming $\Upsilon_{3.6} > 2$, which is difficult to reconcile with stellar population modelling. We find that with a lower fixed $\Upsilon_{3.6} = 0.67$, an NFW halo is compatible with the data, but that this part of parameter space is not strongly favoured when we relax the constraint on $\Upsilon_{3.6}$. We strongly exclude the combination of $\Upsilon_{3.6} < 2$ and a halo profile inner log slope $\gamma_{\rm in} < 0.9$, for a comprehensive range of assumptions.

The constraints we find on $\Upsilon_{3.6}$ and $\gamma_{\rm in}$ admit at least the four following scenarios:

1. there is a great deal more mass in the disk of M33 than is accounted for by standard modelling of stellar populations and molecular gas clouds.

2. the halo of M33 deviates significantly from spherical symmetry, being flattened at small disk radius and less so in the outer part of the galaxy.

3. feedback cannot produce a core in a galaxy with the stellar mass of M33. Di Cintio et al. (2013) make this point but their conclusion depends on the specific feedback physics used in that paper, and only accounts for supernova and early stellar feed-

back. It also predicts a shallower ($\gamma_{\rm in} \simeq 0.75$) inner density profile for a galaxy with the range of stellar masses we calculate.

4. the dark matter halo has a much steeper inner profile than would be expected from hydrodynamical simulations of galaxy formation (e.g. Governato et al., 2010; Maccio et al., 2011). This could occur if M33 were dominated by the process of contraction. The above simulations show both contraction of the halo steepening the inner profile, and feedback flattening it. In the absence of any obvious source of significant additional disk mass, and assuming no fundamental error in the view of baryon-dark matter interaction in galaxy formation, we propose that the history of the dark matter halo in M33 is dominated by contraction. Ram pressure stripping by M31 before feedback flattening the halo is a possible physical mechanism by which this could have happened.

The first scenario is inconsistent with the stellar mass modelling of Corbelli et al. (2014). We will investigate the remaining three possibilities by applying our modelling scheme to cosmological simulations in a future work.

6

Extending MCMC to disk modelling

As kinematic data from external galaxies improves, it is important to develop a more accurate idea of what these data can meaningfully constrain. It is important to know, for instance, how accurately rotation curve studies can constrain the shape of the dark matter halo, or the amount of feedback involved in the formation of the galaxy. Feedback can be modelled in simulations, but in order to test this against observations it is necessary to know how an observed galaxy (for which we have two spatial dimensions and one velocity) would look in the full 6D phase space of the simulation. It is far easier to determine what a simulated galaxy would look like were it observed, and Bayesian methods provide a means to constrain the former based purely on the knowledge of the latter.

In studies of rotation curves (e.g. de Blok et al. (2008)), the azimuthal velocity v_ϕ is calculated around a series of rings, by modelling the inclination at each radial bin with the tilted ring method. It is assumed that the circular velocity $v_c = \overline{v_\phi}$, the average azimuthal velocity, and the errors are assumed to be the difference in $\overline{v_\phi}$ between the approaching and receding sides of the galaxy. Mass models are then compared to this velocity model through χ^2 minimisation. The conclusions of such studies thus depend on the validity of the prior assumptions of the tilted ring approach and the mass model. The MCMC process described in previous chapters addresses the problems with the comparison of models, by weakening the dependence of the result on the absolute (rather than relative) correctness of the errors.

Velocity fields are available for both stars (from infrared observations e.g. Croom et al., 2012) and neutral gas (from HI observations e.g. Walter et al., 2008). The velocities in the former are subject to asymmetric drift, where the peak in the distribution of v_ϕ lags that of the circular velocity v_c. This is not seen in gas disks, as the orbits required to create the effect would cross and thus would be altered by collisions much more so than near-circular orbits.

This chapter describes a new method of producing rotation curves from simulated galaxies, an examination of systematic errors that arise, and uses N-body models to determine the extent to which properties of the galaxy can be constrained by rotation curves. This follows on from Chapter 2, which used simpler rotation curves derived from analytic potentials rather than N-body simulations. This chapter is also a demonstration of the MCMC code introduced in Chapter 1, `RainfallMCMC`, applied to an astrophysical problem.

6.1 Method

The objective here is to convert the velocity field of a simulated galaxy into a rotation curve using MCMC, and then from that rotation curve attempt to retrieve the properties of the dark matter halo via the method described in Chapter 2. This produces a mapping between the dark matter halo properties in the "observed" galaxy, and those that can be inferred from the rotation curve.

In order to obtain the rotation curve, a disk model is constructed from a series of concentric rings, each with a normal vector which defines the expected orientation of angular momentum at each radius. The parameter space is explored using `RainfallMCMC` in serial mode, evaluating the square of the total azimuthal velocity $(\sum v_\phi)^2 = (\sum_\mathrm{i} j_\mathrm{i}/R_\mathrm{i})^2$, for each ring, where j_i is the angular momentum of particle i projected onto the unit normal of the ring. The likelihood estimate is the sum of these values across all rings. Each chain consists of 50,000 models selected through the Metropolis-Hasting algorithm (Hastings, 1970).

To determine realistic errors in v_ϕ, consistent with those calculated using tilted ring methods such as in de Blok et al. (2008), a seperate $\overline{v_\phi}$ is calculated for two sides of the disk and the difference between the two values is taken to be twice the Gaussian error.

`CosmoMC` is then used to recover the dark matter halo properties, in order to make for a consistent comparison with results from Chapters 2-4.

6.1.1 Disks

A purely rotationally supported, infinitely thin disk of matter can be represented by angular momentum as a function of radius $\mathbf{J}(R)$, which can be discretised into a set of values $\mathbf{J}_\mathrm{n}$ for a set of m rings. The stars and gas of a disk galaxy will show both random deviations from this (i.e. dispersion) and systematic deviations from this (e.g. due to asymmetric drift). The following algorithm can be used to find a set of parameters for the rings:

1. Start with the centre of rotation set at the centre of mass of all particles, and a non-warped disk with angular momentum in the direction of the total angular momentum vector of all disk star particles;

2. Propose a new set of disk parameters, which generates an angular momentum unit vector $\hat{J}_\mathrm{n}$ at each radial bin (see below);

3. Calculate the rotation velocity in each radial bin;

4. Iterate over steps 2 and 3 using MCMC, minimising a fitness statistic.

The parameters of the disk are $\mathbf{x}$, $\mathbf{J_0}$, and $\mathbf{J}_{\rm max}$. These describe the origin of a cylindrical coordinate system, $\mathbf{x}$, the angular momentum vector as $R \rightarrow 0$, $\mathbf{J_0}$, and a second angular momentum vector relative to the first, $\mathbf{J}_{\rm max}$, that the disk assumes at the outermost radial bin. Both J vectors are unit vectors parameterised as (θ, ϕ), relative to the coordinate system of the stars for $\mathbf{J_0}$ and to $\mathbf{J_0}$ for $\mathbf{J}_{\rm max}$. In all cases here R is the projected radius in the plane of each ring.

Here the function describing the transition from $\mathbf{J_0}$, and $\mathbf{J}_{\rm max}$ is simply linear, although more complex functions could be used. The angular momentum vector at any radius relative to $\mathbf{J_0}$ is $(\theta R/R_{\rm max}, \phi R/R_{\rm max})$ where θ and ϕ are the spherical coordinates of $\mathbf{J}_{\rm max}$. In cartesian coordinates defined by the basis vectors $\hat{\mathbf{x}}$, $\hat{\mathbf{y}}$ and $\mathbf{J_0}$ this is

$$J(R) = \hat{\mathbf{x}} sin\left[\theta(R)\right] cos\left[\phi(R)\right] + \hat{\mathbf{y}} sin\left[\theta(R)\right] sin\left[\phi(R)\right] + \hat{\mathbf{J}}_{\mathbf{0}} cos\left[\theta(R)\right] \tag{6.1}$$

Coordinates in the plane of each ring are described with basis vectors $\hat{\mathbf{x}}$ and $\hat{\mathbf{y}}$ that are calculated using

$$\hat{\mathbf{x}} = \hat{\mathbf{J}}_{\mathbf{0}} \wedge \hat{\mathbf{A}} \tag{6.2}$$

and

$$\hat{\mathbf{y}} = \hat{\mathbf{J}}_{\mathbf{0}} \wedge \hat{\mathbf{x}} \tag{6.3}$$

where $\hat{\mathbf{A}} = (cos(\phi + \pi/2), sin(\phi + \pi/2), 0)$ in cartesian coordinates[1]. The direction of $\hat{\mathbf{A}}$ maintains a continuous coordinate system throughout the parameter space and avoids aligning closely with $\hat{\mathbf{J}}_{\mathbf{0}}$.

6.1.2 Likelihood estimates

One method to assess the likelihood of a particular $\mathbf{J}$ vector representing a disk is the fraction of kinetic energy that is in ordered rotation about the z axis, defined in Sales et al. (2012) as

$$\kappa_{\rm rot} = \frac{1}{K} \sum_{\rm i} \frac{1}{2} m_{\rm i} \left(\frac{j_{\rm z,i}}{r_{\rm i}} \right)^2 \tag{6.4}$$

[1]This particular vector is one of many that could work here. The only requirement of $\hat{\mathbf{A}}$ is that it never be parallel with $\hat{\mathbf{J}}_{\mathbf{0}}$.

Where K is the total kinetic energy of all particles, and m_i, r_i and $j_\mathrm{z,i}$ are the mass, radius and angular momentum of the ith particle. This chapter uses the squared average azimuthal velocity in each bin that contains particles. The azimuthal velocity v_ϕ for each particle is calculated using

$$v_\mathrm{rot,i} = (\hat{\mathbf{J}}_\mathrm{n}.(\mathbf{r}_\mathrm{i} \wedge \mathbf{v}_\mathrm{i}))/R_\mathrm{i} \tag{6.5}$$

where $\hat{\mathbf{J}}_\mathrm{n} = \mathbf{J}_\mathrm{n}/|\mathbf{J}_\mathrm{n}|$ is the unit vector representing the proposed disk angular momentum in the bin, $\mathbf{r}_\mathrm{i}$ and $\mathbf{v}_\mathrm{i}$ are the position and velocity of the particle, and R_i is the radius projected onto the plane of the ring. In cases where similar numbers of particles are found in each bin (which is to be expected once the centre of rotation is located) then our likelihood function $\sum_\mathrm{n}(\sum_\mathrm{i} v_\mathrm{rot,i,n})^2$ will give the same likelihood ratio between models as comparing κ_rot would.

6.1.3 Asymmetric drift

In real galaxies, the azimuthal velocity distribution $f(v_\phi)$ of stars has a peak which lags the circular velocity v_c. This is due to the fact that stars on non-circular orbits spend more time near apoapsis than near periapsis, and the fact that the density of stars decreases with radius so there is a larger population of stars currently at a specific radius R whose orbits lie mainly inside R (and thus are moving at $< v_\mathrm{c}$) than there are with orbits mainly lying outside R. The formula for the difference in velocity peak v_a (as derived in Binney and Tremaine, 2008, §4.8.2) is

$$v_\mathrm{a} \simeq \frac{\overline{v_\mathrm{R}^2}}{2v_\mathrm{c}} g(R, \nu, \sigma_\mathrm{ij}^2) \tag{6.6}$$

where g is a function of the radius R, the density distribution ν, and velocity dispersion tensor σ_ij^2. I assume, due to the symmetrical starting conditions of the galaxy models, this will be the main source of systemic error, and will test to see if it makes an impact on the ability to determine dark matter halo shape.

6.2 Models

A summary of the models used are shown in Table 1.

Name	Particles	Total Mass
Simple Halo	10,000	$10^5 M_\odot$
Simple Disk	10,000	$10^5 M_\odot$
Realistic Disk + Core	1,440,000	$5.6 \times 10^{11} M_\odot$
Realistic Disk + Cusp	1,440,000	$5.6 \times 10^{11} M_\odot$

Table 6.1: Properties of galaxy models used in this chapter

6.2.1 Simple models

The first models represent a rotationally supported galaxy and one supported by random motion, although neither involved any attempt at dynamic self consistency and both feature star particles only. The latter model has particles distributed on each axis according to a Gaussian with width $\sigma = 10\,kpc$ and velocities equal to $v_n = -Ax_n$ where $A = 1\,\mathrm{kms}^{-1}\mathrm{kpc}^{-1}$ (the aim here is not to give a realistic velocity structure, merely one with small magnitude velocities and no net angular momentum). The former has a thinner Gaussian width $\sigma_z = 1\mathrm{kpc}$ in the vertical axis, and has rotational motion around that axis with a magnitude of $|v| = 100\,\mathrm{kms}^{-1} arctan(R/10\,\mathrm{kpc})$ - which is a simple way to provide the approximate shape of a rotation curvre. Vertical velocity is calculated as in the randomly supported galaxy. In order to check that the algorithm does not depend on the galaxy being aligned with the coordinate system, I repeated the disk case rotated by 30, 60 and 90 degrees relative to the (x,y) plane.

These galaxies are not realistic beyond gross morphology, but provide very clear examples of rotating and non-rotating ensembles of particles for use in a first order test of the algorithm.

6.2.2 N-body rotation

Next are four galaxies provided by Mark Wilkinson, that feature combinations of thin and thick disks and cored and cusped dark matter haloes. These galaxies have been generated with the `mkgalaxy` program (McMillan and Dehnen, 2007), and are generated from initial conditions featuring an exponential stellar disk of mass $M_d = 5 \times 10^{10}\,M_\odot$, scale length $R_d = 2.5\,kpc$, and $sech^2$ vertical profile with scale height $z_s = 125\,pc$. The dark matter halo has mass $M_h = 5 \times 10^{11}\,M_\odot$ and scale radius $r_s = 15\,kpc$. It follows an $\alpha - \beta - \gamma$ profile, with parameters (1, 4, 0.2) in the cored profile case and parameters (1, 4, 1) in the cusped case i.e. a Hernquist profile.

These models feature more realistic stellar dynamics; most importantly they include asymmetric drift, because the particles in these galaxies are evolved from their initial

positions and velocities through an N-body simulation prior to use. It is important to know if the systemic bias introduced by this makes it impossible to distinguish between the cusped and cored dark matter haloes.

6.3 Results

Figure 6.1 shows the distribution of θ_0 the θ component of $\mathbf{J_0}$, as expressed in spherical coordinates. This demonstrates that the algorithm can detect a rotating structure, and does not falsely detect one when it is not present. As rotation direction is not relevant, θ_0 only covers half the normal range in order to avoid a bimodal distribution, and the fact that it does not go to zero at $\theta_0 = 0$ and $\theta_0 = \pi/2$ is not an issue because all the angular parameters have a periodic boundary.

In Figure 6.2 the simplified disk galaxy is rotated relative to the coordinate system. This is an important test if the method is to be applied autonomously to generate rotation curves from simulated galaxies, as they cannot be assumed to be coaxial with the chosen spherical coordinates. Towards $\theta_0 = 0$, the other spherical coordinate ϕ_0 ceases to alter the orientation of the disk, which creates a volume effect (as described in Chapter 1) that adds noise to the distribution by biasing the chain towards lower likelihood models in this part of parameter space. To remove this noise and highlight the peaks, only the most likely 10% of models are shown in Figures 6.1 and 6.2. These plots show that the algorithm is able to detect the axis of the disk when it is not aligned with the coordinate system of the particles.

Figure 6.3 shows the circular speed implied by the particles in bins of width 200 pc, given the most likely configuration of disk parameters, compared to one calculated from the simulation directly. In order to find this curve, the potential was calculated at a ring of points for each bin, and then the circular speed worked out from $v_c^2 = R(\partial\phi/\partial R)$. The errors used here are the difference in $\overline{v_\phi}$ between the two sides of the galaxy, in order to provide a comparison with observed rotation curves. Fitting a disk to the simulated galaxies produces a systematic deficit in velocity compared to the actual circular velocity curve (as calculated above) which is due to asymmetric drift. If the curve were displaced in the v_c axis it could match closely to the curve corresponding to the cored density profile (solid curve), but the errors are large enough to encompass both cored and cusped profiles (although as previous chapters have shown, this may not necessarily be a barrier to differentiating between them).

6.3.1 MCMC processing of rotation curves

The method described in Chapter 2 was applied to the rotation curves produced above, proposing an exponential disk with a scale length fixed at the value given in the initial conditions of the galaxies, but no prior on mass-to-light ratio. For the cored galaxy (Figure 6.4), there is a constraint on r_1, the radius at which the log slope of the dark matter halo profile reaches -1. There is a slight degeneracy with the mass-to-light ratio Υ (relative to the stellar mass profile found in the simulation), which is to be expected as a larger stellar contribution means a shallower dark matter halo profile is required. However the shape of this degeneracy does not favour the combination of $\Upsilon = 1$ with the value for r_1 calculated from the initial conditions of the galaxy simulation (4 kpc). This value of r_1 may not be the correct answer in the evolved simulation which is being studied here, as the N-body process may have altered the shape of the halo.

Correcting v_c for the asymmetric drift moves the peak into regions of higher r_1 and Υ, favouring a maximal stellar contribution in the inner components and thus a larger dark matter core. The most favoured part of parameter space is represented by the rotation curve shown in Figure 6.5.

In the case of the cusped halo the MCMC algorithm is unable to converge on the presumed correct model, as shown by the relation of the log slope at the inner most data point, γ_{in} with Υ in Figure 6.6. The MCMC does favour cusped models, but skips between several small peaks. This is due to the very small size of the errors, smaller than those in the cored model - the model is unable to match all the data, and the small error bars strongly exclude models that miss data points. Correcting for asymmetric drift leads to a maximal disk being strongly favoured, with a more cored halo.

Fixing the mass-to-light ratio at the input value (i.e. making the stellar contribution equal to the one inferred from force summation in the simulation) leads the corrected model back towards cusped haloes, as shown in Figure 6.7, although the MCMC still does not converge on a single peak. However, when the mass-to-light ratio is fixed for the non-corrected halo, a constraint emerges. This seems to indicate that some of the assumptions used to construct the ideal mass model may be incorrect.

Examining the axis ratios of the simulated haloes shows that the cusped one is significantly more oblate in the inner regions (Figure 6.8. This means the correct halo profile is different from the one based on the assumption of spherical symmetry.

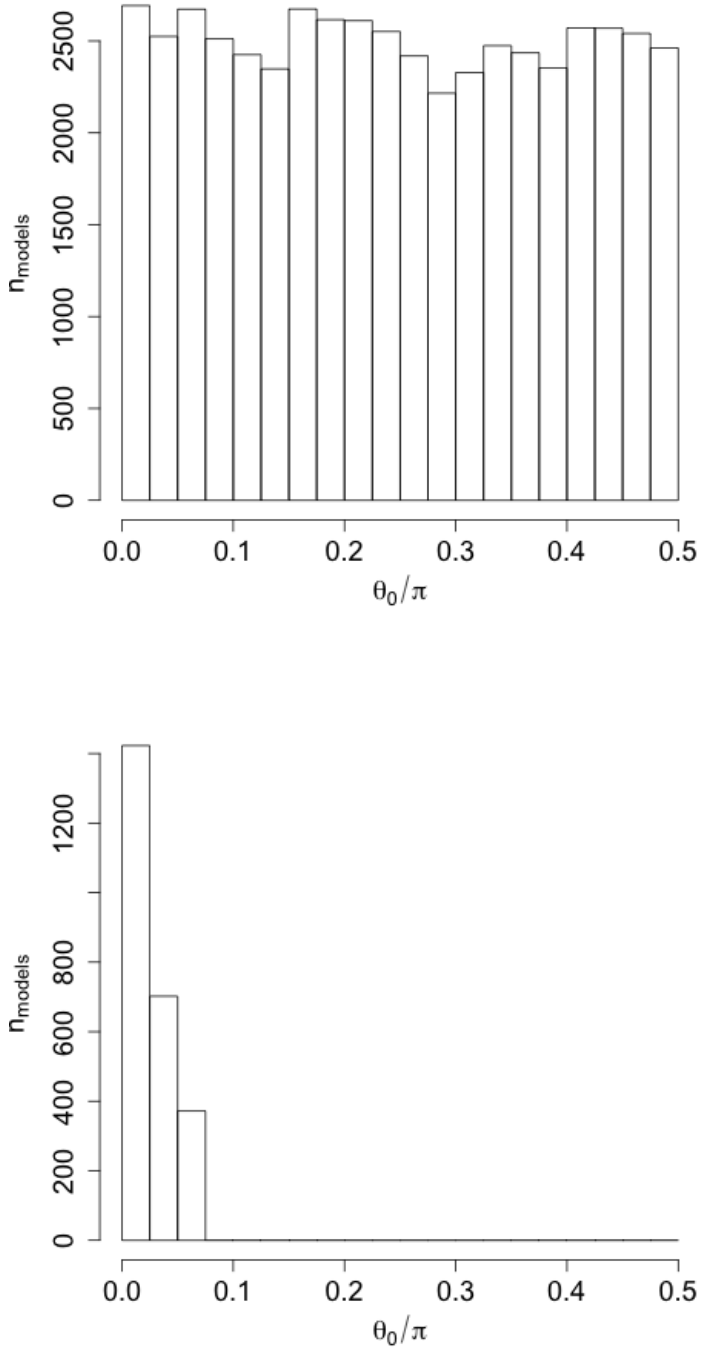

Figure 6.1: Comparison of θ_0 values for the first two models in Table 1. **Top** the halo model, with no rotational motion, showing only a uniform distribution in θ_0. and **bottom** the disk model, with only rotation in the x-y plane, showing a tight constraint. The axis is given as a fraction of π. Only models in the top decile of likelihood are included.

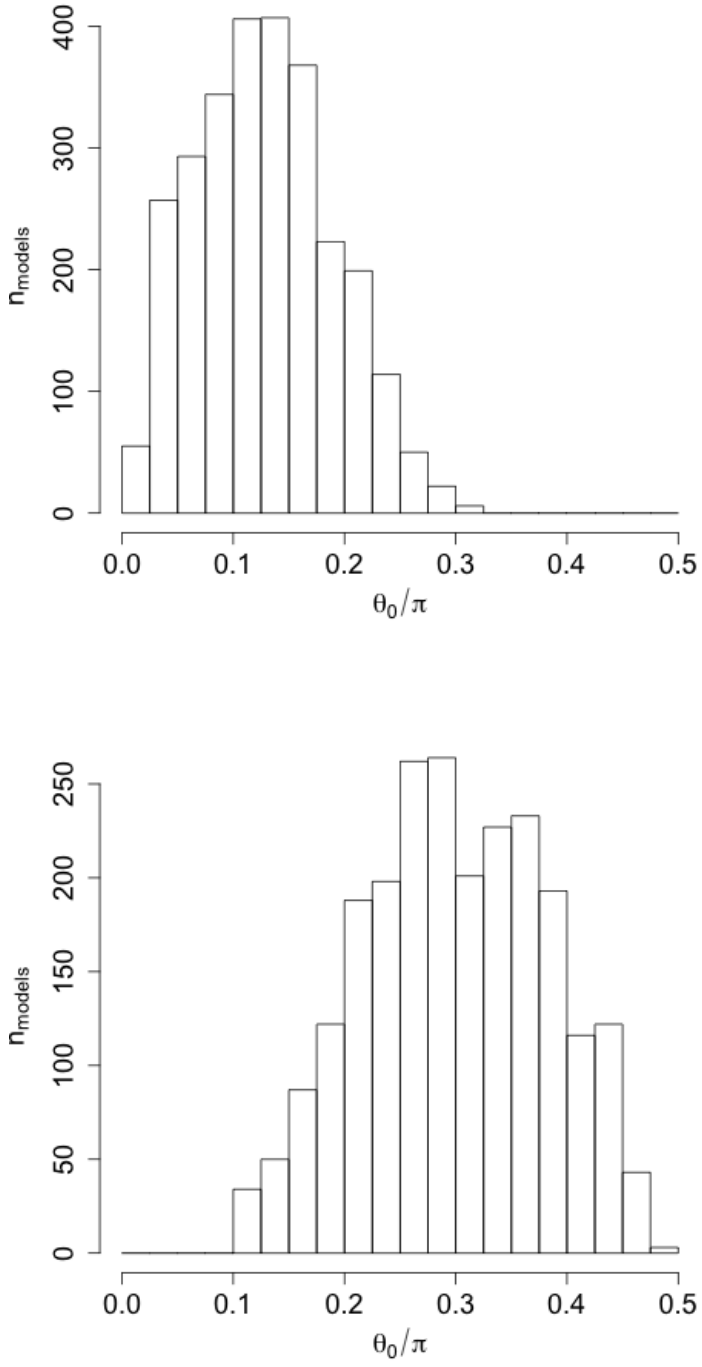

Figure 6.2: The result for the disk model shown in Figure 6.1, but rotated 30 degrees (**top**) and 60 degrees (**bottom**) clockwise in the x, z plane.

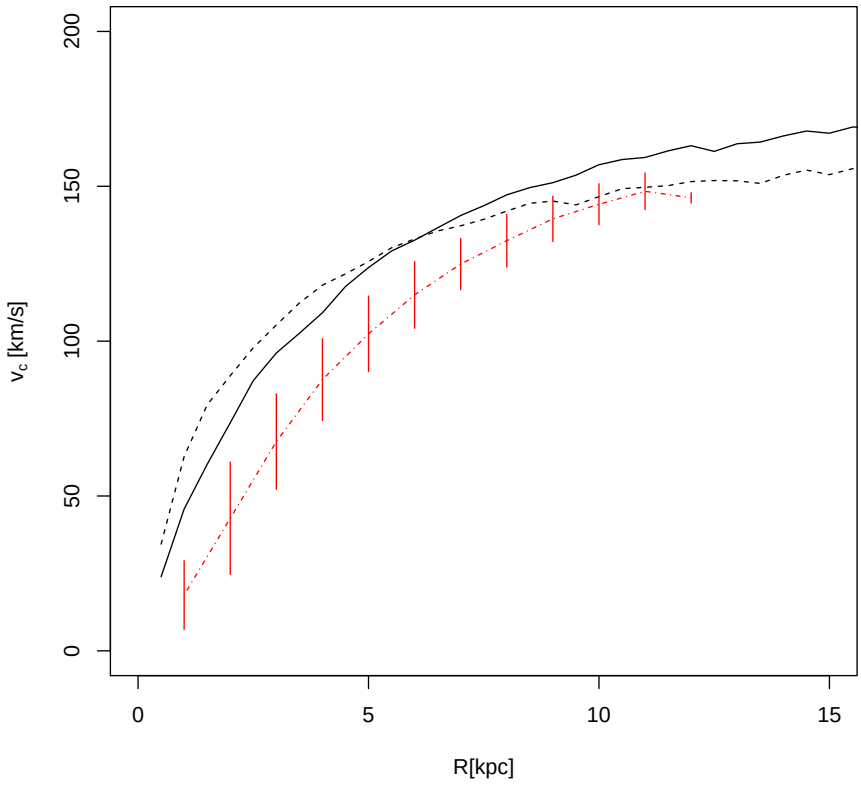

Figure 6.3: Comparison of the rotation curves derived through disk fitting of a realistic stellar disk with a cored halo. Solid line is the actual circular velocity in the case of a cored halo profile and dashed line in the case of a cusped halo profile. The red dotted line connects the points of the rotation curve determined by the MCMC process.

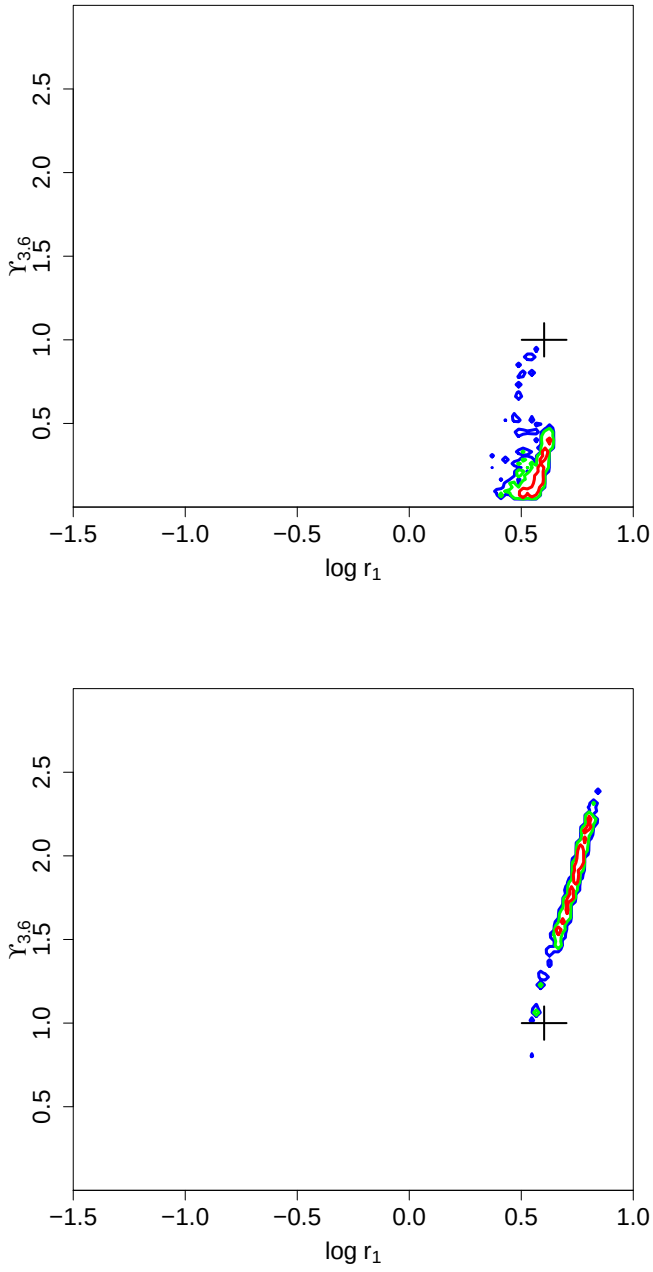

Figure 6.4: The relationship between r_1 (the radius at which the log slope of the dark matter halo profile is equal to -1) and the mass-to-light ratio, Υ. The red contour encloses 68% of models, the green contour 95% and the blue contour 99%. **Top** shows the result using the output of the MCMC chains and **bottom** shows the result corrected for asymmetric drift. The cross shows the parameter combination inferred from the initial conditions of the galaxy.

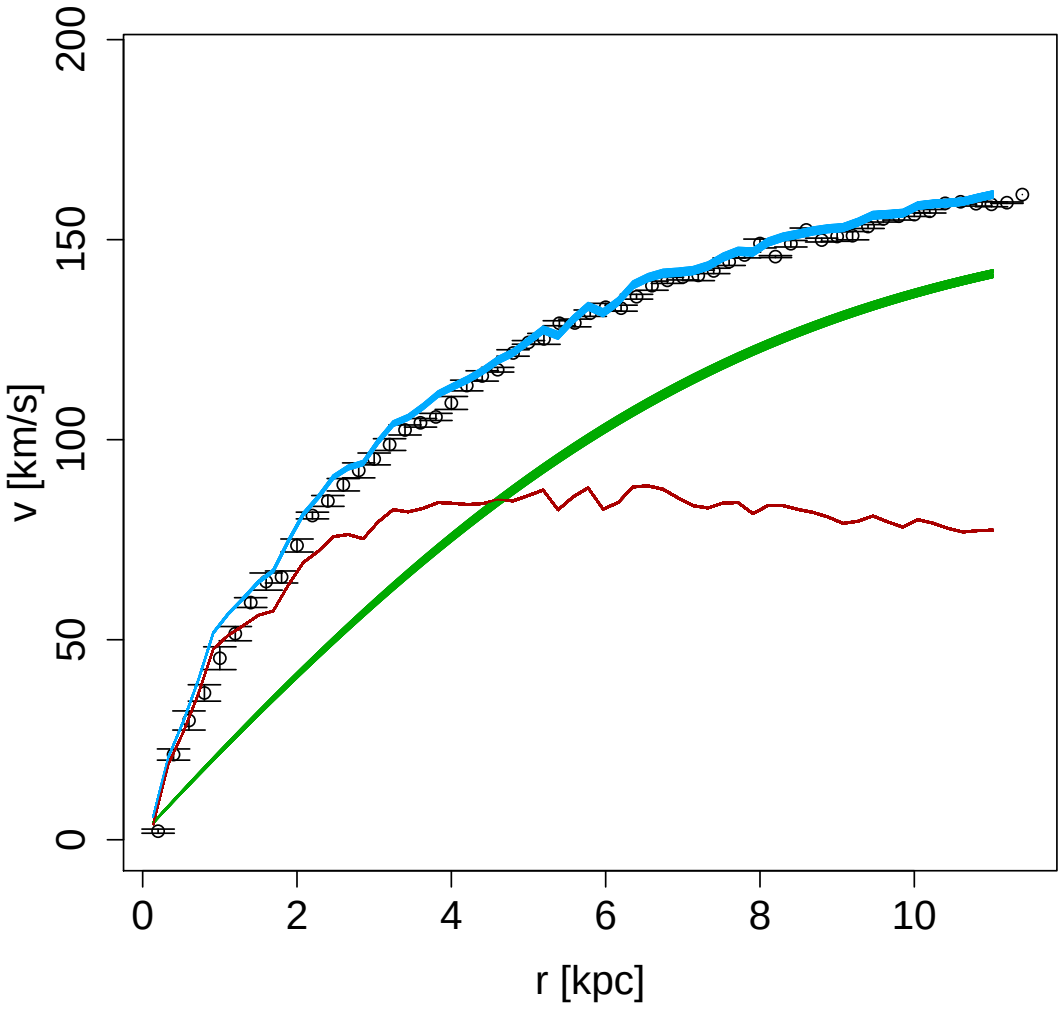

Figure 6.5: The rotation curve corresponding the the most populated bin in the parameter space of the cored model, using data corrected for asymmetric drift. The red line is the stellar contribution to the rotation curve, the green line the dark matter contribution, the light blue line the proposed rotation curve and the black points are the data derived from force summation in the simulation. Errors are derived from the MCMC process

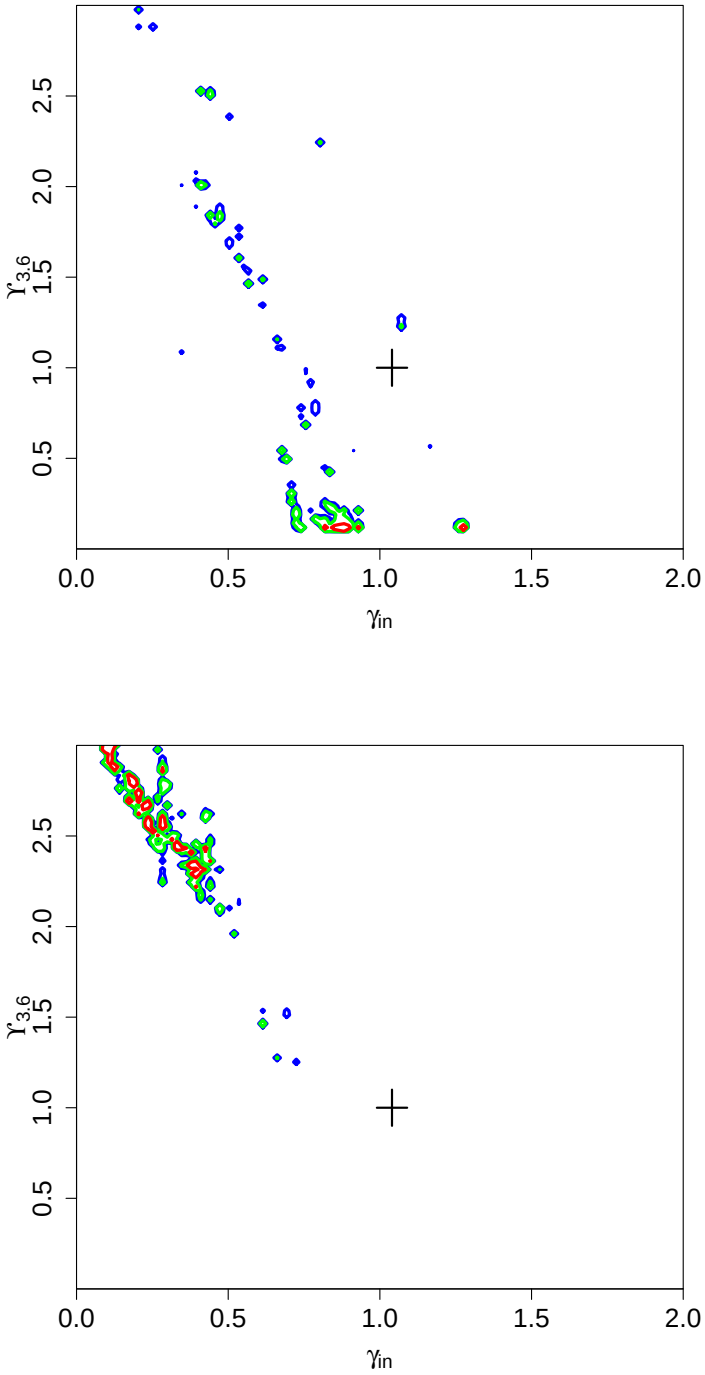

Figure 6.6: The relationship between γ_{in} (the negative log slope at the innermost data point) and the mass-to-light ratio, Υ, for the cusped model. The red contour encloses 68% of models, the green contour 95% and the blue contour 99%. **Top** shows the result using the output of the MCMC chains and **bottom** shows the result corrected for asymmetric drift.

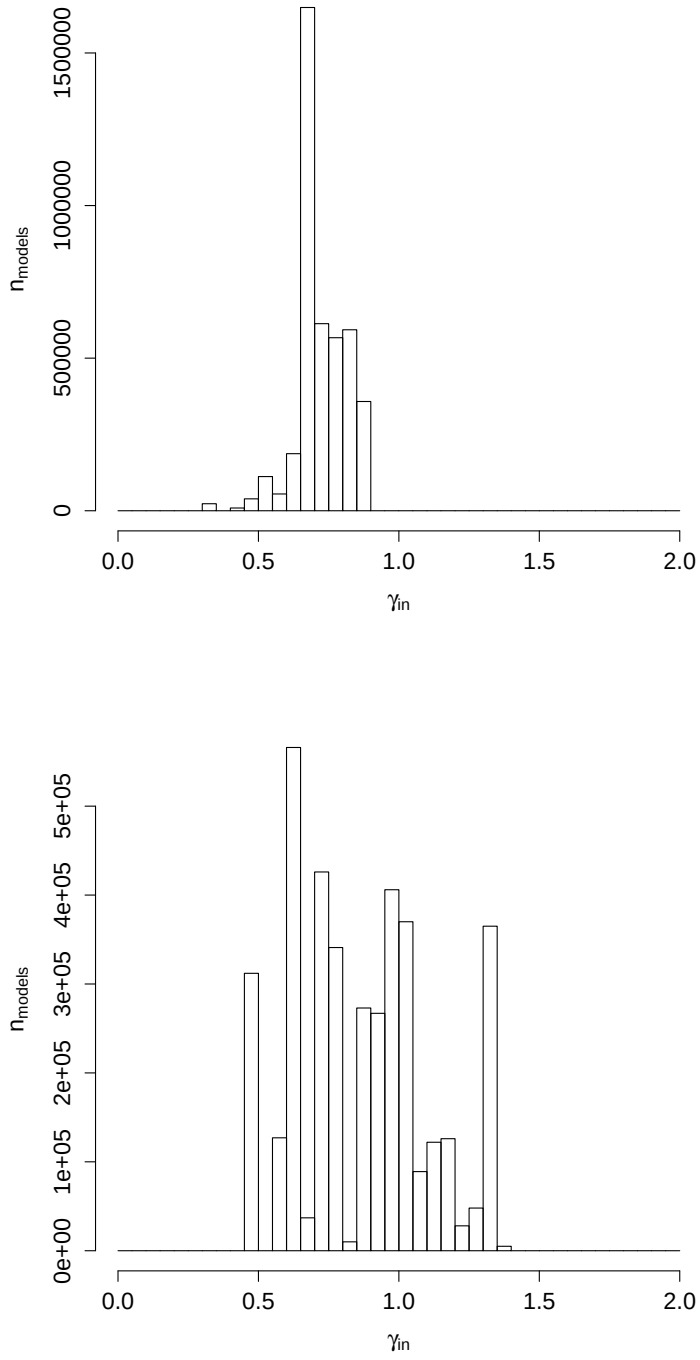

Figure 6.7: The distribution of $\gamma_{\rm in}$ values for the cusped galaxy, **top** uncorrected and **bottom** corrected for asymmetric drift, with a Υ value fixed at 1

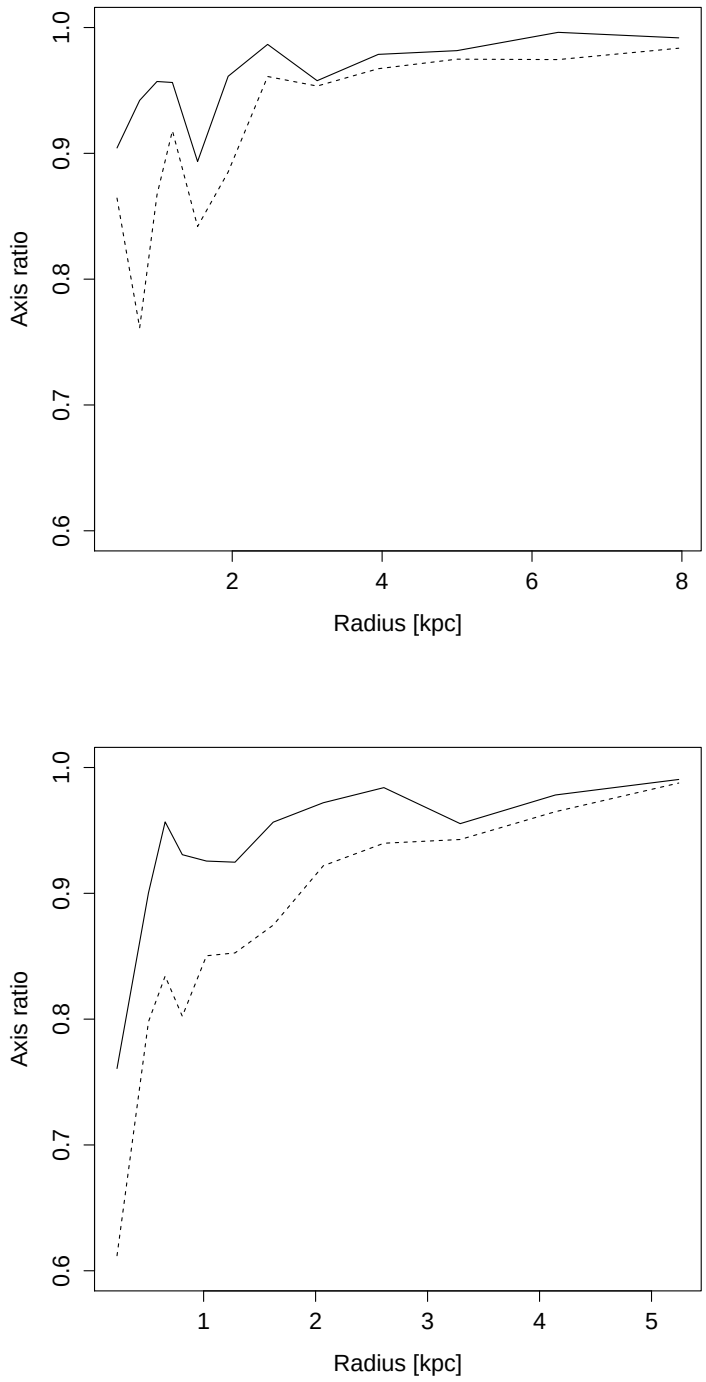

Figure 6.8: The axis ratios b/a (solid line) and c/a (dashed line) where a is the major axis length and c is the minor axis length. **Top** is the cored halo and **bottom** the cusped halo model.

6.4 Discussion

This chapter has established that:

1. `RainfallMCMC` evaluating the likelihood estimator shown here can find disks from particle data, and the parameterisation of the disk has no obvious problems. This has applications not only in producing rotation curves for further analysis, but also in extracting bulk rotation properties from simulated galaxies. As the code is able to locate the axis of rotation accurately without human supervision, it is suitable for large batch processes. Further testing is required in order to measure the ability to capture more complex disks that are asymmetric or warped, and MCMC is likely to best approach to do this due to its ability to handle many dimensions.

2. The inferred rotation curves are compatible with the actual matter content of the simulated galaxies. Although asymmetric drift appears to be present in the models (as will be the case for observed stellar rotation curves), it does not automatically preclude measuring the shape of the dark matter halo. Cores and Cusps can be discerned through this method. The single incorrect answer for the cusped case can be corrected for by using a narrower prior on the mass-to-light ratio, which should be possible through stellar population modelling.

3. As the poor convergence of some of the outputs shows, the χ^2 statistic is not always an ideal likelihood estimator for use with MCMC. Such an effect is a failure mode of the χ^2 statistic, which whilst useful as a broad estimate of which are "good" and "bad" models can distort the parameter space by undue favouring of outliers with small error bars. As this produces a clear fragmentation of the peak in parameter space, there is no chance of such a failure mode going unnoticed, and it can be confidently stated is has not impacted the results of previous chapters.

7

Conclusion

In this thesis I have shown that Markov Chain Monte Carlo (MCMC) is a powerful method for exploring the complex parameter spaces involved in modelling the rotation of disk galaxies. I have derived more useful information from existing data sources than has previously been possible using more simple profile fitting techniques. The ability to place better constraints on galaxy properties has permitted me to begin investigating how these properties relate to the histories and formation scenarios of galaxies. By extending the MCMC process to the initial extraction of circular velocities from observed velocity fields, and being able to apply this to synthetic observations produced by the latest hydrodynamic simulations, there is great scope to advance this field further with the methods described here.

7.1 Chapter 3

Extensive testing of the MCMC technique on rotation curves showed that, contrary to χ^2 minimisation, MCMC is robust against over-estimated errors. In this chapter I established the derived parameter $\gamma_{\rm in}$, the negative log slope at the inner data point, as a more physically meaningful estimate of inner profile shape than γ, the asymptotic log slope in the $\alpha - \beta - \gamma$ profile.

The test galaxy here, DDO 154, showed an inner log slope $-\gamma_{\rm in} = -0.39 \pm 0.11$. This is compatible with previous estimates using the same data but, I argue, a more robust estimate due to the strength of the method.

7.2 Chapter 4

A survey of selected THINGS galaxies further demonstrated the utility of the MCMC on real observations. Another derived parameter is introduced here - r_1, the radius at which the log slope of the halo reaches -1. Inside this radius, the halo cannot be described by an NFW profile, so this provides an estimate of the length scale over which baryonic physics must be able to impact the dark halo for it to be responsible for its shape differing from that which would be produced purely by non-baryonic physics.

This chapter also links this radius to the fraction of gas $f_{\rm g}$ that must be ejected in order to produce the inferred halo from an NFW halo that encloses the same mass at the outer data point. This calculation is subject to a number of simplifications, and the sample of galaxies is too small to draw any firm conclusions, but suggest a link between observational constraints and formation scenarios.

7.3 Chapter 5

This chapter modelled M33 in detail using the MCMC method, and was able to map the degeneracy between inner log slope $\gamma_{\rm in}$ and mass-to-light ratio $\Upsilon_{3.6}$. Comparison with previous results was able to reproduce their log slopes when the same mass-to-light prior was assumed. We found that it appears to either have a steeper halo than has been anticipated by previous hydrodynamical modals is required, or a high ($\Upsilon_{3.6} > 2$) mass-to-light ratio.

Possible explanations for this are that the mass modelling of M33 greatly underestimates the amount of baryons in the galaxy, that the halo of M33 deviates significantly from spherical symmetry, or that the process of feedback in M33 did not occur in the manner modelled in hydrodynamic simulations - possibly due to interaction with M31.

7.4 Chapter 6

Here I added a new step to the MCMC process by marginalising over the parameter space of a disk model, applied to a simulated galaxy. The rotation curves were then run through the same MCMC code as used in previous chapters. Although the weaknesses of the χ^2 statistic as a likelihood estimator for rotation curves became more problematic here, I was still able to differentiate between cusps and cores, even if disks were not aligned to the coordinate system or were subject to asymmetric drift.

This is useful from the perspective both of being able to study the rotation curves of simulated galaxies, but also from the future application to the tilted ring modelling of observed galaxies. A standard method of going from the best available data (6D particle data for simulations and velocity fields for real galaxies) to constraints on dark matter halo parameters is a vital tool for comparative study between the two.

7.5 Future work

There is a glut of new kinematic surveys of external galaxies in the coming years; the continued development of new analytic techniques is vital to making the most of these new data. My near term goal is to investigate mapping between hydrodynamic models and observed galaxies. To this end I am working with the EAGLE team (Schaye et al., 2014) to apply these techniques to the simulated galaxies.

In order to further investigate the constraint that can be placed on formation scenarios

using properties of the currently observed dark matter density profile, I intend to apply the MCMC method above to artificial galaxies produced in cosmological simulations that include baryon physics. This will allow a study of the mapping of formation scenario to current observables such as r_1. I am currently studying the outputs of simulations in Governato et al. (2010) (kindly provided by the authors) in order to put this into practice.

Reyes et al. (2011) presented a survey of 189 disk galaxies from SDSS, calculating rotation curves for each from Hα emission. I intend to use these rotation curves (and future surveys) to constrain relations between dark matter haloes and the baryonic components of disk galaxies using MCMC. Rather than fitting individual curves, I will fit the entire survey simultaneously using a halo density profile whose parameters are functions of observed properties of the galaxy. The constraints found in this way should constrain galaxy formation simulations.

MCMC is becoming a more popular technique in the analysis of rotation curves and other dynamical models. However, radial density profiles have numerous problems that are seldom addressed in the literature, and require careful mitigation when used in an MCMC method. Generally scale densities and scale radii are degenerate, which we mitigated in Chapter 2 by substituting ρ_s for v_{max}. NFW, Burkert, Hernquist and psuedo-isothermal haloes all impose an artificial relation between the log slope in the inner radial bins of the galaxy and the outermost ones, making them useless for unbiased resolution of the cusp-core problem. Einasto profiles cannot model cored haloes at all (see the best fits of NGC925 in Chemin et al., 2011). The $\alpha - \beta - \gamma$ halo is the best profile of these to use in an MCMC scenario. However, there is little physical basis for its use other than that its parameter space comfortably encloses all physically motivated parameters, so in future a non-parametric approach, constrained only by monotonically steepening log slope, should be used to provide the most general prior.

Rotation curves are also built from a number of assumptions, notably for the tilted ring model the assumption that circular motion corresponds to the peak line-of-sight velocity. This can potentially raise questions about the conclusions that it is possible to draw from their analysis - or at the very least restrict the range of galaxies that can be analysed at all. I therefore intend to move from applying MCMC to derived rotation curves to directly modelling galaxies in the data space i.e. the velocity fields.

A

Removing degeneracy from the $\alpha - \beta - \gamma$ model

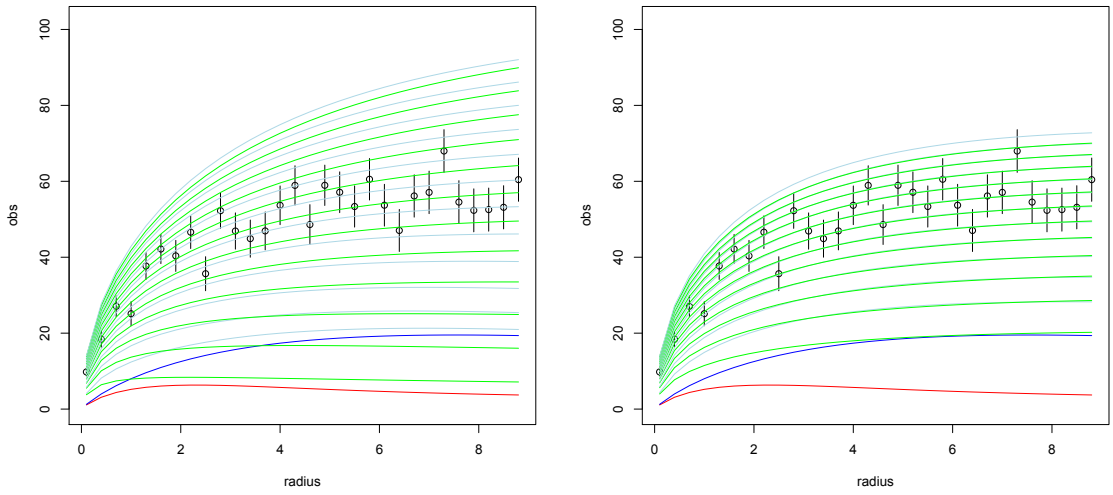

Figure A.1: Comparison of the rotation curves obtained from a family of NFW profiles, illustrating the effect of varying r_s (left panel) and ρ_s (right panel). In each panel, the red line is the stellar contribution to the rotation curve, the blue line is the gas contribution, and the green line is the dark matter halo (with the corresponding total rotation curve shown in light grey). In the upper panel, r_s varies from 1 kpc (lowest curve) to 12 kpc (highest curve) in steps of 1 kpc while in the lower panel ρ_s varies from $10^6\,M_\odot\,kpc^{-3}$ to $1.2\times10^7\,M_\odot\,kpc^{-3}$ (highest curve). In the upper panel, $\rho_s = 6\times10^6\,M_\odot\,kpc^{-3}$ while in the lower panel $r_s = 6\,kpc$.

A.1 Parameter Transform

Our MCMC chains include the parameter v_{max}, the peak of the halo rotation curve, from which we must derive the corresponding ρ_s for the (α,β,γ) profile. Our use of v_{max} in preference to ρ_s is motivated by the fact that when ρ_s and r_s are used as chain parameters, their mutual degeneracy means that both contribute to the amplitude of the halo profile (see Fig. A.1). MCMC algorithms are more efficient when the parameters in the chains are chosen to minimise any degeneracies and we found significant improvements in the performance of our algorithm when one parameter scales the halo circular speed curve purely in velocity amplitude, and one scales it purely radially. An additional advantage is that v_{max} is also a physical halo property and hence can be meaningfully compared between galaxies.

For completeness, in this appendix we derive the relation between v_{max} and ρ_s explicitly.

We first define r_{max}, the radius at which the circular speed curve of the dark matter

halo reaches its maximum value $v_{\rm max}$. Differentiating the expression for the circular speed

$$v_{\rm circ}^2(r) = \frac{GM(r)}{r} \tag{A.1}$$

we obtain

$$\frac{d}{dr}v_{\rm circ}^2(r) = 2v_{\rm circ}(r)G\left(4\pi r\rho(r) - \frac{M(r)}{r^2}\right) \tag{A.2}$$

whose maximum occurs when

$$M(r_{\rm max}) = 4\pi r_{\rm max}^3\rho(r_{\rm max}) = r_{\rm max}\frac{v_{\rm max}^2}{G} \tag{A.3}$$

This is a general result that must be true of any halo profile whose density is only a function of radius. Defining the scaled mass $\tilde{M}(r)$ via

$$M(r) = \rho_{\rm s}\tilde{M}(r) \tag{A.4}$$

and rearranging, we obtain the expression to convert between $v_{\rm max}$ and $\rho_{\rm s}$

$$\rho_{\rm s} = \frac{r_{\rm max}v_{\rm max}^2}{G\tilde{M}(r_{max})}. \tag{A.5}$$

where $r_{\rm max}$ is obtained via Eq. A.3, given the values of $v_{\rm max}$ and $r_{\rm s}$. In the text we combine part of this into the value $\Sigma_{\rm max}$, given by

$$\Sigma_{\rm max} = \frac{r_{\rm max}}{\tilde{M}(r_{max})}. \tag{A.6}$$

References

Adams, J. J., Simon, J. D., Fabricius, M. H., et al.: 2014, *ApJ* **789(1)**, 63

Andersen, D. R., Bershady, M. A., Sparke, L. S., et al.: 2006, *The Astrophysical Journal Supplement Series* **166(2)**, 505

Banerjee, A., Jog, C. J., Brinks, E., and Bagetakos, I.: 2011, *Monthly Notices of the Royal Astronomical Society* **415(1)**, 687

Begeman, K. G.: 1989, *Astronomy and Astrophysics* **223**, 47

Bekki, K.: 2008, *Monthly Notices of the Royal Astronomical Society: Letters* **390(1)**, L24

Bell, E. F. and de Jong, R. S.: 2001, *ApJ* **550(1)**, 212

Bershady, M. A., Verheijen, M. A. W., Swaters, R. A., et al.: 2010, *ApJ* **716**, 198

Binney, J. and Merrifield, M.: 1998, *Galactic astronomy / James Binney and Michael Merrifield Princeton, NJ : Princeton University Press, 1998 (Princeton series in astrophysics)* -1

Binney, J. and Tremaine, S.: 2008, *Galactic Dynamics: (Second Edition)*, Princeton Series in Astrophysics, Princeton University Press

Bosma, A.: 1978, *Ph.D. thesis*, PhD Thesis, Groningen Univ., (1978)

Bosma, A.: 1981, *The Astronomical Journal* **86**, 1791

Bosma, A.: 2003, *Revista Mexicana de Astronomia y Astrofisica Conference Series* **17**, 15

Bourne, M. A., Nayakshin, S., and Hobbs, A.: 2014, *Monthly Notices of the Royal Astronomical Society* **441(4)**, 3055

Bullock, J. S., Kolatt, T. S., Sigad, Y., et al.: 2001, *MNRAS* **321**, 559

Burkert, A.: 1995, *The Astrophysical Journal* 447(1)

Burles, S., Nollett, K. M., and Turner, M. S.: 2000, *arXiv.org*

Byrd, R., Lu, P., Nocedal, J., and Zhu, C.: 1995, *SIAM Journal on Scientific Computing* **16**, 1190

Carignan, C., Chemin, L., Huchtmeier, W. K., and Lockman, F. J.: 2006, *ApJ* **641(2)**, L109

Carignan, C. and Purton, C.: 1998, *ApJ* **506**, 125

Casertano, S.: 1983, *Monthly Notices of the Royal Astronomical Society* **203**, 735

Chemin, L., de Blok, W. J. G., and Mamon, G. A.: 2011, *The Astronomical Journal* **142(4)**, 109

Collaboration, T. P., Ade, P. A. R., Aghanim, N., et al.: 2013, *Astronomy and Astrophysics*

Corbelli, E.: 2003, *Monthly Notices of the Royal Astronomical Society* **342(1)**, 199

Corbelli, E. and Salucci, P.: 2000, *Monthly Notices of the Royal Astronomical Society* **311(2)**, 441

Corbelli, E., Thilker, D., Zibetti, S., Giovanardi, C., and Salucci, P.: 2014, *Astronomy and Astrophysics* **572**, A23

Cram, T. R., Roberts, M. S., and Whitehurst, R. N.: 1980, *Astronomy and Astrophysics Supplement Series* **40**, 215

Croom, S. M., Lawrence, J. S., Bland-Hawthorn, J., et al.: 2012, *Monthly Notices of the Royal Astronomical Society* pp no–no

Dame, T. M., Hartmann, D., and Thaddeus, P.: 2001, *ApJ* **547(2)**, 792

de Blok, W. J. G., Bosma, A., and McGaugh, S.: 2003, *Monthly Notices of the Royal Astronomical Society* **340(2)**, 657

de Blok, W. J. G., Walter, F., Brinks, E., et al.: 2008, *Nature* **136**, 2648

de Naray, R. K., McGaugh, S. S., and de Blok, W. J. G.: 2008, *ApJ* **676(2)**, 920

Dehnen, W.: 2000, *ApJ* **536**, L39

Dehnen, W.: 2002, *Journal of Computational Physics* **179**, 27

Dekel, A. and Silk, J.: 1986, *ApJ* **303**, 39

Di Cintio, A., Brook, C. B., Maccio, A. V., et al.: 2013, *Monthly Notices of the Royal Astronomical Society* **437(1)**, 415

Donato, F., Gentile, G., and Salucci, P.: 2004, *MNRAS* **353**, L17

Dubinski, J. and Carlberg, R. G.: 1991, *ApJ* **378**, 496

Einasto, J.: 1965, *Trudy Astrofizicheskogo Instituta Alma-Ata* **5**, 87

Einasto, J.: 1969, *Astronomische Nachrichten* **291**, 97

Elmegreen, B. G., Wilcots, E., and Pisano, D. J.: 1998, *ApJ* **494**, L37

Flores, R. A. and Primack, J. R.: 1994, *ApJ* **427**, L1

Freedman, W. L. and Madore, B. F.: 1990, *ApJ* **365**, 186

Gamow, G.: 1946, *Phys. Rev.* **70(7-8)**, 572

Gelato, S. and Sommer-Larsen, J.: 1999, *Monthly Notices of the Royal Astronomical Society* **303(2)**, 321

Gentile, G., Burkert, A., Salucci, P., Klein, U., and Walter, F.: 2005, *ApJ* **634**, L145

Gentile, G., Salucci, P., Klein, U., Vergani, D., and Kalberla, P.: 2004, *MNRAS* **351**, 903

Gnedin, O. Y. and Zhao, H.: 2002, *Monthly Notices of the Royal Astronomical Society* **333(2)**, 299

Governato, F., Brook, C., Mayer, L., et al.: 2010, *Nature* **463(7278)**, 203

Governato, F., Willman, B., Mayer, L., et al.: 2007, *Monthly Notices of the Royal Astronomical Society* **374(4)**, 1479

Governato, F., Zolotov, A., Pontzen, A., et al.: 2012, *Monthly Notices of the Royal Astronomical Society* **422(2)**, 1231

Gültekin, K., Richstone, D. O., Gebhardt, K., et al.: 2009, *ApJ* **698(1)**, 198

Hague, P. R. and Wilkinson, M. I.: 2013, *Monthly Notices of the Royal Astronomical Society* **433(3)**, 2314

Hague, P. R. and Wilkinson, M. I.: 2014, *Monthly Notices of the Royal Astronomical Society* **443(4)**, 3712

Hague, P. R. and Wilkinson, M. I.: 2015, *ApJ* **800(1)**, 15

Hastings, W. K.: 1970, *biomet.oxfordjournals.org*

Hernquist, L.: 1990, *ApJ* **356**, 359

Jarrett, T. H., Chester, T., Cutri, R., Schneider, S. E., and Huchra, J. P.: 2003, *The Astronomical Journal* **125(2)**, 525

Kahn, F. D. and Waltjer, L.: 1959, *ApJ* **130**, 705

Kapteyn, J. C.: 1922, *ApJ* **55**, 302

Katz, H., McGaugh, S. S., Sellwood, J. A., and de Blok, W. J. G.: 2014, *MNRAS* **439**, 1897

Kennicutt, Jr., R. C., Armus, L., Bendo, G., et al.: 2003, *PASP* **115**, 928

Kim, C.-G., Kim, W.-T., and Ostriker, E. C.: 2011, *ApJ* **743(1)**, 25

King, A.: 2003, *ApJ* **596(1)**, L27

Kroupa, P.: 2001, *Monthly Notices of the Royal Astronomical Society* **322(2)**, 231

Kuzio de Naray, R., McGaugh, S. S., de Blok, W. J. G., and Bosma, A.: 2006, *The Astrophysical Journal Supplement Series* **165(2)**, 461

Leroy, A. K., Walter, F., Bigiel, F., et al.: 2009, *The Astronomical Journal* **137(6)**, 4670

Leroy, A. K., Walter, F., Brinks, E., et al.: 2008, *The Astronomical Journal* **136(6)**, 2782

Lewis, A. and Bridle, S.: 2002, *Phys. Rev.* **D66**, 103511

Maccio, A. V., Stinson, G., Brook, C. B., et al.: 2011, *ApJ* **744(1)**, L9

McConnachie, A. W., Irwin, M. J., Ferguson, A. M. N., et al.: 2005, *Monthly Notices of the Royal Astronomical Society* **356(3)**, 979

McMillan, P. J. and Dehnen, W.: 2007, *Monthly Notices of the Royal Astronomical Society* **378(2)**, 541

Meidt, S. E., Schinnerer, E., van de Ven, G., et al.: 2014, *ApJ* **788(2)**, 144

Metropolis, N. and Rosenbluth, A. W.: 1953, *The journal of* . . .

Milgrom, M.: 1983, *ApJ* **270**, 365

Miller, M. and Bregman, J.: 2013, *ArXiv e-prints*

Moore, B.: 1994, *Nature* **370**, 629

Navarro, J. F., Frenk, C. S., and White, S. D. M.: 1996, *ApJ* **462**, 563

Navarro, J. F., Frenk, C. S., and White, S. D. M.: 1997, *ApJ* **490**, 493

Navarro, J. F., Hayashi, E., Power, C., et al.: 2004, *MNRAS* **349**, 1039

Nayakshin, S. and Wilkinson, M. I.: 2013, *Monthly Notices of the Royal Astronomical Society* **433(1)**, 324

Ogiya, G. and Mori, M.: 2012, *eprint arXiv:1206.5412*

Oh, S.-H., de Blok, W. J. G., Brinks, E., Walter, F., and Kennicutt, Jr., R. C.: 2011, *AJ* **141**, 193

Oh, S.-H., de Blok, W. J. G., Walter, F., Brinks, E., and Kennicutt, R. C.: 2008, *The Astronomical Journal* **136(6)**, 2761

Oort, J. H.: 1932, *Bulletin of the Astronomical Institutes of the Netherlands* **6**, 249

Parry, O. H., Eke, V. R., Frenk, C. S., and Okamoto, T.: 2011, *Monthly Notices of the Royal Astronomical Society* **419(4)**, 3304

Persic, M. and Salucci, P.: 1988, *MNRAS* **234**, 131

Persic, M. and Salucci, P.: 1991, *ApJ* **368**, 60

Persic, M., Salucci, P., and Stel, F.: 1996, *MNRAS* **281**, 27

Pizzella, A., Corsini, E. M., Sarzi, M., et al.: 2008, *Monthly Notices of the Royal Astronomical Society* **387(3)**, 1099

Pontzen, A. and Governato, F.: 2012, *Monthly Notices of the Royal Astronomical Society* **421(4)**, 3464

Press, W. H., Teukolsky, S. A., Vetterling, W. T., and Flannery, B. P.: 2007, *Numerical Recipes 3rd Edition: The Art of Scientific Computing*, Cambridge University Press, New York, NY, USA, 3 edition

Puglielli, D., Widrow, L. M., and Courteau, S.: 2010, *The Astrophysical Journal* **715(2)**, 1152

Read, J. I. and Gilmore, G.: 2005, *Monthly Notices of the Royal Astronomical Society* **356(1)**, 107

Reyes, R., Mandelbaum, R., Gunn, J. E., Pizagno, J., and Lackner, C. N.: 2011, *Monthly Notices of the Royal Astronomical Society* **417(3)**, 2347

Rubin, V. C. and Ford, W. K. J.: 1970, *ApJ* **159**, 379

Rubin, V. C., Thonnard, N., and Ford, Jr., W. K.: 1978, *ApJ* **225**, L107

Sales, L. V., Navarro, J. F., Theuns, T., et al.: 2012, *Monthly Notices of the Royal Astronomical Society* **423(2)**, 1544

Salpeter, E. E.: 1955, *ApJ* **121**, 161

Salucci, P., Lapi, A., Tonini, C., et al.: 2007, *MNRAS* **378**, 41

Sanders, R. H.: 2003, *Monthly Notices of the Royal Astronomical Society* **342(3)**, 901

Schaye, J., Crain, R. A., Bower, R. G., et al.: 2014, *Monthly Notices of the Royal Astronomical Society* **446(1)**, 521

Schoenmakers, R. H. M., Franx, M., and de Zeeuw, P. T.: 1997, *Monthly Notices of the Royal Astronomical Society* **292**, 349

Seigar, M. S.: 2011, *ISRN Astronomy and Astrophysics* **2011(2)**, 1

Seigar, M. S., Barth, A. J., and Bullock, J. S.: 2008, *Monthly Notices of the Royal Astronomical Society* **389(4)**, 1911

Sofue, Y. and Kato, T.: 1981, *Publications of the Astronomical Society of Japan* **33**, 449

Solomon, P. M., Rivolo, A. R., Barrett, J., and Yahil, A.: 1987, *ApJ* **319**, 730

Spergel, D. N., Verde, L., Peiris, H. V., et al.: 2003, *The Astrophysical Journal Supplement Series* **148(1)**, 175

Stark, A. A. and Binney, J.: 1994, *ApJ* **426**, L31

Su, M., Slatyer, T. R., and Finkbeiner, D. P.: 2010, *ApJ* **724**, 1044

Trachternach, C., de Blok, W. J. G., Walter, F., Brinks, E., and Kennicutt, R. C.: 2008, *The Astronomical Journal* **136(6)**, 2720

Trujillo-Gomez, S., Klypin, A., Primack, J., and Romanowsky, A. J.: 2011, *ApJ* **742(1)**, 16

van den Bosch, F. C. and Swaters, R. A.: 2001, *MNRAS* **325**, 1017

van der Kruit, P. C. and Shostak, G. S.: 1982, *Astronomy and Astrophysics* **105**, 351

van der Marel, R. P., Fardal, M., Besla, G., et al.: 2012, *ApJ* **753(1)**, 8

van der Marel, R. P. and Guhathakurta, P.: 2008, *ApJ* **678(1)**, 187

Vera-Ciro, C. A., Sales, L. V., Helmi, A., et al.: 2011, *MNRAS* **416**, 1377

Vogelsberger, M., Genel, S., Springel, V., et al.: 2014, *Monthly Notices of the Royal Astronomical Society* **444(2)**, 1518

Wagoner, R. V.: 1973, *ApJ* **179**, 343

Walter, F., Brinks, E., de Blok, W. J. G., et al.: 2008, *The Astronomical Journal* **136(6)**, 2563

Widrow, L. M., Perrett, K. M., and Suyu, S. H.: 2003, *ApJ* **588(1)**, 311

Wilson, C. D.: 1995, *The Astrophysical Journal* **448(2)**, L97

Zhao, H.: 1996, *Monthly Notices of the Royal Astronomical Society* **278(2)**, 488

Zubovas, K., King, A. R., and Nayakshin, S.: 2011, *MNRAS* **415**, L21

Zubovas, K. and Nayakshin, S.: 2014, *Monthly Notices of the Royal Astronomical Society* **440(3)**, 2625

Zubovas, K., Nayakshin, S., King, A., and Wilkinson, M.: 2013, *Monthly Notices of the Royal Astronomical Society* **433(4)**, 3079

Zwicky, F.: 1937, *ApJ* **86**, 217